Jiye Cai *Editor*

Atomic Force Microscopy in Molecular and Cell Biology

Springer

Atomic Force Microscopy in Molecular and Cell Biology

Jiye Cai
Editor

Atomic Force Microscopy in Molecular and Cell Biology

Springer

Editor
Jiye Cai
State Key Laboratory of Quality Research in Chinese Medicines
Macau University of Science and Technology
Macau, China

Department of Chemistry
Jinan University
Jinan, China

ISBN 978-981-13-1509-1 ISBN 978-981-13-1510-7 (eBook)
https://doi.org/10.1007/978-981-13-1510-7

Library of Congress Control Number: 2018957463

This Springer imprint is published by the registered company Springer Nature Singapore Pte Ltd.
The registered company address is: 152 Beach Road, #21-01/04 Gateway East, Singapore 189721, Singapore

Preface

The progress in biomedical and life sciences made in twenty-first century is significant to human health. On the other hand, the human body is formed by a huge number of cells and each of them is composed of countless biomolecules. To improve the efficacy of therapies for human diseases, a better understanding of how different types of human cells work in both physiological and pathological conditions is crucial. Cell biomolecules, including proteins, DNA, and RNA, cooperate to form a living system that can realize cell endocytosis and exocytosis, growth, migration, proliferation, differentiation, and apoptosis. Each biomolecule is in the size range of a few nanometers to dozens of nanometers, and these biomolecules work together like a nanoscale "robot." However, nanoscale biomolecules are too small to be imaged with traditional microscopes, and vacuum-based electron microscopes cannot be used to image living cells in physiological conditions. Fortunately, the development of scanning probe microscopy(SPM), such as scanning tunneling microscopy(STM), near-field scanning optical microscopy(NSOM), and atomic force microscopy (AFM), provides a new type of powerful tool for life science and cell research. Scanning probe microscopes can be used to directly image cell surface at an atomic/molecular level resolution and detect local cellular properties in different conditions even in solution. With SPM great achievement has been realized in various research fields.

The aim of this book is to describe AFM and introduce some of recent important results by using AFM. The main contents include (i) principles of AFM, (ii) in situ single molecule imaging of cell membranes, (iii) single molecule force spectroscopy, (iv) high resolution imaging of cells, (v) mechanical property changes of diseased versus healthy cells, (vi) observation of cell-drug interactions, (vii) novel high speed high resolution AFM techniques, and (viii) established and potential applications for AFM in molecular and cell biology. The authors are experts in AFM application and working in cell research for a long time. I believe this book will provide a useful reference to the people interested in AFM and its application including but not limited to cell biomolecules and life science.

Institute of Chemistry, Chinese Academy of Sciences
Beijing, China

Li-Jun Wan

Acknowledgments

I am grateful to Ms. Becky Zhao and Springer Nature for their many efforts toward completing this book.

I am grateful to all chapter authors of this book and many journals who permitted to quote their published papers as references in this book.

I am grateful to State Key Laboratory of Quality Research in Chinese Medicines, Macau University of Science and Technology, and FDCT(Macau) 028/0416/A1 for supporting our work and helping us in completing this book.

Contents

List of Contributors

Hongjie An Division of Physics and Applied Physics, Nanyang Technological University Singapore, Singapore, Singapore

Huai-Hong Cai College of Chemistry and Materials Science, Jinan University, Guangzhou, China

Jiye Cai State Key Laboratory of Quality Research in Chinese Medicines, Macau University of Science and Technology, Macau, China

Department of Chemistry, Jinan University, Jinan, China

Filomena A. Carvalho Instituto de Medicina Molecular, Faculdade de Medicina, Universidade de Lisboa, Lisbon, Portugal

Zhengwei Chen Department of Microbiology and Immunology, Center for Primate Biomedical Research, University of Illinois College of Medicine, Chicago, IL, USA

Xing-Xing Cheng Department of Chemistry, College of Chemistry and Materials Science, Jinan University, Guangzhou, People's Republic of China

Sui-Ping Deng Department of Chemistry, College of Chemistry and Materials Science, Jinan University, Guangzhou, People's Republic of China

Colin E. Evans Department of Pediatrics, Feinberg School of Medicine, Northwestern University, Chicago, IL, USA

Youjie Fan JPK Instruments AG, Shanghai, China

Xiao Feng Food Science and Technology Programme, c/o Department of Chemistry, National University of Singapore, Singapore, Singapore

Yunchang Guo JPK Instruments AG, Shanghai, China

Jinhuan Jiang State Key Laboratory of Quality Research in Chinese Medicines, Macau University of Science and Technology, Macau, China

Hua Jin State Key Laboratory of Quality Research in Chinese Medicines, Macau University of Science and Technology, Macau, China

Feinberg School of Medicine, Northwestern University, Evanston, IL, USA

Junhong Lü Shanghai Institute of Applied Physics, Chinese Academy of Sciences, Shanghai, China

Wen-Rong Li Department of Chemistry, College of Chemistry and Materials Science, Jinan University, Guangzhou, People's Republic of China

Jiang Pi Department of Immunology and Microbiology, University of Illinois at Chicago, Chicago, IL, USA

State Key Laboratory of Quality Research in Chinese Medicines, Macau University of Science and Technology, Macau, China

Nuno C. Santos Instituto de Medicina Molecular, Faculdade de Medicina, Universidade de Lisboa, Lisbon, Portugal

Hao Sun Bruker Nano Surface, Singapore, Singapore

Wanxin Sun Bruker Nano Surface, Singapore, Singapore

Chao Tang Shanghai Institute of Applied Physics, Chinese Academy of Sciences, Shanghai, China

Xiao Tang College of Chemistry and Materials Science, Jinan University, Guangzhou, China

Wandang Wang State Key Laboratory of Quality Research in Chinese Medicines, Macau University of Science and Technology, Macau, China

Yi-Li Yang Department of Chemistry, College of Chemistry and Materials Science, Jinan University, Guangzhou, People's Republic of China

Hongshun Yang Food Science and Technology Programme, c/o Department of Chemistry, National University of Singapore, Singapore, Singapore

Ming Ye Bruker Nano Surface, Singapore, Singapore

Xueyi Zeng College of Chemistry and Materials Science, Jinan University, Guangzhou, China

Yue Zhao State Key Laboratory of Quality Research in Chinese Medicines, Macau University of Science and Technology, Macau, China

Liyun Zhong School of Information and Optoelectric Science and Engineering, South China Normal University, Guangzhou, Guangdong, China

About the Editor

Jiye Cai, Ph.D., Distinguished Professor of State Key Laboratory of Quality Research in Chinese Medicines, Macau University of Science and Technology; Professor of Department of Chemistry, Jinan University. 1962–1968 studied and graduated from Department of Physics, Peking University; 1983–1985 visiting scholar at Columbia Radiation laboratory, Columbia University; 1992–1994 senior visiting scholar at Department of Chemistry, Stanford University. He and his collaborator have published more than 100 SCI papers and 12 patents. He has trained over 60 graduated students and 25 students have been professors and senior engineers.

Chapter 1
Principles of Atomic Force Microscopy

Wanxin Sun

Abstract Clearly understanding the working principles of different modes of atomic force microscopy (AFM) is important for users to choose suitable measurement modes for their research projects, optimize working parameters, identify artifacts, and interpret data. In this chapter, conventional imaging modes and force modes will be discussed first, followed by the introduction of recent developments in AFM quantitative nano-mechanical properties measurement.

Since it was invented three decades ago (Binnig G, Quate CF, Gerber C, Phys Rev Lett 56:930–933, 1986), AFM has been becoming a more and more important instrument in nano science and technology. The uniqueness of AFM is its capability of providing nanometer spatial resolution in three dimensions while no vacuum or contrast reagent is needed. AFM has been extensively used in virtually every branch of science and engineering and contributes to many discoveries in nanomaterials, such as the discovery of graphene. In recent years, AFM has been further developed in three aspects. 1. conveying more material related information, such as mechanical, electrical, magnetic and thermal properties at nanometer scale; 2. integrating with different advanced optical techniques, including Raman, fluorescence, infrared spectroscopy; 3. incorporating with environment control for life science and material researches, such as temperature, liquid environment with pH and other ion strength control, light illumination. With these developments, AFM has been extending it applications beyond topographic imaging, such as polymer phase transition under different temperature, I-V characteristics in today's semiconductor devices, live cell dynamics under different chemical/mechanical stimuli, molecular dynamics under different temperature and chemical environments.

On the other hand, the expanded capabilities of AFM make it difficult for users to choose a proper measurement mode, suitable probes and optimize operation parameters. Many efforts have been made to develop different smart scan modes, including peak force tapping developed by Bruker, where software can tune operation parameters to achieve optimized image quality. However, it is still users' task

W. Sun (✉)
Bruker Nano Surface, Singapore, Singapore
e-mail: wanxin.sun@bruker.com

J. Cai (ed.), *Atomic Force Microscopy in Molecular and Cell Biology*,
https://doi.org/10.1007/978-981-13-1510-7_1

to choose measurement modes, identify artifacts, interpret data for their research projects. All these need users to clearly understand the working principles of different modes. In this chapter, conventional imaging modes and force modes will be discussed first, followed by the introduction of recent developments in AFM quantitative nano-mechanical properties measurement.

1 AFM Working Principles

In AFM, a sharp probe runs a raster scan across the sample surface with a positioning accuracy in sub-nanometer level. During the scan, the probe is moved up and down by a feedback close loop to maintain a constant probe-sample interaction. The vertical movements are recorded against XY position to form a surface topography of the sample, as shown in Fig. 1.1. The nano positioning in an AFM is achieved by

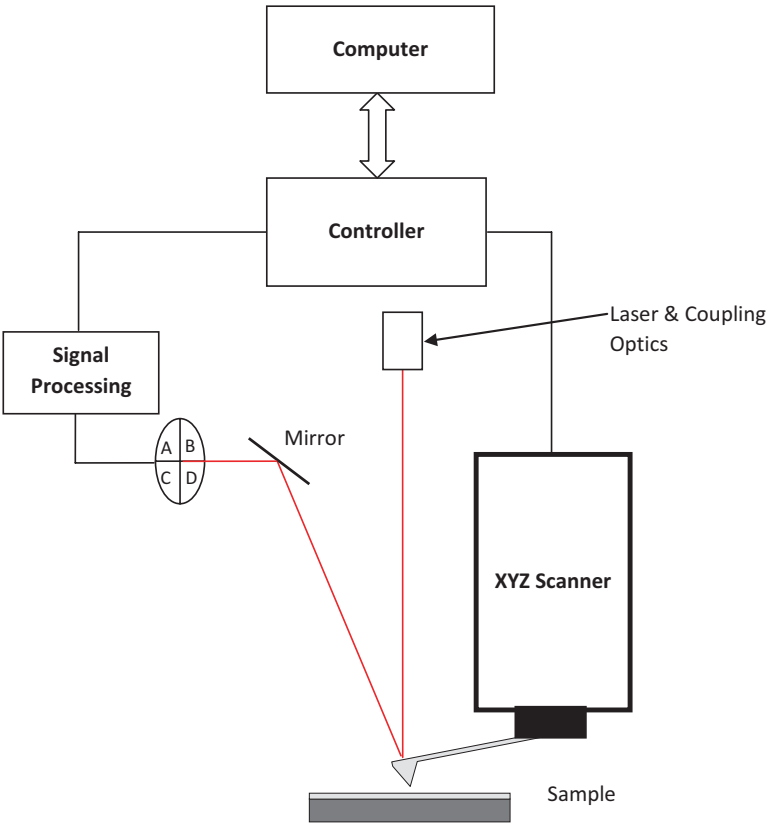

Fig. 1.1 Schematic diagram of an atomic force microscope. (The diagram is not in scale.) The laser emitted from the laser diode is focused onto the end of the cantilever. The reflected laser beam is redirected to a quadrant photodiode. The vertical and lateral movements of the cantilever is detected by the photodiode. The feedback close loop is implemented in the controller. The computer is used to setup parameters for the controller and collect data from it to form images

piezoelectric scanners, where the movements in XYZ are driven by high voltages in the range of hundreds of volts. Intrinsically, piezoelectric material does not response linearly to the voltage applied. If linear voltages are applied to the scanner, the recorded images are distorted by the nonlinear motion of piezo scanner. To correct this issue, there are two prevailing methods in today's AFMs. One is to add XYZ position sensors to monitor actual movements of the scanner and correct the nonlinearity through a feedback close loop, where the voltages applied to the scanner are tuned until the scanner reaches the desired positions. This method is usually called close loop. Different position sensors have been developed for AFM, including capacitive sensor, inductive sensor, strain gauge, and optical sensors. All of them work well as long as they are implemented properly. The other approach is to model the nonlinearity first, and then use nonlinear voltage to drive the scanner to obtain linear movement. In this approach, a certified calibration grid is scanned by the scanner with different scan speed, scan size, scan angle etc. After a series of images are collected, the parameters in the model of scanner movement against applied voltage and scan conditions are extracted by fitting all the images. This method is usually called open loop. Traditionally, open loop is used for high resolution scan as it does suffer from the added noise from the position sensors. With the advances in sensor developments, close loop in today's AFM can achieve similar high resolution performance to open loop. Therefore, more and more users use close loop for routine sample measurement and open loop for atomic resolution measurement.

The commonly used AFM probes consist of a sharp tip and a micro cantilever, as shown in Fig. 1.2. The radius of curve of the today's AFM tip ranges from a few nm to 30 nm, depending on fabrication process and their applications. The micro cantilever is 30–40 μm in width and 125–450 μm in length. The thickness ranges from a fraction of μm to a few μm.

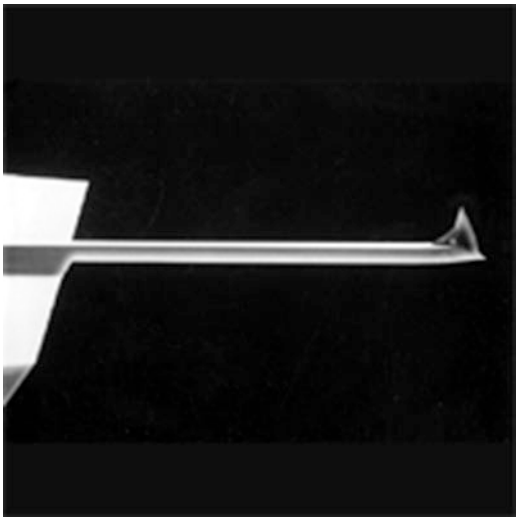

Fig. 1.2 Scanning electron microscopic image of a typical AFM probe, consisting of a sharp tip and a micro cantilever

The cantilever works as a sensor to detect the probe-sample interaction. The interaction between the probe and sample surface is complicating and many types of forces are involved [2]. The detailed discussion about the origins of the interaction forces is beyond the scope of this chapter. Only the aspects directly related to AFM instrumentation and applications, for example, the magnitude of the overall interaction forces, cantilever dynamics changes due to force gradient or energy dissipation during probe-sample interaction, will be discussed. The normal force between the probe and the sample is measured by the cantilever bending, which simply follows Hook's law,

$$F = k\Delta z \tag{1.1}$$

where k is the spring constant of the cantilever, Δz is the cantilever bending in nm.

With a variety of cantilevers available commercially, AFM can measure forces ranging from a few pN to hundreds of μN.

To measure the tiny bending or twisting of cantilever, an optical lever detection scheme is well adopted in AFM, as shown in Fig. 1.3. The laser beam from a laser diode is focused onto the end of the cantilever. The reflected beam from the cantilever surface is redirected to a quadrant photodiode, which is usually called position sensitive photodiode (PSPD) in AFM. When the cantilever bends vertically, the direction of the reflected laser beam changes accordingly. Then the laser spot on the PSPD shifts vertically. In the same way, the twist of the cantilever will cause laser spot on PSPD move laterally. The position of the laser spot is measured by the output of PSPD, i.e. ((A + B)-(C + D))/(A + B + C + D) is proportional to vertical position. ((A + C)-(B + D))/(A + B + C + D) is proportional to lateral position. The

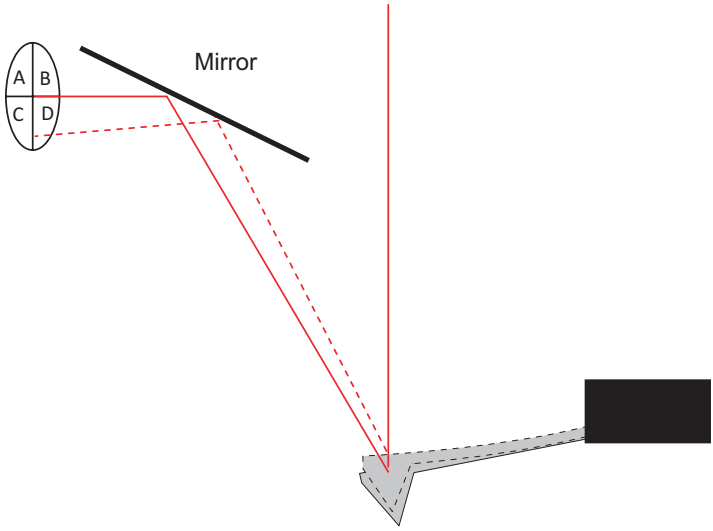

Fig. 1.3 Schematic diagram of optical lever detection system. The solid line drawing and dashed line drawing are laser beams for two cantilever deflection states

normalization to the sum signal of (A + B + C + D) is to eliminate the effect of cantilever reflectivity. It is noted that the optical lever measures the angle of cantilever deflection, not the displacement. Therefore, short cantilever is more sensitive to detect deflection changes.

2 Contact Mode

In contact mode, the normal force, i.e. the vertical deflection of cantilever, is maintained at a constant during scan. When the probe scans across a protruding feature, the cantilever is pushed up, generating an error in vertical deflection. To eliminate this error, the controller will lift the probe until the error becomes zero. For a recessed feature, the probe is lowered to eliminate the deflection error. With an optimized feedback loop, the probe tracks the surface with a constant force to form the topography of the sample. During the scan, lateral/frictional force always exists between the probe and sample. Lateral force can form an image mapping the lateral/friction force distribution across the sample surface, which is called lateral force microscopy (LFM). This has been used to study self-assembled monolayer [3], where different function groups show different frictional forces while their heights are almost the same. While providing rich information about local friction, lateral force also causes problems, for example, lateral force, if not controlled properly, can cause damage to delicate samples and wear out the sharp tip. Take live cells as an example, the measured Young's modulus is in the magnitude of kPa. Force higher than a few nN will cause significant deformation, which leads to low resolution, damage of features and molecules on the cell membrane, and inaccurate morphology. In addition, the force exerted by probe can also work as mechanical stimuli, which may induce a series of responses of cells, including cytoskeleton, focal adhesion complex etc. For biomolecules, large force may induce conformation changes. For live cells, the force should be control from sub nN to several nN. For biomolecules, the force should be ideally controlled to lower than 100pN.

To achieve sub nN force control, cantilever spring constant is a critical parameter. Softer cantilever deflects more under the same load, which is favorable for force detection sensitivity. However, the thermal noise of cantilever and environmental interference prevent users from using cantilevers with ultralow spring constant. For example, cantilevers with a lower spring constant suffer more thermal drift with the temperature variation. The heat generated by the AFM laser or microscope illumination often causes significant drift in deflection for cantilevers with spring constant lower than 0.01 N/m, in the range of a few volts in the PSPD output. Besides temperature, protein adsorption on the cantilever generates stress on one side, resulting in observable deflection change, which has been used as a sensor for protein detection [4]. The drift in cantilever deflection causes instability in imaging. For example, if the cantilever deflection increases with time, the probe will be lifted from the sample surface gradually. This is because the increase in cantilever deflection means higher repulsive force to the controller although it is caused by cantilever deflection

drift only. The response of the controller is to lift the cantilever. The probe may not track the surface anymore if the lift is significant, resulting in part of the image not bearing any sample information. To overcome this issue, higher force must be set to compensate the cantilever drift. Then the image is not obtained at a constant force. Higher force in some part of the image will cause the deleterious effects discussed above. Therefore, too stiff or too soft cantilever is not advisable for live cell imaging. In practice, cantilevers with a spring constant between 0.01 N/m and 0.1 N/m are usually good for imaging live cells. This kind of cantilever is made of silicon nitride in V shape, as shown in Fig. 1.4. Silicon nitride is less reflective than silicon. To increase its reflectivity, a thin layer of Au or Pt is coated on the backside of the cantilever. The thermal expansion coefficient of metal is different from that of silicon nitride, making cantilever bend with temperature change. To relieve the thermal drift, Bruker released a probe with Au coating only at the end of cantilever for laser reflection, the rest of cantilever is uncoated. This probe is insensitive to temperature change and good for cell imaging and force measurement.

AFM can image cells under pseudo physiological conditions with temperature and chemical environment control. To image with AFM, cells must be attached to a support surface. 50–70% confluence is a good trial for most cell types. Too low concentration will make it difficult to locate a cell for AFM imaging. Too high concentration sometimes causes cells overlapping with each other or loosely attached. A large number of cell types can adhere directly onto glass cover slip and plastic ware, e.g. petridish, by normal cell culturing. Whenever needed, Bunsen burner flame treatment [5] and adhesives [6, 7] can be used to enhance cell adhesion. The commonly used adhesives include polylysine, collagen, laminin, Cell-Tak, and PEG derivatives. To avoid debris or unattached cells sticking to the cantilever during imaging, it is advisable to rinse the cell preparation with filtered medium or buffer to remove the cell debris and unattached cells. To maintain the viability of cells, today's biological AFM is equipped with temperature control, CO_2 atmosphere control, gas purging, and perfusion apparatus.

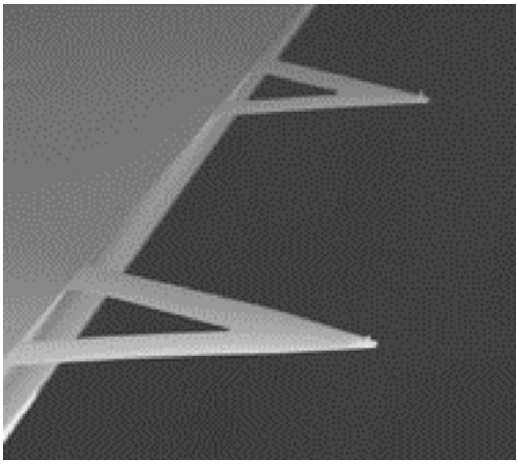

Fig. 1.4 Scanning electron microscopic image of a typical silicon nitride probe suitable for liquid imaging. This kind of probe usually has several cantilevers with different spring constants

As discussed previously, contact force is critically important for live cell imaging. Force adjustment is achieved by changing a parameter called deflection setpoint, at which the cantilever deflection is maintained during scan by the feedback loop. Larger setpoint means higher force. A force between 200pN and 500pN is a good starting point to try for contact mode imaging. A scan rate of 0.5–1 Hz is usually used for cell imaging. In AFM software, the line profiles in both directions (trace and retrace) are displayed. By adjusting the feedback loop gains and scan speed, the trace and retrace profiles will overlap with each other. Higher feedback loop gains make the probe tracking surface faster. On the other hand, oscillation will happen if the gains are set too high. In real operation, increase the gains until slight oscillation is observed. Then decrease the gains slightly to eliminate the oscillation. The highest gains without oscillation are the gains desired. With light force, AFM can produce the fine details on cell surface and accurate height of the cell. Accurate cell height is important to measure cell volume change of neurons during apoptosis. With large force, large deformation on the cell membrane is induced by the probe. The probe can "feel" the hard cytoskeleton filaments, the deflection error image provides rich information on cytoskeleton, as shown in Fig. 1.5. Researchers sometimes increase the force intentionally to get better contrast in cytoskeleton images.

In most time, the cantilever deflection baseline (deflection before the probe touches sample surface) is not zero due to thermal drift or laser adjustment. We need to consider the baseline when we set the setpoint. For example, if the deflection baseline is 200pN, and we want to use 300pN force to image, then setpoint will be 500pN. Therefore, deflection baseline must be measured before imaging. Force-distance curve is well accepted to determine the baseline. It will be discussed in details in the force measurement section. Here we just briefly introduce how to use force-distance curve to determine deflection baseline. After the cantilever is engaged onto the sample surface, the XY scan is stopped and the cantilever is ramped up and down at a specific point by the Z scanner. The cantilever deflection, which is proportional to the force, is recorded against the Z position of the cantilever. The typical

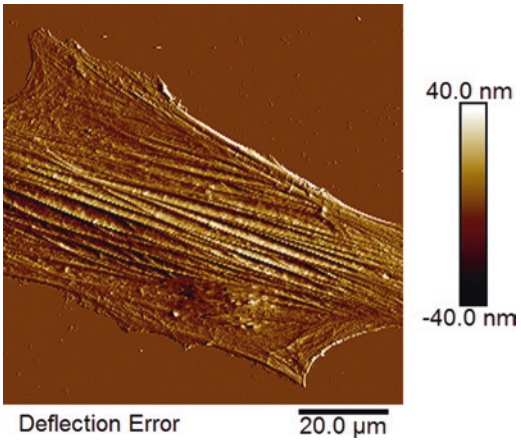

Fig. 1.5 Cytoskeleton revealed by deflection error in contact mode

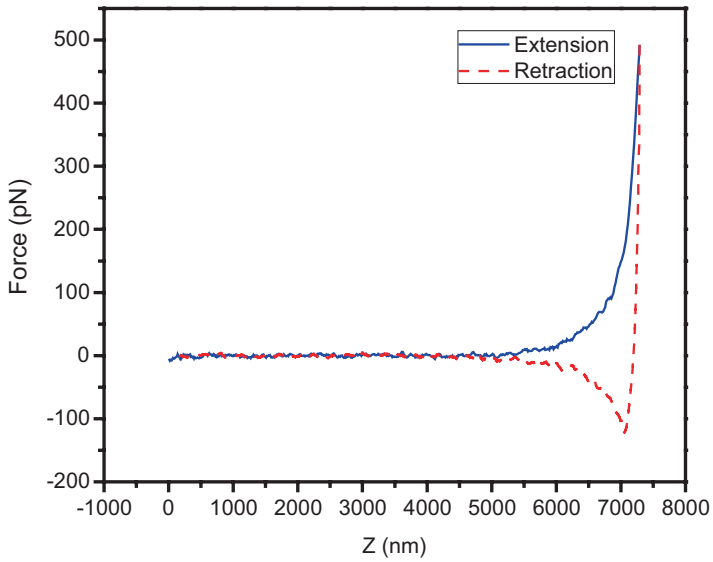

Fig. 1.6 Force-distance curve measured on a live cell. The solid line records the cantilever bending with the probe approaching the cell. The dashed line records the cantilever bending with the probe retracting from the cell. The retraction curve shows an adhesion force of about 150pN

force-distance curve on live cell is shown in Fig. 1.6. The flat region on the left is the cantilever deflection when the probe is not in touch with sample. The average of the flat region will be used as deflection baseline. After the force-distance curve is measured and a proper setpoint is set, the AFM is switched back to imaging mode.

3 Tapping Mode

Tapping mode is also known as intermittent contact mode or AC mode, where the cantilever is oscillated at its resonance frequency or slightly lower frequency. The oscillation is usually driven by a small piece of piezoelectric material embedded in the probe holder. The cantilever oscillation is measured by the changes in laser position on PSPD. The resonance frequency is found by sweeping drive frequency and finding the maximum oscillation amplitude. When the probe is brought to the sample surface by the engaging mechanism, the interaction between tip and sample causes decrease in oscillation amplitude and time lag between the drive signal and cantilever oscillation. At the bottom-most point of each oscillation cycle, the tip contacts the surface instantaneously. That is why tapping mode is also called intermittent contact mode. The amplitude decreases further when the probe is brought closer to the surface, and vice-versa. Thus, the amplitude is a direct measure of tip-sample interaction and the probe is moved up/down during XY raster scan to maintain constant amplitude. The up/down movements against XY position are recorded to form

topography. The time lag is measured by the phase difference between drive signal and cantilever oscillation. Both the amplitude and the phase lag are measured by a lock-in amplifier in AFM. Phase lag is caused by the energy dissipation during each oscillation cycle of the cantilever. When the probe contacts the sample surface, the sample surface undergoes both elastic and plastic deformation, causing energy lost. When it retracts from the sample surface, it often needs to overcome the attractive force and adhesive force. The adhesive force is also a cause for energy lost. Phase lag is related to viscoelastic properties of the sample. Phase lag mapping, also called phase imaging, has been extensively used to differentiate different materials [8].

In practical AFM operation, the operation amplitude (amplitude setpoint) is chosen at about 80% of the free cantilever amplitude. The origin of the phase shift is the resonance frequency shift under tip-sample interaction. How much the phase shifts depends on the material viscoelasticity and the operation parameters. Although phase image has been used extensively in differentiating different materials, such as phase separation in copolymer [9], there is ambiguity in material identification due to its intrinsic nature that phase shift is affected by operation parameters as well as material viscoelasticity. The contrast in phase image can be reversed under different operation conditions. Under light tapping, phase contrast is caused by the adhesive force sensed by the probe. With the increase in tapping force, the material deformation contributes more in the phase contrast. Therefore, the phase contrast under light tapping originates from the adhesiveness, which is often affected by relative humidity in ambient environment. In liquid environment, phase contrast under light tapping has been used to recognize molecules [10]. Under hard tapping, the phase contrast is the combination of adhesive force and material deformation.

Compared with contact mode, the probe contacts sample surface instantaneously in tapping mode. The lateral force is negligible. Tapping mode is good for loosely bound samples, which are easily pushed away by the probe in contact mode. In general, biomolecules and nanoparticles are bound to a substrate loosely. For example, proteins and DNAs are usually bound to mica by charges. In contact mode, the image is not stable as the molecules move with probe during scan. Tapping mode is well adopted for general imaging because it in general induces less sample damage and tip wear, and generates sharper images than contact mode. However, tapping mode is slower than contact mode if the same scanner is used. In principle, it is the cantilever oscillation amplitude used to control the movement in Z direction in tapping mode. Scanning across a recessed feature, such as a hole, it takes time in the scale of milliseconds for the cantilever oscillation amplitude to increase. Therefore, the cantilever dynamics is the bottleneck in tapping mode. No matter how fast the scanner is, 1–2 Hz is usually used in tapping mode for rough samples. In contrast, the deflection in contact mode changes about 1000 times faster than amplitude in tapping mode. The bottleneck is the scanning mechanism rather than the cantilever itself. For samples with large feature heights, such as cells, contact mode is preferred as it can scan faster over a large area.

Different cantilevers have different resonance frequency. For each cantilever mounted into the instrument, its resonance frequency is usually determined by sweeping frequency and searching the maximum oscillation amplitude, which is

done by a function called “auto tune” in software. The viscoelasticity and density of the medium surrounding the cantilever affect its resonance significantly. In aqueous solution, the resonance frequency drops significantly compared with that in air. For example, the resonance frequency in air of a commonly used silicon nitride cantilever is around 50KHz, while it is about 15KHz in water. In air, the response curve in “auto tune” shows a symmetric Gaussian profile and software can detect its resonance frequency automatically. The same cantilever may show a forest of peaks in aqueous solution. Traditionally, AFM users follow the guideline in the AFM manual to choose a suitable frequency. However, with more and more probes are designed for different applications, it may not be easy to find a recommended frequency in manuals or references for new probes. In today’s AFM, thermal tune is usually equipped to determine the cantilever spring constant. The details of thermal tune will be discussed in the force measurement section. For the sake of easy reading, its principle is briefed here. The thermal noise of the cantilever is measured with PSPD after the tapping piezo is stopped. The power spectra density is calculated for different frequency. Then the resonance frequency is clearly identified, as shown in Fig. 1.7.

The cantilever oscillation amplitude affects the imaging stability and resolution. Larger oscillation amplitude is preferred for rough surface, and smaller amplitude is preferred for high resolution. To make the data consistent and comparable among different AFM instruments, it is desirable to use the same oscillation amplitude, at least comparable if not the same. In practical operation, the amplitude measured by PSPD and lock-in amplifier is a voltage. Different AFM may have different gain in PSPD amplifier and different optical path in the optical lever detection scheme. Therefore, the same voltage output from the lock-in amplifier may measure differ-

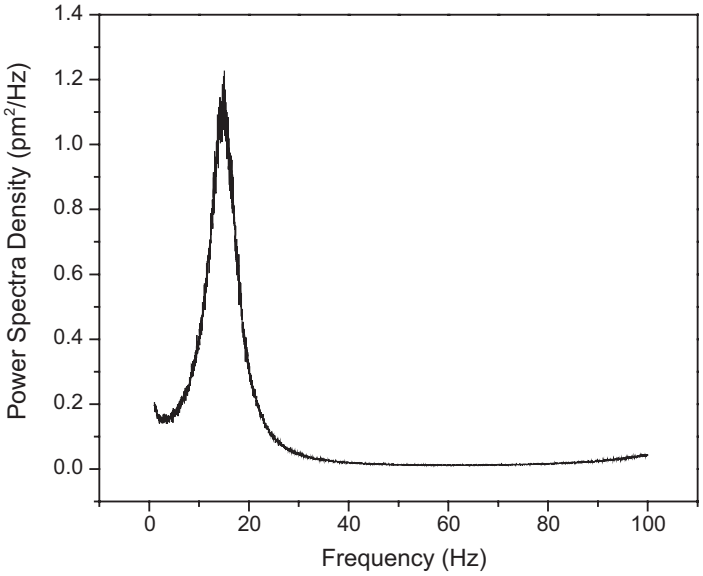

Fig. 1.7 Power spectra density of a silicon nitride cantilever measured in water. The resonance frequency in water is 15 kHz while it is 57 kHz in air

ent oscillation amplitude. Then the scaling factor between voltage and amplitude in nm, also called amplitude sensitivity, must be determined for each type of probe. Here a simple method is described to determine the amplitude sensitivity, the same method can also tell whether the frequency chosen is suitable for tapping mode imaging in aqueous solution. Similar to the force-distance curve in contact mode, the cantilever in tapping mode is ramped by the Z scanner while XY position is fixed. The oscillation amplitude is recorded against the Z position, as shown in Fig. 1.8. When the probe is far from the sample surface, the amplitude does not change significantly with Z position. The slight decrease is caused by the damping effect from the surrounding medium. The narrower the gap between the cantilever and sample surface, the stronger the damping. Once the probe touches the surface at the bottom-most point of each oscillation cycle (shown as mark A in Fig. 1.8), the amplitude starts to decrease rapidly as it is pushed against the surface further. Mark B is the position where the probe fully contacts the sample surface. The slope between A and B is used to measure amplitude sensitivity in nm/V. The steeper the slope, the better the cantilever for imaging as steeper slope means oscillation amplitude is more sensitive to height changes in sample surface. When there are more than one peaks in the tuning curve, the one with steepest slope should be chosen for tapping mode imaging. The amplitude dropping 20% from the corner A is usually a good setpoint.

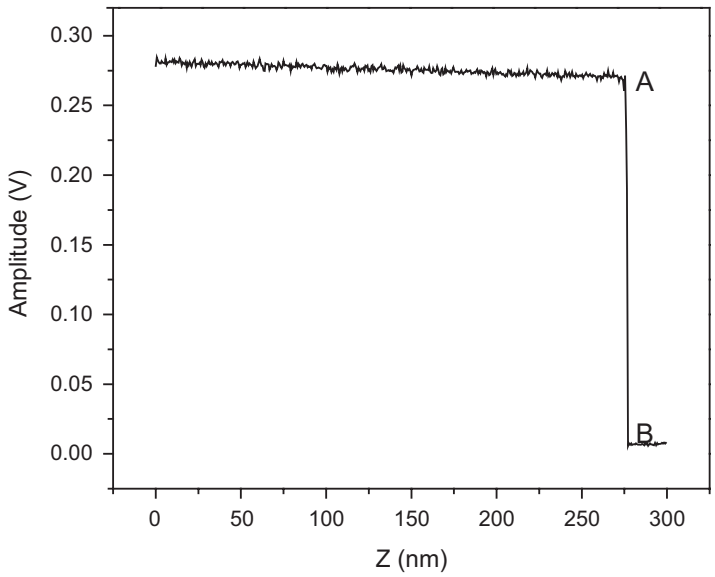

Fig. 1.8 Cantilever oscillation amplitude changes with the Z position in ramp mode. Point A marks the cantilever starts to touch the sample surface at the bottom-most point in each oscillation cycle. Before that, the oscillation amplitude does not decrease significantly. After that, the amplitude decreases rapidly with further decrease in probe-sample distance, until the probe fully contacts the surface, marked as B in the figure. The slope from A to B is used to determine the amplitude sensitivity

Regarding the optimization of feedback loop gains, the tapping mode is similar to contact mode. As discussed earlier, cantilever deflection changes much faster than oscillation amplitude. Contact mode can tolerate higher gains than tapping mode. For example, the gains high enough to cause oscillation in tapping mode may not cause any deleterious effect in contact mode. Optimization of gains is more critical in tapping mode. The oscillation in feedback loop caused by high gains results in noisy images or artifacts. If the gains are too low, the probe will not track the surface properly, resulting in artifacts in images, increased tip wear and sample damage. Therefore, experimental parameters must be tuned more carefully in tapping mode. Among all the parameters, proportional gain, integral gain, setpoint and scan rate are the top parameters to be taken care in tapping mode.

4 PID Feedback Loop

Due to its simplicity and robustness, proportional–integral–derivative controllers (PID controllers) are well adopted in AFM feedback loops, including XY linearization close loop and feedback loop used for topographic imaging. The principle of PID controller and tuning procedure can be found in many text books on process control [11] and articles [12]. Here, we just discuss briefly about its working principle and the tuning procedure suitable for AFM. The schematic diagram of a PID feedback loop is shown in Fig. 1.9.

When the interaction between the tip and sample changes, the output from the optical lever detection system will deviate from the setpoint. The difference *E(t)* is called error signal. It is logical that the adjustment in Z voltage, ΔV_z, should be proportional to *E(t)*, i.e. $\Delta V_z = PE(t)$. If the proportional gain *P* is set too low, the response of the system is slow also, and the tip cannot track the sample surface with

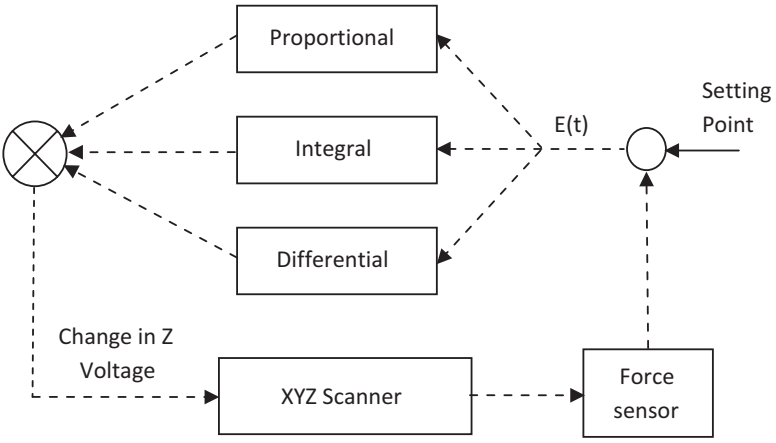

Fig. 1.9 Schematic diagram of PID feedback loop, *E(t)* is the error signal

a constant probe-sample interaction. If P is set too high, the system will oscillate. The system with a proportional gain only is not sensitive to small error signals. Even the error is small, its integration over time might be large if the error has the same sign. For example, small steady error caused by smooth but slightly slant surface has the same sign. In this case, the integration of error is used to eliminate the steady error. For some small but sharp features, error signal is small but changes rapidly. The proportional and integral components are insensitive to this kind of error. This kind of error can be reduced if the derivative of the error signal is included the feedback loop. Synthesizing the three components, PID feedback loop can be expressed as

$$\Delta V_z = PE(t) + I\int_t^0 E(t)\,dt + D\frac{dE(t)}{dt} \tag{1.2}$$

In order to obtain good AFM images and extend the tip's life time, the PID parameters must be optimized. The universal method for generic PID feedback loop will not be discussed in this chapter. The tuning procedure described in this chapter is adapted for AFM imaging.

1. Set the scan size to a few μm, say 1–2 μm, even the final scan size is tens of μm.
2. Increase the integral gain until slight oscillation or noise appears in the trace/retrace profiles. The oscillation or noise can usually be eliminated by increase the proportional gains gradually. If it cannot be eliminated, integral gain should be decreased until oscillation/noise disappears.
3. Check the trace/retrace profile, if the probe cannot track the falling slope while the rising slope is tracked properly, reduce the setpoint in tapping mode (or increase the setpoint in contact mode) gradually to improve the tracking.
4. Reduce scan rate if the probe tracking cannot be improved further by reducing setpoint. It should be noted that reducing scan rate must be taken as the last choice because drift and environmental interference might be pronounced during the long imaging time, resulting in distorted images.
5. Increase the scan size to the desired size. If the tracking becomes poor, repeat step 2 to 4 until the image quality is acceptable.

To improve the resolution, sharper probe and less tapping force are always preferred. Less tapping force is usually achieved by smaller cantilever oscillation amplitude. Therefore, 1/3 of normal tapping amplitude is usually used in molecular imaging, e.g. DNA, protein, polysaccharide and other biomolecules. Fig. 1.10 shows a DNA image obtained in tapping mode.

5 Force Mode

In force mode, the AFM probe is ramped up/down by retracting/extending the Z scanner and the cantilever deflection is recorded against Z position, forming a force-distance curve. A typical force-distance curve measured on mica is shown in

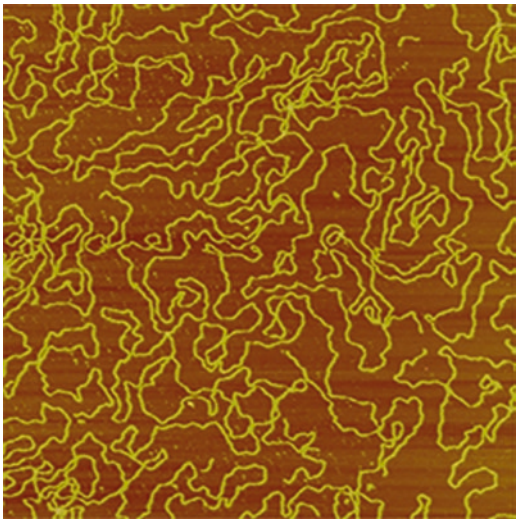

Fig. 1.10 DNA image obtained by tapping mode in buffer solution. The image size is 2 μm. The DNA height measured from the image is more than 2 nm, showing the interaction force between probe and sample is lower than 300pN, otherwise the height is in general less than 2 nm

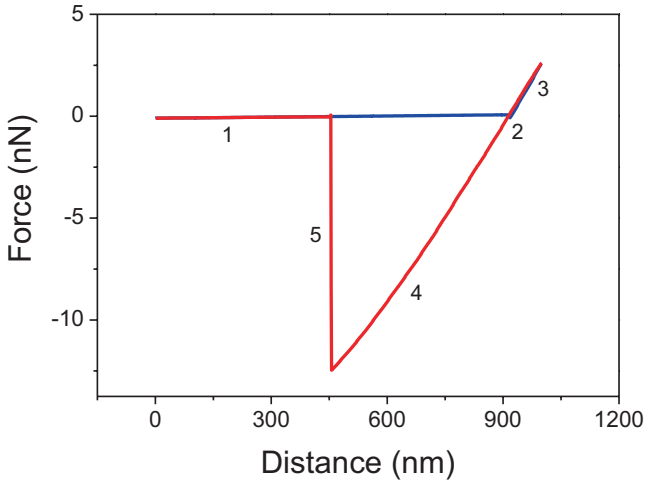

Fig. 1.11 Force-distance curve measured on mica in ambient environment with a relative humidity of 80%. The probe used is a silicon nitride probe (DNP, Bruker)

Fig. 1.11. Before the tip contacts the sample surface, the deflection is a constant, shown as a flat baseline in the force-distance curve, i.e. the segment 1. When the probe is close enough to the sample surface, the attractive force gradient may be greater than the spring constant of the cantilever, snap in will happen, denoted as 2 in the graph. After the probe contacts the surface, the cantilever will bend up with further push against the surface, shown in segment 3. When the preset force is reached, the cantilever will retract from the surface, and deflection decreases accordingly, shown as segment 4. The adhesion force between the probe and sample will

pull the cantilever down further till the force generated by the cantilever is equal to the maximum adhesion force, then the cantilever jumps off from the surface, shown as segment 5, which is usually used to measure the adhesion force. The adhesion force is often used to determine the binding force between antigen and antibody, study surface hydrophobicity by measuring capillary force, and conduct molecular recognition. In ambient environment, capillary force dominates the overall adhesion force. The magnitude of capillary force is determined by the relative humidity and surface hydrophobicity [13]. If the probe and sample are put into controlled environment, interaction mechanism, e.g. the types of interaction force and how the environment changes the interactions, can also be studied. In segment 3, the sample undergoes deformation as well as the cantilever bends up. By studying the relationship between sample deformation and force, material stiffness and modulus can be obtained. If sample undergoes significant plastic deformation, segment 3 and 4 will separate. To obtain modulus under that situation, segment 4 instead 3 will be used to eliminate the effect of plastic deformation. The area enclosed by the different segments is the energy dissipated during each ramp cycle. Material mechanical properties, e.g. Young's modulus, adhesion force, energy dissipation can be extracted from the force-distance curve. In force mode, XY scan is stopped and no lateral force is applied on the sample surface. Scratching on sample surface is rarely observed, unlike contact mode, where the lateral force exists always. In today's AFM, ramps can be programmed at user defined positions or in an array, which are usually implemented by "point and shoot" or "force volume". A series of force-distance curves can be used to construct the topography at a specific force. This method is usually used to image very soft or sticky samples, which are difficult for contact mode and tapping mode.

Comparing force distance curves shown in Figs. 1.6 and 1.11, extension curve and retraction curve are separated in Fig. 1.6. This is because mica is much harder than live cells and the deformation of mica is negligible while live cell undergoes significant plastic deformation. Another obvious difference is the adhesion force, as shown in segment 5 in Fig. 1.11. Mica is hydrophilic and capillary force is strong when measured in ambient environment. In case of live cells, nonspecific binding dominates the overall adhesion force with absence of capillary force. The nonspecific binding force is much smaller than the adhesion force caused by capillary in ambient environment.

Accuracy in force measurement is important for analyzing the interaction mechanism. To obtain accurate force, two parameters need to be calibrated, i.e. cantilever deflection sensitivity and spring constant. Deflection sensitivity measures how many nm in cantilever deflection correspond to 1 V in the PSPD output. It is measured by ramping the probe on a hard surface, for example sapphire. The deformation of such surface is negligible. So the displacement of Z scanner is the same as the deflection of the cantilever, i.e. the slope of the segment 3 in Fig. 1.11 should be 1. In force-distance curve, deflection sensitivity is determined by fitting the segment 3 to a straight line to obtain the slope. The deflection sensitivity making the slope to be 1 is the calibrated value. This process has been automated in today's AFM. To get accurate and repeatable value, the snap-in point and the approach/retract turning

point are usually excluded from the calculation. Deflection sensitivity is determined by the cantilever length and the sensitivity of PSPD. Short cantilever produces better sensitivity and is preferred in measuring displacement in pm range. For a given AFM, the cantilevers with the same length should have the same deflection sensitivity. In real operation, the laser spot may not be aligned to the same position on the cantilever every time. It is normal that the deflection sensitivity of the same cantilever varies slightly after realigning the laser. This is because the change in laser spot position affects the effective length of the cantilever. It is a good practice to measure the deflection sensitivity each time after the laser is re-aligned. With the calibrated deflection sensitivity, how many nm the cantilever deflects can be calculated from the deflection in voltage.

For a cantilever with rectangular cross section, its spring constant can be expressed as

$$k = \frac{Et^3 w}{4L^3} \tag{1.3}$$

where E is the Young's modulus of the cantilever material, e.g. silicon or silicon nitride,

t, w, and L are the thickness, width, and length of the cantilever respectively.

The width and length of a cantilever can be controlled precisely through micro fabrication technology, while the thickness bears more deviation due to its manufacturing process. 10% thickness error will result in about 30% error in spring constant. The nominal spring constant on probe boxes can only be used as an indicative value. Each cantilever must be calibrated to get correct force value. Several methods have been developed to measure cantilever spring constant. The simplest way is to measure the resonance frequency f and check the probe factor b from reference book. The spring constant is calculated by

$$k = b * f^3 \tag{1.4}$$

This method is very easy to use as the resonance frequency can be obtained by "auto tune" in tapping mode. The major drawback is its poor accuracy because the dimensions may be slightly different from those in the reference. For example, the cantilever width affects its spring constant, but not its resonance frequency. If the actual width of cantilever is different from that in the reference, the calculated spring constant will deviate from the real value.

To improve this situation, top view geometry (length and width) is added into the equation as [14].

$$k = 2\pi^3 \sqrt{\frac{\rho^3}{E}} L^3 w f^3 \tag{1.5}$$

where ρ and E are the density and Young's modulus of cantilever material,

L and w are the length and width respectively, usually measured through a well calibrated micrograph of scanning electron microscopy or optical microscopy.

A more accurate method was developed in reference [14] by adding a known mass and measuring the resonance frequency shift, i.e.

$$k = (2\pi)^2 \frac{M}{\left(1/f_l\right)^2 - \left(1/f_0\right)^2} \tag{1.6}$$

where M is the mass added to the cantilever free end, f_0 and f_l are resonance frequencies before and after the mass is added respectively.

This method involves gluing a particle with known mass to the end of cantilever. It is not trivial even with a detailed protocol available [15, 16]. Furthermore, it is even more troublesome to remove the particle after the spring constant is calibrated. Therefore, force measurements are usually done before the calibration. After all experiments are finished, the calibration is carried out and the measurement results are rescaled with the correct spring constant. This method is complicating and the cantilever cannot be used after calibration. This method is rarely used in biological application despite its accuracy.

All the above discussed methods do not measure cantilever *in-situ*. In practice, the laser may not be aligned to the same position as in spring constant measurement. The difference in laser alignment results in difference in cantilever effective length. With the advances in AFM instrumentation, the thermal noise of cantilever has been used to calculate its spring constant. After the deflection sensitivity is calibrated, the cantilever is lifted from the sample surface by at least 100μm and the random motion of cantilever free end is recorded for a period of time. 10 seconds are usually enough to get accurate results. The power spectral density (PSD) is then calculated by Fourier Transformation over the noise recorded, as shown in Fig. 1.7. According to Equipartition Theorem [17],

$$\frac{1}{2} m\omega_0^2 z^2 = \frac{1}{2} k_B T \tag{1.7}$$

where m is the effective mass of the cantilever,

ω_0 and z are the angular frequency and noise amplitude of cantilever free end respectively,

k_B and T are Boltzman constant = 1.3805×10^{-23}joules/Kelvin and absolute temperature in Kelvin,

$\langle\rangle$means averaging over time, which is obtained by integrating PSD over frequency.

Considering $\frac{1}{2} k z^2 = \frac{1}{2} k_B T$, the cantilever spring constant k can be obtained

$$k = k_B T / z^2 \tag{1.8}$$

The mean square of free end amplitude $\langle z^2 \rangle$ is the area under the peak of power spectra density profile.

This method is well accepted because it neither relies on the cantilever geometry, as in method 1 and 2, nor demands the complicating procedure, as in the mass adding method. After further improvement by Butt and Jaschke [18] followed by Hutter [19], the accuracy achieved by the thermal noise method is reliable [20]. In most of today's AFM, this method is automated in software. The frequency range covers from a few KHz to 2 MHz. Virtually all the commercial available cantilevers can be calibrated with this method. For some ultra soft cantilevers, the resonance frequency in liquid is below 2KHz. The Z scanner noise and laser pointing noise in some AFM may limit the accuracy in spring constant measurement. In such case, the spring constant measured in air is a good estimation.

Determining Young's modulus through force-distance curve has been extensively studied [21]. Hertz, DMT, JKR and Maugis models are commonly used to measure Young's modulus of materials [22]. In all the models, good understanding of the probe shape and size is as important as accurate measurement of force. For sample deformation in a few nm, the AFM tip is usually modeled as a sphere. For polymer samples, a few nm deformation produces enough force for accurate measurement in AFM. DMT model with spherical probe is usually used [2].

$$F = \frac{4}{3} E^* \sqrt{R} d^{3/2} + F_{ad} \tag{1.9}$$

where F is the force measured by the probe,

F_{ad} is the adhesion force between tip and sample,

R is the radius of the tip,

d is the sample deformation,

E^* is the reduced Young's modulus $= \frac{E}{1-\nu^2}$, ν is the Poisson Ratio of the material. Young's modulus of the probe material is usually much higher than that of the sample. The deformation of probe is negligible.

Tip geometry can be obtained by either high resolution electron microscopy or tip deconvolution. In the latter method, a reference sample with sharp features is scanned and the morphological dilation is analyzed to extract the tip geometry [23]. It may cause tip wear to scan over such reference sample as it is rough and very hard. So the scan parameters must be optimized carefully. As the relationship between E^* and $\sqrt{R}$ is linear, $\sqrt{R}$ can also be calibrated after sample measurements and rescale E^* with calibrated $\sqrt{R}$.

For soft materials, such as live cells, the deformation is usually in the range of tens of nm, a conical shape is a good estimation of tip shape. In liquid, adhesion force is negligible, Hertz mode with conical tip shape is usually used for live cell measurement,

$$F = \frac{2}{\pi} E^* \left(\tan \alpha\right) d^2 \tag{1.10}$$

where F is the force measured by the probe,

E^* is the reduced Young's modulus of the material,

d is the sample deformation,

α is the half angle of the conical probe.

In practical operation, probes with pyramidal shape are usually used, where the half angles in the two directions are α and β respectively. Equation (1.10) should be revised accordingly,

$$F = \frac{4}{\pi\sqrt{\pi}} E^* \sqrt{\tan\alpha \cdot \tan\beta}\, d^2 \tag{1.11}$$

In AFM measurement, the force is recorded against the scanner Z position rather than the sample deformation. When the cantilever is pushed against the sample, the cantilever bends up while the sample deforms. The sample deformation can be calculated as follow,

$$d = \left(z - z_c\right) - \left(def - def_0\right) \tag{1.12}$$

where z_c is the scanner position at the contact point,

def_0 is the baseline of cantilever deflection,

z and def are the scanner position and cantilever deflection in the force-distance curve.

Baseline deflection def_0 can be obtained easily from force-distance curve. Contact point z_c for hard materials can be obtained by the intersection of the baseline and linear slope. For soft materials, such as cells, it is not easy to tell accurately where the probe starts to contact the sample, as shown in Fig. 1.6. It is a good practice to keep both E^* and z_c as two unknown parameters to be extracted through fitting the force-distance curve to a suitable model. During the fitting procedure, all others quantities are measured from force-distance curve. The reduced Young's modulus extracted from the force curve shown in Fig. 1.6 is 50 KPa. In this fitting, Hertz model with conical tip shape is adopted. The half angles of pyramidal tip are 20° and 17.5°, and spring constant is 0.01 N/m.

Soft cantilever is preferred for force measurement [24]. Deformation is measured by subtracting cantilever deflection from the scanner movement in Z. For soft cantilever, the cantilever deflection and scanner movement in Z is usually much larger than sample deformation. Therefore, soft cantilevers usually produce more error in deformation measurement. On the other hand, force measurement may less accurate if too stiff cantilever is used. Both situations can lead to less accurate Young's modulus. Therefore, it is important to choose a proper cantilever spring constant for a specific modulus range. As a rule of thumb, the ratio of sample deformation to cantilever deflection between 0.1 and 0.2 is a good start to try. In real measurement, the error in deflection sensitivity contributes a significant part in total error as it affects the accuracy in both force and deformation. It must be calibrated carefully. During the deflection sensitivity calibration, at least 5 measurements are

needed to calculate the average. In model selection, a rule of thumb is that DMT model with spherical tip shape is used for the scenario with deformation less than the radius of the tip and Hertz model with conical tip shape is used for large deformation in tens of nm. The Poisson Ratio is usually unknown for most of materials, especially biomaterials. 0.5 is usually used in live cell measurement.

Adhesion force between AFM tip and sample is obtained directly from force-distance curves. There might be a few binding events existing between the AFM tip and substrate. The last force step (jumping off) can be considered as single unbinding [13]. There is a slim chance that two or more unbinding events happen at the last force step simultaneously. To rule out multi-unbinding event, multiple force-distance curves are recorded, and the last force steps are extracted and plotted in a histogram. By reading the peak position in histogram, the most likelihood rupture force of single binding is obtained. Using functionalized probe, adhesion force has been used in measuring hydrophobicity, function group/molecule recognition, and antigen-antibody binding force study.

Another application of force-distance curve is to stretch single molecules, including proteins, polysaccharides and DNAs. By stretching, a protein molecule is unfolded mechanically. This kind of measurements are pursued for a variety of reasons, including fundamental questions about folding, structure and how protein sequence contributes to that. Protein structures are traditionally determined by X-ray crystallography. However, it might not be practical to perform this technique on membrane proteins. Force curve is one of the few ways to gain insight into the protein structure. Fig. 1.12 is a typical unfolding curve of titin, which is an 8-mer construct of IG27 domain. The saw teeth in the retraction curve are caused by unfolding of the domains. When the stretching force reaches the critical value (marked as A in the figure), one domain is unfolded and force decreases suddenly. After the domain is unfolded (marked as B), the force increases gradually as the cantilever stretches the molecule further. The second domain starts to unfold upon the critical force reached (marked as C).

By the fitting the domain extension curve (e.g. from B to C) to worm like chain model [25],

$$F = \frac{kT}{p}\left[\frac{1}{4}\left(1-\frac{x}{L_c}\right)^{-2} - \frac{1}{4} + \frac{x}{L_c}\right] \tag{1.13}$$

the persistence length p and contour length L_c are obtained. In the fitting, the molecular length x is determined by subtracting cantilever deflection from Z scanner traveling distance, similar to the deformation calculation in indentation experiment.

To perform the stretching experiment, one end of the molecule is tethered to a gold substrate by thiol group. The other end is picked up by a soft probe with spring constant ranging from 0.01 N/m to 0.1 N/m. The probe may pick up many molecules if the concentration is too high. On the other hand, many trial and errors have to be performed to pick up a molecule in case that the concentration is too low. 50μg/ml is a good start concentration of titin. Take 25–50 μL of the titin solution

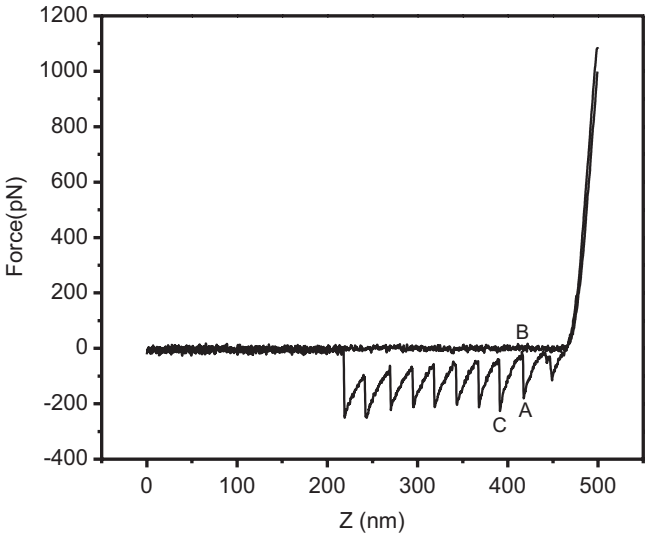

Fig. 1.12 Typical pulling curve of titin unfolding (8-mer construct of IG27 domain). Each saw tooth corresponds to an unfolding event. The probe is retracted after staying on the surface for a fraction of second to catch a protein molecule. During retraction, the adhesion force pulls the cantilever down until reaching critical force at A, where one domain starts to unfold. The force is released because the molecular length increases suddenly. At point B, the domain is fully unfolded. The force increases as the cantilever stretches the molecule further. With the continuing pulling, another critical force is reached at point C, where a new domain starts to unfold

and drop onto a fresh gold surface. After incubation at room temperature for 15 minutes, rinse it with 1–2 mL PBS buffer. Then the sample is mounted into an AFM to perform the force measurement. If the chance of picking up is too low, keeping the probe staying longer on the surface will increase the chance significantly. The stay can be extended to seconds.

6 Peak Force Tapping

AFM was applied to study biological materials from its very start [26]. However, the adoption of this technique in biological and biomedical applications is slow even it is compatible with biological environments. This is mainly because the information provided by AFM is lack of biological specificity. The recent developments in AFM are mainly in expanding its functionalities. Force mode can provide biological specific information by extracting a variety of mechanical properties from force-distance curve, which is typically measured at 1 curve/second. It is prohibitive to achieve the typical spatial resolution of tapping mode due to the intensive time consumption in traditional force mode.

To speed up the force mapping, pulse force mode was introduced in 1997 [27]. In this mode, the probe is modulated by fast sinusoidal ramping rather than the linear ramping in traditional force mode. Pulse force mode improves the efficiency by 3 orders. However, the poor force control in this mode limits its usage in high resolution applications where the probe-sample interaction force should be in the range of sub-nN to several nNs. In force measurement, the cantilever deflection may change with ramping even there is no change in probe-sample interaction because,

1. The ramping motion may not be in parallel with the laser optical axis. Thus, the laser spot on cantilever moves with ramping, resulting in non-flat baseline. In addition, the ramping motion may not follow a straight line. This leads to a nonlinear baseline.
2. When it jumps off from the sample surface in pulling, the cantilever often oscillates at its resonance frequency. The oscillation is severe for soft cantilevers. In ambient environment, the capillary force increases the total adhesion, making the oscillation more pronounced. The oscillation may not be fully damped at the start of the next ramp and it will affect the measurement results.
3. The viscosity of media (liquid or air) can cause deflection change during ramping. This effect becomes severe when the cantilever is close to the sample surface. The damping from the media trapped between the cantilever and sample surface becomes stronger with the decrease in gap.

With the increase in ramping speed, effects of all these factors become even severe. These parasitic deflections contaminate force-distance curves, making accurate force control difficult, especially at high speed. To overcome this issue, Su et al. implemented a method to characterize and parameterize the parasitic deflections for each instrument [28]. After parasitic deflections are removed, clean force-distance curve can be obtained at the speed of KHz by modulating the Z scanner with sinusoidal wave. Within a modulation cycle, the repulsive force reaches its maximum at the bottom-most point, similar to traditional force mode. The peak force (maximum force) is used to control Z scanner movement to make the probe track the sample surface. Compared with traditional force mapping, the peak force tapping mode is more accurate in force measurement (tens of pN can be achieved), and ramping speed is at least 3 orders faster. It is worth noting that the ramping rate is still far below the cantilever resonance frequency, which is typically from tens of KHz to hundreds of KHz. The cantilever works in quasi-static mode. This peak force tapping mode has been implemented in commercial AFM [29], known as ScanAsyst and PeakForce QNM.

Peak force tapping mode does not rely on cantilever dynamics, making it not necessary to search the cantilever resonance frequency. Its operation is also independent of environment. In tapping mode, the cantilever resonance frequency depends on its surrounding media (liquid or air), temperature and as well as cantilever itself. Therefore, the cantilever must be tuned under the same environment as the real experiments. On contrast, no matter which cantilever, no matter in liquid or air, the operation is the same for peak force tapping mode. As discussed early in this chapter, the cantilever deflection drift due to environmental influence, especially

temperature, prohibits the deflection setpoint being set very close to that of free cantilever, making imaging at pN a challenging job. In peak force tapping mode, cantilever deflection drift is corrected at each ramping cycle, so cantilever deflection drift is not an issue anymore. Beside superior force control, another achievement in peak force tapping is that operation parameters are automatically optimized by software. In peak force tapping mode, the Z scanner is moved up/down to maintain a constant peak force. As the error in peak force is linear to topographic error and PID controller is also a linear controller, it is easy to implement automatic parameter optimization. While in tapping mode, the relationship between amplitude and probe-sample distance has hysteresis, i.e. the extension curve and retraction curve do not overlap. This makes it difficult to implement automatic parameter optimization even the amplitude linearly responds to the distance during approach curve, as shown in Fig. 1.8. With superior force control in the range of tens pN, the integrity of biomolecules and probe sharpness are well maintained during the scan. Sub molecular resolution can be readily achieved. DNA double helix structure has been measured with peak force tapping [30].

With a calibrated deflection sensitivity, force-deformation curve is reconstructed by subtracting deflection from the scanner Z movement, as done in traditional force mode. From each curve, Young's modulus, adhesion force, deformation, energy dissipation, and peak force in each tapping cycle are extracted. These material mechanical properties are mapped into different channels and form images for spatial distribution analysis. With the knowledge of tip geometry, the deformation data can be easily converted to indentation hardness [31]. Compared with traditional force mode, the peak force tapping is thousands of times faster as well as providing better force control, making it an ideal mode for high resolution topographic and mechanical imaging. It has been used to image sub-molecular structure of protein molecules [32].

7 Molecular Recognition

Recognizing molecules on substrates or cell membrane based on specific binding has attracted interest from many researchers since more than a decade ago. Force mapping is a commonly used approach to identify molecules and study the ligand-receptor interaction under different environments [33–35]. As discussed previously, force mapping is in general slow and lack of spatial resolution. To improve the speed, a dynamic recognition microscopy was developed [36], where a functionalized probe is oscillated with an amplitude smaller than the length of linker molecule (the typical length is about 6 nm). When recognition happens, the oscillation amplitude of cantilever is decreased due to the interaction force. During the operation, the binding is not disassociated by the cantilever oscillation. The binding pair is ruptured by the lateral pulling force during scan when the distance between the molecule and tip reaches the linker length. Therefore, the size of recognized molecules is dilated by two times of the linker length. With this progress, molecular

recognition can be done at the speed of normal AFM imaging. However, this method cannot provide quantitative binding force.

Another technical challenge is the surface chemistry to functionalize the probe and the substrate. The procedure for probe functionalization includes linkage design and covalently coupling the ligand to the tip surface. The bonding between the ligand and tip surface should be significantly stronger than the ligand - receptor bonds. Otherwise, the functionalized probe may lose its ligand to the substrate, and lose the recognition capability. Poly(ethylene glycol) (PEG) is a well adopted linker because it is water soluble and non-toxic [37]. PEG has been used in a wide range of applications in surface modification and clinical research. The detailed protocols are described in many articles on force measurement, e.g. references [33–37]. To illustrate the concept, the procedure is described here briefly. The first step is to clean the probe thoroughly. This is typically implemented by incubating AFM probe in piranha solution (H_2SO_4/H_2O_2, 90/10 (v/v)) for 30 mins and then rinsing with deionized water. After dried by N_2 blow, the probe is subjected to water plasma to generate SiOH groups on the probe surface [38]. The second step is to bind amines to the tip surface by an esterification protocol described in reference [33]. The third step is to conjugate the linker to the amines on the tip surface. The engineered PEG linker has N-hydroxysuccinimidyl (NHS) residue on one end and a function group to connect the ligand on the other end. The NHS group is used to bind the linker to the amines. The fourth step is to link the ligand to the function group on the end of the engineered linker. PDP (2-pyridyldithiopropionyl residue) and NTA (Ni-Nitriloacetate) [39] are commonly used function groups.

On the substrate side, different surface-binding strategies should be adopted for the different properties of biological samples. Some receptor proteins strongly adhere to mica surface through hydrophobic or electrostatic forces. In this case, direct adsorption provides sufficiently strong anchoring for recognition experiments. Another option is to use sulfur-gold chemistry. Atomically flat gold surface is prepared as a substrate, as in titin pulling experiment discussed previously. If silicon or mica is used as substrate for water-soluble receptors, the same surface chemistry as in probe functionalization can be used. For receptors on cells, directly growing the cells on substrate is typically used. To enhance the cell adhesion to the substrate, the methods discussed in live cell imaging section can also be used in molecular recognition.

Since peak force tapping measures adhesion force directly. With properly functionalized probes, it can be used to recognize molecules or function groups [40]. In addition to molecules on substrate, Fig. 1.13 shows molecular recognition on cell membrane. In this example, red blood cells develop knobs on their surface after infected with malaria parasites. The probe is functionalized with PEG linker and CD36, which is used to recognize Plasmodium falciparum erythrocyte membrane protein 1 (PfEMP1) [41]. It is worth noting that the CD-36 binding sites locate solely on the knobs. Another interesting finding is that the adhesion is free of any topographic artifact, as the debris (marked by white arrow) does not show adhesion force while it is clearly shown in topography. This makes the binding force mapping clean and quantitative.

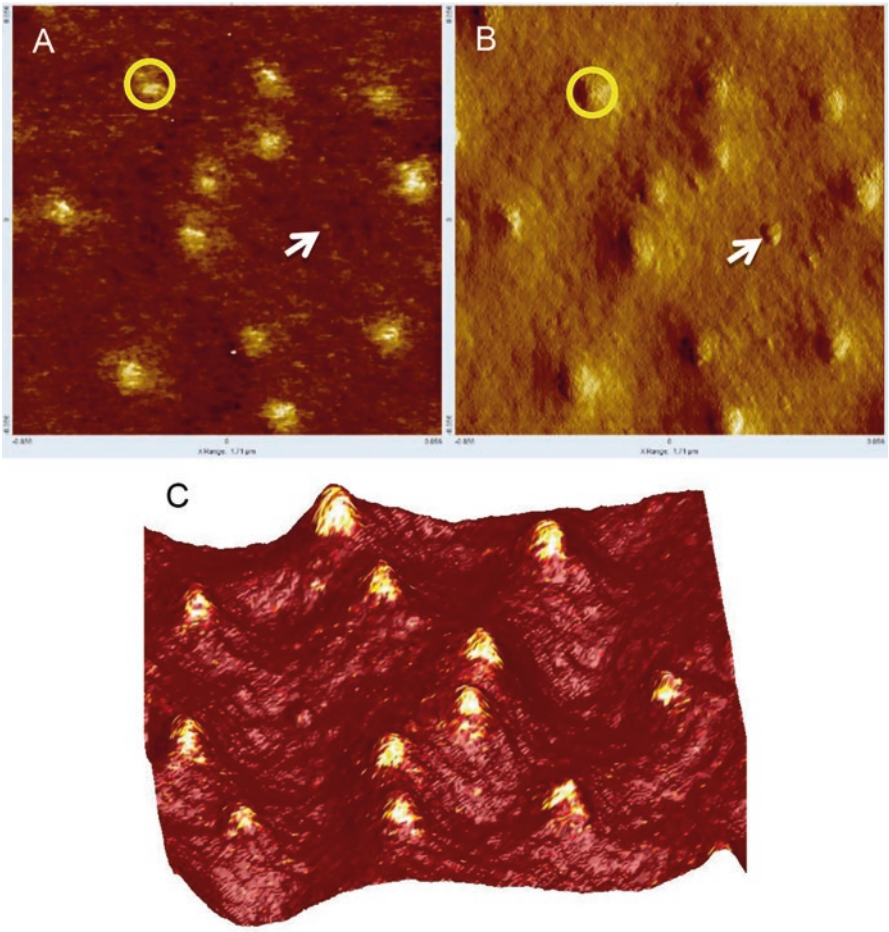

Fig. 1.13 CD-36 binding site recognition on malaria infected red blood cells by peak force tapping mode. (**a**) and (**b**) are adhesion force and peak force error images respectively. Peak force error image reveals the detailed topographic information. (**c**) is the overlay of adhesion force over peak force error. CD-36 binding sites have one-to- one correspondence with knobs, as shown by the circled area in (**a**) and (**b**). The debris marked by arrow in (**b**) does not show adhesion force in A, proving that there is no cross talk between topography and adhesion force. The adhesion force image is topographic artifacts free. (Image courtesy of A. Li, National University of Singapore)

8 Frequency Modulation Mode

Unlike tapping mode where amplitude is used as feedback signal, frequency modulation uses a frequency shift as the feedback signal. It was first introduced by Albrecht T. et al. in 1991 [42]. In this mode, the probe oscillates at a frequency close to its resonance. The resonance frequency of the cantilever is affected by the force gradient between tip and sample. This effect is illustrated in Fig. 1.14. When a

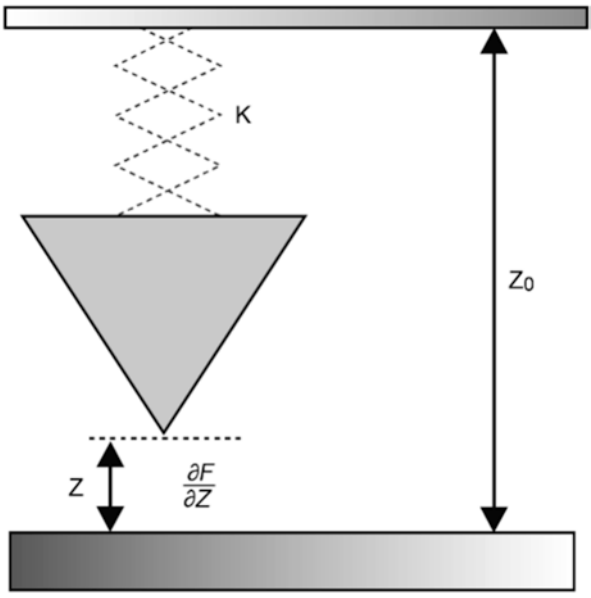

Fig. 1.14 The working principle of a frequency modulation AFM. When a cantilever oscillates in a force field, the force gradient will affect the effective spring constant, and then the resonance frequency

cantilever oscillates in a force field, the effective spring constant of the cantilever is changed by the force gradient; leading to the shift in resonance frequency. Mathematically, the effective spring constant is the superposition of the nature spring constant and the local force gradient. During a scan, the changes of surface topography leads to the resonance frequency shift. The feedback loop maintains a constant frequency by vertically moving the scanner at each location. The constant frequency is called frequency setpoint.

Under small amplitude situation, the frequency shift is proportional to the force gradient of the tip-sample interactions. Compared with long-range interactions, the force gradient of short-range interactions is much higher, so the short-range interactions contribute much more than the long-range interactions. This is believed to be the fundamental reason for high resolution imaging. In spites of its potential in high resolution imaging, frequency modulation is not well adopted in commercial AFM because it does not work stably in ambient environment. The main reason is the capillary between probe and sample cause strong adhesion force. Frequency modulation is mainly used in high vacuum environment, where amplitude modulation does not work due to the high quality factor of the cantilever in vacuum.

In summary, working principles of different AFM modes are discussed in this chapter. Based on the understanding of the working principles, users can choose suitable working mode, proper cantilever, and optimize operation parameters during imaging. It also helps identify image artifacts and interpret AFM results.

Reference

1. Binnig G, Quate CF, Gerber C. Atomic force microscope. Phys Rev Lett. 1986;56:930–3.
2. Israelachvili JN. Intermolecular and surface forces. London: Academic; 1992.
3. Heaton MG, Prater CB, Kjoller KJ Lateral and chemical force microscopy mapping surface friction and adhesion. Bruker application note AN5, Rev. A1. 2004
4. Fritz J. Cantilever biosensors. Analyst. 2008;133:855–63.
5. Thimonier J, Montixi C, Chauvin JP, He HT, Rocca-Serra J, Barbet J. Thy-1 immunolabeled thymocyte microdomains studied with the atomic force microscope and the electron microscope. Biophys J. 1997;73:1627–32.
6. Henderson E, Haydon PG, Sakaguchi DS. Actin filament dynamics in living glial cells imaged by atomic force microscopy. Science. 1992;257:1944–6.
7. Nagayama S, Morimoto M, Kawabata K, Fujito Y, Ogura S, Abe K, Ushiki T, Ito E. AFM observation of three-dimensional fine structural changes in living neurons. Bioimages. 1996;4:111–6.
8. Babcock KL, Prater CB. Phase imaging: beyond topography. Bruker application note AN11, Rev. A1. 2004
9. McLean RS, Sauer BB. Tapping-mode AFM studies using phase detection for resolution of Nanophases in segmented polyurethanes and other block copolymers. Macromolecules. 1997;30:8314–7.
10. Lv Z, Wang J, Chen G, Deng L. Imaging recognition events between human IgG and rat anti-human IgG by atomic force microscopy. Int J Biol Macromol. 2010;47:661–7.
11. Bennett S. A history of control engineering, 1930–1955. London: IET; 1993.
12. Ang KH, Chong G, Li Y. PID control system analysis, design, and technology. IEEE Trans Control Syst Technol. 2005;13:559–76.
13. Sun W, Neuzil P, Kustandi TS, Oh S, Samper VD. The nature of the Gecko Lizard adhesive force. Biophys J. 2005;89:L14–7.
14. Cleveland JP, Manne S, Bocek D, Hansma PK. A nondestructive method for determining the spring constant of cantilevers for scanning force microscopy. Rev Sci Instrum. 1993;64:403–5.
15. Ducker WA, Senden TJ, Pashley RM. Direct measurement of colloidal forces using an atomic force microscope. Nature. 1991;353:239–41.
16. Preuss M, Butt H-J. Direct measurement of particle−bubble interactions in aqueous electrolyte: dependence on surfactant. Langmuir. 1998;14:3164–74.
17. Greiner W, Neise L, Stöcker H. Thermodynamics and statistical mechanics. New York: Springer; 2001.
18. Butt H-J, Jaschke M. Calculation of thermal noise in atomic force microscopy. Nanotechnology. 1995;6:1–7.
19. Hutter JL. Comment on tilt of atomic force microscope cantilevers: effect on spring constant and adhesion measurements. Langmuir. 2005;21:2630–2.
20. Ohler B. Cantilever spring constant calibration using laser Doppler vibrometry. Rev Sci Instrum. 2007;78:063701.
21. Oliver WC, Pharr GM. Measurement of hardness and elastic modulus by instrumented indentation: advances in understanding and refinements to methodology. J Mater Res. 2004;19:3–20.
22. Cappella B, Dietler G. Force-distance curves by atomic force microscopy. Surf Sci Rep. 1999;34:1–104.
23. Belikov S, Erina N, Huang L, Su C, Prater C, Magonov S, Ginzburg V, McIntyre B, Lakrout H, Meyers G. Parametrization of atomic force microscopy tip shape models for quantitative nanomechanical measurements. J Vac Sci Technol B Microelectron Nanometer Struct Process Meas Phenom. 2009;27:984–92.
24. Shao Z, Mou J, Czajkowsky DM, Yang J, Yuan J-Y. Biological atomic force microscopy: what is achieved and what is needed. Adv Phys. 1996;45:1–86.
25. Bustamante C, Marko JF, Siggia ED, Smith S. Entropic elasticity of lambda-phage DNA. Science. 1994;265:1599–600.

26. Butt H-J, Wolff EK, Gould SAC, Dixon Northern B, Peterson CM, Hansma PK. Imaging cells with the atomic force microscope. J Struct Biol. 1990;105:54–61.
27. Krotil H-U, Stifter T, Waschipky H, Weishaupt K, Hild S, Marti O. Pulsed force mode: a new method for the investigation of surface properties. Surf Interface Anal. 1999;27:336–40.
28. Su C, Lombrozo PM Method and apparatus of high speed property mapping. 2010
29. Pittenger B, Erina N, Su C. Quantitative mechanical property mapping at nanoscale with PeakForce QNM. Bruker application note AN128, Rev. B0. 2012
30. Pyne A, Thompson R, Leung C, Roy D, Hoogenboom BW. Single-molecule reconstruction of oligonucleotide secondary structure by atomic force microscopy. Small. 2014;10:3257–61.
31. Swadener JG, George EP, Pharr GM. The correlation of the indentation size effect measured with indenters of various shapes. J Mech Phys Solids. 2002;50:681–94.
32. Rico F, Su C, Scheuring S. Mechanical mapping of single membrane proteins at submolecular resolution. Nano Lett. 2011;11:3983–6.
33. Hinterdorfer P, Baumgartner W, Gruber HJ, Schilcher K, Schindler H. Detection and localization of individual antibody-antigen recognition events by atomic force microscopy. Proc Natl Acad Sci U S A. 1996;93:3477–81.
34. Hinterdorfer P, Schilcher K, Baumgartner W, Gruber HJ, Schindler H. A mechanistic study of the dissociation of individual antibody-antigen pairs by atomic force microscopy. Nanobiology J Res Nanoscale Living Syst. 1998;4:39–50.
35. Baumgartner W, Hinterdorfer P, Ness W, Raab A, Vestweber D, Schindler H, Drenckhahn D. Cadherin interaction probed by atomic force microscopy. Proc Natl Acad Sci. 2000;97:4005–10.
36. Raab A, Han W, Badt D, Smith-Gill SJ, Lindsay SM, Schindler H, Hinterdorfer P. Antibody recognition imaging by force microscopy. Nat Biotechnol. 1999;17:901–5.
37. Hinterdorfer P, Kienberger F, Raab A, Gruber HJ, Baumgartner W, Kada G, Riener C, Wielert-Badt S, Borken C, Schindler H. Poly(Ethylene Glycol): an ideal spacer for molecular recognition force microscopy/spectroscopy. Single Mol. 2000;1:99–103.
38. Kiss E, Gölander C-G. Chemical derivatization of muscovite mica surfaces. Colloids Surf. 1990;49:335–42.
39. Conti M, Falini G, Samorì B. How strong is the coordination bond between a histidine tag and Ni – Nitrilotriacetate? An experiment of Mechanochemistry on single molecules. Angew Chem. 2000;112:221–4.
40. Pfreundschuh M, Alsteens D, Hilbert M, Steinmetz MO, Müller DJ. Localizing chemical groups while imaging single native proteins by high-resolution atomic force microscopy. Nano Lett. 2014;14:2957–64.
41. Baruch DI, Ma XC, Pasloske B, Howard RJ, Miller LH. CD36 peptides that block cytoadherence define the CD36 binding region for Plasmodium falciparum-infected erythrocytes. Blood. 1999;94:2121–7.
42. Albrecht TR, Grütter P, Horne D, Rugar D. Frequency modulation detection using high-Q cantilevers for enhanced force microscope sensitivity. J Appl Phys. 1991;69:668–73.

Chapter 2
Atomic Force Microscopy-Based Single Molecule Force Spectroscopy for Biological Application

Chao Tang, Youjie Fan, and Junhong Lü

Abstract This chapter describes the basic principle of force spectroscopy based on atomic force microscopy, with particular attention to instrumental and applications aspects more strictly related to the study of single biomolecules and cell membrane.

1 Introduction

1.1 AFM (Atomic Force Microscopy)

Invented by IBM scientists in 1982, Atomic force microscopy (AFM) was experimental implemented by Binning, Quate and Gerber in 1986. It is a type of scanning probe microscopy (SPM), with demonstrated resolution on the order of nanometers, more than 1000 times better than the optical diffraction limit. The AFM consists of a cantilever with a sharp tip at its end that is used to scan the sample surface. The cantilevers is typically made up of silicon or silicon nitride with the tip apex radius on the order of nanometers. When the tip was brought into proximity of the sample surface, force between the tip apex and the sample surface lead to a deflection of the cantilever. And the deflection was monitored by the quadrant photodiode then "tell" the piezo scanner to up or down to follow the topography of the sample surface. Normally, three different operation modes were used to scan the surface of the sample, according to the motion of the tip: contact mode; intermittent mode (AC mode or tapping mode); non-contact mode. Let's follow the history to introduce these modes. When AFM was invented, contact mode was used to scan sample. In contact mode, the tip is "dragged" across the surface of the sample and the contours of the surface is measured either using the deflection of the cantilever directly or, more

C. Tang · J. Lü (✉)
Shanghai Institute of Applied Physics, Chinese Academy of Sciences, Shanghai, China
e-mail: lujunhong@sinap.ac.cn

Y. Fan
JPK Instruments AG, Shanghai, China

J. Cai (ed.), *Atomic Force Microscopy in Molecular and Cell Biology*,
https://doi.org/10.1007/978-981-13-1510-7_2

commonly, using the feedback signal which used to keep the piezo scanner follow the surface. In order to decrease the damage and get enough vertical deflection of the tip, low spring constant cantilevers are used for contact mode. As the application area expends, people found that the contact mode will created large later force and damage to the soft sample, like bio-sample. Then intermittent mode (AC, tapping) and non-contact mode was invented to scan the soft sample surface. Due to very hard operation of non-contact mode exceptionally in ambient conditions, intermittent mode is normally used to scan the surface. Because in ambient conditions, most samples develop a liquid meniscus layer, it is very hard to keep the tip above the surface without "snap" into the surface and scan the surface. AC mode can bypass this problem by intermittent contact the surface with oscillation near its resonance frequency. The oscillation of the tip was achieved with small piezo element in the Z scanner, but other possibilities include an AC magnetic field or periodic heating with a modulated laser beam. The amplitude of the oscillation usually varies from below one nanometer to several hundred nanometers. In AC mode, frequency and amplitude of the driving signal are kept constant, leading to constant amplitude of the cantilever oscillation as long as there is no drift or interaction between tip and sample surface. The interaction of forces acting on the cantilever when the tip approach to the surface and decrease the amplitude and change the phase of the oscillation of the tip. This amplitude is used as the parameter that goes into the electronic servo that control the height to maintain a set cantilever oscillation amplitude as the cantilever is scanned over the sample surface. Although the peak force applied during the contacting part of the oscillation can be much higher than typically during contact mode, AC mode generally lessens the damage done to the sample surface and the tip compare done in contact mode. But AC mode is gentle enough ever for the lipid bilayers or adsorbed single polymer molecules under liquid medium. Beside the image, the phase of the cantilever's oscillation with respect to the driving signal can be recorded and analyzed. The phase signal contains information about the energy dissipated by the cantilever in each oscillation cycle. As the development of the life science technology, another image scanning technics (QI™) was invented to get the topography and stiffness of sample at the same time. QI™ (Quantitative imaging, JPK Instrument, AG) is one of the best AFM imaging technics used for life bio-samples. With QI- a force curve based image mode- the user has full control over the tip-sample interacting force at every pixel of the image. There is no longer for setpoint or gain adjustment while scanning anymore, and every raw point data of image are saved for further analysis.

AFM was introduced into three major application areas: force measurement, imaging and manipulation. In force measurement, AFM was used to detect the force between the tip and the sample surface as a function of their mutual separation according to Hooke's law. For imaging, keeping the force between the tip and sample as constant, the probe can follow the topography and give the three dimensional shape with high resolution. In manipulation, the forces between tip and sample can be used to change the properties of the sample in a controlled way, which means that the features of the sample can be removed or changed as we want. Although, image

scanning is the most wide use of AFM. Molecular interactions is the most important subject people use AFM to work on.

1.2 The Importance of Biomolecular Interactions

Because of biomolecular interactions playing important roles in many biological and physiological processes, it has been recognized that the analysis of single biomolecules spectroscopy is of critical importance in fundamental genetic research, clinical analysis, and industrial biotechnological development [1, 2]. Interaction processes between macromolecules on biological surfaces are essential for diverse cellular functions including embryonic development, signal transduction, immune response, cell adhesion, and tissue assembly [3]. Atomic force microscopy (AFM) can provide force-distance curves while scanning the surface of samples. According to the force-distance relationship, we can get data of adhesion and bonding force of mechanical properties [4]. AFM takes unique advantages in isolation of single biomolecules [5] for following reasons: First, force spectroscopy ensures a dynamic analytical method to measurement of interaction forces between single molecules superior to conventional ensemble measurements [6]. Second, AFM has potential to distinguish the target molecules from a complex sample because of evaluating the morphology, mechanical properties, charge, and even chemistry of molecular species by various AFM imaging modes. Moreover, isolation of biomolecules can be done on a surface in ambient conditions by AFM. It enables us to improve the performance in solutions where contaminations are likely to be introduced.

As the base of many biochemical processes, specific molecular interactions involve several types of noncovalent bonds including Van der Waals forces, hydrogen bonds, hydrophobic and electrostatic forces. The highly specific interactions between a ligand and its receptor can be recorded by atomic force microscopy force spectroscopy with a functionalized AFM tip to avoid the detection of non-specific events during the retraction of the tip from the sample surface. These experiments are so called Atomic Force Microscopy-based Single Molecule Force Spectroscopy (AFM-SMFS), since they allow measuring specific interaction forces between even one molecule on the tip and another molecule at the surface of the sample [7].

The unique advantages of AFM including piconewton sensitivity, working under near physiological environments and lateral atomic resolution, making it an excellent approach for biomolecules, especially for soft cell surfaces at single molecule level [8]. For the biological applications, AFM-SMFS is mainly used for measuring protein and glycan on the surface of cells [9]. This chapter mainly reviews single molecule force spectroscopy for biological application, especially on cell membrane. Also, some works on the most advanced front of application will be discussed.

2 Force Spectroscopy of Proteins on Cell Surface

Membrane proteins, mostly serve as membrane receptor in many cell functions [10]. As the barrier of massive pharmacological therapies, the target cell membranes can be studied on delivery system of drugs. Peetla et al. mentioned AFM as a benchmark approach to screen drug candidates [11]. To increase the efficiency of therapeutic discovery and delivery, one should understand the therapeutic-effector interactions and their cell and tissue responses at the molecular level [12].

As the first identified aquaporin of membrane water channels found in all forms of life, Aquaporin-1 (AQP1) is studied for novel drug targets by AFM. Fotiadis D. et al. reveals that AQP1 attributes to a possible secondary function as a cyclic guanosine monophosphate (cGMP) gated ion channel [13]. A striking degree of sequence homology suggests the existence of a Ca^{2+}-binding proteins belonging to Ca^{2+}-binding site at the C terminus of AQP1 instead of the putative cGMP-binding site reported previously. To locate on the acquired surface topographies, 2D crystals AQP1 were treated with carboxypeptidase Y, which cleaves off the intracellular C terminus. Difference maps of AFM topography between the native AQP1 and the carboxypeptidase Y treated AQP1s showed the closed four-fold symmetry axis of the tetramer at carboxylic tail. The unique ability of AFM to provide structural information about molecules on the single molecule level enables thorough study of their behavior at simulated physiological conditions.

Established AFM-SMFS is widely applied to characterize the molecule affinity between antibody and antigen [14]. Hinterdorfer, P et al. studied on the interaction between protein antibody and antigen, and improve the fixation method of protein by connecting protein with a chain of PEG polymer, as an approach to distinguish the specific interaction between antibody and substrate on force-distance curves [15]. They further modified the tip with antibody to probe the sample, and developed a recognition imaging technology that combines the AFM measuring force mode and the scanning imaging, which ensures AFM a certain ability to identify the types and components of the imaging molecules [16].

Macromolecules on cell surface play an important role as the interface link between the cytoplasm and the extracellular region, such as receptors and ion channels. Vascular endothelial growth factor receptor (VEGFR) is an essential transmembrane receptor protein expressed on vascular endothelial cell surfaces [17]. N. Almqvist et al. initially measured the adhesion forces between isolated VEGFR and an AFM tip modified with its antibody [18]. In this research, the maps of interaction forces between antibody conjugated atomic force microscope tips, an anti-Flk-1-antibody-functionalized tip and a specific receptor, a vascular endothelial growth factor (VEGF) receptor reveals the effect of plasma membrane receptor clustering on local cell mechanics in semiquantitative measurements of binding (or unbinding) forces. Depending on the unique advantages of AFM-FS, distribution and density of VEGFRs were mapped in the cell plasma membrane, which shows that antibody and ligand induced real-time clustering and redistribution of VEGFRs. Later, Lee et al. developed a two-step procedure for VEGFRs surface force analysis:

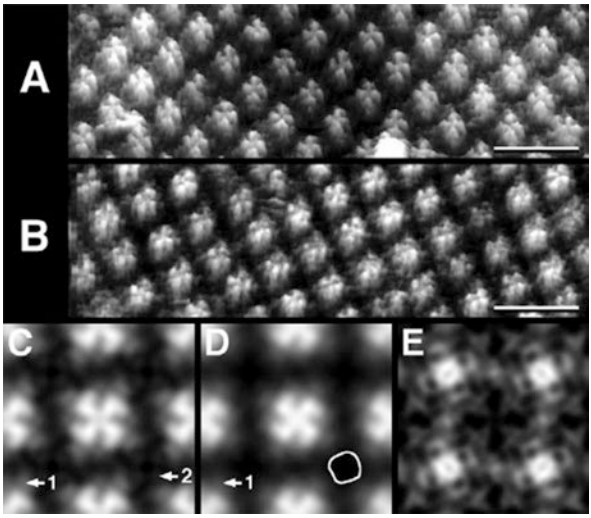

Fig. 2.1 Human aquaporin-1 (AQP1) AFM imaging. (**a**) deglycosylated hAQP1 2D crystals. (**b**) carboxypeptidase Y treated AQP1 2D crystals. (**c**) The symmetrized correlation average of the deglycosylated hAQP1, windmill-shaped peripheral (1) and central protrusions (2) on the other side. (**d**) the symmetrized correlation average of the deglycosylated and decarboxylated hAQP1. On the lower side, the central protrusion, initially present, has disappeared while the peripheral one (1) does not seem to be affected by the digestion. (**e**) Differences in this difference map between the undigested and digested hAQP1 topographs are evident. (Figure reproduced from [13])

first locating the VEGFRs by dynamic recognition imaging, then conducting AFM-FS on the recognition sites to measure the rupture force and unbinding times [19].

Due to the tractability of genetic and biochemical manipulation, the fission yeast *Schizosaccharomyces pombe* (S. pombe) has become a popular tool for analyzing heterologous G protein coupled receptors (GPCRs) [20]. P-factor is a peptide pheromone and Mam2 is a fission yeast pheromone receptor belonging to GPCRs on the cell surface of the fission yeast. Their interaction was examined by AFM in Sasuga et al.'s work [21]. The AFM tips were modified with P-factor derivatives and truncated P-factor derivative lacking specific binding sites to measure the specific interaction forces, which were recorded to be around 120 pN at a probe speed of 1.74 μm/s. As expected, the truncated P-factor derivative modified tips do not show a force jump in the force curves. This yeast based AFM method shows that this approach has the potential for the signaling study of heterologous GPCRs and screening of their ligands.

Als3 protein is an adhesin involved in adhesion during host invasion, while fluorescence image of Als3 proteins in the cell wall lacks spatial resolution and does not show the biophysical property information, such as elasticity and extension. Beaussart et al. therefore used AFM with anti-Als3 antibodies functionalized tips to get Als3 cell surface force spectroscopy [22]. The morphogenesis of C. albicans from yeast to hyphae was observed. In the nongerminating yeast form, adhesion

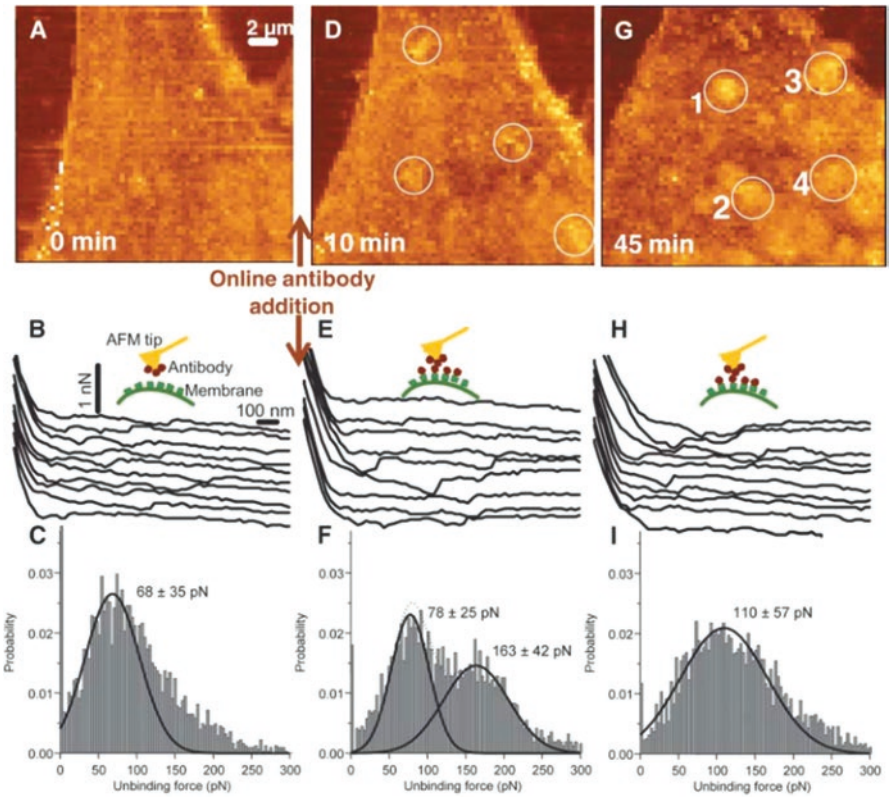

Fig. 2.2 Endothelial cells in real-time atomic force maps. (**a–c**) Specific interaction between an endothelial cell surface and a Si_3N_4 tip functionalized with anti-Flk-1. (**a**) Force map at beginning. (**b**) Force curves taken at various points on the cell surface from the map shown in (**a**). The curves are offset with respect to zero force. (**c**) The unbinding forces probability histogram of the force curves from the force map, fitted with a Gaussian and the corresponding maxima and s is indicated in the figure. The dominant unbinding force (60–70 pN) suggests breakage of single receptor-antibody bonds. (**d–f**) Competitive inhibition probed with the antibody tip at 10 min after adding antibody in the recording medium. The panels correspond to (**a–c**). The characteristic unbinding force is suppressed and the measured forces are shifted toward higher values. (**g–i**) Corresponds to (**a–c**), but at 45 min after adding antibody. The single brighter spots in (**g**) are identified as clusters of receptor. Numbers 1–4 refer to a few of these clusters. (Figure reproduced from [18])

maps show low rates of Als3. While Als3 Proteins on Hyphae show differences including a higher detection frequency and more specifically on the germ tube.

Formosa et al. used AFM as an imaging tool to visualize and localize adhesins nanodomains at the surface of living wild-type *Candida albicans* cells [23]. They observed that the molecules at the origin of these adhesions could aggregate into nanodomains. Further by the use of functionalized with dendrimers presenting CHO functions able to covalently link with NH_2 functions of proteins, they determined that the less adhesive nanodomains were formed by mannoproteins that can

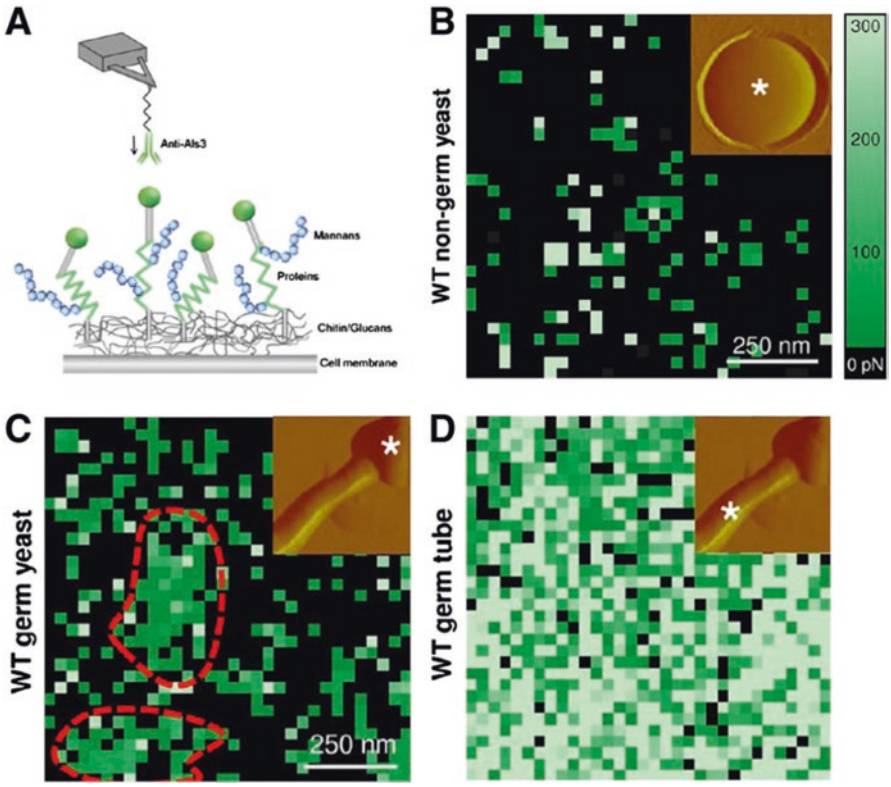

Fig. 2.3 AFM single molecular mapping of Als3 protein on cell membrane. (**a**) Schematic representation of interactions between proteins and anti-Als3 antibody modified AFM tip. (**b**) Adhesion force histogram (1 μm × 1 μm, color scale: 300 pN) of Als3 proteins on nongerminating yeast cell. (**c**) Adhesion force histogram on germinating yeast corresponds to (**b**). (**d**) Adhesion force histogram of a germ tube. (Figure reproduced from [22])

interact specifically with Concanavalin A, and force measurements showed that Als proteins (probably among others) were participating to these nanodomains. This study suggested the ability of AFM force spectroscopy to measure the nanoscale size domains at the surface of living cells.

In a very recent research of Santos's group, AFM has been used as a tool to evaluate the risk of cardiovascular diseases in patients [24]. After pretreatment, the AFM tips were functionalized with human purified fibrinogen to detect the fibrinogen-erythrocyte binding forces. Chronic heart failure (CHF) patients showed altered cell stiffness. Compared with non-ischaemic patients, the fibrinogen-erythrocyte binding forces of ischaemic patients also increased. This experiment showed the potential of AFM-single molecule force spectroscopy for identifying patients with increased risk for cardiovascular diseases.

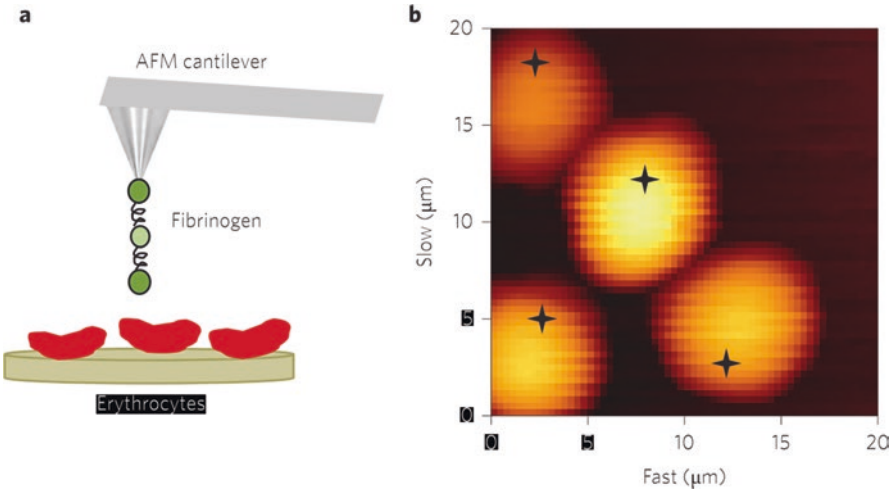

Fig. 2.4 AFM-based force spectroscopy set-up of fibrinogen-erythrocyte binding. (**a**) Schematic representation of erythrocytes deposited on a glass slide and fibrinogen molecules mounted on an AFM tip. (**b**) Example of a force mapping height image of erythrocytes (20 μm × 20 μm, height color scale:1.2 μm). The symbols indicate the surface locations chosen on each cell to perform force spectroscopy measurements. (Figure reproduced from [24])

3 Protein AFM–SMFS with DNA Aptamer Tips

AFM-based single molecule force spectroscopy has the potential for drug design due to its molecular recognition between DNA aptamers and drug molecules. Compared to antibodies, aptammers show higher chemical stability and are easier to manipulate [25].

One of the typical examples is to measue single molecule binding via rupture forces of a split aptamer. Nguyen et al. used a split aptamer by AFM to detect adenosine monophosphate (AMP) [26]. For their atomic force spectroscopy, the sequence of aptamer was split into two parts, oligo a and oligo b, immobilized on tip and gold substrate respectively. In this way, they avoided the target analyte interacting with surface. They found that the rupture force between two oligos were increased in the presence AMP in comparison with the one measured in absence of AMP. Thus, changes in the rupture force could be directly attributed to the specific binding of AMP to the split aptamer.

Protein tyrosine kinase 7 (PTK7), as a protein receptor in tyrosine kinase family, is a surface biomarker member with potential clinical utility in cancer [27]. Aptamers could be a useful bio-probes to detect specific biomarkers on various cell membranes with functionalized AFM tips. To figure out whether synthetic aptamers bind as robustly as natural antibodies, O'Donoghue et al. measured the rupture force between PTK7 and both a natural antibody and a synthetic DNA aptamer by single-molecule AFM technique [28]. The rupture force on live cell membranes between the aptamer and PTK7 was 46 ± 26 pN, while the force with the antibody was

68 ± 33 pN, suggesting that the binding forces are very similar. This study showed that DNA aptamer has the potential for targeted drug delivery to tumors.

Recently, Li et al. demonstrate a simple force-based label-free strategy for the highly sensitive sensing of adenosine [29]. By binding an adenosine ssDNA aptamer onto an AFM probe, this sensor took advantage of the specific molecular recognition between adenosine and an appropriate DNA aptamer, and the recognition resulted in the formation of a folded, hairpin-like DNA structure. This adenosine/aptamer complex showed a variation of the adsorption force at the graphite/water interface. Because of various aptamers reported and methods for discovering new aptamers, this AFM-based single molecule force spectroscopy is simple but promising for the detection of numerous analytes.

4 AFM-SMFS of Cell Surface Glycans

Glycans can be found attached to proteins in glycoproteins and proteoglycans. In general, they are found on the exterior surface of cells. Cell surface glycans, involved in various biological events including immune recognition, cell adhesion, cell migration, bacterial infections, inflammation and cancer, have been well studied in the field of cellular physiology and pathology [30]. Lectins are carbohydrate-binding proteins of macromolecules that are highly specific for sugar moieties. With a specific affinity to glycans, their interactions have been applied into detecting specific glycans on cell surfaces. Several works have been focused on the interactions between lectins and glycans by using AFM-FS. In AFM-based single molecule force spectroscopy, lectins act as functional tips with specificity and high efficiency.

For example, Sletmoen et al. used soybean agglutinin (SBA) as a molecular probe in the structural analysis of glycoproteins in their research [31]. In this study, dynamic force spectroscopy is used to measure the unbinding forces between SBA on a mica surface and a modified porcine submaxillary mucin (Tn-PSM) on AFM tip. A number of force jumps, which consistent with the structure of the carbohydrate chains of mucin, demonstrate that unbinding events or rebinding events were observed up to a distance equal to the length of the mucin chain. These results combined with the long lifetime of the SBA-TnPSM complex can fit with a binding model in which lectin molecules tend to "bind and jump" from a glycan residue to another along the polypeptide chain of mucin before dissociating. In another report, *Ricinus communis* agglutinin-120 (RCA120) was used as a probe to directly measure the interaction forces between RCA120 and galactosyl residues on living HeLa cell surfaces in Li et al.'s research [32]. RCA120, a lectin from *Ricinus communis*, possesses a peculiar affinity for terminal β-D-galactosyl residues, hence it has been developed as a functionalized tip to detect the unbinding force, which was observed to be 43 pN at loading rate of 0.4 $Nn \cdot s^{-1}$. This research successfully applied molecular recognition force spectroscopy to study the specificity of the lectin-carbohydrate interactions.

In a very recent research, Gunning et al. used AFM to unravel the mechanism driving mucus-binding protein(MUB) mediated adhesion to mucins [33]. In this study, MUB was immobilized on the functionalized tips and mucin was immobilized on the glass slide. By single molecule force spectroscopy, they showed a nanospring-like adhesion model between MUB and mucin mediated by unfolding of the multiple repeats constituting the adhesin. The direct evidence for MUB self-interaction was in marked contrast with the mucin adhesion behavior presented by Galectin-3, a mammalian lectin characterized by a single carbohydrate binding domain.

5 Perspective

As shown, AFM-SMFS could be applied in vast cell surface measurements. Its high resolution at the nanoscale size and ability to measure forces in the pN range make it a valuable tool for analysis in biological applications [34]. On the cell surfaces, the AFM-based single molecule force spectroscopy can not only measure interaction forces between various biomolecules, but also mapping recognition sites on cell surfaces directly. Knowledge of these forces contribute to a better understanding of the molecular basis of molecular recognition events. Published data shows that AFM-SMFS could be applied into various areas such as bimolecular recognitions, action mechanisms detection, disease evaluation and drug design [35–37]. The amount of newly published work with AFM-SMFS is astonishing and heralds a bright future for AFM research in this area.

References

1. Hinterdorfer P, Dufrene YF. Detection and localization of single molecular recognition events using atomic force microscopy. Nat Methods. 2006;3:347–55.
2. Branton D, Deamer DW, Marziali A, Bayley H, Benner SA, Butler T, Di Ventra M, Garaj S, Hibbs A, Huang XH, Jovanovich SB, Krstic PS, Lindsay S, Ling XSS, Mastrangelo CH, Meller A, Oliver JS, Pershin YV, Ramsey JM, Riehn R, Soni GV, Tabard-Cossa V, Wanunu M, Wiggin M, Schloss JA. The potential and challenges of nanopore sequencing. Nat Biotechnol. 2008;26:1146–53.
3. Wang CZ, Yadavalli VK. Investigating biomolecular recognition at the cell surface using atomic force microscopy. Micron. 2014;60:5–17.
4. Green NH, Allen S, Davies MC, Roberts CJ, Tendler SJB, Williams PM. Trac-Trends Anal Chem. 2002;21:64–73.
5. Binnig G, Quate CF, Gerber C. Atomic Force Microscope. Phys Rev Lett. 1986;56:930–3.
6. Hoffmann T, Dougan L. Single molecule force spectroscopy using polyproteins. Chem Soc Rev. 2012;41:4781–96.
7. Pillet F, Chopinet L, Formosa C, Dague E. Atomic Force Microscopy and pharmacology: From microbiology to cancerology. Biochim Biophys Acta-Gen Subj. 2014;1840:1028–50.
8. Engel A, Muller DJ. Observing single biomolecules at work with the atomic force microscope. Nat Struct Biol. 2000;7:715–8.

9. Li Q, Zhang T, Pan YG, Ciacchi LC, Xu BQ, Wei G. AFM-based force spectroscopy for bioimaging and biosensing. RSC Adv. 2016;6:12893–912.
10. Dirienzo JM, Nakamura K, Inouye M. The outer membrane proteins of Gram-Negative bacteria: biosynthesis, assembly, and functions. Annu Rev Biochem. 1978;47:481–532.
11. Peetla C, Rao KS, Labhasetwar V. Relevance of biophysical interactions of nanoparticles with a model membrane in predicting cellular pptake: study with TAT peptide-conjugated nanoparticles. Mol Pharm. 2009;6:1311–20.
12. La R, Arnsdorf MF. Life Sci. 2010;86:545–62.
13. Fotiadis D, Suda K, Tittmann P, Jeno P, Philippsen A, Muller DJ, Gross H, Engel A. Identification and structure of a putative Ca2+-binding domain at the C terminus of AQP1. J Mol Biol. 2002;318:1381–94.
14. Maver U, Velnar T, Gaberscek M, Planinsek O, Finsgar M. Recent progressive use of atomic force microscopy in biomedical applications. Trac-Trends Anal Chem. 2016;80:96–111.
15. Hinterdorfer P, Baumgartner W, Gruber HJ, Schilcher K, Schindler H. Detection and localization of individual antibody-antigen recognition events by atomic force microscopy. Proc Natl Acad Sci U S A. 1996;93:3477–81.
16. Kienberger F, Ebner A, Gruber HJ, Hinterdorfer P. Molecular recognition imaging and force spectroscopy of single biomolecules. Accounts Chem Res. 2006;39:29–36.
17. Olsson AK, Dimberg A, Kreuger J, Claesson-Welsh L. VEGF receptor signalling ? in control of vascular function. Nat Rev Mol Cell Biol. 2006;7:359–71.
18. Almqvist N, Bhatia R, Primbs G, Desai N, Banerjee S, Lal R. Elasticity and adhesion force mapping reveals real-time clustering of growth factor receptors and associated changes in local cellular rheological properties. Biophys J. 2004;86:1753–62.
19. Lee S, Mandic J, Van Vliet KJ. Chemomechanical mapping of ligand-receptor binding kinetics on cells. Proc Natl Acad Sci U S A. 2007;104:9609–14.
20. Kohl JV, Atzmueller M, Fink B, Grammer K. Human pheromones: integrating neuroendocrinology and ethology. Neuroendocrinol Lett. 2001;22:309–21.
21. Sasuga S, Abe R, Nikaido O, Kiyosaki S, Sekiguchi H, Ikai A, Osada T. J Biomed Biotechnol. 2012:7.
22. Beaussart A, Alsteens D, El-Kirat-Chatel S, Lipke PN, Kucharikova S, Van Dijck P, Dufrene YF. Single-molecule imaging and functional analysis of Als Adhesins and Mannans during Candida albicans morphogenesis. ACS Nano. 2012;6:10950–64.
23. Formosa C, Schiavone M, Boisrame A, Richard ML, Duval RE, Dague E. Multiparametric imaging of adhesive nanodomains at the surface of Candida albicans by atomic force microscopy. Nanomed-Nanotechnol Biol Med. 2015;11:57–65.
24. Guedes AF, Carvalho FA, Malho I, Lousada N, Sargento L, Santos NC. Nat Nanotechnol. 2016;11 687−+
25. You KM, Lee SH, Im A, Lee SB. Aptamers as functional nucleic acids: In vitro selection and biotechnological applications. Biotechnol Bioprocess Eng. 2003;8:64–75.
26. Nguyen TH, Steinbock LJ, Butt HJ, Helm M, Berger R. Measuring single small molecule binding via rupture forces of a split aptamer. J Am Chem Soc. 2011;133:2025–7.
27. Lewis DB, Haines C, Ross D. Protein tyrosine kinase 7: a novel surface marker for human recent thymic emigrants with potential clinical utility. J Perinatol. 2011;31:S72–81.
28. O'Donoghue MB, Shi XL, Fang XH, Tan WH. Single-molecule atomic force microscopy on live cells compares aptamer and antibody rupture forces. Anal Bioanal Chem. 2012;402:3205–9.
29. Li J, Li Q, Ciacchi LC, Wei G. Label-free sensing of adenosine based on force variations induced by molecular recognition. Biosensors. 2015;5:85–97.
30. Pilobello KT, Mahal LK. Deciphering the glycocode: the complexity and analytical challenge of glycomics. Curr Opin Chem Biol. 2007;11:300–5.
31. Sletmoen M, Dam TK, Gerken TA, Stokke BT, Brewer CF. Single-molecule pair studies of the interactions of the α-GalNAc (Tn-antigen) form of porcine submaxillary mucin with soybean agglutinin. Biopolymers. 2009;91:719–28.

32. Li YJ, Wang JN, Xing CY, Wang ZX, Wang HD, Zhang BL, Tang JL. Molecular recognition force spectroscopy study of the specific Lectin and Carbohydrate interaction in a living cell. ChemPhysChem. 2011;12:909–12.
33. Gunning AP, Kavanaugh D, Thursby E, Etzold S, MacKenzie DA, Juge N. Int J Mol Sci. 2016;17
34. Carvalho FA, Santos NC. Atomic force microscopy-based force spectroscopy biological and biomedical applications. IUBMB Life. 2012;64:465–72.
35. Dharap SS, Wang Y, Chandna P, Khandare JJ, Qiu B, Gunaseelan S, Sinko PJ, Stein S, Farmanfarmaian A, Minko T. Tumor-specific targeting of an anticancer drug delivery system by LHRH peptide. Proc Natl Acad Sci U S A. 2005;102:12962–7.
36. Laidler P, Dulinska J, Lekka M, Lekki J. Expression of prostate specific membrane antigen in androgen-independent prostate cancer cell line PC-3. Arch Biochem Biophys. 2005;435:1–14.
37. Winiarska M, Bil J, Wilczek E, Wilczynski GM, Lekka M, Engelberts PJ, Mackus WJM, Gorska E, Bojarski L, Stoklosa T, Nowis D, Kurzaj Z, Makowski M, Glodkowska E, Issat T, Mrowka P, Lasek W, Dabrowska-Iwanicka A, Basak GW, Wasik M, Warzocha K, Sinski M, Gaciong Z, Jakobisiak M, Parren PWHI, Golab J. PLoS Med. 2008:5.

Chapter 3
In Situ Single Molecule Detection on Cell Membrane and Label Molecule Distributions Using AFM/NSOM

Jiang Pi, Hua Jin, and Jiye Cai

1 Introduction

Consisting of viscous phospholipid bilayer, different kinds of proteins and various nano/micrometer-sized domains, cell membranes have proven to play very important roles in ensuring the stability of the intracellular environment and order of cellular signal transductions. The developments of modern cell biology, immunology, and medicine urge us to explore more precise cell membrane structures and detailed functions of biomolecules on cell membranes. Due to the minuscule size of biomolecules and their clusters on cell membranes (varying from several nanometers to hundreds of nanometers), a high resolution microscopy is needed to explore the cell membrane biomolecule distribution.

Among existing high resolution microscopies, the atomic force microscopy (AFM) is a unique scanning tunneling microscopy (STM) that can be used for single molecule detection by relying on cantilever deflection induced by the forces

J. Pi
Department of Immunology and Microbiology, University of Illinois at Chicago, Chicago, IL, USA

State Key Laboratory of Quality Research in Chinese Medicines, Macau University of Science and Technology, Macau, China

H. Jin
State Key Laboratory of Quality Research in Chinese Medicines, Macau University of Science and Technology, Macau, China

Feinberg School of Medicine, Northwestern University, Evanston, IL, USA

J. Cai (✉)
State Key Laboratory of Quality Research in Chinese Medicines, Macau University of Science and Technology, Macau, China

Department of Chemistry, Jinan University, Jinan, China
e-mail: tjycai@jnu.edu.cn

J. Cai (ed.), *Atomic Force Microscopy in Molecular and Cell Biology*,
https://doi.org/10.1007/978-981-13-1510-7_3

between the AFM tip and sample. High resolution AFM topography imaging hasbeen proven to be a very useful method for single molecule detection; in addition, this unspecific imaging method is very difficult for single molecule detection on the complicated cell membrane. However, the specific force recognition properties of AFM provide possibilities for single molecule detection on cell membranes, based on single-molecule force spectroscopy (SMFS), simultaneous topography, and recognition imaging (TREC). Both SMFS and TREC are based on the functionalization of AFM tips with specific ligands; then these specific ligand functionalized AFM tips are used for distribution studies on cell membranes, simultaneously providing some important information about molecular behavior and interactions.

2 Functionalization of AFM Tips

The functionalization of AFM tips is dependent on the chemical conjunction of specific ligands onto the tips by chemical linkers. The most widely used linkers are APTES linkers, MPTMS linkers, glutaraldehyde linkers, and PEG-derived linkers, that provide active groups for ligand conjunctions. The typical AFM tip functionalization procedures are divided ~~into~~ in two different ways, based on nitride silicon (or silicon) and gold-coated AFM tips. Because nitride silicon or silicon AFM tips provide a large number of silicon atoms on their tip-surfaces that can interact with Si-O groups from ATPES/MPTMS to form Si-O-Si linkers and couple APTES or MPTMS linkers (the most widely used amination reagents), they are the most widely used. The conjunction of APTES/MPTMS onto tip surfaces thus provides active amino groups (-NH_2) that can react with aldehyde groups (-CHO) from glutaraldehyde molecules to provide additional aldehyde groups. As indicated in Fig.3.1, the active aldehyde groups on tip surfaces are very sensitive to amino groups from ligands (such as proteins or other biomolecules), which, therefore, can couple the ligands onto AFM tips [1, 2]. As another kind of widely used linkers, heterobifunctional polyethylene glycol, including NHS–PEG–acetal [3], NHS–PEG–MAL [4], NHS-PEG-PDP, [5] and NHS–PEG–aldehyde [6] can further couple onto the tip surface by the reaction between –NH2 and -NHS. As shown in Fig. 3.1, the –acetal, -MAL, -PDP or –aldehyde end on the tip surface could react with the –NH2 groups on the ligands (proteins, polypeptide or other biomolecules), and finally couple the ligands onto AFM tip.

3 Basic Principle for AFM-SMFS

SMFS relies on measuring force with the pN sensitivity associated with single molecule reactions, thus providing fundamental insights into molecule recognition and interactions on cell membranes. As shown in Fig. 3.2, during the approach of AFM tip to cell membrane, the ligands on the AFM tip can react with specific receptors to

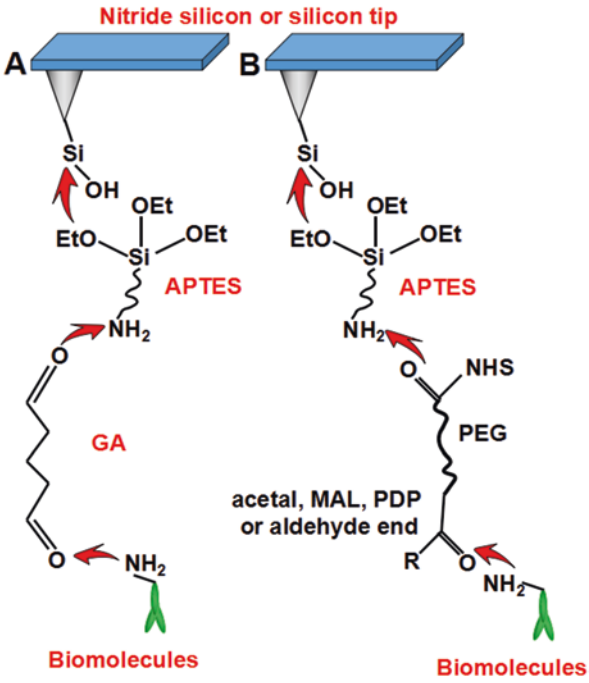

Fig. 3.1 Typical AFM tip (nitride silicon or silicon tips) functionalization methods

show distinct adhesion force events and can also react with other biomolecules to show the non-specific adhesion force events. After calculating the force events between the ligand-functionalized tip and cell membrane, hundreds or thousands of force curves obtained on an area of the cell surface can be reconstructed into an adhesion force map. The location of specific adhesion force events on the cell surface can thus reflect the distribution of specific receptors on cell membrane. Apart from the distribution of biomolecules on cell membrane, this AFM force method can also provide information on the detailed force events between the ligands and their specific receptors on cell membranes, which is impossible to obtain using other in situ single molecule imaging techniques.

4 Basic Principle for AFM–TREC

TREC is another single molecule imaging mode of AFM that can enhance the lateral resolution and imaging speed by a ligand-functionalized oscillating AFM, while scanning across the cell surface to resolve distribution and dynamics of a single biomolecule on cell membranes. Unlike SMFS force mapping, TREC is based on the MAC mode (magnetic alternating current) of AFM, where a magnetically coated cantilever is oscillated through an alternating magnetic field. As shown in Fig. 3.3, the AFM tip functionalized with specific ligands via a flexible PEG

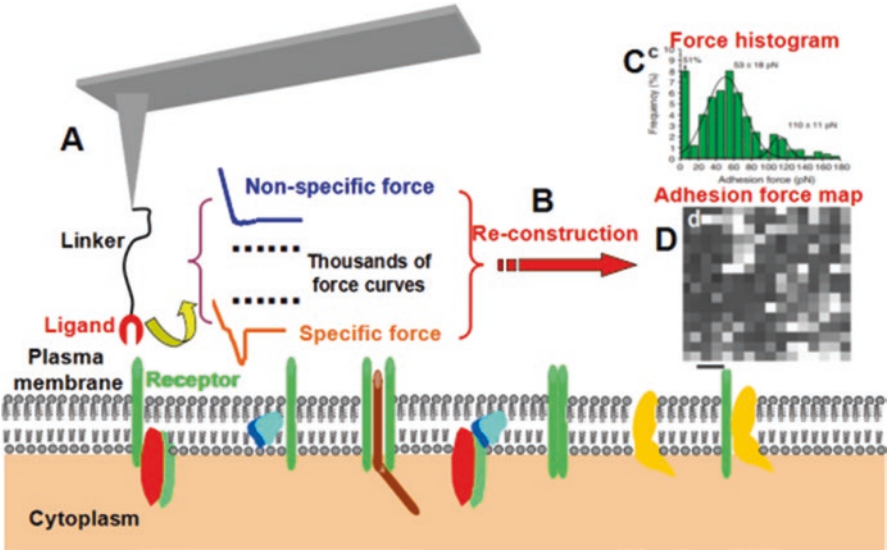

Fig. 3.2 Schematic of AFM for the in situ single molecule imaging of cell membrane by SMFS. (**a**) Ligand-functionalized AFM tips are operated to interact with the cell membrane to distinguish the specific force-distance curves from the non-specific force-distance curves. (**b**) Thousands of force-distance curves can be reconstructed into force histograms and high resolution force adhesion maps. The typical results obtained by AFM-SMFS on living cells with (**c**) force histogram for heparin-HBHA interactions, and (**d**) high resolution adhesion force map using a heparin modified tip, scale bars: 50 nm [7, 8]

linker is oscillated close to its resonance frequency while scanning over the cell surface. When specific molecule recognition occurs, which involves the ligand on the AFM tip binding to its receptor on the cell surface, the PEG linker will be stretched during the upward movement of the cantilever. The resulting loss in energy will, in turn, decrease the top peaks of oscillations; and make the ligand-receptor binding events become visible, due to the clear reduction of the oscillation amplitude. During the lateral scanning of the cell surface, a molecule recognition image is generated by the upper part of the oscillation, and a topography image is simultaneously and independently obtained by a feedback loop driven by the lower part of the oscillation. By combining the high-resolution topography and the molecule recognition image, the locations and dynamics of the biomolecules on the cell surface can be resolved with single molecule sensitivity.

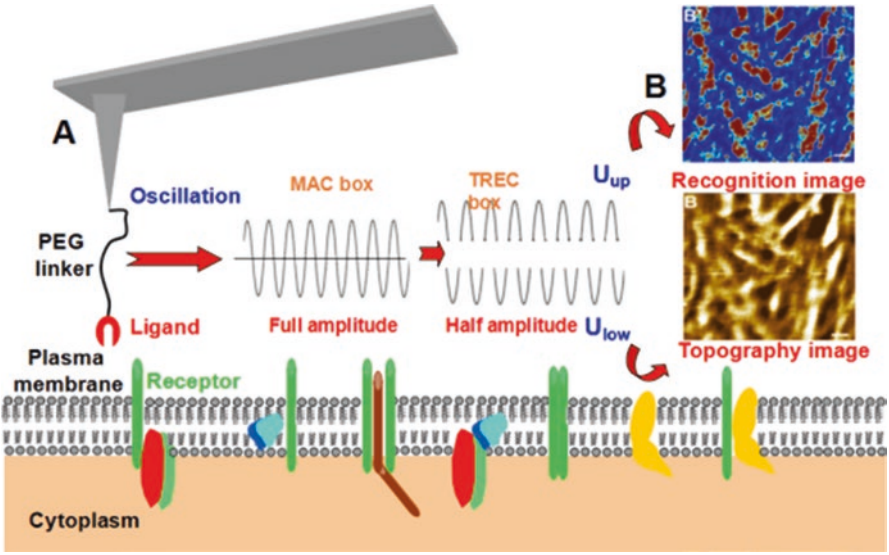

Fig. 3.3 Schematic of AFM for the in situ single molecule imaging of cell membrane by TREC. (**a**) Ligand-functionalized AFM tips are oscillated close to their resonance frequency while scanning over the cell surface, which can generate a molecular recognition image from the upper part of the oscillation and a topography image from the lower part of the oscillation. (**b**) The typical results obtained by AFM-TREC with simultaneously recorded topography and recognition images on MyEnd cells acquired with VE-cadherin-Fc-functionalized AFM tips, scale bars: 100 nm [8, 9]

5 Basic Principle of NSOM for In Situ Single Molecule Detection on Cell Membrane

Based on the force detection principle of AFM, there are also a super-resolution microscopy, called: Near-Field Scanning Optical Microscopy (NSOM), combining both the high resolution morphology and fluorescence images that can be used to explore the cell membrane components at single molecule level. Similar to AFM, NSOM is also a probe-based super microscopy but also has the ability for high resolution optical imaging, developed to surpass the current optical diffraction limit with a new resolution limit higher than 50 nm [10]. Compared with AFM tips, the NSOM probe is generally replaced by a metal-coated tapered optical fiber with a small aperture (diameter: 20–100 nm) at the end to produce optical images. The movement of the interior electric charge in the NSOM probe can change the electromagnetic field around it, which can be divided into the near field area (<10 nm) and the far field area (≥10 nm) [10]. In the far field, resolution of the optical microscopy is decided by the wavelength of the laser, but when the sample is close to the probe in the near field, the resolution of NSOM is not decided by the light wavelength, but rather is given by the aperture size of the probe and the sample–probe distance. The near-field light cannot be collected by the lens of conventional microscopy, as the signals in the near field decay exponentially within a distance of less than the

wavelength. In order to detect the fluorescence emission activated by near-field light, NSOM filters the fluorescence signal from the transmitted light using a long-pass filter before it reaches the detector, thus allowing non-diffraction-limited high-resolution optical imaging of NSOM.

As shown in Fig. 3.4, to create high-resolution optical images of membrane biomolecules by NSOM, the target biomolecules on the cell surface should be labeled with its specific fluorescence markers before the NSOM imaging procedure. The laser passes through the optical fiber in the probe of the NSOM to reach the sub-wavelength aperture and excites the fluorescent markers labeled on the cell surface in the near field. By detecting the near-field fluorescence signal, NSOM is capable of providing high-resolution fluorescence images of the membrane biomolecules. In this process, using the similar method with AFM, the high-resolution surface topography of cells is simultaneously generated by an additional shear-force feedback signal, which is applied to keep the probe in the near-field region of the cell sample. Through this method, NSOM is particularly suitable for investigating single molecule locations with high optical resolutions [11], as well as the distribution of membrane components on cell surface with precise membrane structures at nanoscale [12].

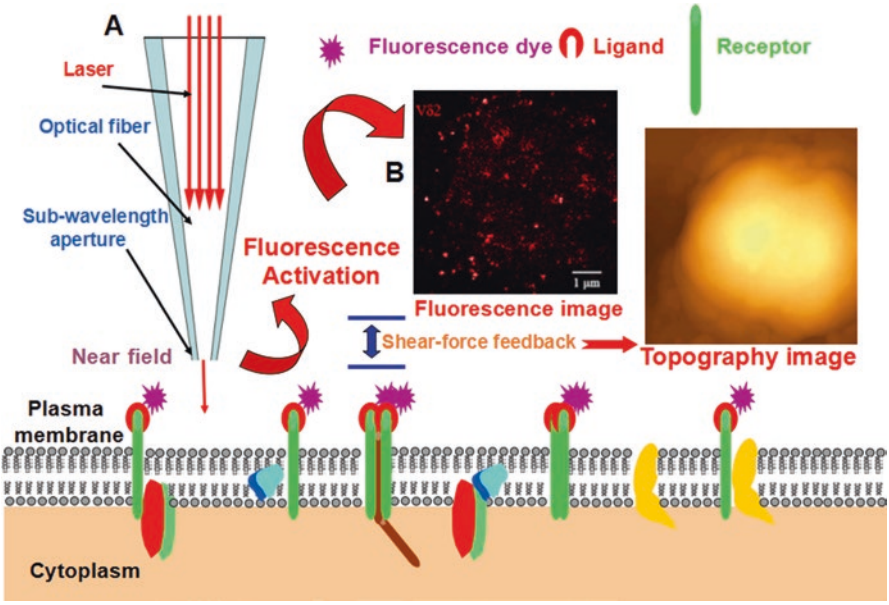

Fig. 3.4 Schematic of NSOM for the in situ single molecule imaging of cell membrane. (**a**) The laser passes through the optical fiber of the NSOM probe to excite the fluorescent dyes on the cell membrane in the near field to obtain a high resolution fluorescence image with a simultaneously generated high resolution topography image of the cell membrane. (**b**) The typical results obtained by NSOM with high resolution fluorescence images of γδTCR on Vγ2+ T cells and the simultaneously recorded topography image of Vγ2+ T cells, scale bar: 1 μm [8, 13]

6 Mapping Cell Membrane Biomolecules by AFM-SMFS

After functionalization, AFM tips can be applied to detect a variety of ligand- receptor interactions on cell membrane using SMFS. Applying this method, the nanoscale explorations of cells using AFM to probe the specific biomolecules in cell membranes at a single molecule level has progressed tremendously in the past few years, especially in bacterial cells [14, 15]. Compared with mammalian cells, bacterial cells have more simplified and much stiffer membrane structures, which makes single molecule imaging of the surface of bacterial cells relatively easier than that of mammalian cells. Dupres et al. [7] reported a method with ligand-activated AFM tips to measure the specific binding forces of individual adhesions and to map their distributions on the surface of living bacteria. In another study, the localization and conformational analysis of individual polysaccharides on the surface of living bacteria were performed by SMFS analyses with Con A and PA-1-functionalized AFM tips [16]. Heinisch et al. [17] then presented a single molecule demonstration of clustering a transmembrane protein on the surface of bacterial cells. These results indicated that AFM-SMFS could be set as a powerful tool to map cell surface biomolecules.

AFM-SMFS could thus provide new insights into the dynamic clustering distribution and signaling behavior of trans-membrane biomolecules on the membranes of living bacterial cells. Francius et al. [18] presented a protocol to analyze polysaccharide chains of different natures on bacteria surfaces that described how functionalized AFM tips with concanavalin A lectins were available for stretching specific polysaccharide molecules on living bacteria and mapping the localizations, adhesions, and extensions of individual polysaccharide chains on bacterial surfaces. Some other membrane biomolecules of bacteria, such as fibronectin attachment proteins [19], Als5 and Als3 cell adhesion proteins [20, 21], wall teichoic acids [22], cell wall-anchored proteins, [23] and filamentous haemagglutinin [24] were also detected on bacterial cell membranes through a similar AFM force spectroscopic method, showing the broad application prospects of AFM for the in situ single molecule imaging of living bacterial surfaces. The AFM-based SMFS exploration of a bacterial surface shows the precise distribution of biomolecules on a bacterial membrane, with detailed force information between the ligands and their specific receptors on a cell membrane, which greatly promotes our understanding of the signaling behaviors of membrane biomolecules in bacteria.

Although the very soft property of mammalian cells is very difficult to be imaged by AFM, AFM-SMFS could also be applied to detect the distribution of biomolecules on the membrane of mammalian cells. The distribution of single HSPG receptors on the surface of living A549 cells was mapped by AFM, following investigation of the specific interactions between heparin-binding hemagglutinin and heparan sulphate proteoglycan receptors [25], which provided new avenues for pathogenesis research, particularly for elucidating the molecular basis of the pathogen-host interactions. Lama et al. [5] mapped the amount and distribution of the functional GnRH-R receptors on the surface of living prostate cancer cells by AFM, which

provided a crucial insight into the stimulatory effect of LA on GnRH-R expressed on the androgen-insensitive prostate cancer cell membranes. AFM force mapping can also be used for single ion channel imaging of living cell membranes [26]. The nanoscale distribution of CD20 on B-cell lymphoma tumour cells and Fc gamma receptors on macrophage were also investigated by AM-SMFS mapping [27, 28] These results obtained at molecular level dramatically enhanced our understanding of the distribution and function of cell membrane signaling biomolecules in mammalian cells.

7 Probing Cell Membrane Biomolecules by AFM-TREC

Unlike AFM-SMFS that are widely used for cell membrane biomolecule distribution studies, AFM-TREC is much more suitable for cell membrane biomolecule distribution studies in mammalian cells. Using TREC, the recognition images revealed single VE-cadherin and irregularly shaped VE-cadherin domains with sizes ranging from 10 to 100 nm [29]. More importantly, this work demonstrated the changes of VE-cadherin upon EDTA exposure at a temporal resolution of 5–10 min [9, 29], which indicated that the AFM-based TREC method could also be applied for the real time imaging of membrane biomolecules.

The nanoscale distribution and localization of CD1d molecules on THP1 cells were also presented by TREC [30]. Then, Ron et al. [31] introduced the specific force mapping of membrane-bound osteopontin and the topography of a mammalian cell, which they used to demonstrate the exact locations of the proteins relative to the cell membrane. Li et al. [32] also presented AFM-TREC to illustrate and evaluate the membrane distribution of TRA-1-81 antigen on fixed hES cells, which provided a platform for unveiling the correlation between the heterogeneity of the membrane proteins and cell development in a complex cell community. The AFM-TREC method was also used to localize FcγRs, revealing the nanoscale distribution of FcγRs on local areas of macrophages [28, 33]. The binding sites of the extracellular part of ion channels on cell surfaces could also be visualized by AFM-based TREC [34]. These works indicated that single biomolecules, such as single receptors, antigens, or ion channels, on fixed cell membranes could be recognized by the biologically functionalized AFM tip, provingthat AFM could be used to image the locations of single biomolecules in cell membranes. Because of the much more complicated dynamic properties of living cells, this operation technique for living cell imaging is much harder than in fixed cells.

A detailed procedure for investigating the proteins in membranes of living cells by AFM was first introduced by Li et al. [35]. Their experimental results showed that single biomolecules, such as receptors on the membranes of living cells, could also be recognized and imaged by AFM, which extensively extended the use of AFM for the in situ single molecule imaging of living cell membranes. Using an anti-VEGFR2-functionalized AFM tip, the number and distribution of VEGFR2 in the membrane of fixed and living endothelial cells were quantified [36]. This direct

single receptor imaging approach simultaneously quantified both the binding kinetics and the non-uniform distributions of these receptors with respect to the underlying cytoskeleton, providing spatio-temporal visualization of the cell surface dynamics that regulated single receptor behaviors. Xiao et al. also demonstrated highly sensitive and specific molecular recognition images and high-resolution topographic images of EGFR on single breast cancer cells, implying that TREC imaging technique could be used as a powerful imaging tool to study different cell surface receptors at molecular levels [37].

8 Application of NSOM for In Situ Single Molecule Detection on Cell Membrane

As expected, the ability of NSOM to map and detect co-localized proteins in cell membranes with a super-resolution of 100 nm was demonstrated [38]; our results proved that NSOM could be specifically applied to the immuno-fluorescence studies of biomolecules on cell surfaces, as well as highlighting the possibility and applicability of NSOM for the in situ single molecule imaging of cell membranes.

To achieve in situ single molecules imaging on a cell membrane by NSOM, a NSOM- and QD-based system conferred nanoscale immunofluorescence imaging of cell membrane was built by our group. By operating NSOM, the super-resolution immune fluorescence imaging of the antigen-specific T-cell receptor (TCR) response in an in vivo model of clonal T-cell expansion was achieved with high resolution [13]. The NSOM imaging system demonstrated that, before Ag-induced clonal expansion, nonengaging Vγ2Vδ2 TCR appeared to be distributed differently from nonengaging αβ TCR on cell membrane; also, the Vγ2Vδ2 TCR nanoclusters not only formed, but were also sustained on the membrane during the in vivo clonal expansion of Vγ2Vδ2 T cells after phosphoantigen treatment and after phosphoantigen plus mycobacterial infection. Additionally, the results indicated that the clonally expanded Vγ2Vδ2 T cells bearing high-density TCR nanoclusters were able to rerecognize antigens and exert better effector functions. This work firstly proved, by single molecule NSOM imaging, that the presence of high-density TCR nanoclusters may arm Vγ2Vδ2 T cells for mounting both innate and adaptive immune responses during infection; therefore, our research confirmed the use of NSOM for in situ single molecule imaging of cell membranes and provided new nanoscale insights into the in vivo/vitro immune responses. Using a similar system, CD3 molecules on human peripheral blood T lymphocyte membrane [39] and CD44 molecules on mesenchymal stem cell membrane [40] were also investigated at a single molecular level.

As a scanning probe-based optical microscopy technique, an important asset of NSOM beyond AFM's capability for molecule imaging is its ability to co-localize multiple molecules on the cell membrane simultaneously using the same probe, which is impossible for AFM imaging. Using the NSOM-based two color nanoscale

molecule imaging method, the distribution of IL-22 and CD44 molecules on the plasma membrane of CD4+ T cells was visualized by Zeng et al. [41] IL-22 produced by CD4 + T cells was found to evolve for retention on the cell membrane and engage as nanoclusters or nanodomains after de novo production in M. tuberculosis infection. Zhong et al. [42] showed the distribution of CD3 and CD4 molecules on T cells using NSOM, which indicated the distributional relationship between TCR/CD3 and CD4 molecules after anti-CD3 Ab stimulation. These reports strongly implied that the NSOM-based dual fluorescence technique could be regarded as a very effective tool for studying different biomolecules in cell membranes, providing a new perspective of the relationships between the distribution and functions of cell membrane biomolecules.

Based on the advantages of combining high-resolution fluorescence images and topographic images to visualize the precise distribution of single biomolecules in the complicated fluctuations of cell membranes, NSOM has been widely used in recent years for in situ single molecule imaging of cell membranes, and has greatly increased our understanding of the distribution of cell membrane biomolecules and its implications in cellular signaling and functions. For instance, information on the distribution of GM1 and CD59 molecules in cell membranes was determined by NSOM through the fluorescence-topographic images, which indicated where the lipid raft markers or lipid rafts were distributed and redistributed at T-cell membrane fluctuations [43]. By combining dual fluorescence images with high-resolution topographic information of the cell membrane, NSOM is a very effective tool for studying the spatial relationship of two different biomolecules in cell membranes and for revealing the nanospatial peakvalley polarities of biomolecules on cell membrane fluctuations. Using high-resolution fluorescence and the topography imaging of NSOM, Zhong et al. [44] found that most CD69 nanodomains were polarized predominantly in the peak of cell membrane fluctuations, while CD71 nanodomains did not colocalize with CD69 nanodomains, but instead were mainly located in the valley of cell membrane fluctuations. This NSOM-based dual fluorescence-topographic imaging technique makes it possible to image the exact distribution relationships of different biomolecules on cell membrane fluctuations at the single molecule level, which is very difficult to achieve by other optical imaging systems.

9 Combining AFM and NSOM for In Situ Single Molecule Imaging on Cell Membrane

Both as probe-based microscopy, AFM and NSOM can also be combined to study the structure of biological samples, which not only provides the optical distribution and structure morphology, but also the force information of biological samples [45]. The nanoscale features of CD69 expression on activated T cells were determined using the AFM topographic and force-binding nanotechnology, as well as NSOM

based nanosacle imaging, which represented the first demonstration of the nanobiology of CD69 expression during T cell activation [46]. Our studies demonstrated the potential use of combining AFM and NSOM for in situ single molecule imaging on cell membranes; however, more research needs to be done for this to be developed into a more functional technique.

10 Conclusions and Future Perspectives

Both AFM-SMFS and AFM-TREC methods rely on the functionalization of AFM tips with ligands to recognize their specific receptors on cell membranes; thus, the detected biomolecules or a portion of their subdomains must be distributed on the outer cell membranes to ensure specific interactions between the ligands and their target receptors. This property makes AFM a surface limited detection technique; therefore, it cannot be used for intracellular molecule imaging, but it is very suitable for in situ single molecule imaging of outer membrane biomolecules.

AFM is a very powerful technique that is capable of resolving the precise distribution of membrane biomolecules, and in particular, it can also be used to investigate the ligand-receptor interaction forces on cell surfaces. However, both AFM-SMFS and AFM-TREC methods are restricted to the detection of only one kind of biomolecule in an individual experiment and the dynamic study of cell membrane biomolecules is very difficult, due to its limited temporal resolution.

AFM-SMFS has proved to be very powerful in demonstrating the localization of cell membrane biomolecules in bacterial cells, due to AFM's ability to provide very precise topography images. Combining the topography images, the localization images could dramatically enhance the understanding regarding more precise distribution of biomolecules on cell membranes. However, the very soft properties of living mammalian cells is much more difficult to find cell membrane locations and precise topography images.Unlike AFM-SMFS, AFM-TREC could provide high resolution molecular recognition images of biomolecules and cell membrane topography images simultaneously; therefore, it could be more suitable for living mammalian cell detection.

As a probe-based imaging technique, high-resolution optical images of NSOM can only be acquired by exciting the fluorescent markers labeled on the cell surface in the nearfield area. Thus, the fact that the intracellular biomolecules cannot be imaged by NSOM is a restriction, making NSOM only suitable for the imaging of biomolecules on cell surfaces. We cannot deny that this property makes NSOM a limited technique for intracellular biomolecule imaging, but it is also an advantage for the in situ single molecule imaging of cell membranes because the fluorescent signals obtained by NSOM are all from conclusive membrane molecules, while the fluorescent molecules inside the cell cannot be detected. Taking advantage of this property, NSOM can also be used to confirm whether the detected biomopeaks of oscillationslecules are located or partially located on the outer plasma membrane of

cells, making NSOM an effective tool for confirming the exact location of biomolecules surrounding cell membranes.

Generally, to expand the applications of NSOM for the in situ single molecule imaging of cell membranes in living cells, further simplification of the NSOM operation system is required, and the stability of the NSOM system also needs to be strengthened. With the maturing and continuing improvement of the equipment, operation system, sample platform, and the laser optics in liquids, the use of the NSOM-based in situ single molecule imaging method for cell membranes should promote advancements in cell biology to the microfields more thoroughly and enable future innovative achievements.

In summary, AFM-SMFS, AFM-TREC and NSOM have proven to be very powerful techniques for in-situ single molecule detection of biomolecule distributions on cell membranes. The most advanced property of AFM is that it can also provide the interaction force information between the ligands on AFM tips and the receptors on cell membranes, which allows us to further study the signaling events of cell membrane biomolecules. Additionally, the most powerful property of NSOM is that it can provide the precise morphology of cell membranes with the distribution of biomolecules. We believe that further developments of equipment and AFM and NSOM methods would further extend our understanding of the roles and mechanisms of the membrane biomolecules involved in some key biological phenomena, and finally promote important future developments in cell biology, immunology, and medicine.

Acknowledgment This work is supported by China Postdoctoral Science Foundation (2018M631026) and Macau Science and Technology Development Fund (Grant No. 028/2014/A1). This chapter was adapted from the paper published by our group in Nanoscale (Pi Jiang, Jin Hua, Yang Fen, Chen ZhengW., Cai Jiye, 2014 Nov 7; 6; 21; 12229-12249). The related contents are reproduced with permission from The Royal Society of Chemistry.

References

1. Santini S, Di Agostino S, Coppari E, Bizzarri AR, Blandino G, Cannistraro S. Biochim Biophys Acta. 2014;1840:1958–64.
2. Carvalho FA, Connell S, Miltenberger-Miltenyi G, Pereira SV, Tavares A, Ariens RAS, Santos NC. Atomic force microscopy-based molecular recognition of a fibrinogen receptor on human erythrocytes. ACS Nano. 2010;4:4609–20.
3. Zhang J, Liu H, Zhu R, Hinterdorfer P, Zhang B, Tang J. Single molecular dissection of the ligand binding property of epidermal growth factor receptor. Analyst. 2013;138:5325–31.
4. Zhang X, Shi X, Xu L, Yuan J, Fang X. Atomic force microscopy study of the effect of HER 2 antibody on EGF mediated ErbB ligand–receptor interaction. Nanomedicine. 2013;9:627–35.
5. Lama G, Papi M, Angelucci C, Maulucci G, Sica G, De Spirito M. Leuprorelin acetate long-lasting effects on GnRH receptors of prostate cancer cells: an atomic force microscopy study of agonist/receptor interaction. PLoS One. 2013;8:e52530.
6. Puntheeranurak T, Neundlinger I, Kinne RK, Hinterdorfer P. Single-molecule recognition force spectroscopy of transmembrane transporters on living cells. Nat Protoc. 2011;6:1443–52.
7. Dupres V, Menozzi FD, Locht C, Clare BH, Abbott NL, Cuenot S, Bompard C, Raze D, Dufrene YF. Nanoscale mapping and functional analysis of individual adhesins on living bacteria. Nat Methods. 2005;2:515–20.

8. Pi J, Jin H, Yang F, Chen ZW, Cai J. In situ single molecule imaging of cell membranes: linking basic nanotechniques to cell biology, immunology and medicine. Nanoscale. 2014;6:12229–49.
9. Chtcheglova LA, Hinterdorfer P. Simultaneous topography and recognition imaging on endothelial cells. J Mol Recognit. 2011;24:788–94.
10. Betzig E, Trautman JK. Near-field optics: microscopy, spectroscopy, and surface modification beyond the diffraction limit. Science. 1992;257:189–95.
11. Garcia-Parajo MF, Veerman JA, van Noort SJT, de Grooth BG, Greve J, van Hulst NF. Near-field optical microscopy for DNA studies at the single molecular level. Bioimaging. 1998;6:43–53.
12. de Lange F, Cambi A, Huijbens R, de Bakker B, Rensen W, Garcia-Parajo M, van Hulst N, Figdor CG. Cell biology beyond the diffraction limit: near-field scanning optical microscopy. J Cell Sci. 2001;114:4153–60.
13. Chen Y, Shao L, Ali Z, Cai J, Chen ZW. NSOM/QD-based nanoscale immunofluorescence imaging of antigen-specific T-cell receptor responses during an in vivo clonal V 2V 2 T-cell expansion. Blood. 2008;111:4220–32.
14. Dufrene YF. Using nanotechniques to explore microbial surfaces. Nat Rev Microbiol. 2004;2:451–60.
15. Dufrene YF. Towards nanomicrobiology using atomic force microscopy. Nat Rev Microbiol. 2008;6:674–80.
16. Francius G, Lebeer S, Alsteens D, Wildling L, Gruber HJ, Hols P, De Keersmaecker S, Vanderleyden J, Dufrene YF. Detection, localization, and conformational analysis of single polysaccharide molecules on live bacteria. ACS Nano. 2008;2:1921–9.
17. Heinisch JJ, Dupres V, Wilk S, Jendretzki A, Dufrene YF. Single-molecule atomic force microscopy reveals clustering of the yeast plasma-membrane sensor wsc1. PLoS One. 2010;5:e11104.
18. Francius G, Alsteens D, Dupres V, Lebeer S, De Keersmaecker S, Vanderleyden J, Gruber HJ, Dufrene YF. Stretching polysaccharides on live cells using single molecule force spectroscopy. Nat Protoc. 2009;4:939–46.
19. Verbelen C, Dufrene YF. Direct measurement of Mycobacterium–fibronectin interactions. Integr Biol (Camb). 2009;1:296–300.
20. Alsteens D, Dupres V, Klotz SA, Gaur NK, Lipke PN, Dufrene YF. Unfolding individual Als5p adhesion proteins on live cells. ACS Nano. 2009;3:1677–82.
21. Beaussart A, Alsteens D, El-Kirat-Chatel S, Lipke PN, Kucharikova S, Van Dijck P, Dufrene YF. Single-Molecule Imaging and Functional Analysis of Als Adhesins and Mannans during Candida albicans Morphogenesis. ACS Nano. 2012;6:10950–64.
22. Andre G, Deghorain M, Bron PA, van Swam II, Kleerebezem M, Hols P, Dufrene YF. *ACS Chem Biol*. 2011;6:366–76.
23. Herman-Bausier P, Dufrene YF. Atomic force microscopy reveals a dual collagen-binding activity for the staphylococcal surface protein SdrF. Mol Microbiol. 2016;99:611–21.
24. Arnal L, Longo G, Stupar P, Castez MF, Cattelan N, Salvarezza RC, Yantorno OM, Kasas S, Vela ME. Localization of adhesins on the surface of a pathogenic bacterial envelope through atomic force microscopy. Nanoscale. 2015;7:17563–72.
25. Dupres V, Verbelen C, Raze D, Lafont F, Dufrene YF. Force spectroscopy of the interaction between mycobacterial adhesins and heparan sulphate proteoglycan receptors. ChemPhysChem. 2009;10:1672–5.
26. Maciaszek JL, Soh H, Walikonis RS, Tzingounis AV, Lykotrafitis G. Topography of native SK channels revealed by force nanoscopy in living neurons. J Neurosci. 2012;32:11435–40.
27. Li M, Xiao X, Zhang W, Liu L, Xi N, Wang Y. Nanoscale distribution of CD20 on B-cell lymphoma tumour cells and its potential role in the clinical efficacy of rituximab. J Microsc. 2014;254:19–30.
28. Li M, Liu L, Xi N, Wang Y, Xiao X, Zhang W. Imaging and measuring the biophysical properties of Fc gamma receptors on single macrophages using atomic force microscopy. Biochem Biophys Res Commun. 2013;438:709–14.

29. Chtcheglova LA, Waschke J, Wildling L, Drenckhahn D, Hinterdorfer P. Nano-scale dynamic recognition imaging on vascular endothelial cells. Biophys J. 2007;93:L11–3.
30. Duman M, Pfleger M, Zhu R, Rankl C, Chtcheglova LA, Neundlinger I, Bozna BL, Mayer B, Salio M, Shepherd D, Polzella P, Moertelmaier M, Kada G, Ebner A, Dieudonne M, Schutz GJ, Cerundolo V, Kienberger F, Hinterdorfer P. Improved localization of cellular membrane receptors using combined fluorescence microscopy and simultaneous topography and recognition imaging. Nanotechnology. 2010;21:115504.
31. Ron A, Singh RR, Fishelson N, Socher R, Benayahu D, Shacharn-Diamand Y. Site localization of membrane-bound proteins on whole cell level using atomic force microscopy. Biophys Chem. 2008;132:127–38.
32. Li ZX, Qiu DL, Xu KM, Sridharan I, Qian XP, Wang R. Analysis of affinity maps of membrane proteins on individual human embryonic stem cells. Langmuir. 2011;27:8294–301.
33. Ahmad SF, Chtcheglova LA, Mayer B, Kuznetsov SA, Hinterdorfer P. Nanosensing of Fcγ receptors on macrophages. Anal Bioanal Chem. 2011;399:2359–67.
34. Chtcheglova LA, Atalar F, Ozbek U, Wildling L, Ebner A, Hinterdorfer P. Localization of the ergtoxin-1 receptors on the voltage sensing domain of hERG K+ channel by AFM recognition imaging. Pflugers Arch. 2008;456:247–54.
35. Li G, Xi N, Wang DH. In situ sensing and manipulation of molecules in biological samples using a nanorobotic system. Nanomedicine. 2005;1:31–40.
36. Lee S, Mandic J, Van Vliet KJ. Chemomechanical mapping of ligand-receptor binding kinetics on cells. Proc Natl Acad Sci USA. 2007;104:9609–14.
37. Xiao L, Chen Q, Wu Y, Qi X, Zhou A. Biochim Biophys Acta. 1848;2015:1988–95.
38. Enderle T, Ha T, Ogletree DF, Chemla DS, Magowan C, Weiss S. Membrane specific mapping and colocalization of malarial and host skeletal proteins in the Plasmodium falciparum infected erythrocyte by dual-color near-field scanning optical microscopy. Proc Natl Acad Sci U S A. 1997;94:520–5.
39. Zhong LY, Liao WT, Wang XP, Cai JY. Colloids Surf A. 2008;313:642–6.
40. Chen J, Pei Y, Chen Z, Cai J. Quantum dot labeling based on near-field optical imaging of CD44 molecules. Micron. 2010;41:198–202.
41. Zeng G, Chen CY, Huang D, Yao S, Wang RC, Chen ZW. Membrane-bound IL-22 after de novo production in tuberculosis and anti-mycobacterium tuberculosis effector function of IL-22+ CD4+ T cells. J Immunol. 2011;187:190–9.
42. Zhong L, Zeng G, Lu X, Wang RC, Gong G, Yan L, Huang D, Chen ZW. NSOM/QD-based direct visualization of CD3-induced and CD28-enhanced nanospatial coclustering of TCR and coreceptor in nanodomains in T cell activation. PLoS One. 2009;4:e5945.
43. Chen Y, Qin J, Cai J, Chen ZW. Cold induces micro- and nano-scale reorganization of lipid raft markers at mounds of T-cell membrane fluctuations. PLoS One. 2009;4:e5386.
44. Zhong L, Zhang Z, Lu X, Huang D, Chen CY, Wang R, Chen ZW. NSOM/QD-based fluorescence–topographic image fusion directly reveals nano-spatial peak–valley polarities of CD69 and CD71 activation molecules on cell-membrane fluctuations during T-cell activation. Immunol Lett. 2011;140:44–51.
45. Zeng G, Chen J, Zhong L, Wang R, Jiang L, Cai J, Yan L, Huang D, Chen CY, Chen ZW. NSOM- and AFM-based nanotechnology elucidates nano-structural and atomic-force features of a Y. pestis V immunogen-containing particle vaccine capable of eliciting robust response. Proteomics. 2009;9:1538–47.
46. Hu M, Chen J, Wang J, Wang X, Ma S, Cai J, Chen CY, Chen ZW. AFM- and NSOM-based force spectroscopy and distribution analysis of CD69 molecules on human CD4+T cell membrane. J Mol Recognit. 2009;22:516–20.

Chapter 4
AFM Imaging-Force Spectroscopy Combination for Molecular Recognition at the Single-Cell Level

Filomena A. Carvalho and Nuno C. Santos

Abstract Molecular recognition at the single-cell level is an increasingly important issue in Biomedical Sciences. With atomic force microscopy, cell surface receptors may be recognized through the interaction with their ligands, inclusively for the identification of cell-cell adhesion proteins. The spatial location of a specific interaction can be determined by adhesion force mapping, which combines topographic images with local force spectroscopy measurements. Another valuable possibility is to simultaneously record topographic and recognition images (TREC imaging) of cells, enabling the mapping of specific binding events on cells in real time. This review is focused on recent developments on these molecular recognition approaches, presenting examples of different biological and biomedical applications.

Intermolecular recognition may be considered as the beginning for many biochemical processes. It involves several types of forces between single molecules. Different approaches have been developed to measure intermolecular forces, such as optical trapping [1–3], pipette suction [4] and surface forces apparatus (SFA) experiments [5]. Optical trapping is a very sensitive technique, but it is limited to measurements of less than tens of piconewtons and can only be applied to a small group of samples. Pipette suction and SFA experiments are sensitive techniques, but both have poor spatial resolution. The use of atomic force microscopy (AFM) in this context may overcome the problems associated to the previous techniques.

AFM is a very powerful technique, with great spatial resolution, which can probe surfaces maintaining their physiological environments and measure forces down to the piconewton range [6–10]. AFM can be used not only for imaging but, since the mid 1990's, with the first force spectroscopy study [10, 11], it can also be used to record force-distance curves of biological systems. This enables AFM to measure

F. A. Carvalho (✉) · N. C. Santos
Instituto de Medicina Molecular, Faculdade de Medicina, Universidade de Lisboa, Lisbon, Portugal
e-mail: filomenacarvalho@fm.ul.pt

J. Cai (ed.), *Atomic Force Microscopy in Molecular and Cell Biology*,
https://doi.org/10.1007/978-981-13-1510-7_4

intermolecular forces between single molecules (*e.g.*, ligand-receptor interactions), which can be used for molecular recognition studies.

The combination of molecular recognition and topographic information has been studied by two different approaches: 1) adhesion force mapping mode, and 2) topographic and recognition (TREC) imaging.

1 Adhesion Force Mapping Using Force Spectroscopy

Adhesion force mapping can be performed by applying the force-volume mode or by collecting the topographic image with the maximum adhesion map on the retract part of a force-distance curve. On the force-volume mode, all force-distance curves are collected, leading to a huge amount of data, with difficult post-processing. The maximum adhesion map is created by recording whole force-distance curve(s) for every pixel of the scan. However, the ability to distinguish a molecule on the adhesion map is very limited as compared with the topography image; thus, usually no correlation between both images can be performed [12].

Force spectroscopy can be performed at a single sample spot, by selecting it on the AFM scanning image, or it can be record spatially in the x,y plane. Quantitative tip-sample adhesion maps may then be generated. The principle is to record spatially resolved force-distance curves by moving the AFM scanner across the biological samples over an area of a given size with n × n points to be probed (typically, 32, 64 or 128) [13–15]. The x,y AFM image is divided into a square grid of n^2 pixels and the system performs one or more approach/retract cycle(s) on the center of each square/pixel, with a common lateral resolution from a few tens to hundreds of nanometers per pixel (Fig. 4.1) [16]. At the same time, the system creates maps (of height, adhesion or elasticity), which data may be processed and quantified. Thus, for each force-distance curve, a given property of the sample can be extracted, quantified and displayed on maps. Color or grey scale can be used to display the pixels on the maps of each analyzed property of the sample. Brightness pixels reflect the magnitude of the measured property at a defined location [17–20]. Due to speed limitations and poorer spatial resolution on the most common atomic force microscopes, this method did not have significant scientific progress before the 2000's. Only after 2001, with the development of high-speed scanners, free of resonant vibrations up to 60 kHz, it was possible to build a high-speed AFM. This microscope was capable to capture a 100 × 100 $pixel^2$ images within 80 ms and, therefore, generate a movie of biological samples under physiological conditions [21]. This AFM provided a way to record and correlate data from structure, adhesion and elasticity maps of samples faster, achieving molecular resolution.

In 2008, Sahin et al. conducted a nanomechanical mapping by the real-time analysis of time-varying tip-sample forces in tapping-mode AFM [23]. For the first time, they constructed maps of local elastic modulus and adhesion forces, together with conventional phase and topography images, in tapping mode. This new approach allowed the nanomechanical analysis of samples with gentle forces and high spatial

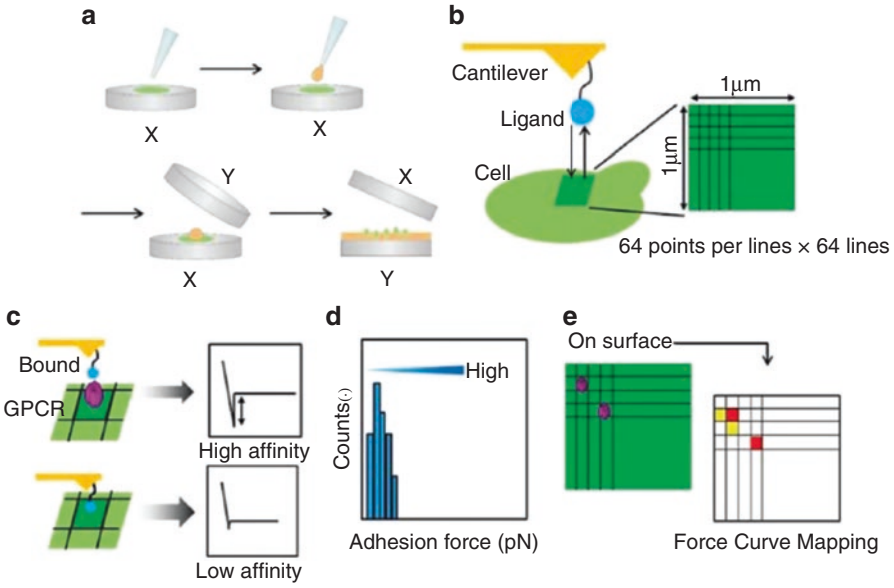

Fig. 4.1 Schematic representation of adhesion force mapping. (**a**) Immobilization procedure for a sample on a glass slide. (**b**) A cantilever derivatized with a ligand approaches to the surface of a cell to conduct force measurements of n × n points within 1 × 1 µm^2. (**c**) Differences between high and low affinity systems. (**d**) Adhesion force histogram. (**e**) Force curve adhesion mapping, representing high (*red*), low (*yellow*) and very low (*white*) affinity binding measurements. Reprinted with permission from [22]

resolution [23]. A new dynamic AFM method to quantitatively map the nanomechanical properties of live cells with a throughput 10 to 1000 times higher than that achieved with quasi-static AFM techniques was introduced in 2011 [24]. In 2015, a new fast scanning quantitative dynamic AFM method for nanomechanical imaging of heterogeneous live cells in solution was introduced, using the cantilever mean deflection as feedback signal, instead of standard amplitude reduction. This new method was able to achieve a 10 to 20-fold improvement in imaging throughput, compared to amplitude-modulation AFM [25].

Moreover, combining force spectroscopy mapping with an AFM-mounted fluorescence microscope enables dual fluorescence and AFM adhesion map imaging, allowing the detection and local determination of potential submicron-sized adhesive regions [26]. Nanoparticle tracking analysis and quantitative nanomechanical mapping AFM were also combined to determine size and nanomechanical properties of exosomes isolated from non-malignant and malignant (metastatic and non-metastatic) cell lines [27]. Authors revealed that malignant cell line exosomes have lower stiffness and adhesion compared to non-malignant cell line exosomes.

AFM-based adhesion nanomechanical mapping provides insights into the functions of different biological systems [28]. This technology has already been applied by different researchers to simultaneously image and quantify biophysical proper-

ties of complex samples, such as diatoms [29], lipid phases in supported bilayers [30], diverse membrane proteins [31–33], yeasts [34], virus capsids [35], human cells [25, 36–40] and neurodegenerative amyloid fibrils [41].

In 1998, Willemsen et al. demonstrated that the resolution of the topographical image in adhesion mode is only limited by tip convolution and, thus, comparable to tapping mode images. By comparing the high-resolution height image with the adhesion image, it is possible to show that specific molecular recognition is highly correlated with topography. This was possible by studying recognition events for individual antibody-antigen pairs when authors imaged individual ICAM-1 antigens both in tapping mode and the adhesion mode [42].

The characterization of the local mechanical properties of polymer cushioned membranes [43], as well as nanofibers [44], was also possible by applying force mapping methodologies. An AFM tip functionalized with cytochrome C2 molecules was also used to map native protein-protein interactions found in bacterial photosynthesis (electron donor/intrinsic membrane acceptor pair) [45]. AFM was also used to measure the adhesion force between targeting receptors and their ligands, and to map the targeting receptors (*e.g.*, Ste2p, a G protein-coupled receptor [22]). At the level of protein-protein interactions, the measurement of the binding force between glyceraldehyde-3-phosphate dehydrogenase (GAPDH) and Ras homologue enriched in brain (Rheb) was also performed [46]. By AFM-recognition mapping using specific DNA aptamers, it was possible to study the binding between human α-thrombin and vascular endothelial growth factor (VEGF), two proteins involved on the clotting cascade [47]. It is therefore possible to generate high resolution maps to spatially and temporally identify proteins at the molecular level on complex surfaces.

On other fields of research, such as crime scene investigations, PeakForce quantitative nanomechanical mapping (PF QNM) AFM has been used to study the variations in surface adhesion and topography of latent fingermark droplets over time [48].

On this review, we will highlight the application of adhesion force mapping methodologies to study different types of cells.

In 2015, Rigato et al. performed AFM-based mechanical mapping on cells plated on micropatterns, demonstrating a pattern-specific reproducible mechanical response [49]. This yields the possibility of average the data of the elasticity maps allowing to specifically locate intracellular elasticity differences, which are maintained among cells, and to identify regions characterized by higher or lower mechanical stability [49].

One of the first studies that was performed with microbial cells was done by Gad et al. [20], whom focused on the distribution of mannan, a particular type of polysaccharides, on the surface of a living microbial cell. Specific AFM mapping molecular recognition events were only detected on specific areas of the cell surface, which was interpreted as reflecting a non-uniform distribution of mannan on the cell surface. Specific procedures are necessary to conduct these AFM measurements. Methods for: (i) functionalizing AFM tips with *Pseudomonas aeruginosa* or concanavalin A, (ii) for stretching specific polysaccharide molecules on live bacteria using single-molecule force spectroscopy with lectin-coated tips, and (iii) for

mapping the localization, adhesion and extension of individual polysaccharide chains were described in detail [50].

Experiments to measure the interaction forces of bacterial adhesins (HBHA) and for assessing their distribution on the surface of living cells (*Mycobacterium bovis* BCG cells) were successfully conducted by Dupres et al. [19, 51]. High-resolution image and adhesion force maps of a sodium dodecyl sulphate-treated *Aspergillus fumigatus* spore revealed high correlation between structural and hydrophobic heterogeneities [52].

In 2013, Alsteens et al. reported the correlation between structural, adhesion and elasticity images of complex biological samples, recorded at high temporal and spatial resolutions, and with biochemical specificity [18]. Using this method, they provided a direct visualization of the assembly machinery of bacteriophages on living cells, revealing that they localize near the septum, in the form of soft nanodomains surrounded by stiffer cell wall material [18]. The assessment of the electric charge distribution on the surface of the cell wall of Gram-positive bacteria was also proven to be feasible by AFM mapping images at a spatial resolution better than a few tens of nanometers [53].

On another report, the hydrophobic forces engaged in Epa6-mediated cell adhesion were successfully measured by AFM [54]. Using single-cell force spectroscopy, the authors conclude that *Candida glabrata* wild-type (WT) cells bind to hydrophobic surfaces via strongly adhesive macromolecular bonds, while mutant cells with impaired in Epa6 expression are weakly adhesive (Fig. 4.2).

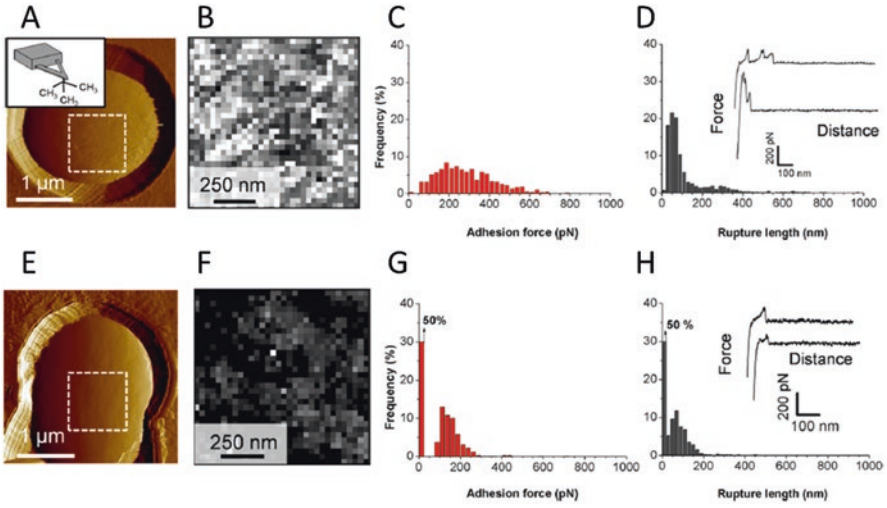

Fig. 4.2 Mapping and quantification of hydrophobic forces on *C. glabrata* cells using chemical force microscopy. AFM deflection images of WT (**A**) and Epa6 mutant (**E**) cells. The dashed white squares indicate the regions where the force maps were recorded. Adhesion force maps (1 µm × 1 µm; bright pixels correspond to hydrophobic binding events) of WT (**B**) and mutant (**F**) cells; respective adhesion force (**C**, **G**) and rupture length (**D**, **H**) histograms. Adapted and reprinted with permission from [54]

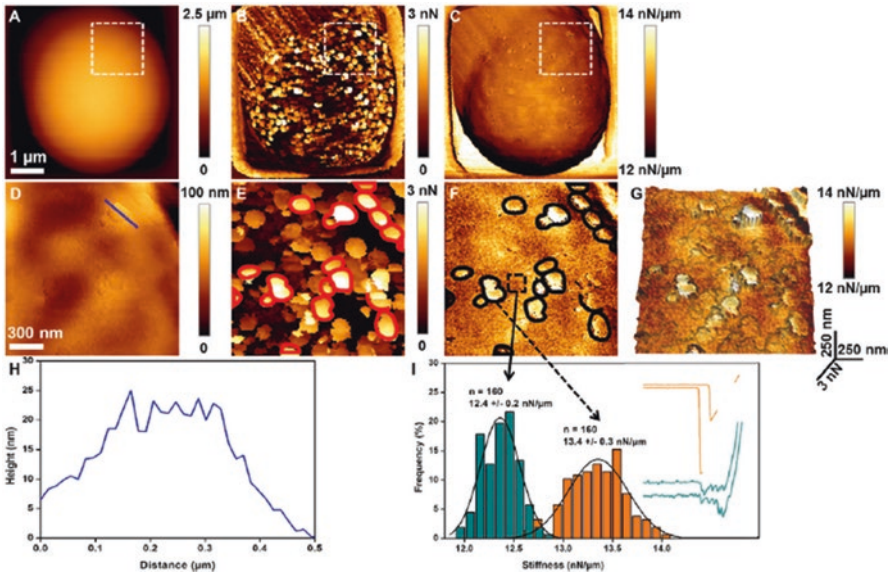

Fig. 4.3 Nanomechanics of the adhesive domains of *C. albicans* cells. Height image (**A**), and corresponding adhesion (**B**) and stiffness (**C**) images. Height (**D**), adhesion (**E**) and stiffness (**F**) images of a small area on top of the cell, corresponding to the white dashed square on A. Adhesive nanodomains circled in red on (**E**) are also found on the stiffness image (black circles on (**F**)). 3D-image of the adhesion mapped with the stiffness (**G**). Cross-section (**H**) taken along the blue line on (**D**). Distribution of the stiffness values (**I**) corresponding to the cell wall and the less adhesive domains (blue columns) or to the most adhesive domains (orange columns). Reprinted with permission from [55]

The observation that adhesins at the surface of *Candida albicans* cells are organized in nanodomains composed of free or aggregated mannoproteins was possible by AFM mapping of the adhesive properties of these cells (Fig. 4.3) [55].

Using a dynamic AFM technique operating in the intermittent contact regime to quantitatively map the local electro-mechanical force gradient, adhesion, and hydration layer viscosity within individual f29 virions, other authors provided new evidences of how bacteriophages like pressurized vessels, releasing DNA through any fracture present on the viral shell [56].

By studying the effect of plasma membrane receptor clustering on local cell mechanics, Almqvist et al. obtained adhesion force maps for the interaction between an antibody at the AFM tip and a specific VEGF receptor [17]. VEGF receptors were found to concentrate toward the cell boundaries and cluster rapidly, with local stiffness reductions (Fig. 4.4).

Mapping images of the distribution of sugar chains on epithelium and of the receptor associated protein (RAP) binding proteins on fibroblasts were also obtained [57, 58].

In 2007, the local mechanical characteristics of different cell types (namely, muscle, endothelial, epithelial and glial cells, neurons, fibroblasts, osteoblasts,

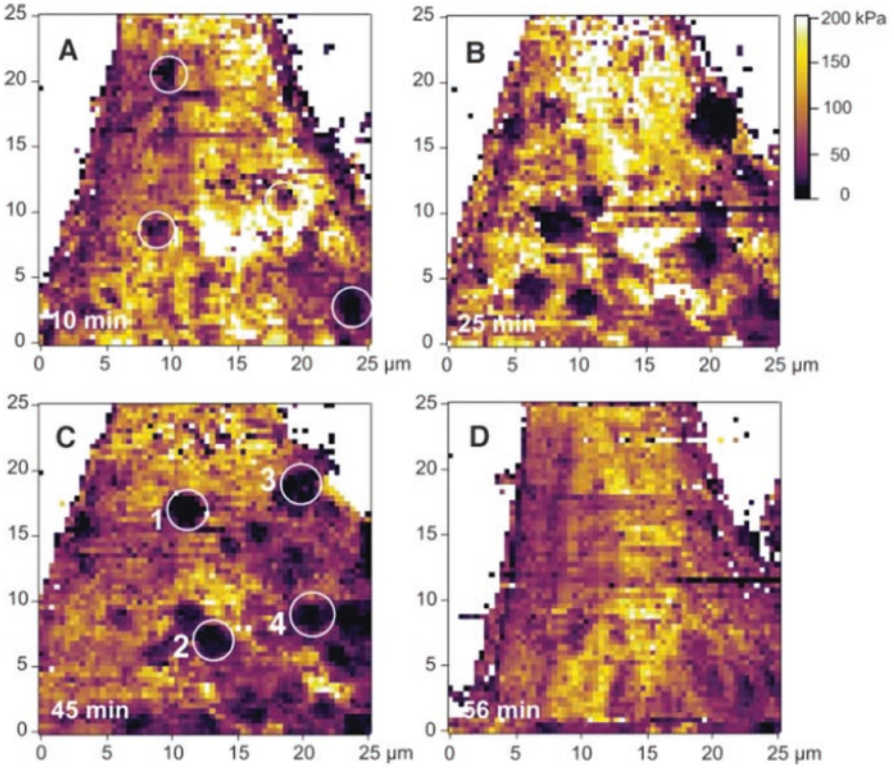

Fig. 4.4 Elasticity maps of the evaluated Young's modulus on endothelial cells in real-time, showing clustering of VEGF receptors on the cell surface. Images are colour-coded according to the bar, from 0 kPa (*dark*) to 200 kPa (*bright yellow*). Images show the elasticity at different time points after adding anti-flk-1 antibody: 10 min (**A**), 25 min (**B**), 45 min (**C**) and 56 min (**D**) after addition. A few regions with lower elasticity are marked with numbers 1–4 in (**C**). The regions underlying the receptor clusters appeared as less stiff. Reprinted with permission from [17]

blood cells and sensory cells) were analysed by Kuznetsova et al. [59]. According to this work, normal cells are one order of magnitude stiffer than cancer cells. Authors suggested that such change in elastic properties might be attributed to a difference in cytoskeleton organization. In another study, mapping of the local Young's modulus of a living astrocytes revealed that stiffer areas correspond to the sites where the cytoskeleton fibers are located (Fig. 4.5) [60].

Cassina et al. demonstrated that a peptide obtained from the cleavage of the neuroprotein VGF stimulates intracellular calcium mobilization in Chinese Hamster Ovary (CHO) cells [61]. The sub-cellular localization of the tyrosine kinase receptor (Met) for hepatocyte growth factor on hippocampal neurons was also studied by AFM force spectroscopy adhesion mapping. Authors found that multimeric activated Met is concentrated in the dendritic compartment, while the inactivated monomeric form of Met was prominent on the soma [62]. An adhesion force

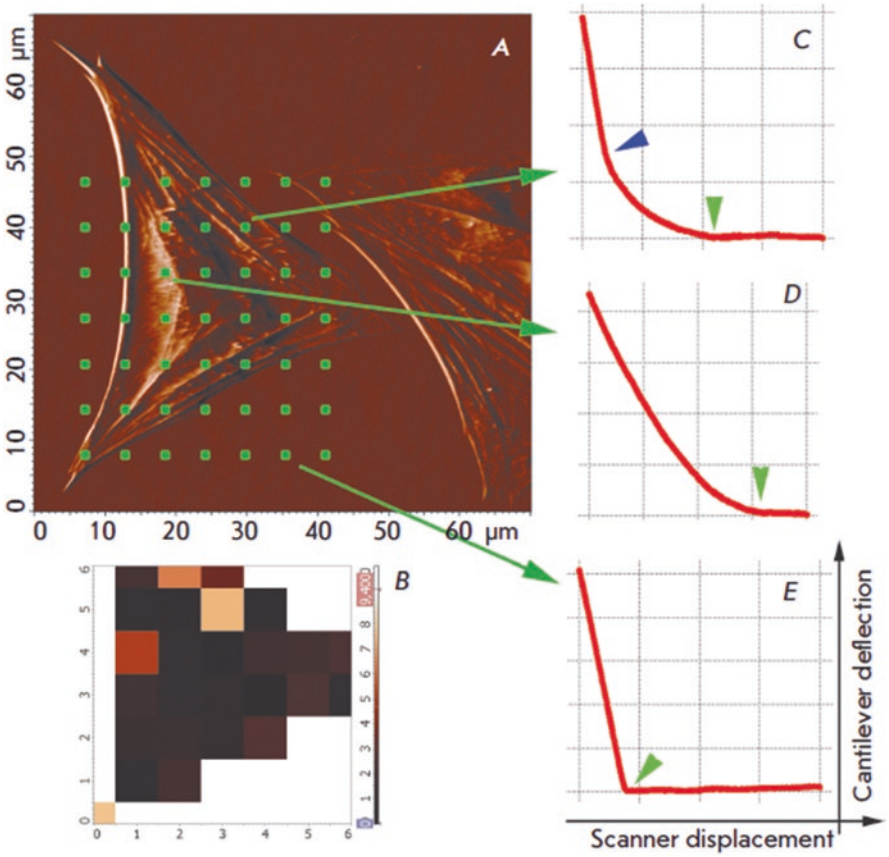

Fig. 4.5 Mapping the local Young's modulus of astrocytes. (**A**) Deflection image of a living astrocyte, with a grid of points indicating where the force curves were obtained. (**B**) Map of the local Young's modulus in the grid nodes (colour scale in kPa, with lighter squares corresponding to stiffer areas). (**C**) Force curve obtained in a point above the cell edge; the upper part of the curve coincides with the curve obtained on the substrate (**E**). Green arrows mark the contact point and the blue arrow the point where the cantilever touches the substrate. (**D**) Force curve obtained in a point above the cell nucleus. Reprinted with permission from [60]

mapping methodology was also applied to reveal the nanoscale distribution of Fc gamma receptors on local areas of macrophages, which have an important role in clinical cancer immunotherapy [38].

The morphology and the elastic properties of live cultured, non-malignant human mammalian epithelial cells (HMEC) and cancerous breast epithelial cells (MCF7) were also investigated through AFM force mapping [40]. The quantification of the surface density and the spatial organization of CXCR4 on breast cancer cell membranes were also assessed by AFM, leading the authors conclude that the CXCR4 density, spatial organization, and matrix stiffness are paramount to achieve strong binding [63].

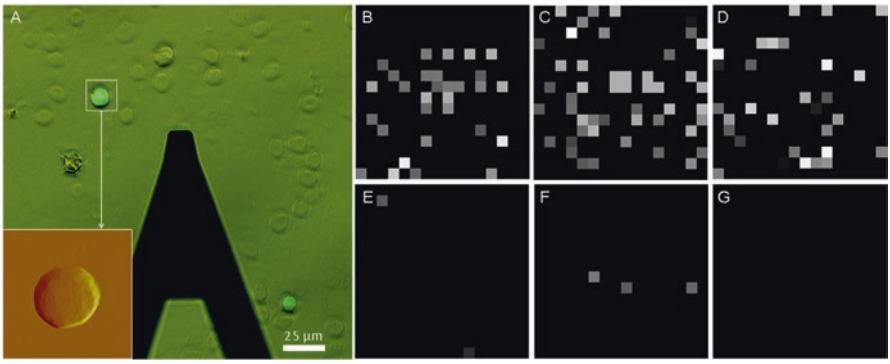

Fig. 4.6 Detection of specific CD20-rituximab interactions on cancer cells. (**A**) Fluorescence image of a clinical bone marrow cell sample, with the AFM image of a single cell as inset. (**B, C, D**) CD20 distribution maps on the cancer cells. (**E, F, G**) CD20 distribution maps on the cancer cells after blocking with rituximab, a monoclonal antibody against CD20. Grayscale is from black to white, up to 200 pN. Reprinted with permission from [39]

Specific molecular-receptor interactions on living human colorectal cancer cells were also already tested as *in vitro* models for gut epithelium [36]. On this study, authors measured the binding of wheat germ agglutinin to the surface of living Caco-2 human intestinal epithelial cells.

Using fast scanning dynamic AFM, it was possible to observe the nanomechanical spatio-temporal response of the cortical actin cytoskeleton, including the formation and movement of lateral actin bands [25]. These bands are characteristic of the retrograde actin flow machinery rapidly formed by inhibiting Syk expression in MDA-MB-231 breast cancer cells.

AFM was also applied to map the nanoscale distribution of CD20 molecules on the surface of cancer cells from clinical B-cell non-Hodgkin's lymphoma (NHL) patients, with the assistance of ROR1 (a cell surface marker expressed exclusively on cancer cells) fluorescence recognition (Fig. 4.6) [39]. The membrane protein CD20 is an effective target for treating B-cell NHL, as demonstrated in clinical practice. That study provided a new approach to directly investigate the nanoscale distribution of a target protein on individual clinical cancer cells.

2 Topographic and Recognition (TREC) Imaging

The second approach to study molecular recognition is a very powerful technique, which combines imaging at high resolution and single-molecule interaction measurements [64–66]. TREC imaging is a dynamic approach that uses an oscillating tip close to its resonant frequency [65, 67]. This technique is faster and has better lateral resolution (few nanometers) than adhesion force mapping [15, 65, 66]. Topographic and recognition images are obtained at the same time, allowing to

distinguish sites of receptors in the recognition image, spatially correlating them with features of the topographic image. TREC imaging uses a molecule (ligand) covalently attached to the AFM tip, usually via a flexible crosslinker (*e.g.*, poly(ethylene glycol) – PEG) [68–70]. During the scanning of the surface, the functionalized tip oscillates close to its resonance frequency. The binding sites are evident from the reduction in the oscillation amplitude, as a result of specific recognition during the lateral scan. Enhanced signal processing, in combination with a modified feedback loop [64], provides a recognition image simultaneously acquired alongside the topography image. The separation of topographical and recognition signals is achieved by splitting the cantilever's oscillation amplitude into lower and upper parts (relative to the cantilever's resting position), containing solely topography and recognition information, respectively. The maxima of these parts are then used to record the topography (lower part) and recognition image (upper part) at the same time (Fig. 4.7) [71, 72].

TREC imaging on AFM offers different advantages [73]: (i) high resolution of samples and high tracking capacity of target molecules on cells; (ii) high recognition specificity; (iii) less sample damage and no sample pre-treatment; and, (iv) simple and clear output, demonstrating the exact location of target molecules on the surface of the scanned sample. The use of TREC imaging offers a wide range of biological applications. It enables the study of the real location of single molecules on a tissue or cell surface, providing new perceptions of cell physiological mechanisms.

Applying TREC imaging, it is possible to investigate interactions of single molecules with their specific receptors, while simultaneously recording a high-resolution topography image. The combination of topographic and recognition images has been demonstrated on different biological systems with great success. This technique has already been useful to study chromatin structures [65], receptor-ligand pairs [64, 66, 72], proteins [75], isolated erythrocyte membranes [76] and cells [77, 78].

Radmacher et al. reported one of the first adhesion mapping studies, which was done by mapping lysozyme aggregates adsorbed onto mica [79]. A decrease of the adhesion of the tip with the lysozyme compared to mica was observed. This study was performed with a non-functionalized tip and the adhesion map was based on the physicochemical properties of the molecule and the substrate, rather than on specific biomolecular interactions. Ludwig et al. used a biotin-functionalized tip to map a streptavidin pattern and, with specific high-affinity interaction measurements, were able to create an adhesion map [80].

In 2005, Agnihotri et al. used binary recognition images to differentiate specific from unspecific interactions between fibrinogen on the surface and its specific antibody [81]. The number of recognition events had a major decrease after blocking the surface with anti-fibrinogen antibodies. The positive events observed in the recognition image were considered as specific antibody-fibrinogen interactions.

An adaptation of this technique was proposed by Wang et al. which used an AFM tip with two tethered antibodies and sequential blocking to identify two types of proteins in single AFM images of compositionally complex molecules [82]. By

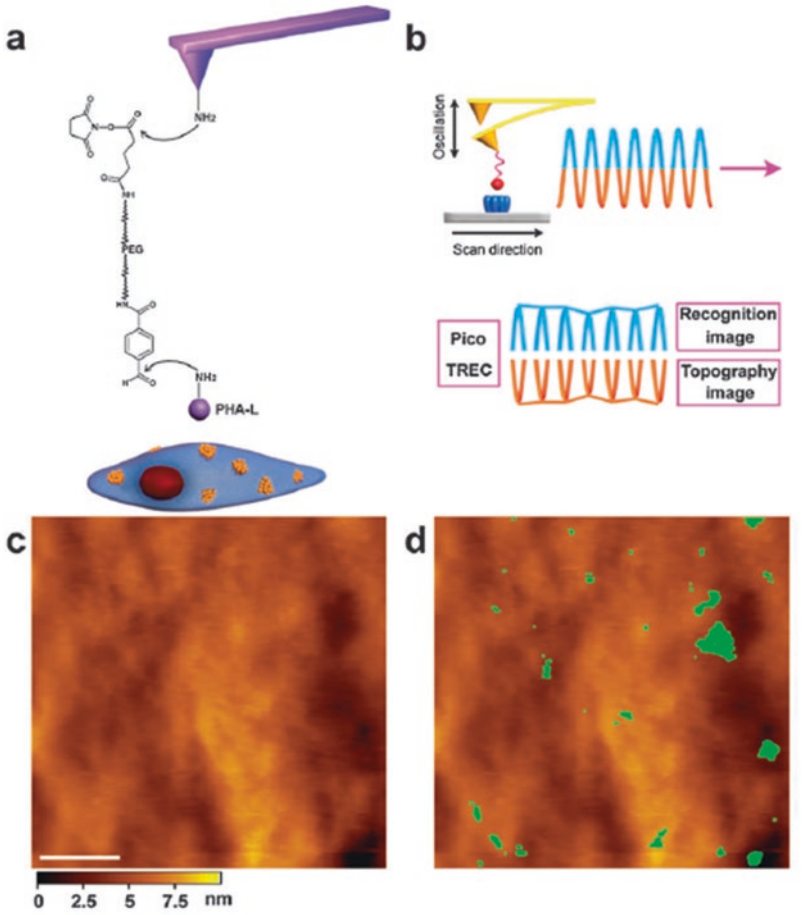

Fig. 4.7 TREC molecular recognition imaging of galactose on the surface of HeLa cells. (**a**) Scheme of the AFM tip modified with a lectin (PHA-L). (**b**) Principles of TREC imaging, scanning the cell with the modified tip (scale bar: 300 nm). (**c**) Topography image. (**d**) Topography image with the recognition signal superimposed. Adapted and reprinted with permission from [74]

applying this methodology, authors were able to analyse two specific components, BRG1 and β-actin, of the human Swi-Snf ATP-dependent nucleosome remodelling complex and two types of histones, H2A and H3, on the chromatin samples (Fig. 4.8).

Sotres et al. proposed other mode of performing force scanning by AFM, named jumping mode [12]. Topographic and tip-sample adhesion maps are acquired simultaneously. Lateral resolved adhesion maps of avidin-biotin unbinding forces highly correlated with single avidin molecules in the corresponding topographic map were achieved after testing this method.

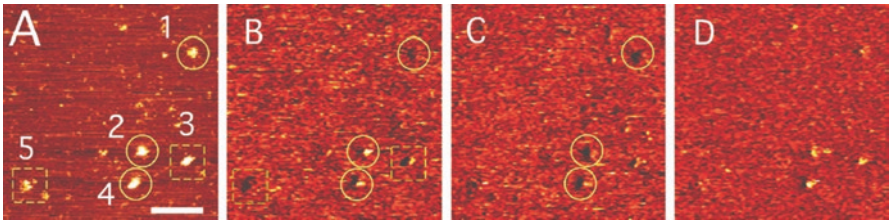

Fig. 4.8 Identification of different subunits in a multiprotein complex. Human Swi-Snf ATP-dependent nucleosome remodelling complexes were deposited and scanned with an AFM tip with both anti-BRG1 and anti-β-actin antibodies, rescanned in the presence of β-actin blocking peptide, and then rescanned in the presence of BRG1 and β-actin blocking peptides. (**A**) Topographic image from the initial scan. (**B**) Corresponding recognition image (no blocking). (**C**) Recognition image obtained after blocking with β-actin peptide. (**D**) Recognition image obtained when both BRG1 and β-actin blocking peptides are present. Dashed squares identify complexes whose recognition disappears after blocking with β-actin peptide and solid circles identify complexes whose recognition disappears only when BRG1 blocking peptide is present. Squares and circles are shown only when molecular recognition occurs, *i.e.*, in (**B**) and (**C**). Reprinted with permission from [82]

A simple procedure for adjusting the optimal amplitude for TREC imaging was described by Preiner et al. [71]. This method takes advantage of the sharp localization of the TREC signal within a small range of oscillation amplitudes. Using this procedure, authors imaged single avidin molecules immobilized on a mica substrate with an AFM tip functionalized with a biotinylated IgG.

In 2014, van Es et al. presented a new way to look at AFM TREC data. TREC imaging was used on a model system comprising an S-layer surface modified with Strep-tag II for binding sites and Strep-Tactin bound to the AFM tip [83]. They have shown that high resolution TREC images contain information on binding and unbinding rates for surface bound molecules. They also presented a method to analyse the TREC images to extract these rates as a function of distance between the AFM tip and the binding site. The authors concluded that high resolution TREC imaging is a valid method to determine k_{on} values at the single-molecule level [83].

Force clamp force mapping (FCFM), an AFM-based technique for measuring the viscoelastic creep behaviour of live cells with sub-micrometer spatial resolution, can also be successfully applied [84].

A study from 2009 evaluated the changes in surface topography, surface adhesion, indentation depth and Young's modulus on a metal-tolerant marine bacterium after its exposure to cobalt (II) ions [85]. An overall increase on the elasticity of the bacterial membrane and an increase in adhesiveness were observed.

Detailed procedures for all stages of TREC experiments with cells (*e.g.*, vascular endothelial cells), from tip and sample preparations to the operating principles and visualization, were described by Chetcheglova et al. [86].

The distribution of osteopontin (OPN) over pre-osteogenic cell membrane was tracked by mapping the adhesion forces between an anti-OPN coated probe and the cell surface. Authors were able to recognize specific OPN nanodomains on the cell membrane (Fig. 4.9) [73].

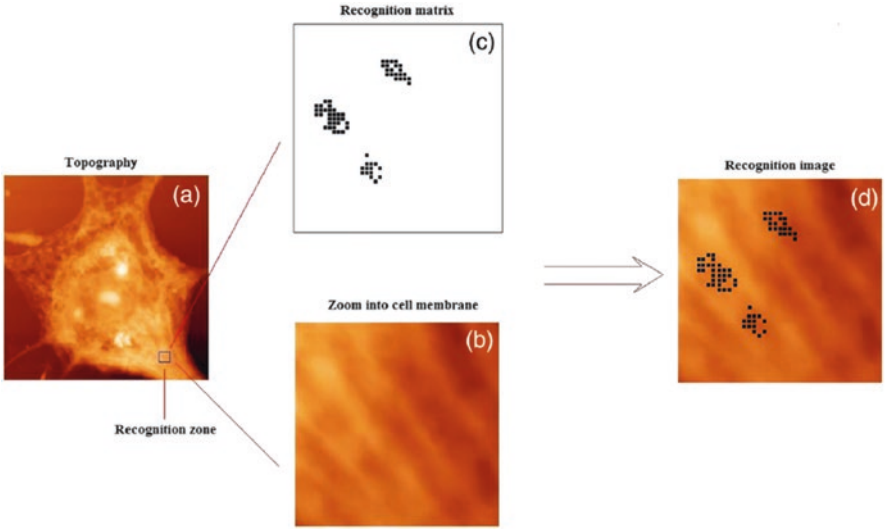

Fig. 4.9 (**a**) Topographic AFM image of a pre-osteogenic cell (the black frame on the right corner shows the chosen recognition zone). (**b**) High resolution topography image of the recognition zone. (**c**) Recognition matrix demonstrates the location of all specific binding events between anti-OPN tip and the OPN proteins on the cell surface. (**d**) The recognition image was created by merging the binary matrix image (**c**) and the high resolution topography image of the recognition zone (**b**). The image reveals the location of all OPN sites over the recognition zone. Each black square indicates the location of an OPN site. AFM images of 30 × 30 μm^2 (**a**) and 1 × 1 μm^2 (**b**–**d**). Reprinted with permission from [73]

On another TREC imaging study, galactose was detected and localized on the surface of cancer and normal cells [74]. Authors revealed that there are more galactose residues on cancer cells than on normal ones, and that the stability of galactose-lectin binding on cancer cells is much lower than that on normal cells.

Recently, the interaction of the specific DNA aptamer sgc8c immobilized at the AFM tip with its corresponding receptor, protein tyrosine kinase-7 (PTK7), embedded in the membrane of acute lymphoblastic leukaemia (ALL) cells (Jurkat T-cells) was investigated [87]. A homogeneous distribution of PTK7 molecules on the outer regions of ALL cells with a surface density of 325 ± 12 PTK7 receptors (or small receptor clusters) per μm^2 was demonstrated (Fig. 4.10).

TREC mapping was also applied to the imaging of α actinin-4 filaments and mapping of the epitopic region within α actinin-4 molecule using an antibody functionalized tip [88]. To gain a comprehensive view of the structural and chemical properties of *Staphylococcus epidermidis*, four different strains (biofilm positive and biofilm negative strains) were also analysed using the same methodology [89]. On this study, force measurements performed using bare hydrophilic silicon nitride tips disclosed similar adhesive properties for each strain. However, the use of hydrophobic tips showed that hydrophobic forces are not the driving forces for adhesion

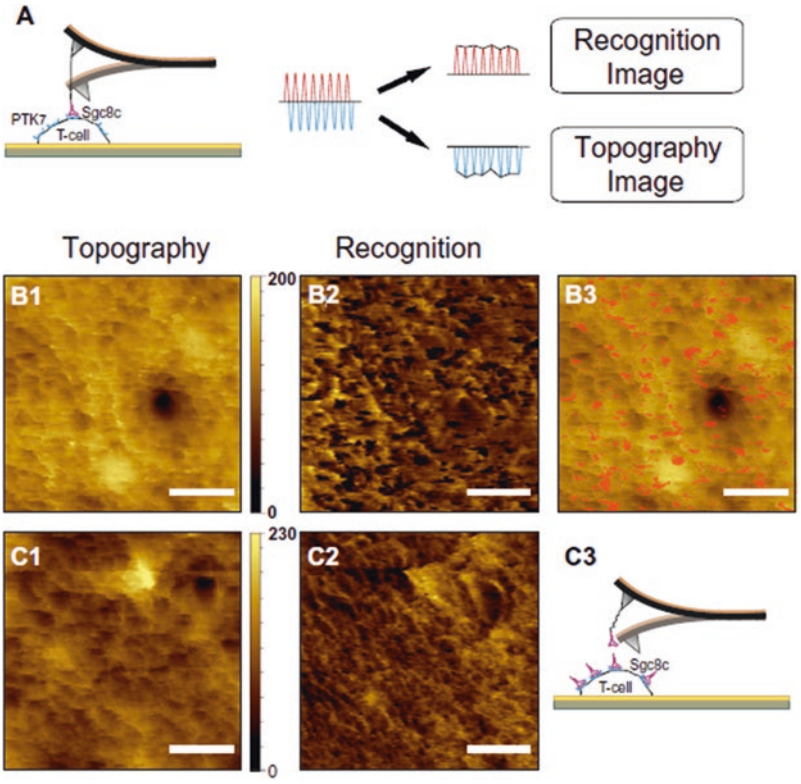

Fig. 4.10 (**A**) Schematic representation of the TREC setup. Simultaneously acquired topography (**B1**) and recognition (**B2**) images on a T-cell membrane using sgc8c functionalized tips. A superimposition of topography and recognition is also shown (**B3**). After addition of free aptamers, the topography image (**C1**) remains unchanged, whereas the recognition spots (**C2**) are completely abolished, as a result of blocked PTK7 receptors, as illustrated in (**C3**). Scale bars: 500 nm. Reprinted with permission from [87]

of the four strains. Treatment of two biofilm positive strains with two chemical inhibitor compounds leads to a loss of adhesion, suggesting that AFM could be a valuable tool to screen for anti-adhesion molecules.

Studying the binding affinity of peptides binding to various materials is also possible with quantitative force mapping methods [90].

TREC can be combined with other techniques. One example of this was presented by Zhu *et al*., which used native-protein nanolithography (NPNL) and TREC to synergistically use AFM tips to write and image nanoscale protein patterns on a surface [91]. The approach was validated using surface-bound biotinylated bovine serum albumin (BSA) and AFM tips carrying streptavidin tethered via a flexible PEG linker. Another example is the combination of AFM with scanning electrochemical microscopy (SECM) in peak force tapping (PFT) mode, thereby offering spatially correlated electrochemical and nanomechanical information

paired with high-resolution topographical data under force control [92]. The development of this approach may also be used to study complex biological samples, such as bacterial cells. Hinterdorfer et al. have shown that AFM combined with near-field scanning optical microscopy (NSOM) provide a broad range of possibilities for mapping the distribution of single molecules on the surfaces of cells with nanometer spatial resolution, thereby shedding new light on their highly sophisticated functions, namely on the study of the adhesion of *C. albicans* to proteins (Fig. 4.11) [93, 94].

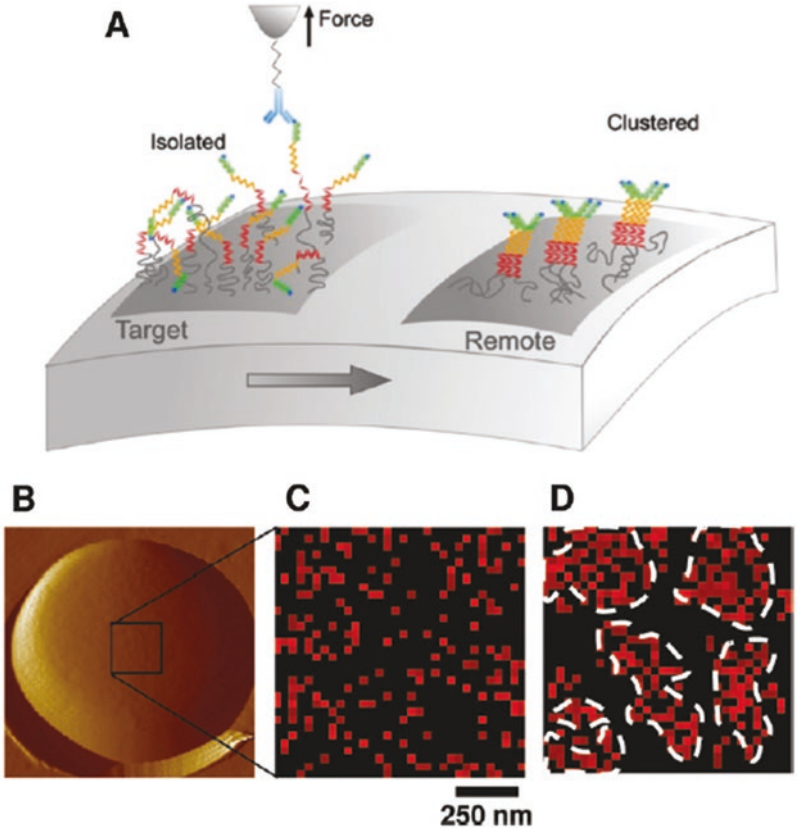

Fig. 4.11 Single-molecule AFM imaging unravels the dynamic clustering of cell adhesion proteins on yeast cells. (**A**) Single Als proteins from *C. albicans* were localized and stretched using an AFM tip bearing specific antibodies. (**B**) AFM topographic image of a single live cell. (**C**) Adhesion force map recorded on a cell that was never subjected to force. Red pixels document the detection of single proteins. Most proteins were isolated and evenly distributed, without any clear evidence for clustering. (**D**) Subsequent mapping recorded on the same cell after mechanical stimulation. Unlike native cells, cells that had been preactivated by force displayed adhesion nanodomains referred to as "nanoadhesomes" (**A**). Reprinted with permission from [93, 94]

3 Conclusions

The molecular recognition of the specific interactions between two molecules, proteins, membranes, or the entire surface of cells is essential to understand both structure and function(s). The recent advances on single-molecule imaging approaches, as for atomic force microscopy, allowed researchers to take advantages of these methods, with high improvements in spatial/temporal resolution, cell imaging speed, ease of use, higher throughput analysis and maintenance of *in vivo* cell physiological conditions.

Here, two different methods that combine AFM imaging and force spectroscopy were explained in detail: adhesion force mapping and TREC imaging. Both methods have expanded AFM beyond basic imaging studies, giving researchers the possibility to record and correlate data from structure, adhesion and elasticity maps, as well as to quantify molecular recognition events on different biological samples. Several applications of both methods led to numerous discoveries in cell biology, immunology, pharmacology and medical field. Some of the most recent studies are compiled on this review. We believe that the evolution and extension of the use of both methods will lead to important scientific discoveries and future developments in Biology and Medicine.

Acknowledgements This work was funded by Fundação para a Ciência e a Tecnologia – Ministério da Ciência, Tecnologia e Ensino Superior (FCT-MCTES, Portugal) projects PTDC/BBB-BMD/6307/2014 and PTDC/BBB-BQB/3494/2014.

Conflict of Interest Disclosures The authors declare no competing financial interests.

References

1. Ashkin A, Dziedzic JM, Yamane T. Optical trapping and manipulation of single cells using infrared laser beams. Nature. 1987;330(6150):769–71. https://doi.org/10.1038/330769a0.
2. Kuo SC, Sheetz MP. Force of single kinesin molecules measured with optical tweezers. Science. 1993;260(5105):232–4.
3. Svoboda K, Schmidt CF, Schnapp BJ, Block SM. Direct observation of kinesin stepping by optical trapping interferometry. Nature. 1993;365(6448):721–7. https://doi.org/10.1038/365721a0.
4. Evans E, Berk D, Leung A. Detachment of agglutinin-bonded red blood cells I forces to rupture molecular-point attachments. Biophys J. 1991;59(4):838–48. https://doi.org/10.1016/S0006-3495(91)82296-2.
5. Israelachvili JN. Force-measuring techniques. In: Intermolecular and surface forces. 3rd ed. San Diego: Academic; 2011. p. 223–52. https://doi.org/10.1016/B978-0-12-375182-9.10012-0.
6. Dammer U, Hegner M, Anselmetti D, Wagner P, Dreier M, Huber W, Guntherodt HJ. Specific antigen/antibody interactions measured by force microscopy. Biophys J. 1996;70(5):2437–41. https://doi.org/10.1016/S0006-3495(96)79814-4.
7. Florin EL, Moy VT, Gaub HE. Adhesion forces between individual ligand-receptor pairs. Science. 1994;264(5157):415–7.

8. Hinterdorfer P, Baumgartner W, Gruber HJ, Schilcher K, Schindler H. Detection and localization of individual antibody-antigen recognition events by atomic force microscopy. Proc Natl Acad Sci U S A. 1996;93(8):3477–81.
9. Lee GU, Kidwell DA, Colton RJ. Sensing discrete streptavidin-biotin interactions with atomic force microscopy. Langmuir. 1994;10(2):354–7. https://doi.org/10.1021/la00014a003.
10. Moy VT, Florin EL, Gaub HE. Intermolecular forces and energies between ligands and receptors. Science. 1994;266(5183):257–9.
11. Ishijima A, Doi T, Sakurada K, Yanagida T. Sub-piconewton force fluctuations of actomyosin in vitro. Nature. 1991;352(6333):301–6. https://doi.org/10.1038/352301a0.
12. Sotres J, Lostao A, Wildling L, Ebner A, Gomez-Moreno C, Gruber HJ, Hinterdorfer P, Baro AM. Unbinding molecular recognition force maps of localized single receptor molecules by atomic force microscopy. ChemPhysChem. 2008;9(4):590–9. https://doi.org/10.1002/cphc.200700597.
13. Grandbois M, Dettmann W, Benoit M, Gaub HE. Affinity imaging of red blood cells using an atomic force microscope. J Histochem Cytochem. 2000;48(5):719–24. https://doi.org/10.1177/002215540004800516.
14. Heinz WF, Hoh JH. Spatially resolved force spectroscopy of biological surfaces using the atomic force microscope. Trends Biotechnol. 1999;17(4):143–50.
15. Hinterdorfer P, Dufrene YF. Detection and localization of single molecular recognition events using atomic force microscopy. Nat Methods. 2006;3(5):347–55. https://doi.org/10.1038/nmeth871.
16. Willet N, Lamprecht C, Rankl C, Rangl M, Creasey R, Ebner R, Voelcker N, Hinterdorfer P. Molecular Recognition Force Spectroscopy. In: Molecular manipulation with atomic force microscopy: CRC Press; 2011. p. 3–46. https://doi.org/10.1201/b11269-3.
17. Almqvist N, Bhatia R, Primbs G, Desai N, Banerjee S, Lal R. Elasticity and adhesion force mapping reveals real-time clustering of growth factor receptors and associated changes in local cellular rheological properties. Biophys J. 2004;86(3):1753–62. https://doi.org/10.1016/S0006-3495(04)74243-5.
18. Alsteens D, Trabelsi H, Soumillion P, Dufrene YF. Multiparametric atomic force microscopy imaging of single bacteriophages extruding from living bacteria. Nat Commun. 2013;4:2926. https://doi.org/10.1038/ncomms3926.
19. Dupres V, Menozzi FD, Locht C, Clare BH, Abbott NL, Cuenot S, Bompard C, Raze D, Dufrene YF. Nanoscale mapping and functional analysis of individual adhesins on living bacteria. Nat Methods. 2005;2(7):515–20. https://doi.org/10.1038/nmeth769.
20. Gad M, Itoh A, Ikai A. Mapping cell wall polysaccharides of living microbial cells using atomic force microscopy. Cell Biol Int. 1997;21(11):697–706. https://doi.org/10.1006/cbir.1997.0214.
21. Ando T, Kodera N, Takai E, Maruyama D, Saito K, Toda A. A high-speed atomic force microscope for studying biological macromolecules. Proc Natl Acad Sci U S A. 2001;98(22):12468–72. https://doi.org/10.1073/pnas.211400898.
22. Takenaka M, Miyachi Y, Ishii J, Ogino C, Kondo A. The mapping of yeast's G-protein coupled receptor with an atomic force microscope. Nanoscale. 2015;7(11):4956–63. https://doi.org/10.1039/c4nr05940a.
23. Sahin O, Erina N. High-resolution and large dynamic range nanomechanical mapping in tapping-mode atomic force microscopy. Nanotechnology. 2008;19(44):445717. https://doi.org/10.1088/0957-4484/19/44/445717.
24. Raman A, Trigueros S, Cartagena A, Stevenson AP, Susilo M, Nauman E, Contera SA. Mapping nanomechanical properties of live cells using multi-harmonic atomic force microscopy. Nat Nanotechnol. 2011;6(12):809–14. https://doi.org/10.1038/nnano.2011.186.
25. Cartagena-Rivera AX, Wang WH, Geahlen RL, Raman A. Fast, multi-frequency, and quantitative nanomechanical mapping of live cells using the atomic force microscope. Sci Rep. 2015;5:11692. https://doi.org/10.1038/srep11692.

26. Chirasatitsin S, Engler AJ. Detecting cell-adhesive sites in extracellular matrix using force spectroscopy mapping. J Phys Condens Matter. 2010;22(19):194102. https://doi.org/10.1088/0953-8984/22/19/194102.
27. Whitehead B, Wu L, Hvam ML, Aslan H, Dong M, Dyrskjot L, Ostenfeld MS, Moghimi SM, Howard KA. Tumour exosomes display differential mechanical and complement activation properties dependent on malignant state: implications in endothelial leakiness. J Extracellular Vesicles. 2015;4:29685. https://doi.org/10.3402/jev.v4.29685.
28. Zhang S, Aslan H, Besenbacher F, Dong M. Quantitative biomolecular imaging by dynamic nanomechanical mapping. Chem Soc Rev. 2014;43(21):7412–29. https://doi.org/10.1039/c4cs00176a.
29. Pletikapic G, Berquand A, Radic TM, Svetlicic V. Quantitative Nanomechanical mapping of marine diatom in seawater using peak force tapping atomic force microscopy(1). J Phycol. 2012;48(1):174–85. https://doi.org/10.1111/j.1529-8817.2011.01093.x.
30. Picas L, Rico F, Scheuring S. Direct measurement of the mechanical properties of lipid phases in supported bilayers. Biophys J. 2012;102(1):L01–3. https://doi.org/10.1016/j.bpj.2011.11.4001.
31. Medalsy I, Hensen U, Muller DJ. Imaging and quantifying chemical and physical properties of native proteins at molecular resolution by force-volume AFM. Angew Chem. 2011;50(50):12103–8. https://doi.org/10.1002/anie.201103991.
32. Pfreundschuh M, Hensen U, Muller DJ. Quantitative imaging of the electrostatic field and potential generated by a transmembrane protein pore at subnanometer resolution. Nano Lett. 2013;13(11):5585–93. https://doi.org/10.1021/nl403232z.
33. Rico F, Su C, Scheuring S. Mechanical mapping of single membrane proteins at submolecular resolution. Nano Lett. 2011;11(9):3983–6. https://doi.org/10.1021/nl202351t.
34. Chopinet L, Formosa C, Rols MP, Duval RE, Dague E. Imaging living cells surface and quantifying its properties at high resolution using AFM in QI mode. Micron. 2013;48:26–33. https://doi.org/10.1016/j.micron.2013.02.003.
35. Carrasco C, Carreira A, Schaap IA, Serena PA, Gomez-Herrero J, Mateu MG, de Pablo PJ. DNA-mediated anisotropic mechanical reinforcement of a virus. Proc Natl Acad Sci U S A. 2006;103(37):13706–11. https://doi.org/10.1073/pnas.0601881103.
36. Gunning AP, Chambers S, Pin C, Man AL, Morris VJ, Nicoletti C. Mapping specific adhesive interactions on living human intestinal epithelial cells with atomic force microscopy. FASEB J. 2008;22(7):2331–9. https://doi.org/10.1096/fj.07-100578.
37. Heu C, Berquand A, Elie-Caille C, Nicod L. Glyphosate-induced stiffening of HaCaT keratinocytes, a peak force tapping study on living cells. J Struct Biol. 2012;178(1):1–7. https://doi.org/10.1016/j.jsb.2012.02.007.
38. Li M, Liu L, Xi N, Wang Y, Xiao X, Zhang W. Imaging and measuring the biophysical properties of Fc gamma receptors on single macrophages using atomic force microscopy. Biochem Biophys Res Commun. 2013;438(4):709–14. https://doi.org/10.1016/j.bbrc.2013.07.114.
39. Li M, Xiao X, Liu L, Xi N, Wang Y, Dong Z, Zhang W. Nanoscale mapping and organization analysis of target proteins on cancer cells from B-cell lymphoma patients. Exp Cell Res. 2013;319(18):2812–21. https://doi.org/10.1016/j.yexcr.2013.07.020.
40. Saab MB, Bec N, Martin M, Estephan E, Cuisinier F, Larroque C, Gergely C. Differential effect of curcumin on the nanomechanics of normal and cancerous Mammalian epithelial cells. Cell Biochem Biophys. 2013;65(3):399–411. https://doi.org/10.1007/s12013-012-9443-1.
41. Wegmann S, Medalsy ID, Mandelkow E, Muller DJ. The fuzzy coat of pathological human Tau fibrils is a two-layered polyelectrolyte brush. Proc Natl Acad Sci U S A. 2013;110(4):E313–21. https://doi.org/10.1073/pnas.1212100110.
42. Willemsen OH, Snel MM, van der Werf KO, de Grooth BG, Greve J, Hinterdorfer P, Gruber HJ, Schindler H, van Kooyk Y, Figdor CG. Simultaneous height and adhesion imaging of antibody-antigen interactions by atomic force microscopy. Biophys J. 1998;75(5):2220–8. https://doi.org/10.1016/S0006-3495(98)77666-0.

43. Canale C, Jacono M, Diaspro A, Dante S. Force spectroscopy as a tool to investigate the properties of supported lipid membranes. Microsc Res Tech. 2010;73(10):965–72. https://doi.org/10.1002/jemt.20834.
44. Cinar G, Ceylan H, Urel M, Erkal TS, Deniz Tekin E, Tekinay AB, Dana A, Guler MO. Amyloid inspired self-assembled peptide nanofibers. Biomacromolecules. 2012;13(10):3377–87. https://doi.org/10.1021/bm301141h.
45. Vasilev C, Brindley AA, Olsen JD, Saer RG, Beatty JT, Hunter CN. Nano-mechanical mapping of the interactions between surface-bound RC-LH1-PufX core complexes and cytochrome c 2 attached to an AFM probe. Photosynth Res. 2014;120(1–2):169–80. https://doi.org/10.1007/s11120-013-9812-7.
46. Kim IH, Lee MN, Ryu SH, Park JW. Nanoscale mapping and affinity constant measurement of signal-transducing proteins by atomic force microscopy. Anal Chem. 2011;83(5):1500–3. https://doi.org/10.1021/ac102695e.
47. Wang C, Yadavalli VK. Spatial recognition and mapping of proteins using DNA aptamers. Nanotechnology. 2014;25(45):455101. https://doi.org/10.1088/0957-4484/25/45/455101.
48. Dorakumbura BN, Becker T, Lewis SW. Nanomechanical mapping of latent fingermarks: a preliminary investigation into the changes in surface interactions and topography over time. Forensic Sci Int. 2016;267:16–24. https://doi.org/10.1016/j.forsciint.2016.07.024.
49. Rigato A, Rico F, Eghiaian F, Piel M, Scheuring S. Atomic force microscopy mechanical mapping of micropatterned cells shows adhesion geometry-dependent mechanical response on local and global scales. ACS Nano. 2015;9(6):5846–56. https://doi.org/10.1021/acsnano.5b00430.
50. Francius G, Alsteens D, Dupres V, Lebeer S, De Keersmaecker S, Vanderleyden J, Gruber HJ, Dufrene YF. Stretching polysaccharides on live cells using single molecule force spectroscopy. Nat Protoc. 2009;4(6):939–46. https://doi.org/10.1038/nprot.2009.65.
51. Dupres V, Alsteens D, Andre G, Dufrene YF. Microbial nanoscopy: a closer look at microbial cell surfaces. Trends Microbiol. 2010;18(9):397–405. https://doi.org/10.1016/j.tim.2010.06.004.
52. Dague E, Alsteens D, Latge JP, Verbelen C, Raze D, Baulard AR, Dufrene YF. Chemical force microscopy of single live cells. Nano Lett. 2007;7(10):3026–30. https://doi.org/10.1021/nl071476k.
53. Marliere C, Dhahri S. An in vivo study of electrical charge distribution on the bacterial cell wall by atomic force microscopy in vibrating force mode. Nanoscale. 2015;7(19):8843–57. https://doi.org/10.1039/c5nr00968e.
54. El-Kirat-Chatel S, Beaussart A, Derclaye S, Alsteens D, Kucharikova S, Van Dijck P, Dufrene YF. Force nanoscopy of hydrophobic interactions in the fungal pathogen Candida glabrata. ACS Nano. 2015;9(2):1648–55. https://doi.org/10.1021/nn506370f.
55. Formosa C, Schiavone M, Boisrame A, Richard ML, Duval RE, Dague E. Multiparametric imaging of adhesive nanodomains at the surface of Candida albicans by atomic force microscopy. Nanomedicine (NBM). 2015;11(1):57–65. https://doi.org/10.1016/j.nano.2014.07.008.
56. Cartagena A, Hernando-Perez M, Carrascosa JL, de Pablo PJ, Raman A. Mapping in vitro local material properties of intact and disrupted virions at high resolution using multi-harmonic atomic force microscopy. Nanoscale. 2013;5(11):4729–36. https://doi.org/10.1039/c3nr34088k.
57. Osada T, Itoh A, Ikai A. Mapping of the Receptor-Associated Protein (RAP) binding proteins on living fibroblast cells using an atomic force microscope. Ultramicroscopy. 2003;97(1–4):353–7. https://doi.org/10.1016/S0304-3991(03)00060-3.
58. Osada T, Takezawa S, Itoh A, Arakawa H, Ichikawa M, Ikai A. The distribution of sugar chains on the vomeronasal epithelium observed with an atomic force microscope. Chem Senses. 1999;24(1):1–6.
59. Kuznetsova TG, Starodubtseva MN, Yegorenkov NI, Chizhik SA, Zhdanov RI. Atomic force microscopy probing of cell elasticity. Micron. 2007;38(8):824–33. https://doi.org/10.1016/j.micron.2007.06.011.

60. Efremov YM, Dzyubenko EV, Bagrov DV, Maksimov GV, Shram SI, Shaitan KV. Atomic force microscopy study of the arrangement and mechanical properties of astrocytic cytoskeleton in growth medium. Acta Nat. 2011;3(3):93–9.
61. Cassina V, Torsello A, Tempestini A, Salerno D, Brogioli D, Tamiazzo L, Bresciani E, Martinez J, Fehrentz JA, Verdie P, Omeljaniuk RJ, Possenti R, Rizzi L, Locatelli V, Mantegazza F. Biophysical characterization of a binding site for TLQP-21, a naturally occurring peptide which induces resistance to obesity. Biochim Biophys Acta. 2013;1828(2):455–60. https://doi.org/10.1016/j.bbamem.2012.10.023.
62. Kawas LH, Benoist CC, Harding JW, Wayman GA, Abu-Lail NI. Nanoscale mapping of the met receptor on hippocampal neurons by AFM and confocal microscopy. Nanomedicine (NBM). 2013;9(3):428–38. https://doi.org/10.1016/j.nano.2012.08.008.
63. Wang B, Guo P, Auguste DT. Mapping the CXCR4 receptor on breast cancer cells. Biomaterials. 2015;57:161–8. https://doi.org/10.1016/j.biomaterials.2015.04.023.
64. Ebner A, Kienberger F, Kada G, Stroh CM, Geretschlager M, Kamruzzahan AS, Wildling L, Johnson WT, Ashcroft B, Nelson J, Lindsay SM, Gruber HJ, Hinterdorfer P. Localization of single avidin-biotin interactions using simultaneous topography and molecular recognition imaging. ChemPhysChem. 2005;6(5):897–900. https://doi.org/10.1002/cphc.200400545.
65. Stroh C, Wang H, Bash R, Ashcroft B, Nelson J, Gruber H, Lohr D, Lindsay SM, Hinterdorfer P. Single-molecule recognition imaging microscopy. Proc Natl Acad Sci U S A. 2004;101(34):12503–7. https://doi.org/10.1073/pnas.0403538101.
66. Stroh CM, Ebner A, Geretschlager M, Freudenthaler G, Kienberger F, Kamruzzahan AS, Smith-Gill SJ, Gruber HJ, Hinterdorfer P. Simultaneous topography and recognition imaging using force microscopy. Biophys J. 2004;87(3):1981–90. https://doi.org/10.1529/biophysj.104.043331.
67. Raab A, Han W, Badt D, Smith-Gill SJ, Lindsay SM, Schindler H, Hinterdorfer P. Antibody recognition imaging by force microscopy. Nat Biotechnol. 1999;17(9):901–5. https://doi.org/10.1038/12898.
68. Ebner A, Wildling L, Kamruzzahan AS, Rankl C, Wruss J, Hahn CD, Holzl M, Zhu R, Kienberger F, Blaas D, Hinterdorfer P, Gruber HJ. A new, simple method for linking of antibodies to atomic force microscopy tips. Bioconjug Chem. 2007;18(4):1176–84. https://doi.org/10.1021/bc070030s.
69. Ebner A, Wildling L, Zhu R, Rankl C, Haselgrubler T, Hinterdorfer P, Gruber HJ. Functionalization of probe tips and supports for single-molecule recognition force microscopy. Top Curr Chem. 2008;285:29–76. https://doi.org/10.1007/128_2007_24.
70. Kamruzzahan AS, Ebner A, Wildling L, Kienberger F, Riener CK, Hahn CD, Pollheimer PD, Winklehner P, Holzl M, Lackner B, Schorkl DM, Hinterdorfer P, Gruber HJ. Antibody linking to atomic force microscope tips via disulfide bond formation. Bioconjug Chem. 2006;17(6):1473–81. https://doi.org/10.1021/bc060252a.
71. Preiner J, Ebner A, Chtcheglova L, Zhu R, Hinterdorfer P. Simultaneous topography and recognition imaging: physical aspects and optimal imaging conditions. Nanotechnology. 2009;20(21):215103. https://doi.org/10.1088/0957-4484/20/21/215103.
72. Preiner J, Losilla NS, Ebner A, Annibale P, Biscarini F, Garcia R, Hinterdorfer P. Imaging and detection of single molecule recognition events on organic semiconductor surfaces. Nano Lett. 2009;9(2):571–5. https://doi.org/10.1021/nl802721g.
73. Ron A, Singh RR, Fishelson N, Socher R, Benayahu D, Shacham-Diamand Y. Site localization of membrane-bound proteins on whole cell level using atomic force microscopy. Biophys Chem. 2008;132(2–3):127–38. https://doi.org/10.1016/j.bpc.2007.10.016.
74. Zhao W, Liu S, Cai M, Xu H, Jiang J, Wang H. Detection of carbohydrates on the surface of cancer and normal cells by topography and recognition imaging. Chem Commun. 2013;49(29):2980–2. https://doi.org/10.1039/c3cc38885a.
75. Tang J, Ebner A, Badelt-Lichtblau H, Vollenkle C, Rankl C, Kraxberger B, Leitner M, Wildling L, Gruber HJ, Sleytr UB, Ilk N, Hinterdorfer P. Recognition imaging and highly ordered molecular templating of bacterial S-layer nanoarrays containing affinity-tags. Nano Lett. 2008;8(12):4312–9. https://doi.org/10.1021/nl802092c.

76. Ebner A, Nikova D, Lange T, Haberle J, Falk S, Dubbers A, Bruns R, Hinterdorfer P, Oberleithner H, Schillers H. Determination of CFTR densities in erythrocyte plasma membranes using recognition imaging. Nanotechnology. 2008;19(38):384017. https://doi.org/10.1088/0957-4484/19/38/384017.
77. Chtcheglova LA, Atalar F, Ozbek U, Wildling L, Ebner A, Hinterdorfer P. Localization of the ergtoxin-1 receptors on the voltage sensing domain of hERG K channel by AFM recognition imaging. Pflugers Arch: Eur J Physiol. 2008;456(1):247–54. https://doi.org/10.1007/s00424-007-0418-9.
78. Chtcheglova LA, Waschke J, Wildling L, Drenckhahn D, Hinterdorfer P. Nano-scale dynamic recognition imaging on vascular endothelial cells. Biophys J. 2007;93(2):L11–3. https://doi.org/10.1529/biophysj.107.109751.
79. Radmacher M, Cleveland JP, Fritz M, Hansma HG, Hansma PK. Mapping interaction forces with the atomic force microscope. Biophys J. 1994;66(6):2159–65. https://doi.org/10.1016/S0006-3495(94)81011-2.
80. Ludwig M, Dettmann W, Gaub HE. Atomic force microscope imaging contrast based on molecular recognition. Biophys J. 1997;72(1):445–8. https://doi.org/10.1016/S0006-3495(97)78685-5.
81. Agnihotri A, Siedlecki CA. Adhesion mode atomic force microscopy study of dual component protein films. Ultramicroscopy. 2005;102(4):257–68. https://doi.org/10.1016/j.ultramic.2004.10.006.
82. Wang H, Bash R, Lohr D. Two-component atomic force microscopy recognition imaging of complex samples. Anal Biochem. 2007;361(2):273–9. https://doi.org/10.1016/j.ab.2006.11.039.
83. van Es MH, Tang J, Preiner J, Hinterdorfer P, Oosterkamp TH. Single molecule binding dynamics measured with atomic force microscopy. Ultramicroscopy. 2014;140:32–6. https://doi.org/10.1016/j.ultramic.2014.02.005.
84. Hecht FM, Rheinlaender J, Schierbaum N, Goldmann WH, Fabry B, Schaffer TE. Imaging viscoelastic properties of live cells by AFM: power-law rheology on the nanoscale. Soft Matter. 2015;11(23):4584–91. https://doi.org/10.1039/c4sm02718c.
85. Kumar U, Vivekanand K, Poddar P. Real-time nanomechanical and topographical mapping on live bacterial cells-Brevibacterium casei under stress due to their exposure to Co_2 ions during microbial synthesis of Co_3O_4 nanoparticles. J Phys Chem B. 2009;113(22):7927–33. https://doi.org/10.1021/jp902698n.
86. Chtcheglova LA, Hinterdorfer P. Atomic force microscopy functional imaging on vascular endothelial cells. Methods Mol Biol. 2013;931:331–44. https://doi.org/10.1007/978-1-62703-056-4_16.
87. Leitner M, Poturnayova A, Lamprecht C, Weich S, Snejdarkova M, Karpisova I, Hianik T, Ebner A. Characterization of the specific interaction between the DNA aptamer sgc8c and protein tyrosine kinase-7 receptors at the surface of T-cells by biosensing AFM. Anal Bioanal Chem. 2017;409(11):2767–76. https://doi.org/10.1007/s00216-017-0238-5.
88. Takahashi H, Hizume K, Kumeta M, S HY, Takeyasu K (2009) Single-molecule anatomy by atomic force microscopy and recognition imaging. Arch Histol Cytol 72 (4–5):217–225.
89. Hu Y, Ulstrup J, Zhang J, Molin S, Dupres V. Adhesive properties of Staphylococcus epidermidis probed by atomic force microscopy. Phys Chem Chem Phys. 2011;13(21):9995–10003. https://doi.org/10.1039/c0cp02800b.
90. Mochizuki M, Oguchi M, Kim SO, Jackman JA, Ogawa T, Lkhamsuren G, Cho NJ, Hayashi T. Quantitative evaluation of peptide-material interactions by a force mapping method: guidelines for surface modification. Langmuir. 2015;31(29):8006–12. https://doi.org/10.1021/acs.langmuir.5b01691.
91. Zhu R, Ebner A, Kastner M, Preiner J, Howorka S, Hinterdorfer P. Topography and recognition imaging of protein-patterned surfaces generated by AFM nanolithography. ChemPhysChem. 2009;10(9–10):1478–81. https://doi.org/10.1002/cphc.200900245.

92. Knittel P, Mizaikoff B, Kranz C. Simultaneous Nanomechanical and electrochemical mapping: combining peak force tapping atomic force microscopy with scanning electrochemical microscopy. Anal Chem. 2016;88(12):6174–8. https://doi.org/10.1021/acs.analchem.6b01086.
93. Alsteens D, Garcia MC, Lipke PN, Dufrene YF. Force-induced formation and propagation of adhesion nanodomains in living fungal cells. Proc Natl Acad Sci U S A. 2010;107(48):20744–9. https://doi.org/10.1073/pnas.1013893107.
94. Hinterdorfer P, Garcia-Parajo MF, Dufrene YF. Single-molecule imaging of cell surfaces using near-field nanoscopy. Acc Chem Res. 2012;45(3):327–36. https://doi.org/10.1021/ar2001167.

Chapter 5
Atomic Force Microscopy: A Nanoscopic Application in Molecular and Cell Biology

Huai-Hong Cai, Xueyi Zeng, Xiao Tang, and Jiye Cai

Abstract At the prosperous fields of nanoscience and biology, the nanoscale analysis of cells and cell membrane using atomic force microscopy (AFM) is an exciting and rapidly developing research area. Over the past decade, there has been tremendous progress in the use of AFM to observe living cells and membrane proteins at high resolution. Remarkable advances have been made in applying AFM-based force spectroscopy techniques to characterize surface biomechanical properties, to map receptor sites on cell surface, and to measure cellular interactions at the single-cell or single-molecule level. Moreover, recent developments in AFM combining advanced optical microscopy, such as confocal microscopy and near-field scanning optical microscopy, opened up new avenues for cell imaging at nanoscale resolution.

1 Introduction

Cell is the fundamental unit of the living things. The human body is composed of trillions of cells, which plays an important role in converting the nutrients into energy and fabricating biostructure in the body. The cell membrane is a biological interface that separates the interior of cell from the outside environment. Cell membrane has several important biofunctions, including maintaining cell shape, regulating membrane protein functions, and mediating signal pathway [1]. Although biological properties of cells are well-investigated, little is known about their

These authors of Huai-Hong Cai and Jiye Cai contributed equally to this chapter and share the corresponding authorship.

H.-H. Cai (✉) · X. Zeng · X. Tang
College of Chemistry and Materials Science, Jinan University, Guangzhou, China
e-mail: thhcai@jnu.edu.cn

J. Cai (✉)
State Key Laboratory of Quality Research in Chinese Medicines, Macau University of Science and Technology, Macau, China

Department of Chemistry, Jinan University, Jinan, China
e-mail: tjycai@jnu.edu.cn

J. Cai (ed.), *Atomic Force Microscopy in Molecular and Cell Biology*,
https://doi.org/10.1007/978-981-13-1510-7_5

ultrastructure, spatial distribution and conformational changes at the single cell or single molecule level. This is largely due to the fact that traditional methods in cell biology mostly focus on large ensembles of cells or biomolecules, rather than on nanoscale level. In fact, individual cell has its unique physiological activity, which has an important impact on its biological behaviors [2].

The invention of atomic force microscopy (AFM) in 1986 [3], a milestone in the history of nanotechnology, has provided great opportunities for investigating single cell and single molecule at (sub-)nanometre resolution [3, 4]. The key breakthrough that led to biological AFM was the design of a fluid chamber, enabling cell imaging in physiological conditions, which is an exciting advantage over electron-microscopy techniques. In particular, real-time imaging of single cell provides novel insight into dynamic structural changes [5]. Like the morphological imaging, AFM in the single molecule force spectroscopy (SMFS) is an useful toolkit to investigate the intermolecule binding forces, map the localization of surface receptors, and quantitatively measure their interactions [6, 7].

2 Basic Principles of AFM

To characterize the complexity of biological systems, ranging from nucleic acids and membrane proteins to cells and tissues, a variety of AMF imaging modes have been created over the years (Fig. 5.1). Major advances in high-resolution imaging have been achieved by using complementary methods, including super-resolution microscopy and cryo-electron microscopy, which enriches the imaging toolboxes now available to single molecule level [8].

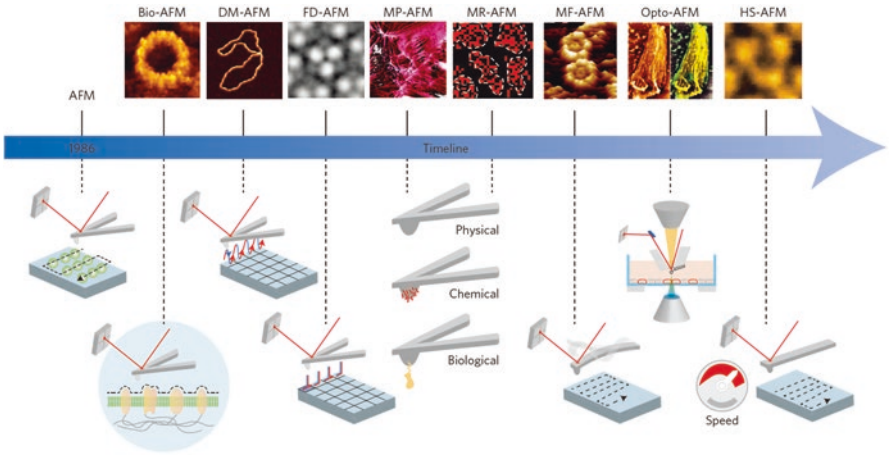

Fig. 5.1 Timeline of AFM imaging modes in molecular and cell biology, including AFM operates in aqueous solution (Bio-AFM), dynamic mode AFM (DM-AFM), forceic mode AFM (DM-AFM) odes in molecu, multiparametric AFM (MP-AFM), multifrequency AFM (MF-AFM), correlating advanced optical imaging and AFM (Opto-AFM), and high-speed AFM (HS-AFM). Reproduced with permission from refs [8]

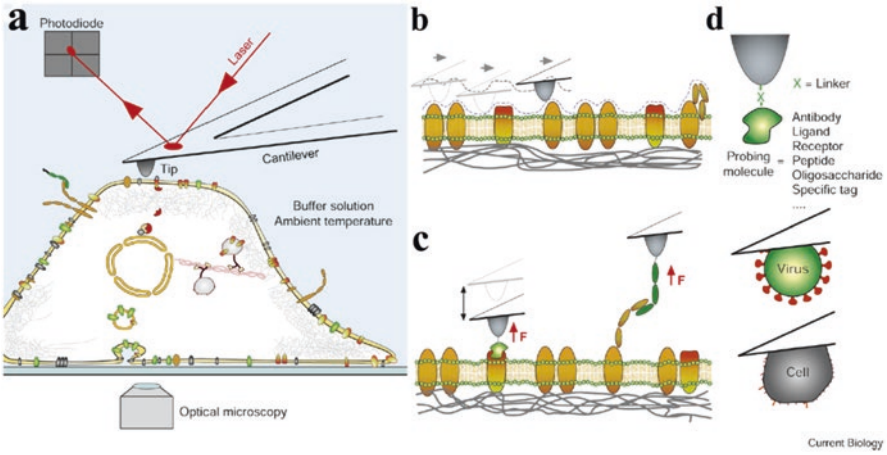

Fig. 5.2 AFM nanoscopy of living cells. (**a**) Cell morphological imaging works by probing the forces between a AFM tip and cell surface. (**b**) In the contact imaging mode, the AFM tip scans the cell surface and obtains its topography (dashed line). (**c**) In force spectroscopy, molecule-modified AFM tip is used to measure the binding forces. (**d**) Functionalize AFM tip or cantilever to conjugate specific molecule or cell. Reproduced with permission from refs [12]

In morphological imaging, AFM imaging modes differ mainly in the way that the tip moves over the cell sample, including contact and dynamic mode (Fig. 5.2a). Although contact mode is widely used to image solid substrates, the applications to soft biological systems require adjusting the force applied to the tip. For cell imaging, forces >100 pN can be deemed that they can cause irreversible sample deformations [9]. Dynamic mode imaging (originally termed tapping or oscillation mode) is therefore invented to minimize the force applied between tip and cell sample (Fig. 5.2b). In the dynamic mode, an oscillating tip is scanned over cell surface, and the amplitude and phase of the cantilever are monitored at or near its resonance frequency [10], providing the possibility in the obtainment of high-resolution cell imaging.

In force spectroscopy techniques, including single molecule force spectroscopy (SMFS), chemical force microscopy (CFM), molecule recognition mapping (MRM), single cell force spectroscopy (SCFS) and simultaneous topography and recognition imaging (TREC), the AFM tip is functionalized with chemical groups, biological molecules, or even a living cell [11]. The modified tip is approached towards and retracted from the biological sample, and the cantilever deflection measures its rupture force (Fig. 5.2c). Such approach and retraction cycles are recorded by the force-distance curves, providing information on specific receptor-ligand interactions, spatial distribution of individual receptors, and the forces that govern cell–cell interactions.

3 Submolecular Imaging of Cell Membranes

Cell membranes, consisting of lots of membrane proteins, are biointerface that fulfill various crucial functions in maintaining cell integrity and biofunctions.

AFM topographic imaging can visually characterize the nanoscale organization of membrane proteins in the physiological environment, which is a powerful complement technique to fluorescence spectroscopy [13, 14], X-ray and electron-crystallography techniques [15]. For high-resolution biological imaging, studies reported the observation of mammalian and bacterial cells [7, 16], viruses [17], nucleic acids [18, 19], or membrane protein [20–22] (Fig. 5.3).

AFM imaging can observe the isolated cell membrane adsorbed onto flat substrates with sub-nanometre resolution (Fig. 5.4). The best spatial resolution obtained by AFM on membrane is of 10 nm [23]. Prominent examples include the ion-driven rotors of FoF1-ATP synthases (Fig. 5.4a), and G-protein coupled receptors (GPCRs) (Fig. 5.4b), which covers key functions of the human body and potential targets of therapeutic drugs. High-resolution topographies of light-harvesting complexes [4] provide the evidence of the molecular rearrangements on the photosynthetic membrane (Fig. 5.4c). Similar resolution was achieved on tubulin protofilaments that

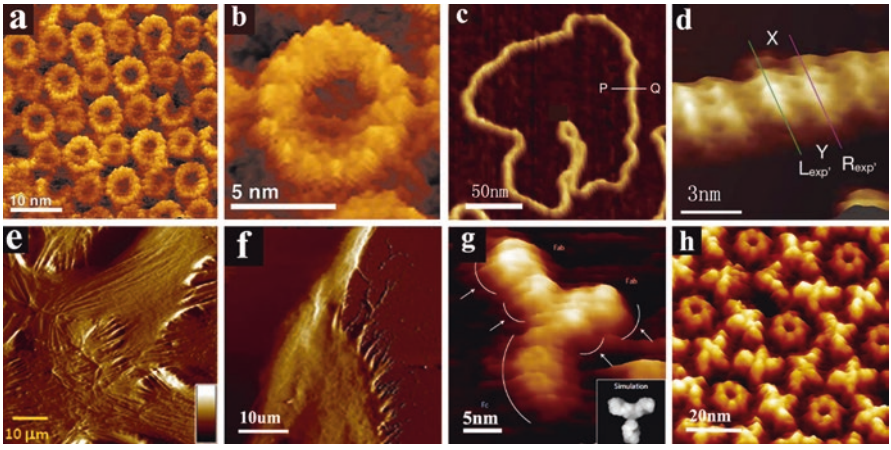

Fig. 5.3 AFM imaging applications charactering DNA, proteins and cell. (**a**) Subunit-III oligomers of chloroplast ATP synthase visualized in 25 mM $MgCl_2$, 10 mM Trisapplications charactering DNA, proteins and cell. (**a** [21]. (**b**) the distinct wide and narrow rings represent wide oligomer ends. Reproduced with permission from refs [21]. (**c**) The plasmid DNA in 50 mM $NiCl_2$ solution. P-Q line representing the vertical cross-section profile. Reproduced with permission from refs [18]. (**d**) The (sub-)nanometre resolution for the plasmid DNA. X and Y representing its cross-sectional profile. Reproduced with permission from refs [18]. (**e**) HaCaT cell morphological imaging. Reproduced with permission from refs [39]. (**f**) Cell morphological changes under the quercetin treatment. Reproduced with permission from refs [39]. (**g**) High-resolution FM-AFM image of an anti-HSA mouse monoclonal antibody (IgG) in 50 mM $ZnCl_2$. Reproduced with permission from refs [20]. (**h**) High-resolution FM-AFM image of self-assembled 2D IgG crystals in 50 mM $MgCl_2$. Reproduced with permission from refs [20]

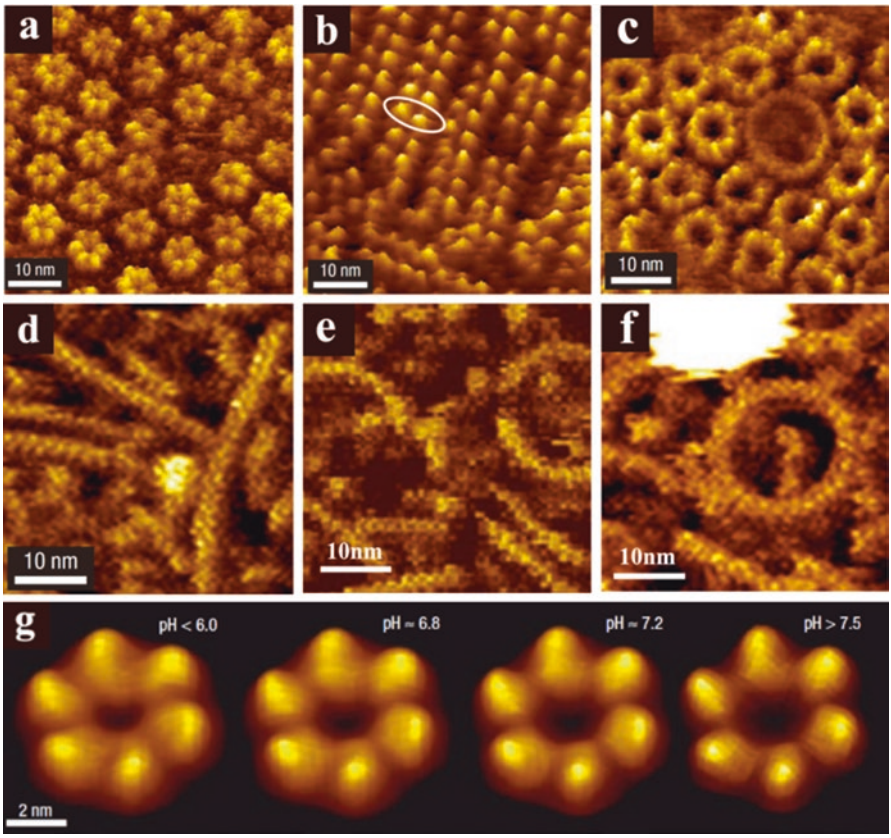

Fig. 5.4 Observing the individuality of cellular machines at high resolution. (**a**) Human communication channels known as gap junctions form hexameric pores. (**b**) Bovine rhodopsin, the visual pigment of the eye, assembles into rows of dimers (circled in white). (**c**) Assembly of light-harvesting II (small doughnuts) and light-harvesting I complexes (large doughnuts, surrounding the reaction centre) change with intensity of the incident light to optimize the collection of photons and their conversion into electric energy. (**d**) The anti-cancer drug taxol slows down the tubulin hydrolysis of straight protofilaments to form rings of 22 nm in diameter (far right panel). (**e**) In the presence of aminosulphonate compounds, human communication channels change from a closed (pH < 6.0) to an open state (pH > 7.5). Reproduced with permission from refs [23]

were assembled into microtubule [24], whose nanostructures were involved in cell migration and division. AFM allows researchers to visually observe the anti-cancer agent taxol inducing the polymerization of tubulin into microtubules, which inhibits the division of cancer cells (Fig. 5.4d). In another study [25], AFM revealed the reversible closure of communication channels in response to the ligand Ca^{2+}. It is validated that an aminosulphonate compound can induce the pH change and subsequently close this communication channel using a different gating mechanism (Fig. 5.4e) [26]. Whereas in the presence of Ca^{2+}, the gap junction hemichannels move their subunits towards closing the channel entrance, suggesting that the pH-induced closure can twist the subunits like a camera iris.

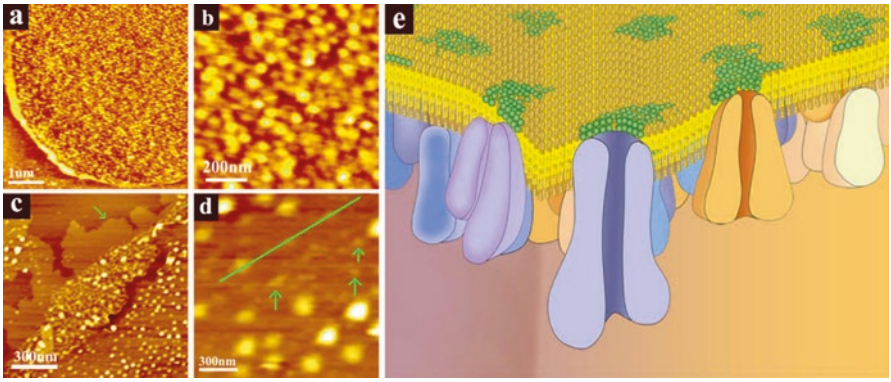

Fig. 5.5 High-resolution imaging of inner membrane for erythrocyte. (**a**) Image of the inner membrane. (**b**) Image of a dense protein layer on the inner membrane. (**c**) Inner membrane treated by trypsin. (**d**) Inner membrane ultrastructure. Arrows point to the possible peptides after trypsin digestion. (**e**) The proposed protein layer-lipid-protein island model of cell membranes. Membrane proteins are semi-mosaic in the lipid bilayer. Reproduced with permission from refs [40]

Observing cellular nanomachines on inner membrane provides a fascinating and direct way to investigate the connection of structures with their biofunctions. A representative progress for the investigation of cell functions is the use of AFM ultrastructural imaging for characterizing membrane structure of red blood cell [27], mammalian cell [28], and microbial cell [2]. Erythrocyte (red blood cell) is traditionally used as a cell model to investigate membrane proteins distribution. AFM revealed the presence of a dense protein layer on the inner membrane (Fig. 5.5a), suggesting that membrane proteins were aggregated as nanoclusters to realize Na^+-K^+ ATPases signal transduction (Fig. 5.5b). Most of the protein disappeared after trypsin digestion, thus exposing a smooth phospholipid bilayer (Fig. 5.5c, d). The protein layer-lipid-protein island model for the nucleated mammalian cell therefore was proposed (Fig. 5.5e). This provides direct evidence that the dense protein layer on the inner membrane can form a barrier to protect intracellular structure and maintain cell integrity [29].

Real-time visualization and quantitative measure of the ligand-receptor binding on cell surface is a challenging task in cell biology. Simultaneous topography and recognition imaging (TREC) is a molecular recognition mapping mode, in which molecular recognition signals are detected during dynamic force microscopy imaging, rather than using traditional force-distance curves (Fig. 5.6a). Dynamic recognition force mapping was used to localize cadherins distribution, which was organized into nanodomains ranging from 10 to 100 nm on microvascular endothelial cell surface [30]. TREC also makes the possibility of quantifying both the binding kinetics and the distribution of growth factor receptors on human microvascular endothelial cells [31]. The recognition spots reveal the locations of VE-cadherins in the topographical image with high lateral resolution (Fig. 5.6b). Therefore, the simultaneous information of both topography and recognition opens a wide field for investigating nanostructure-biofunction relationships at the nanometer level.

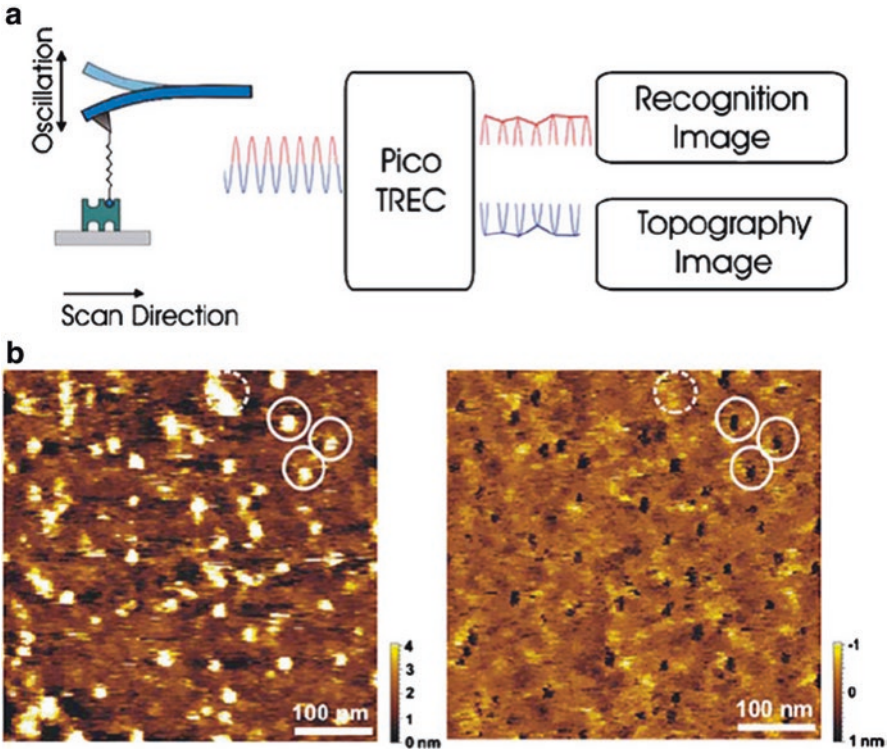

Fig. 5.6 Simultaneous topography and recognition mapping of membrane proteins. (**a**) Principle: the cantilever split into lower and upper parts, correspondingly topography and recognition images. (**b**) Avidin was electrostatically adsorbed to mica and imaged with a biotintethered tip. A good correlation between topography (left image, bright spots) and recognition (right image, dark spots) was found (solid circles). Topographical spots without recognition show the lacking specific interaction (dashed circle). Reproduced with permission from refs [6]

High-resolution AFM imaging has the good advantage for visually characterizing living microbial cells [32]. AFM has allowed observation of the supramolecular organization of major cell-wall constituents on live microbes, such as rodlets [33], surface-layer proteins [34], and peptidoglycan (Fig. 5.7a–c) [35, 36]. Molecular recognition mapping (MRM) was applied to *Lactococcus lactis* to localize single peptidoglycan molecules [37] (Fig. 5.7a–c). The correlation between morphological imaging and force recognition provided direct evidence that peptidoglycan localized in the form of parallel cables in *L. lactis* (Fig. 5.7c), supporting the classic model of peptidoglycan assembly. MRM was used to discover the relationships between the spatial localization and the functional roles of cell wall teichoic acids (WTAs) in *Lactobacillus plantarum* [38]. Results demonstrated that the polarized surface structure (Fig. 5.7d) correlates with a heterogeneous distribution of WTAs (Fig. 5.7e, f), and that this polarized cell-wall organization plays a key role in controlling cell morphogenesis.

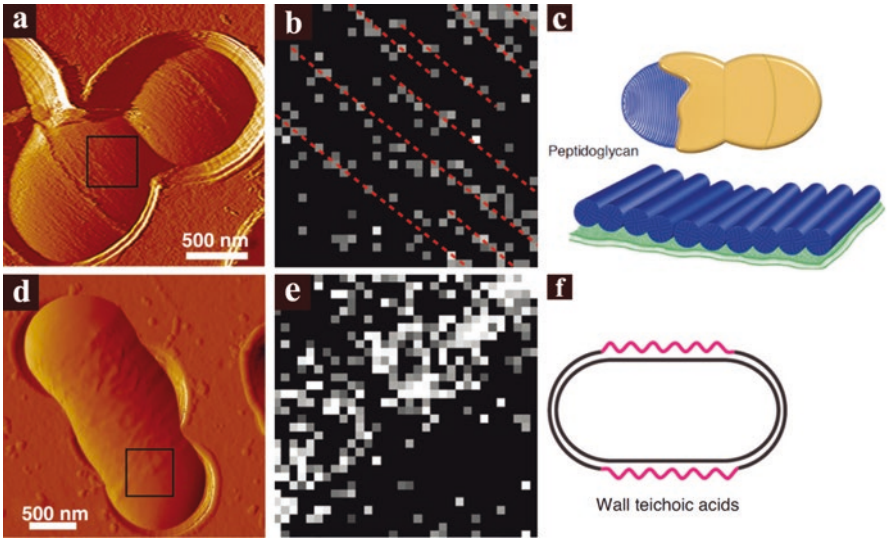

Fig. 5.7 The correlation between morphology and recognition images of living microbial cell. (**a**) Topographic image of two dividing *L. lactis* cells lacking cell-wall exopolysaccharides. (**b**) Single-molecule recognition map (400 × 400 nm) recorded with a LysM probe in the topographic image, peptidoglycan molecules were detected (bright pixels), and found to be arranged as lines running parallel to the short cell axis (red lines). (**c**) Schematic views of the architecture of the bacterial cell wall, the peptidoglycan (blue) is covered by cell-wall polysaccharides (brown), and the bottom drawing is an enlarged view of the peptidoglycan nanocables (blue) lying on the membrane (green). (**d**) Topographic image of a single *L. plantarum* cell revealing a highly smooth morphology than the side walls. (**e**) Single-molecule recognition map (400 × 400 nm) records with a lectin probe in the topographic image, WTAs is detected on the side walls (bright pixels) but is essentially lacking on the poles (dark pixels). (**f**) Schematic view of the architecture of the *L. plantarum* cell wall, WTAs localize exclusively to the side walls (red). Reproduced with permission from refs [41]

4 Nanoscale Functional Imaging of Cells

The important part of biological AFM is the development of a fluid chamber, enabling imaging in buffer solution [8, 16]. The resolution of topographic imaging depends on the AFM tip radius, the sample surface property, and how precisely the feedback system contours the tip over the soft biological sample. Up to date, AFM topographic imaging is a powerful complementary tool to fluorescence [13, 14] and electron microscopy, offering new opportunity for approaching (sub-)nanometer resolution in native biological systems [42].

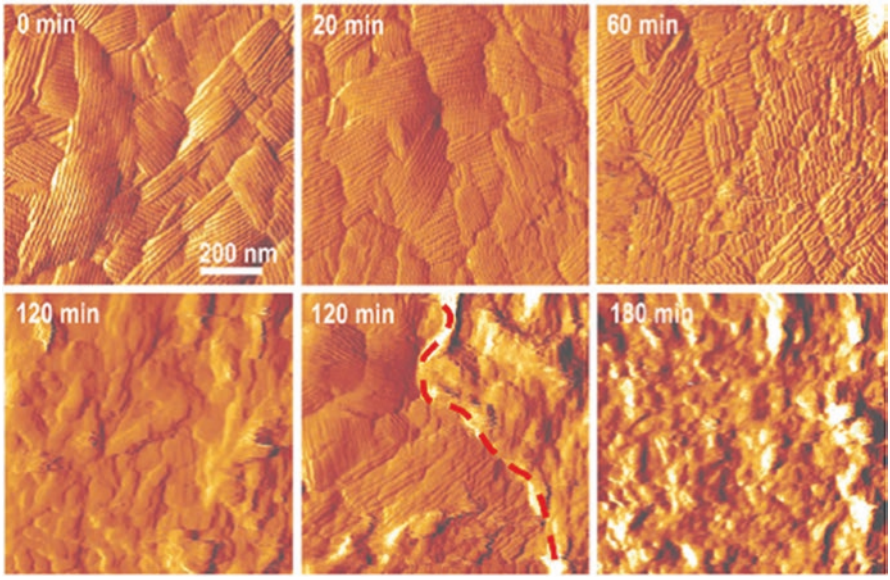

Fig. 5.8 Real-time AFM imaging and structural dynamics analysis of a living single microbial cell. Series of AFM deflection images were recorded on a single spore during germination, showing the topographical changes on the cell surface. Reproduced with permission from refs [45]

4.1 Real-Time Imaging of Living Cells

Living cells are dynamically, and continuously responding to environmental changes. AFM has the ability to track the nanostructural changes in response to environmental stimulants or therapeutic drugs [43–46]. In biomedicine, the real-time imaging of drug interaction opens up new possibilities for investigating pharmaceutical mechanism and screening new drug [43]. For example, drug-treated mycobacteria has the membrane ultrastructural alterations, inhibiting the synthesis of the cell-wall constituents, including mycolic acids, arabinans, and proteins [44]. For real-time imaging, high-resolution AFM images recorded on a single spore during germination (Fig. 5.8), clearly showing the crystalline rodlet layer of the bacteria surface was changed under the stimulus of a layer of amorphous material [45].

The migration of mesenchymal stem cells (MSCs) is closely related to the bioactivity of vascular endothelial growth factor (VEGF). There is little information about the distribution of CD44 and CD29 during VEGF-induced MSCs migration. Quantum dots (QDs)-labeled near-field optical microscopy (NSOM) combining with AFM is used to simultaneously capture the spatial rearrangements of both

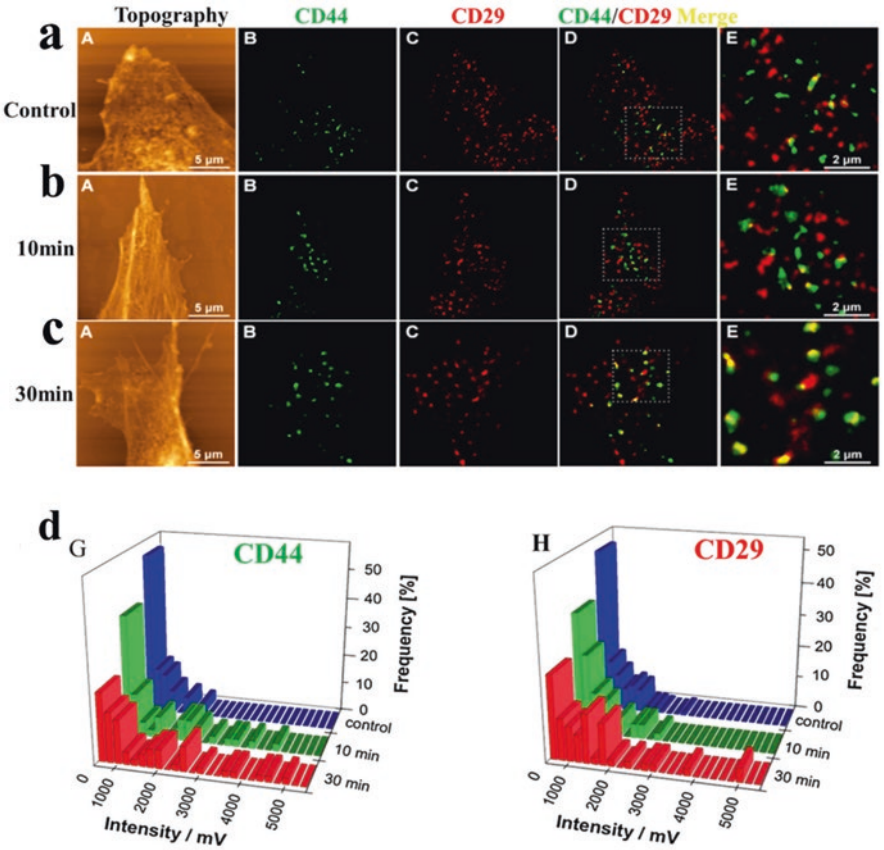

Fig. 5.9 *In situ* NSOM/QDs-based dual color fluorescence imaging in mesenchymal stem cells (MSCs) induced by VEGF for 30 mins. (**a**) Topographic images of MSCs. (**b**) and (**c**), NSOM fluorescence images of CD44 labeled using QD565 after stimulation by VEGF for 10 mins and 30 mins respectively. (**d**) Histograms of the frequency distribution of all the CD44 and CD29 fluorescent spots, blue: control group; green: 10 mins VEGF stimulation; and red: 30 mins VEGF stimulation. Reproduced with permission from refs [46]

Acknowledgment This chapter was modified from the paper published by our group in *Biochimica et Biophysica Acta* (Changhong Ke, Jianan Chen, Yajun Guo, Zheng W. Chen, Jiye Cai; 19 December 2014; 2015; 1848; 859–868). The related contents are re-used with permission

CD44 and CD29 on MSC surface [46]. Before VEGF-induced migration of MSCs, both CD44 and CD29 formed 200–220 nm nanodomains, little co-localization was probed on those two domains. After VEGF treatment, both CD44 and CD29 were aggregated into nanoclusters and higher co-localization was observed on membrane (Fig. 5.9). The AFM morphology and fluorescent co-localization of those molecules visually show cytoskeleton rearrangement under VEGF stimulation.

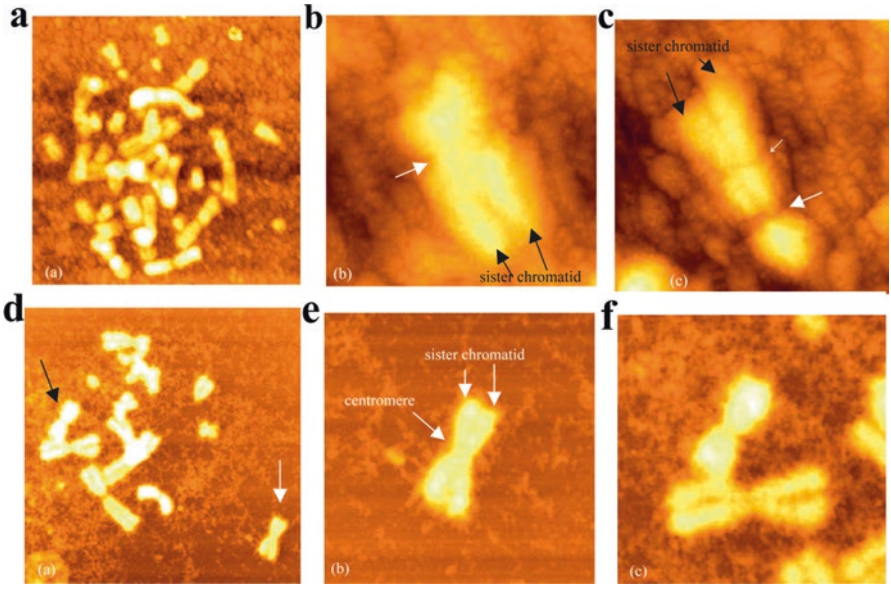

Fig. 5.10 AFM images of chromosomes. (**a**) The metaphase I chromosomes are barely distinguished from each other. (**b**) and (**c**): Enlarged images show the sister chromatids (black arrowheads), primary (large white arrowheads) and secondary (small white arrowhead) constrictions clearly. Scan range: (**a**) 35 μm; (**b**) 5 μm; (**c**) 7 μm. (**d**) The metaphase II chromosomes connect only at their centromeres and the arms divide from each other. (**e**) and (**f**): Enlarged images of the areas marked by the white (**e**) and black (**f**) arrows in (**d**). Scan range (**a**) 28 μm; (**b**, **c**) 10 μm. Reproduced with permission from refs [51]

Acknowledgment This chapter was modified from the paper published by our group in *Micron* (Yangzhe Wu, Jiye Cai, Longqiu Cheng, Yanfang Xu, Zhiyan Lin, Chenxi Wang, Yong Chen; 31 August 2005; 2006; 37; 139–145). The related contents are re-used with permission

4.2 Imaging of Organelles and Proteins

In cell biology, an organelle, including nucleus [47], chromosome [48] and chromatophore [49], is a specialized subunit within a cell that has a specific biofunction. By isolating cellular organelles from the cell, the nanostructural properties of those isolated organelles can be obtained by AFM imaging [50], providing meaningful information about intracellular molecular behaviors.

Chromatin is the DNA-protein complex. In cells, chromatin usually folds into characteristic formations called chromosomes. AFM imaging visually shows chromosome ultrastructures and cytokinesis [51]. In metaphase I, the sister chromatids were tightly connected together (Fig. 5.10a). In metaphase II, the chromatids were connected only at the centromere to form metaphase chromosomes in the characteristic X-shape (Fig. 5.10b), in accordance with the obtained knowledge of chromosome. In another study, AFM probe the topography of bacterial chromatophore at

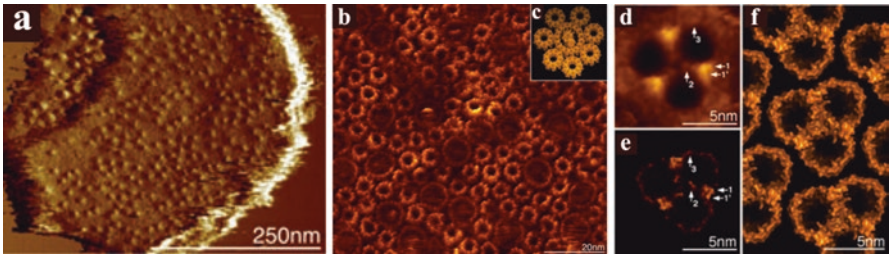

Fig. 5.11 High-resolution AFM analysis of the intracytoplasmic membrane of the photosynthetic bacterium. (**a**) AFM deflection image of a chromatophore. The strongly protruding membrane particles are the reaction centres (RC). (**b**) High-resolution AFM topography of the supramolecular assembly of light-harvesting complexes 2 (LH2) and core-complexes, ensemble of a reaction centre (RC) surrounded by light-harvesting complexes 1 (LH1). (**c**) Atomic model of a RC-LH1 core-complex surrounded by seven LH2 complexes, as depicted by AFM in the native membrane. (**d**) Average topography of the periplasmic surface of trimeric porin revealed major protrusions (turn β2-β3, arrow 1 and turn b14-b15, arrow 1′), fine protrusions close to the trimer axis (N-terminal Asp1, arrow 2), and a peripheral protrusion (turn β12-β13, arrow 3). (**e**) Structure of the periplasmic side of the Rb. capsulatus porin (PDB: 1PRN) is highly similar to the AFM average topography. (**f**) Atomic model of the native supramolecular assembly of porins in the outer membrane. Reproduced with permission from refs [53]

the single-molecule level, providing direct structural information about its photosynthetic functions [52–54]. A chromatophore is a multicomponent assembly of pigment-protein photosynthetic complexes, including light-harvesting complexes (LH1 and LH2) and reaction centers (RCs) (Fig. 5.11) [53]. An intact chromatophore was characterized by the AFM deflection image, the membrane particles had homogeneous distribution on the RCs (Fig. 5.11a). High resolution imaging demonstrated the supramolecular assembly of LH2 rings, core complexes, and the ensemble of RCs and LH1 (Fig. 5.11b). Morphological imaging of individual core complex showed that the LH1 assembly around the RC formed a closed ellipse [54], in accordance with the atomic model (Fig. 5.11c). High resolution images of those densely packed porins showed the detailed molecular information of trimeric porin atomic structure on the surface of the Rhodobacter blasticus (Fig. 5.11d, e). An atomic model of the porin supramolecular association was proposed based on the average assembly pattern in ordered regions (Fig. 5.11f).

A cytoskeleton is the fundamental composition in cell. In eukaryotes, the cytoskeletal matrix is a dynamic structure, which has the functions of cell growth or division [55]. After drug treatment, nanoscaled changes in cytoskeleton is observed, attributing to the cytoskeleton remodeling [56]. Immunoglobulin (Ig) is the Y-shaped antibody produced mainly by plasma cells that is used by the immune system to neutralize pathogens. Single PE-conjugated IgG molecule exhibited globular shape with approximately 60 nm in diameter and 5 nm in height (Fig. 5.12a) [57]. PE-conjugated IgG molecules can self-assemble and form different structures, including monomers, spindle-like trimers, and hexamers through an end-to-end connection of two trimers. Interestingly, these multimers aggregate in different

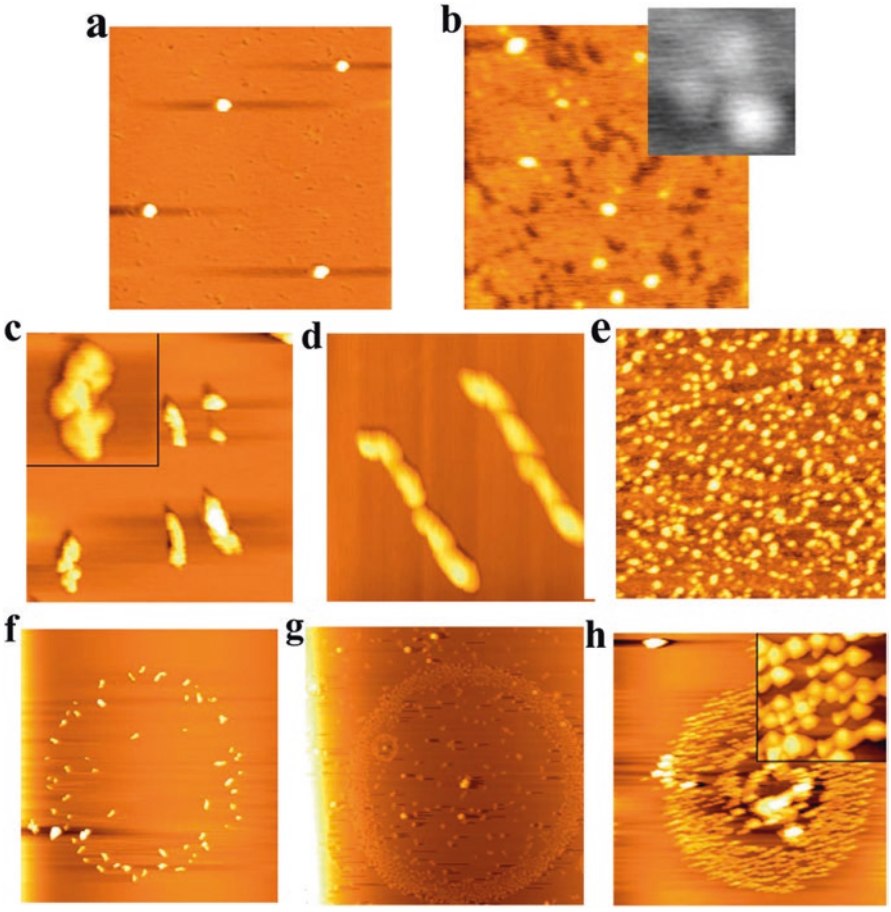

Fig. 5.12 Images of IgG molecules at different conditions: (**a**) single PE-conjugated IgG molecule is globular, with a diameter of about 60 nm and a height of about 5 nm (scanning size: 1.5 μm). (**b**) single non-labeled IgG molecule is 20–40 nm in diameter and about 2 nm in height (scanning size: 0.5 μm). The insect image reveals the characteristic Y shape of an IgG molecule with a diameter of about 40 nm (scanning size for inset, 50 nm). (**c**) and (**d**): PE-conjugated IgG molecules were able to form a monomer, trimer or polymer with different sizes and shapes. Scanning size: (**c**) 1 μm; (**d**) 0.6 μm. (**e**) non-labeled IgG molecules are unable to form end-to-end connected polymers and circular monolayers even at high concentrations. Scanning size: 1 μm. (**f**) and (**g**): PE-conjugated IgG molecules are able to form circular aggregates comprised well-assembled polymers. Scanning size: (**f**) 7 μm; (**g**) 25 μm. (**h**) A monolayer of circular polymers with a thickness of around 5 nm. Shown on the top right corner is an enlarged image with a scanning size of 500 nm, in which hexamers are assembled or arrayed orderly or synchronously in end-to-end and side-by-side fashions. Scanning size: 7 μm. Reproduced with permission from refs [57]

Acknowledgment This chapter was modified from the paper published by our group in Molecular Immunology (Yong Chen, Jiye Cai, Qingcai Xu, Zheng W. Chen; 29 July 2004; 2004; 41; 1247–1252). The related contents are re-used with permission

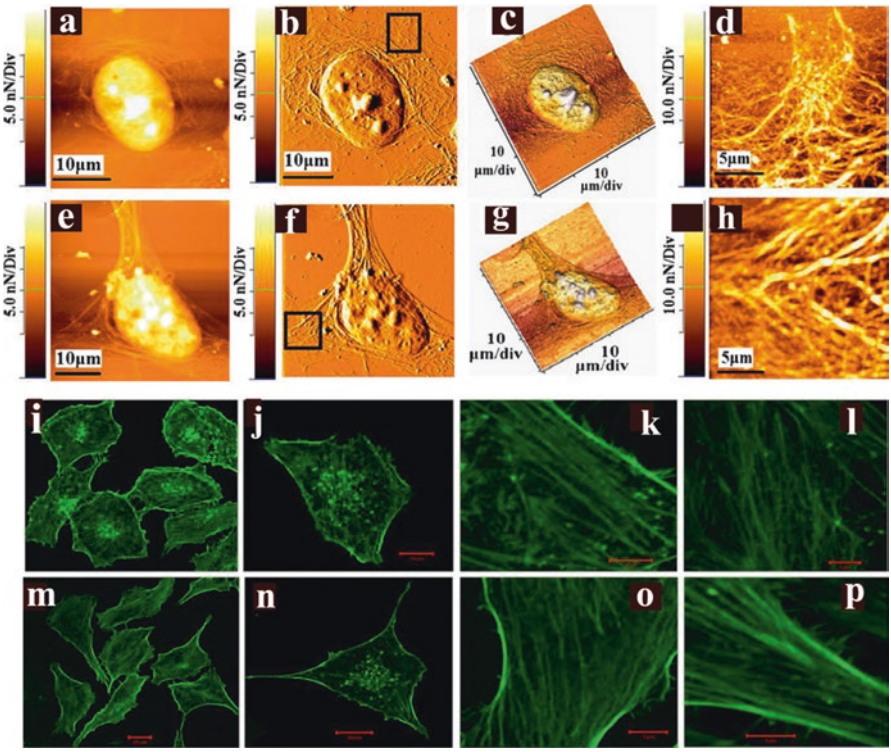

Fig. 5.13 AFM and fluorescent imaging for MCF-7 cell and its cytoskeleton. (**a, e**): Topography mode. (**b, f**): Error-signal mode. (**c, g**): 3-D mode. (**d**) and (**h**) were AFM topographical images enlarged from the square-indicated areas in (**b**) and (**f**), respectively. Scanning area: (**a–c**), (**e–g**) $35 \times 35\ \mu m^2$; (**d, h**) $10 \times 10\ \mu m^2$. In the fluorescent images (**i–p**), phalloidin-FITC was used to label cytoskeleton. The enlarge cytoskeleton location presented a random mesh-like arrangement (**i–l**),while the cytoskeleton of BMP2-induced cells displayed an aligned actin structure (**m–p**). Reproduced with permission from refs [58]

Acknowledgment This chapter was modified from the paper published by our group in *Appl Microbiol Biotechnol* (Hua Jin, Jiang Pi, Xun Huang, Feicheng Huang, Wenxiang Shao, Shengpu Li, Yong Chen, Jiye Cai; 21 January 2012; 2012; 93; 1715–1723). The related contents are re-used with permission

directions and form circular monolayers with larger dense core of IgG polymers (Fig. 5.12h). This visual evidence helps the researcher to understand self-assembled properties of those biolabeled IgG or antibodies. Bone morphogenetic protein 2 (BMP2) can modulate cell proliferation and differentiation. After BMP2 treatment, cell morphology is changed from a round shape to a spindle-like shape with the appearance in lamellipodia, filopodia, and membrane protrusions (Fig. 5.13) [58], which is essential for cellular migration. This indicates that BMP2 can promote cancer cell migration and invasion by regulating cytoskeleton reorganization and expressing adhesion molecules on cell surface.

4.3 Multiparametric Force Probing and Molecular Recognition

The combination of AFM imaging and force spectroscopy created new possibilities for the multi-parametric investigation of biological samples [59, 60]. Currently, AFM-based force spectroscopy is an useful toolkit to investigate the interaction force between or within biomolecules, including the ligand-receptor, antibody-antigen and other systems. The force-distance curves, obtained from force spectroscopy, provide detailed information of biomechanical properties, such as cell elasticity and stiffness. Examples for mapping the biophysical characteristics on biological samples include mammal cells [61], eukaryotic and bacterial cells [62, 63], viruses [64], membranes and membrane proteins [65, 66], and amyloid fibrils [67]. For example, mapping viscoelastic distribution of non-tumourigenic cells and breast tissues indicated that cancerous cell and malignant breast tissues had more deformable in comparison with normal cells [68]. This led to the conclusion that cellular systems in pathologic condition showed significant alteration of their biomechanical properties. Morphological imaging and force mapping of yeast cells (*Saccharomyces cerevisiae*) also revealed a more stiffening of the chitin-accumulating bud scar compared with the surrounding cell wall [69].

Determining how membrane receptors are self-assembled into nanodomains remains a difficult task in cell biology [70]. By applying molecular recognition mapping (MRM), the results show that cell surface receptors, such as growth factor receptors [71, 72], cell adhesion proteins [73] and drug receptors [74], can aggregate as nanoclusters to respond to environmental changes. For example, dynamic recognition imaging was used to identify cadherin binding sites on microvascular endothelial cells, and to co-localize the receptor positions on the cell surface (Fig. 5.14) [66] and the cortical cytoskeleton [72]. The ability of MRM to sensi-

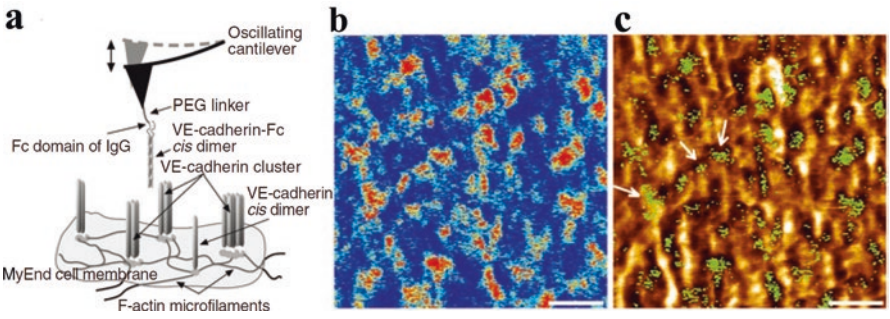

Fig. 5.14 Localizing VE-cadherin domains on vascular endothelial cell surfaces. (**a**) Scheme of molecular recognition imaging to visualize cadherin binding sites on endothelial cell surfaces. (**b**) Recognition image (512 × 512 pixels) of VE-cadherin domains. A pixel was colored red if cadherin binding of the functionalized AFM tip. (**c**) Mapping the recognition image (colored green) onto the corresponding cell surface topography (brown). Scale bars, 200 nm. Reproduced with permission from refs [83]

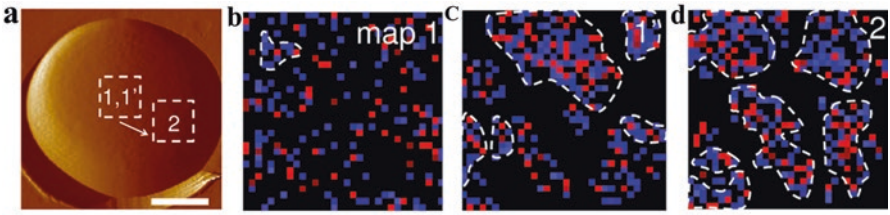

Fig. 5.15 Molecular recognition imaging of formation and propagation for Als5p nanodomains. (**a**) AFM topographic images for the wildtype S. cerevisiae cells expressing V5-tagged Als5p proteins. (**b**) Adhesion force maps (1 × 1 μm) recorded with an anti-V5 tip on a given target area of the native cells (map 1; recorded on the dashed squares in a). Blue and red pixels correspond to forces smaller and larger than 150 pN, respectively, and thus to V5-tagged Als5p recognition and unfolding. (**c**) Second adhesion force maps (1 × 1 μm) recorded on the same target area (map 1′). The heterogeneous distribution of colored pixels, which represents the detection of single Als5p, documents the formation of nanoscale clusters (*highlighted by dashed lines*). (**d**) Adhesion force maps (1 × 1 μm) recorded on remote areas (map 2) localized several hundred nanometers away from each other (see dashed squares in **a**). Reproduced with permission from refs [84]

tively probe compositional changes of membrane opens wide applications for investigating their structure-function relationship on the nanometer scale.

Based on the force-distance curves, the idea to map specific chemical and biological properties on membrane was proposed [75, 76]. This approach requires the tip-sample interactions, facilitating by AFM tip functionalization with specific chemical groups or ligands [76, 77]. Single-molecule force spectroscopy (SMFS) with biomolecules-modified tip [78] can measure the intermolecular binding forces and dynamics of receptor-ligand interactions on cell surface, including avidin-streptavidin [79, 80], antibodies [77], DNA [81] and cell adhesion proteins [82]. Using ligands-functionalized tip, typical force-distance curves are obtained from cerevisiae cells expressing V5-tagged Als5p proteins (Fig. 5.15). This molecule-modified AFM tip can specifically bind to the transporter molecule Als5p on cell surface, validating the specific binding interaction. Dufrêne et al. [12] used SMFS to demonstrate the force-induced formation and propagation of adhesion nanodomains on the surface of living fungal cells, showing that the distribution of Als5p antibodies on membrane was localized with nanodomains of 100–500 nm (Fig. 5.15), particularly for understanding the relationship between antibacterial effect and protein organization.

5 Combining Advanced Optical Microscopy with AFM

Optical microscopy is an indispensable tool in cell biological research. By fluorescent labeling, optical microscopy provides a useful way to identify specific components and to investigate interactions among different components. Due to the diffraction limit of light, conventional fluorescence microscopes, such as confocal

laser scanning microscopy (CLSM), have a limited resolution—a lateral resolution of about 250 nm and a vertical resolution of about 500 nm—and, thus, conventional fluorescence microscopy cannot be used to investigate biological samples at the single-molecule level [85]. Fortunately, several super-resolution imaging techniques, such as stimulated emission depletion (STED) [86], stochastic optical reconstruction microscopy (STORM) [87], near-field scanning optical microscopy (NSOM) [88], and photoactivated localization microscopy (PALM) [89], have been developed and broken through the diffraction barrier. For example, STED achieves a lateral resolution of 20–70 nm and a vertical resolution of 40–150 nm; single-molecule localization microscopy, such as NSOM, STORM and PALM, has a lateral resolution of 10–30 nm and an axial resolution of 10–75 nm [90]. The combination of AFM with advanced optical microscopy techniques provide an excellent opportunity to investigate proteins distribution and their interactions at nanometer resolution.

5.1 Combining CLSM with AFM

Combining AFM with confocal laser scanning microscopy (CLSM) has been increasingly used to investigate biological structures. The optical-topographic organization from CLSM-AFM set-up showed the irregularly-shaped protein nanodomains in both resting and activated immunoglobin E receptors [91]. Haga et al. [92] used the CLSM/AFM technique to simultaneously correlate cell topography, biophysical property, and fluorescence images of microtubules in a living cell, revealing that the cellular elasticity was closely related to the distribution of the actin network. Importantly, in AFM/CLSM microscopy, the AFM tip can be used as a micro-manipulator to stimulate cells, and the confocal microscopy is used as a detector to reveal the cellular responses [93].

Viral infection is dynamic and heterogeneous, imaging living cells and simultaneously quantifying the first viral binding to cell surface receptors is difficult. An atomic force and confocal microscopy set-up allows the surface receptor landscape of cells to be imaged, and the virus binding events within the first millisecond can be mapped at high resolution (< 50 nm) (Fig. 5.16). Functionalizing AFM tip with the labeled virus and virus-receptor binding events are precisely localized at pico-force level, and the first bond formed between the viral glycoprotein and its cell surface receptor has relatively low lifetime and free energy [94]. Therefore, the combination of AFM and confocal microscopy can be used to investigate the relationships between biomechanical properties and the release of microcapsules that were useful for targeted drug design [95, 96].

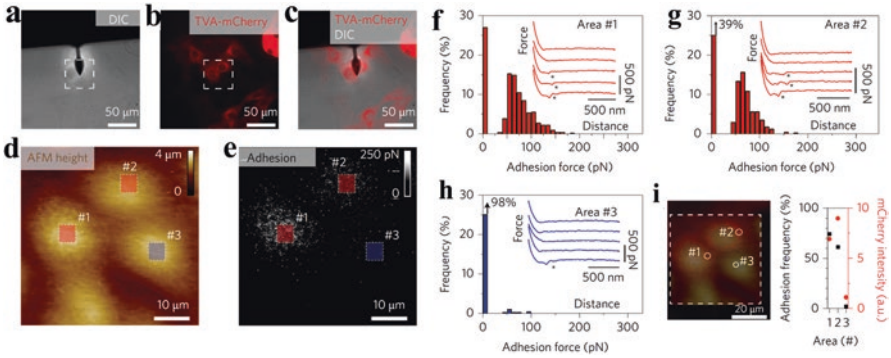

Fig. 5.16 Mapping EnvA-RABV (ΔG) virus binding to MDCK-TVA cells using correlative confocal microscopy and force-distance curve based AFM. (**a–c**): DIC image, mCherry channel, and superimposition of both images of wild-type MDCK cells and MDCK-TVA cells (red). (**d–e**): Force-curve based AFM height image and adhesion channel of MDCK cells recorded in the dashed square shown in a and b. (**f–h**): Distribution of adhesion forces measured between the AFM tip bearing EnvA-RABV (ΔG) and three areas of MDCK cells (highlighted in **d** and **e**). The red data (areas 1 and 2) are recorded on MDCK-TVA cells (as proved by the mCherry channel) and the blue data (area 3) on control wild-type MDCK cells expressing no TVA receptors. Insets: representative force-distance curves with asterisks indicating maximum adhesion peaks. (i) The superimposition of AFM topography and the mCherry channel showed good agreement between the adhesion frequency (black) (n > 1000) and the relative fluorescence intensity (red) taken from three different areas 1–3. Reproduced with permission from refs [94]

5.2 Combining NSOM with AFM

Near-field scanning optical microscopy (NSOM) is a useful nanotechnology tool for studying membrane at high optical resolution [97]. Compared with AFM tip, the NSOM probe is replaced by a metal-coated tapered optical fiber with a small aperture (diameter of 20–100 nm) producing optical images (Fig. 5.17a). The movement of the NSOM probe can change the surrounding electromagnetic field, which is divided into the near field area (<10 nm) and the far field area (≥10 nm) [48]. In order to detect the fluorescence emission signal activated by near-field light, NSOM filters the fluorescence intensity from the transmitted light using a long-pass filter (Fig. 5.17b), thus obtaining the non-diffraction-limited high-resolution optical imaging.

To create optical images at high resolution, the target biomolecules on the cell surface are labeled with specific fluorescent markers, such as quantum dots (QDs), before the NSOM imaging. Using fluorescent labeling from QDs, Zhong et al. [98] reported for the first time the visualization of CD3 molecules on the human peripheral blood T lymphocyte membrane by NOSM, showing the important application prospect of NSOM for the *in situ* single molecule imaging. NSOM is therefore proved to possess better resolution than confocal microscopy in the optical imaging of membrane proteins. Using QDs labeling, Chen et al. [99] investigated the nanoscale organization of hyaluronan receptor CD44 molecules on mesenchymal

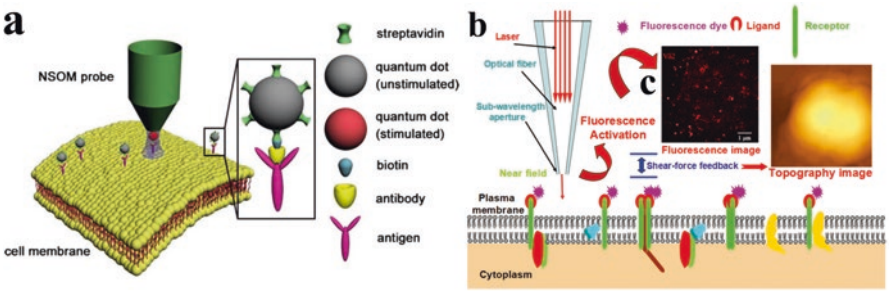

Fig. 5.17 Schematic NSOM for the *in situ* single molecule imaging on cell membrane. (**a**) Schematic depiction of quantum dots (QDs)-labeling based NSOM imaging. First, the biotinylated antibody is conjugated to cell membrane antigen, and then the QDs-streptavidin is connected to the biotinylated antibody though streptavidin-biotin binding. This procedure allows us to map the distribution of membrane protein though the fluorescence of QDs stimulated by the localized light coming from the NSOM probe. (**b**) The laser passes through NSOM probe to excite the fluorescent dyes on the cell membrane in the near field, simultaneously obtaining a high resolution topographical and fluorescent image on membrane. (**c**) The typical NSOM images of γδTCR on $V\gamma2^+$ T cells, scale bar: 1 μm. Reproduced with permission from refs [101, 102]

Acknowledgment This chapter was modified from the paper published by our group in *Micron* (Jianan Chen, Yin Pei, Zhengwei Chen, Jiye Cai; 8 November 2009; 2010; 41; 198–202). The related contents are re-used with permission

Acknowledgment This chapter was modified from the paper published by our group in *Nanoscale* (Jiang Pi, Hua Jin, Fen Yang, Zheng W. Chen, Jiye Cai; 24th August 2014; 2014, 6, 12229). The related contents are re-used with permission

stem cells (MSCs), with an optical resolution of down to 50 nm (Fig. 5.18). The fluorescence-topographic organization of CD44 molecules was clearly visible (Fig. 5.19), where the NSOM topographic and fluorescent images were superimposed to generate 3D imaging of the cell surface. The bright features that correspond to CD44 molecules were uniformly dispersed on cell membrane. Results show NSOM is an ideal technique to study the organization of the plasma membrane in detail at single-molecule level, by taking the advantage of QDs fluorescent labeling. Interestingly, using the NSOM-based two-color nanoscale molecule imaging strategy, Zeng et al. [100] simultaneously visualized the distribution of IL-22 and CD44 molecules on the plasma, showing IL-22 produced by $CD4^+$ T cells could aggregate as nanoclusters after bacterial infection (Fig. 5.20).

6 Conclusions

AFM is revolutionizing nanobiotechnological research in the life sciences. In this review, we have endeavoured to highlight the application of AFM in multiparametric imaging and multifunctional force measuring for biological systems. These AFM-based nanoscale analyses offer exciting opportunities in biomedicine.

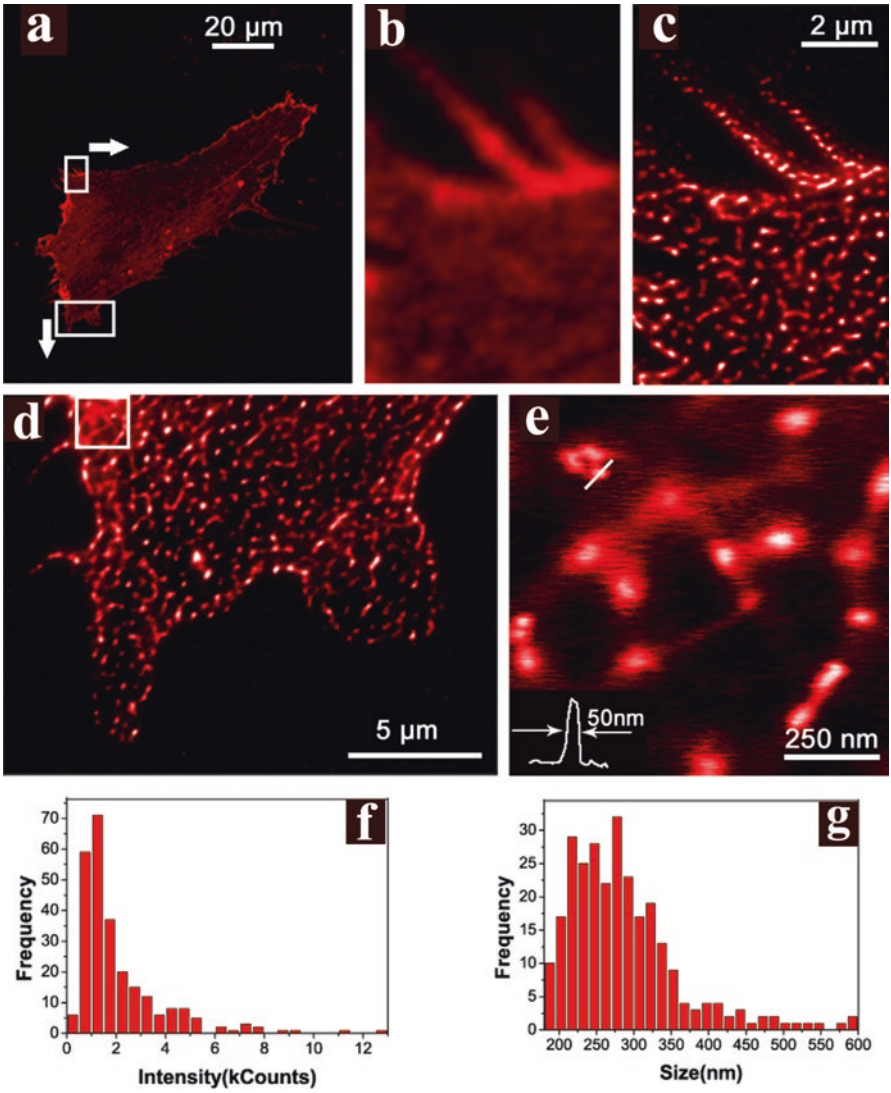

Fig. 5.18 NSOM/QDs-based fluorescent imaging of CD44 on mesenchymal stem cells (MSCs). (**a**) Confocal fluorescence image of the single MSC. (**b**) Confocal fluorescence image of the marked area in (**a**). The optical resolution is too low to resolve individual CD44 domains. (**c**) NSOM fluorescence image of the same area in (**b**), showing individually resolved domains. Note that the filopodia zone is brighter than cell body zone. (**d**) NSOM fluorescence imaging of the marked area (the lower one) in (**a**). (**e**) The smaller-scale image was obtained in the indicated area of (**d**), the inset shows one of the fluorescence spots has a resolution of ~50 nm. (**f**) Intensity-distribution histogram and (**g**) size-distribution histogram of fluorescence spots in (**d**), revealing microclusters of CD44 molecules. Reproduced with permission from refs [102]

Acknowledgment This chapter was modified from the paper published by our group in *Micron* (Jianan Chen, Yin Pei, Zhengwei Chen, Jiye Cai; 8 November 2009; 2010; 41; 198–202). The related contents are re-used with permission

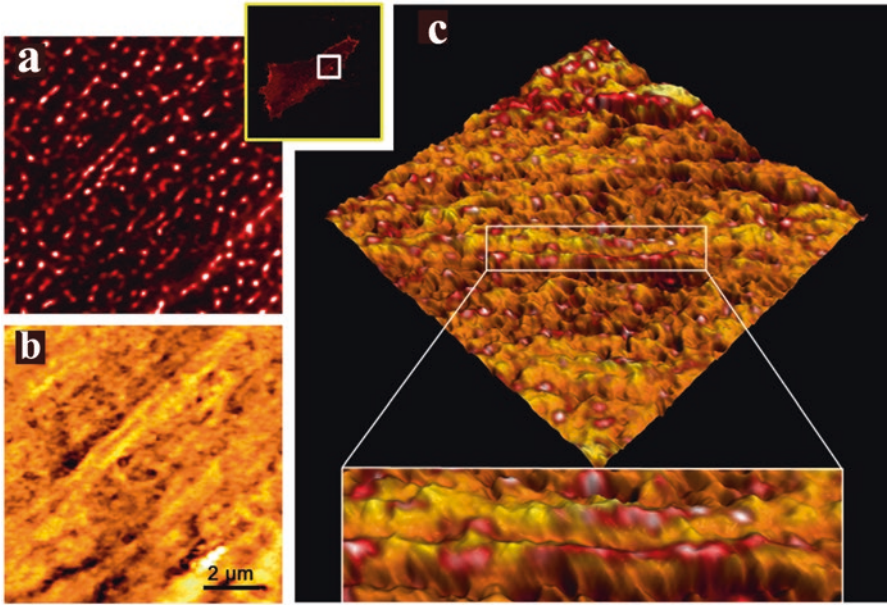

Fig. 5.19 NSOM imaging of the CD44 localization on MSCs using QDs. (**a**) NSOM fluorescence image obtained in the indicated area of the inset. (**b**) Corresponding NSOM topographic image. (**c**) Composite 3D image, the 3D image displays a combination of the topographic and fluorescence images. The inset shows CD44 molecules are located on slender, microvillus-type plasma membrane protrusions. Reproduced with permission from refs [102]

Acknowledgment This chapter was modified from the paper published by our group in *Micron* (Jianan Chen, Yin Pei, Zhengwei Chen, Jiye Cai; 8 November 2009; 2010; 41; 198–202). The related contents are re-used with permission.

For instance, AFM should help refine our understanding of cell-cell binding events by imaging of native membrane proteins at high resolution and simultaneous mapping of the biomechanical properties of the binding sites. The exciting application of AFM in cell biology is seen when combined with the advanced optical techniques, such as confocal fluorescence microscopy or NSOM. Combining this technique with AFM permits the imaging, manipulation and probing of biological matter down to nanoscopic scales, providing new ways to unravel the structure-function relationship of cell-cell interaction.

There are many challenges in AFM technology. High throughput, multicontent sensing platforms are needed, and these can be achieved using multifunctional devices with thousands of cantilevers working in parallel. Another difficult challenge will be to develop biological laboratories on AFM tips, making cantilever assays easy to personalize and to probe cells' sophisticated biofunctions.

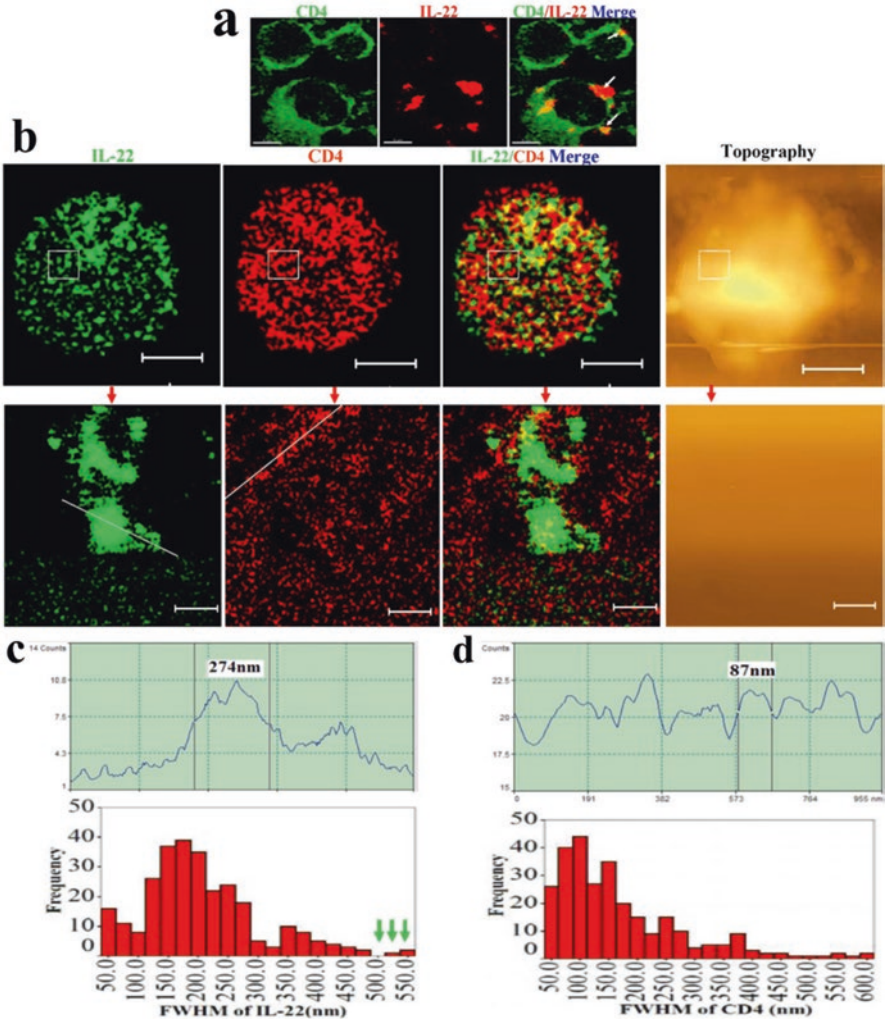

Fig. 5.20 NSOM imaging and analysis of membrane-bound IL-22 molecules on IL-22$^+$CD4$^+$ T cell surface. (**a**) Confocal microscopic images show that IL-22 forms capping domains on CD4 T cells after *in vivo* M. tuberculosis infection. (**b**) Representative NSOM/QDs-based nanoscale imaging shows that IL-22 are engaged as ~100–200 nm nanoclusters or as ~300–600 nm high density nanodomains. (**c**) A representative fluorescent intensity profile of an IL-22 nanocluster. Histogram graph shows the frequency of different sizes of FWHM of IL-22 nanoclusters on the CD4$^+$ T cells. The green arrow shows a resolution of IL-22 microdomains (>500 nm). (**d**) A representative fluorescence intensity profile of a CD4 nanocluster. Histogram graph shows the different sizes of CD4 nanoclusters or nanodomains are observed on the CD4$^+$ T cells. Reproduced with permission from refs [100]

Acknowledgment This chapter was modified from the paper published by our group in *The Journal of Immunology* (Gucheng Zeng, Crystal Y. Chen, Dan Huang, Shuyu Yao, Richard C. Wang, Zheng W. Chen; 1 June, 2011; 2011; 187; 190–199). The related contents are re-used with permission

Acknowledgements This work was supported by the Macao Science and Technology Development Fund (Grant No. 028/2014/A1).

Conflict of Interest Disclosures The authors declare no competing financial interests.

References

1. Shi Y, Cai M, Zhou L, Wang H. The structure and function of cell membranes studied by atomic force microscopy. Semin Cell Dev Biol. 2017;73:31–44.
2. Dufr YF. Ecirc, towards nanomicrobiology using atomic force microscopy. Nat Rev Microbiol. 2008;6(9):674.
3. Alsteens D, Gaub HE, Newton R, Pfreundschuh M, Gerber C, Müller DJ. Atomic force microscopy-based characterization and design of biointerfaces. Nat Rev Mater. 2017;2:17008.
4. Scheuring S, Sturgis JN. Chromatic adaptation of photosynthetic membranes. Science. 2005;309:484–7.
5. Viani MB, Pietrasanta LI, Thompson JB, Chand A, Gebeshuber IC, Kindt JH, Richter M, Hansma HG, Hansma PK. Probing protein|[ndash]|protein interactions in real time. Nat Struct Biol. 2000;7:644–7.
6. Hinterdorfer P, Dufrêne YF. Detection and localization of single molecular recognition events using atomic force microscopy. Nat Meth. 2006;3:347–55.
7. Müller DJ, Helenius J, Alsteens D, Dufrêne YF. Force probing surfaces of living cells to molecular resolution. Nat Chem Biol. 2009;5:383–90.
8. Dufrêne YF, Ando T, Garcia R, Alsteens D, Martinezmartin D, Engel A, Gerber C, Müller DJ. Imaging modes of atomic force microscopy for application in molecular and cell biology. Nat Nanotechnol. 2017;12:295–307.
9. Engel A, Müller DJ. Observing single biomolecules at work with the atomic force microscope. Nat Struct Biol. 2000;7:715–8.
10. Viani MB, Schaffer TE, Chand A, Rief M. Small cantilevers for force spectroscopy of single molecules. J Appl Phys. 1999;86:2258–62.
11. Afrin R, Arakawa H, Osada T, Ikai A. Extraction of membrane proteins from a living cell surface using the atomic force microscope and covalent crosslinkers. Cell Biochem Biophys. 2003;39:101–17.
12. Müller DJ, Dufrêne YF. Atomic force microscopy: a nanoscopic window on the cell surface. Trends Cell Biol. 2011;21:461–9.
13. Yuste R. Fluorescence microscopy today. Nat Methods. 2005;2:902–4.
14. Hell S. Microscopy and its focal switch. Nat Methods. 2009;6:24–32.
15. Radmacher M, Tillamnn RW, Fritz M, Gaub HE. From molecules to cells: imaging soft samples with the atomic force microscope. Science. 1992;257:1900–5.
16. Drake B, Prater CB, Weisenhorn AL, Gould SAC, Albrecht TR, Quate CF, Cannell DS, Hansma HG, Hansma PK. Imaging crystals, polymers, and processes in water with the atomic force microscope. Science. 1989;243:1586–9.
17. Kuznetsov YG, Mcpherson A. Atomic force microscopy in imaging of viruses and virus-infected cells. Microbiol Mol Biol Rev. 2011;75:268–85.
18. Ido S, Kimura K, Oyabu N, Kobayashi K, Tsukada M, Matsushige K, Yamada H. Beyond the helix pitch: direct visualization of native DNA in aqueous solution. ACS Nano. 2013;7:1817–22.
19. Pyne A, Thompson R, Leung C, Roy D, Hoogenboom BW. Single-molecule reconstruction of oligonucleotide secondary structure by atomic force microscopy. Small. 2014;10:3257–61.

20. Ido S, Kimiya H, Kobayashi K, Kominami H, Matsushige K, Yamada H. Immunoactive two-dimensional self-assembly of monoclonal antibodies in aqueous solution revealed by atomic force microscopy. Nat Mater. 2014;13:264–70.
21. Seelert H, Poetsch A, Dencher NA, Engel A, Stahlberg H, Müller DJ. Proton powered turbine of a plant motor. Nature. 2000;405:418–9.
22. Fotiadis D, Liang Y, Filipek S, Saperstein DA, Engel A, Palczewski K. Atomic-force microscopy: rhodopsin dimers in native disc membranes. Nature. 2003;421:127–8.
23. Müller DJ, Dufrêne YF. Atomic force microscopy as a multifunctional molecular toolbox in nanobiotechnology. Nat Nanotechnol. 2008;3:261–9.
24. Elie-Caille C, Severin F, Helenius J, Howard J, Muller DJ, Hyman AA. Straight GDP-tubulin Protofilaments form in the presence of Taxol. Curr Biol CB. 2007;17:1765–70.
25. Müller DJ, Hand GM, Engel A, Sosinsky GE. Conformational changes in surface structures of isolated connexin 26 gap junctions. EMBO J. 2002;21:3598–607.
26. Yu J, Bippes CA, Hand GM, Muller DJ, Sosinsky GE. Aminosulfonate modulated pH-induced conformational changes in connexin26 hemichannels. J Biol Chem. 2007;282:8895–904.
27. Grandbois M, Dettmann W, Benoit M, Gaub HE. Affinity imaging of red blood cells using an atomic force microscope. J Histochem Cytochem. 2000;48:719–24.
28. Zhao W, Tian Y, Cai M, Wang F, Wu J, Gao J, Liu S, Jiang J, Jiang S, Wang H. Studying the nucleated mammalian cell membrane by single molecule approaches. PLoS One. 2014;9:e91595.
29. Devaux PF, Morris R. Transmembrane asymmetry and lateral domains in biological membranes. Traffic. 2004;5:241–6.
30. Chtcheglova LA, Waschke J, Wildling L, Drenckhahn D, Hinterdorfer P. Nano-scale dynamic recognition imaging on vascular endothelial cells. Biophys J. 2007;93:11–3.
31. Lee S, Mandic J, Vliet KJV. Chemomechanical mapping of ligand-receptor binding kinetics on cells. Proc Natl Acad Sci U S A. 2007;104:9609–14.
32. Y.F. Dufr, Ecirc, Towards nanomicrobiology using atomic force microscopy. Nat Rev Microbiol 6 (2008) 674.
33. Plomp M, Leighton TJ, Wheeler KE, Hill HD, Malkin AJ. In vitro high-resolution structural dynamics of single germinating bacterial spores. Proc Natl Acad Sci U S A. 2007;104:9644–9.
34. Dupres V, Alsteens D, Pauwels K, Dufrêne YF. In vivo imaging of S-layer Nanoarrays on Corynebacterium glutamicum. Langmuir ACS J Surf Colloids. 2009;25:9653–5.
35. Touhami AM, Jericho H, Beveridge TJ. Atomic force microscopy of cell growth and division in Staphylococcus aureus. J Bacteriol. 2004;186:3286.
36. Turner RD, Thomson NH, Kirkham J, Devine D. Improvement of the pore trapping method to immobilize vital coccoid bacteria for high-resolution AFM: a study of Staphylococcus aureus. J Microsc. 2010;238:102–10.
37. Andre G, Kulakauskas S, Chapotchartier MP, Navet B, Deghorain M, Bernard E, Hols P, Dufrêne YF. Imaging the nanoscale organization of peptidoglycan in living Lactococcus lactis cells. Nat Commun. 2010;1:27.
38. Andre G, Deghorain M, Bron PA, Swam IIV, Kleerebezem M, Hols P, Dufrêne YF. Fluorescence and atomic force microscopy imaging of wall teichoic acids in lactobacillus plantarum. ACS Chem Biol. 2011;6:366–76.
39. Heu C, Berquand A, Elie-Caille C, Nicod L. Glyphosate-induced stiffening of HaCaT keratinocytes, a peak force tapping study on living cells. J Struct Biol. 2012;178:1–7.
40. Wang H, Hao X, Shan Y, Jiang J, Cai M, Shang X. Preparation of cell membranes for high resolution imaging by AFM. Ultramicroscopy. 2010;110:305–12.
41. Müller DJ, Dufrêne YF. Atomic force microscopy: a nanoscopic window on the cell surface. Trends Cell Biol. 2011;21:461–9.
42. Pfreundschuh M, Hensen U, Müller DJ. Quantitative imaging of the electrostatic field and potential generated by a transmembrane protein pore at subnanometer resolution. Nano Lett. 2013;13:5585–93.

43. Braga PC, Ricci D. Detection of rokitamycin-iduced morphostructural alterations in helicobacter pylori by atomic force microscopy. Chemotherapy. 2000;46:15–22.
44. Alsteens D, Verbelen C, Dague E, Raze D, Baulard AR, Dufrêne YF. Organization of the mycobacterial cell wall: a nanoscale view. Pflugers Arch - Eur J Physiol. 2008;456:117–25.
45. Dague E, Alsteens D, Latgé JP, Dufrêne YF. High-resolution cell surface dynamics of germinating aspergillus fumigatus conidia. Biophys J. 2008;94:656–60.
46. Ke C, Chen J, Guo Y, Chen ZW, Cai J. Migration mechanism of mesenchymal stem cells studied by QD/NSOM. Biochim Biophys Acta. 2015;1848:859–68.
47. Knockenhauer KE, Schwartz TU. The nuclear pore complex as a flexible and dynamic gate. Cell. 2016;164:1162–71.
48. Ushiki T, Hoshi O. Atomic force microscopy for imaging human metaphase chromosomes. Chromosom Res Int J Mol Supramolecular Evol Aspects Chromosom Biol. 2008;16:383–96.
49. Scheuring S, Sturgis JN. Atomic force microscopy of the bacterial photosynthetic apparatus: plain pictures of an elaborate machinery. Photosynth Res. 2009;102:197–211.
50. Norregaard K, Metzler R, Ritter CM, Berg-Sørensen K, Oddershede LB. Manipulation and motion of organelles and single molecules in living cells. Chem Rev. 2017;117:4342–75.
51. Wu Y, Cai J, Cheng L, Xu Y, Lin Z, Wang C, Chen Y. Atomic force microscope tracking observation of Chinese hamster ovary cell mitosis. Micron. 2006;37:139–45.
52. Liu LN, Scheuring S. Investigation of photosynthetic membrane structure using atomic force microscopy. Trends Plant Sci. 2013;18:277–86.
53. Scheuring S, Dufrêne YF. Atomic force microscopy: probing the spatial organization, interactions and elasticity of microbial cell envelopes at molecular resolution. Mol Microbiol. 2010;75:1327–36.
54. Scheuring S, Sturgis JN. Chromatic adaptation of photosynthetic membranes. Science. 2005;309:484–7.
55. Rotsch C, Radmacher M. Drug-induced changes of cytoskeletal structure and mechanics in fibroblasts: an atomic force microscopy study. Biophys J. 2000;78:520–35.
56. Cuerrier CM, Benoit M, Guillemette G, Gobeil F, Grandbois M. Real-time monitoring of angiotensin II-induced contractile response and cytoskeleton remodeling in individual cells by atomic force microscopy. Pflugers Arch - Eur J Physiol. 2009;457:1361–72.
57. Chen Y, Cai J, Xu Q, Chen ZW. Atomic force bio-analytics of polymerization and aggregation of phycoerythrin-conjugated immunoglobulin G molecules. Mol Immunol. 2004;41:1247–52.
58. Jin H, Pi J, Huang X, Huang F, Shao W, Li S, Chen Y, Cai J. BMP2 promotes migration and invasion of breast cancer cells via cytoskeletal reorganization and adhesion decrease: an AFM investigation. Appl Microbiol Biotechnol. 2012;93:1715–23.
59. Zhang S, Aslan H, Besenbacher F, Dong M. Quantitative biomolecular imaging by dynamic nanomechanical mapping. Chem Soc Rev. 2014;43:7412–29.
60. Dufrêne YF, Martínezmartín D, Medalsy I, Alsteens D, Müller DJ. Multiparametric imaging of biological systems by force-distance curve-based AFM. Nat Methods. 2013;10:847–54.
61. Matzke R, Jacobson K, Radmacher M. Direct, high-resolution measurement of furrow stiffening during division of adherent cells. Nat Cell Biol. 2001;3:607–10.
62. Hecht FM, Rheinlaender J, Schierbaum N, Goldmann WH, Fabry B, Schäffer TE. Imaging viscoelastic properties of live cells by AFM: power-law rheology on the nanoscale. Soft Matter. 2015;11:4584–91.
63. Beaussart A, El-Kirat-Chatel S, Fontaine T, Latgé JP, Dufrêne YF. Nanoscale biophysical properties of the cell surface galactosaminogalactan from the fungal pathogen Aspergillus fumigatus. Nanoscale. 2015;7:14996.
64. Marchetti M, Wuite G, Roos WH. Atomic force microscopy observation and characterization of single virions and virus-like particles by nano-indentation. Curr Opin Virol. 2016;18:82–8.
65. Medalsy ID, Müller DJ. Nanomechanical properties of proteins and membranes depend on loading rate and electrostatic interactions. ACS Nano. 2013;7:2642–50.

66. Medalsy I, Hensen U, Muller DJ. Imaging and quantifying chemical and physical properties of native proteins at molecular resolution by force-volume AFM. Angew Chem. 2011;50:12103–8.
67. Wegmann S, Medalsy I, Mandelkow E, Müller D. The fuzzy coat of pathological human tau fibrils is a two-layered polyelectrolyte brush. Proc Natl Acad Sci U S A. 2013;110:313–21.
68. Plodinec M, Loparic M, Monnier CA, Obermann EC, Zanetti-Dallenbach R, Oertle P, Hyotyla JT, Aebi U, Bentires-Alj M, Lim RY. The Nanomechanical signature of breast cancer. Nat Nanotechnol. 2012;7:757–65.
69. Touhami A, Nysten B, Dufrêne YF. Nanoscale mapping of the elasticity of microbial cells by atomic force microscopy. Langmuir. 2003;19:4539–43.
70. Gerber C, Lang HP. How the doors to the nanoworld were opened. Nat Nanotechnol. 2006;1:3–5.
71. Viani MB, Schäffer TE, Chand A, Rief M, Gaub HE, Hansma PK. Small cantilevers for force spectroscopy of single molecules. J Appl Phys. 1999;86:2258–62.
72. Ando T, Kodera N, Naito Y, Kinoshita T, Furuta KY, Toyoshima YY. A high-speed atomic force microscope for studying biological macromolecules in action. Proc Natl Acad Sci U S A. 2001;98:12468–72.
73. Alcaraz J, Buscemi L, Puigdemorales M, Colchero J, Baró AA, Navajas D. Correction of microrheological measurements of soft samples with atomic force microscopy for the hydrodynamic drag on the cantilever. Langmuir. 2002;18:716–21.
74. Sahin O, Magonov S, Su C, Quate CF, Solgaard O. An atomic force microscope tip designed to measure time-varying nanomechanical forces. Nat Nanotechnol. 2007;2:507–14.
75. Frisbie CD, Lieber CM. Functional group imaging by chemical force microscopy. Science (New York, NY). 1994;265:2071–4.
76. Ludwig M, Dettmann W, Gaub HE. Atomic force microscope imaging contrast based on molecular recognition. Biophys J. 1997;72:445–8.
77. Hinterdorfer P, Baumgartner W, Gruber HJ, Schilcher K, Schindler H. Detection and localization of individual antibody-antigen recognition events by atomic force microscopy. Proc Natl Acad Sci U S A. 1996;93:3477–81.
78. Sotomayor M, Schulten K. Single-molecule experiments in vitro and in silico. Science. 2007;316:1144–8.
79. Moy VT, Florin EL, Gaub HE. Intermolecular forces and energies between ligands and receptors. Science. 1994;266:257–9.
80. Lee GU, Kidwell DA, Colton RJ. Sensing discrete streptavidin-biotin interactions with atomic force microscopy. Langmuir. 1994;10:354–7.
81. Lee GU, Chrisey LA, Colton RJ. Direct measurement of the forces between complementary strands of DNA. Science. 1994;266:771–3.
82. Franz CM, Taubenberger A, Puech PH, Muller DJ. Studying integrin-mediated cell adhesion at the single-molecule level using AFM force spectroscopy. Sci STKE. 2007;2007
83. Chtcheglova LA, Waschke J, Wildling L, Drenckhahn D, Hinterdorfer P. Nano-scale dynamic recognition imaging on vascular endothelial cells. Biophys J. 2007;93:11–3.
84. Alsteens D, Garcia MC, Lipke PN, Dufrêne YF. Force-induced formation and propagation of adhesion nanodomains in living fungal cells. Proc Natl Acad Sci U S A. 2010;107:20744–9.
85. Huang B, Babcock H, Zhuang X. Breaking the diffraction barrier: super-resolution imaging of cells. Cell. 2010;143:1047–58.
86. Hein B, Willig KI, Wurm CA, Westphal V, Jakobs S, Hell SW. Stimulated emission depletion Nanoscopy of living cells using SNAP-tag fusion proteins. Biophys J. 2010;98:158–63.
87. Rust MJ, Bates M, Zhuang X. Sub-diffraction-limit imaging by stochastic optical reconstruction microscopy (STORM). Nat Methods. 2006;3:793.
88. Nguyen TQ, Schwartz BJ, Schaller RD, Johnson JC, Lee LF, Haber LH, Saykally RJ. Near-Field Scanning Optical Microscopy (NSOM) studies of the relationship between interchain interactions, morphology, photodamage, and energy transport in conjugated polymer films. J Phys Chem B. 2016;105:5153–60.

89. Sengupta P, Engelenburg SBV, Lippincottschwartz J. Superresolution imaging of biological systems using photoactivated localization microscopy. Chem Rev. 2014;114:3189–202.
90. Sydor AM, Czymmek KJ, Puchner EM, Mennella V. Super-resolution microscopy: from single molecules to supramolecular assemblies. Trends Cell Biol. 2015;25:730–48.
91. Frankel DJ, Pfeiffer JR, Surviladze Z, Johnson AE, Oliver JM, Wilson BS, Burns AR. Revealing the topography of cellular membrane domains by combined atomic force microscopy/fluorescence imaging. Biophys J. 2006;90:2404–13.
92. Haga H, Sasaki S, Kawabata K, Ito E, Ushiki T, Sambongi T. Elasticity mapping of living fibroblasts by AFM and immunofluorescence observation of the cytoskeleton. Ultramicroscopy. 2000;82:253–8.
93. Charras GT, Horton MA. Single cell mechanotransduction and its modulation analyzed by atomic force microscope indentation. Biophys J. 2002;82:2970–81.
94. Alsteens D, Newton R, Schubert R, Martinez-Martin D, Delguste M, Roska B, Müller DJ. Nanomechanical mapping of first binding steps of a virus to animal cells. Nat Nanotechnol. 2016;12:177–83.
95. Delcea M, Schmidt S, Palankar R, Fernandes PAL, Fery A, Möhwald H, Skirtach AG. Mechanobiology: correlation between mechanical stability of microcapsules studied by AFM and impact of cell-induced stresses. Small. 2010;6:2858–62.
96. Paskaramoorthy R, Bugarin S, Reid RG. Mechanical strength and intracellular uptake of CaCO3-templated LbL capsules composed of biodegradable polyelectrolytes: the influence of the number of layers. J Mater Chem B. 2013;1:1175–81.
97. Abulrob A, Lu Z, Brunette E, Pulla D, Stanimirovic D, Johnston LJ. Near-field scanning optical microscopy detects nanoscale glycolipid domains in the plasma membrane. J Microsc. 2008;232:225–34.
98. Zhong L, Liao W, Wang X, Cai J. Detection the specific marker of CD3 molecules of human peripheral blood T lymphocytes using SNOM and quantum dots. Colloids Surf A Physicochem Eng Asp. 2008;313–314:642–6.
99. Chen Y, Shao L, Ali Z, Cai J, Chen ZW. NSOM/QD-based nanoscale immunofluorescence imaging of antigen-specific T-cell receptor responses during an in vivo clonal Vγ2Vδ2. Blood. 2008;111:4220–32.
100. Zeng G, Chen CY, Huang D, Yao S, Wang RC, Chen ZW. Membrane-bound IL-22 after de novo production in tuberculosis and anti-M.tuberculosis effector function of IL-22+CD4+ T cells. J Immunol. 2011;187:190.
101. Pi J, Jin H, Yang F, Chen ZW, Cai J. In situ single molecule imaging of cell membranes: linking basic nanotechniques to cell biology, immunology and medicine. Nanoscale. 2014;6:12229–49.
102. Chen J, Pei Y, Chen Z, Cai J. Quantum dot labeling based on near-field optical imaging of CD44 molecules. Micron. 2010;41:198–202.

Chapter 6
The Hyphenated Technique of High Speed Atomic Force Microscopy and Super Resolution Optical Detection System

Xiao Feng, Yunchang Guo, Hongjie An, and Hongshun Yang

Abstract The fast scanning AFM combination with super resolution optical technique allow co-localized imaging and manipulation with sub-diffraction resolution in a few seconds. The hybrid technique opens up new fields of in-situ dynamic study in living cells, enzymatic reactions, fibril growth and biomedical research.

1 Introduction

Atomic force microscopy (AFM) is a versatile technology for the study of biological samples. A flexible cantilever is used as a force sensor for measuring extremely small forces between the AFM tip and sample surfaces. Dynamic mode AFM using small imaging forces allows nondestructive measurement. That makes AFM more popular in the study of native biomolecules than Scanning Electron Microscopy (SEM) and Transmission Electron Microscopy (TEM). However, slow imaging speed hinders the use of AFM, comparing to an optical microscope, SEM and TEM. Apart from the superb lateral and vertical resolution, researchers expect to know sample changes over time during the cellular bioprocess, such as protein folding and unfolding, DNA assembly, DNA-protein interaction and drug-cell interaction, etc. Most of the reactions are too fast to be recorded by an AFM which usually takes more than one minute per frame. The dynamic imaging at single-molecule level in a bio-system is difficult to resolve until the invention of high speed AFM and super-resolution optical microscopy.

X. Feng · H. Yang
Food Science and Technology Programme, c/o Department of Chemistry, National University of Singapore, Singapore, Singapore

Y. Guo
JPK Instruments AG, Shanghai, China

H. An (✉)
Division of Physics and Applied Physics, Nanyang Technological University Singapore, Singapore, Singapore
e-mail: hjan@ntu.edu.sg

J. Cai (ed.), *Atomic Force Microscopy in Molecular and Cell Biology*,
https://doi.org/10.1007/978-981-13-1510-7_6

Many AFM specialists devote considerable efforts in developing new imaging systems to increase the scanning rate of AFM. To date, the commercially available high speed AFM enables several tens Hertz frame rate [1]. The fast scan techniques allow the AFM tip to trace the dynamic bioprocess with a tiny scan force without sacrificing the image qualities. The high speed AFM is able to investigate the structure and dynamics of single molecules, indicating the molecular movement and diffusion dynamics. High speed AFM enabled many tremendous discoveries recently, such as the nature of myosin V motor mechanism [2], the diffusion dynamics of protein through a membrane [3], and the killing process of an anti-microbial peptide towards *Escherichia coli* (*E. coli*) [4]. More and more dynamic process at the nanoscale have been captured and reported as high scanning speed and the wide application in air, vacuum, and liquids [5]. In the life science researches, the optical microscopes are widely used and record the images in sub-second. However, the use of classical optical microscopy for the single-molecule image is limited by the Abbe diffraction of light, which depends on the wavelength of light λ and the numerical aperture of the optical system (NA): $Resolution_{x,y} = \lambda/2NA$ [6]. To overcome the Abbe limit, several advanced fluorescence methods have been developed to obtain the super-resolution, either by photo-activation, photo-switching, or by selective deactivation of individual fluorophores in fluorescence microscopy. The development of stimulated emission depletion (STED) microscopy, photoactivated localization microscopy (PALM) and stochastic optical reconstruction microscopy (STORM) allow widespread applications in the study of biological samples with sub-Abbe limit, 20–30 nm [6].

Both AFM and optical microscopy provide different information. The AFM detect the topology and mechanical properties of the investigated samples. For the objects having the similar size and mechanical properties, it is difficult to distinguish and specify them simply by AFM images. Moreover, a high-resolution of AFM is not enough to detect the binding of very tiny ligands. On the other hand, an optical microscope can obtain dynamic bioprocess with the specific fluorescence labeling. However, the structure and the mechanical details are missing even at a super-resolution and high signal-to-noise ratios. The coupling of AFM and optical techniques meet the demands for the achievement of the specification, structure, and mechanical information simultaneously. The details of high speed AFM and super-resolution microscopy can be seen in the literature [7]. In this chapter, we mainly focused on the combination of the high speed AFM and super-resolution optical techniques, such as AFM-STED, AFM-STORM and AFM-PALM, for imaging of living systems, and for precise manipulations for demanding experiments and cutting-edge researches fundamentally *in situ* and in real time.

2 High Speed AFM

High speed AFM is scanning faster than normal AFM, and is getting popular in life sciences. Commercial available high speed AFM also called as ultra speed AFM (JPK) or fast scan AFM (Bruker), all of them comes out with outstanding designs for good quality images in short sample acquisition time. The core techniques for the new designs is to develop a system which can acquire the data with time resolution and spatial resolution at the same time. Generally, fast scan always comes at the expense of an increase of imaging forces, and thus results in image quality unacceptable and may damage the tip or samples easily.

2.1 A High Bandwidth Z–Scanner

A high sampling frequency requires a fast scanning control system, including a high speed scanner and a big bandwidth for the feedback loop [5]. A high resonant frequency of z-scanner is required because Z-movement needs to be faster than the X and Y movement. As Z-response time needs to be less than the pixel time in the X-Y movement. Assuming an image is captured in scan size $L \times L$ with scan lines N and pixels N each scan line in scan time t. The scan rate in X-direction $\nu_x = 2LN/t$, and a pixel time is $t_p = L/N\nu_x = t/2\,N^2$. Therefore, the Z-scanner needs to move in Z-direction a frequency $f_z = 2\,N^2/t$ to follow the surface up and down to resolve each pixel in X-direction. If $L = 300$ nm, $N = 100$, and $t = 20$ ms, then one needs a Z-scanner with resonance frequency $f >= 1$ MHz. The X-Y movement is relatively slow and does not require very high resonance frequency. Generally, the resonance frequency of the Z-scanner is influenced by the size and shape of a scanner. Usually a sample scanner is much bigger and moves slower than a tip scanner. Basically, a smaller scanner has a higher resonance frequency than a larger one. This is why most AFM use separated X-Y and Z-scanner system, while Z-scanner is fixed at the tip side. Some type of AFM fix both the X-Y and a separated Z-scanner on the tip side, also called as tip-scan AFM (JPK NanoWizard®). The minimal requirement for Z-scanner resonance frequency also defines the minimal feedback bandwidth. The shorter acquisition image time, the bigger bandwidth for feedback control system.

2.2 A Small Cantilever

To improve the time resolution, a delicate detecting system is highly demanded for faster information flow from the surface. Obtaining more information per time unit needs more interactions from the sample surfaces. A smaller cantilever should deliver information faster with similar interactions comparing with a bigger cantilever [8]. A small laser spot and a small spring constant are required to reduce the

acquisition time. However, this increases the noise level. In dynamic mode AFM, the acquisition time is influenced by the amplitude reading time, the sensor and scanner response time, and the error correction time through the feedback controller. The amplitude detector needs to be fast enough to catch several oscillation cycles at X and Y pixel to detect the phase delay and get an accurate amplitude value. A sensor response time is expressed as $Q/\pi f_0$ [9]. A cantilever with low Q factor and high resonance frequency delivers shorter response time. A cantilever with small Q factor is less sensitive to surface interactions and needs less energy to restore the dampened oscillations than one with high Q factor. The AFM tip detaching from the surface also delay the sensor response time, called parachuting [10].

High speed AFM is easy for survey scan at single-molecule level. High speed AFM can be applied to detect particulate contaminants to reveal contamination during DNA purification [11]. The single-molecular sensitivity enables High speed AFM to detect DNA molecules without amplification required in PCR, and no chemical labels are required in High speed AFM. Using High speed AFM, trace levels of filamentous contamination were discovered. High speed AFM provides an alternative to characterize and quantify trace contaminants in biomolecular reagents and instruments in the cases when other conventional techniques fail. Importantly, High speed AFM provides highly accurate information of the dsDNA molecule size, which is related to the nature of the contamination sources [11].

For the dynamic study, DNA-protein interactions, such as short-range slide of protein along DNA and hop of protein on DNA, can be visualized by high speed AFM, which were usually inaccessible by other high resolute microscopies. High speed AFM provides nanoscale and sub-second temporal resolution figures of single molecules [12]. The individual protein motion was measured using single-particle tracking mode, and it was observed that the composition of imaging-buffer has a significant effect on the random walk of proteins. The non-Brownian diffusion was investigated in the absence and in the presence of nucleotide cofactors. It was found out that the Brownian motion was hindered and prevented as the double-stranded DNA was immobilized on the surface of proteins. However, RAD54 monomers showed a diffusive behavior, which is not related to the motor activity [12].

High speed AFM imaged and visualized that M5-HMM was advancing progressively with ~36 nm steps in Fig. 6.1 [2]. Consecutive high-speed AFM images show the progressive movement of M5-HMM in 1 μM ATP solution at 7 fps [13]. Molecular motor mechanism is also investigated by high-speed AFM [14], which shows that the rotorless F_1-ATPase still rotates; the three β subunits cyclically display conformational changes in the contraclockwise direction in the separated α_3/β_3 stator ring, which shows similarity to the rotation of rotary shaft in F_1. The stator ring showed unidirectional structure basis. These findings suggest and imply the cooperative interaction between subunits in other hexameric ATPases.

Figure 6.2 shows the application of high speed AFM for observing the protein movement on DNA in 0.5 sec interval (a) [12] and (b) GltPh elevator domain movements in 1 sec interval [15]. The improved speed enables the observation of many biological phenomena. Meanwhile, high speed AFM is able to capture images at 1

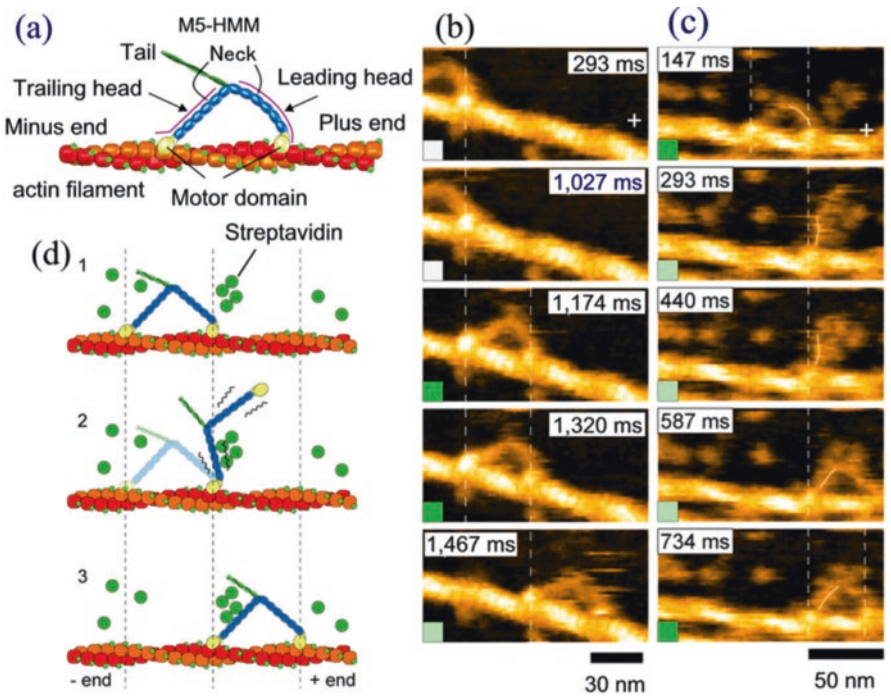

Fig. 6.1 High-speed AFM images of walking M5-HMM. (**a**), AFM images of M5-HMM movement in 1 mM ATP solution. (**b**), Image of two-headed M5-HMM bound to actin filaments. (**c**), Explanation of (**d**) and (**e**). (**d**) & (**e**), Time-resolved AFM images of hand over hand movement in 1 mM ATP solution and in 2 mM ATP. All images were captured at 146.7 ms per frame. Scale bar: (a) 30 nm; (d) 50 nm; (e) 30 nm. Reprinted with permission from Kodera et al. [2] © Springer Nature (2010)

frame per second (fps) for the investigation of cell membrane reconstruction, crystal dynamics of purple membrane and annexin V. With the smaller cantilevers, small biomolecules such as DNA can be imaged by 1 fps, while larger biomolecules like bacteria can be imaged at 10 s for every frame [4]. However, this improved speed is used in the scan sizes are up to ~ 400 nm, and it is still not rapid enough to understand the fast large-scale biological phenomenon. A scan of 500 nm × 500 nm, imaging with 100 × 100 pixel resolution at 10 fps requires a scan rate of 1 mm/s, while the line scan rate reaches 1 kHz. For a scan of 10 μm × 10 μm, imaging at 1 mm/s with 256 × 256 pixel resolution, it takes 5.12 s. This requires the support of a scanner with large scan range. The scan rate of 1 mm/s is the standard rate, and to pursue a frame rate of 10 Hz is challenging to current techniques.

A force-feedback high speed AFM has been developed using a commercial available dimensional micro-actuated silicon probe based on a cantilever-based optical interfacial microscope, which is shown in Fig. 6.3 [9]. This protocol is successful in obtaining large images of *E. coli* biofilm morphology using zero Newton force as feedback at about 1 fps in air. In this method, the removal of bending error of

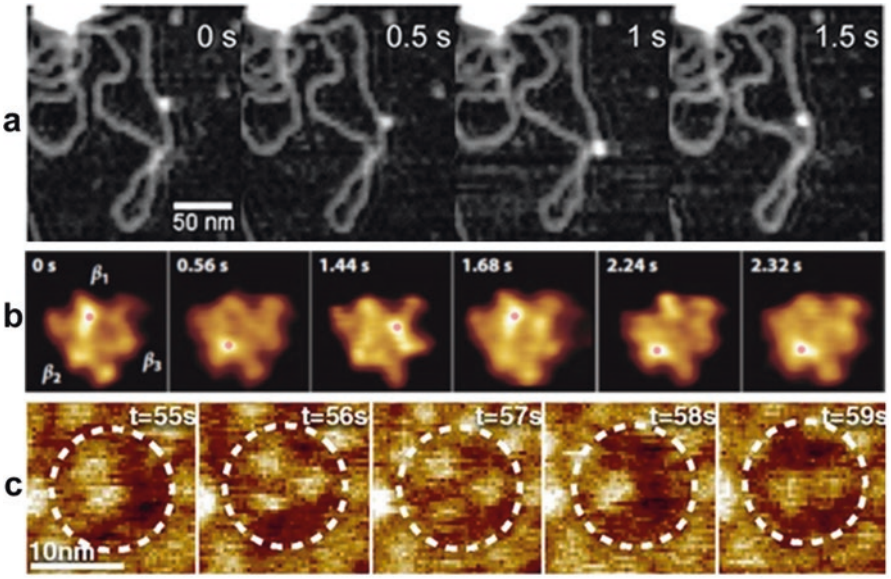

Fig. 6.2 Examples of high speed AFM observations of (**a**) protein hopping and sliding on DNA [12] (Reproduced by permission of The Royal Society of Chemistry) and (**b**) GltPh elevator domain movements (reprinted with permission from Ruan el al [15]. © NAS (2017))

cantilever by self-actuating imposes a counter force to the sample, which causes sample deformation. Both the AFM tip and the sample may be contaminated or damaged during this process. Moreover, the use of sample scanner limits the fast scan speed. There is plenty room to improve the scan speed to 30 fps.

3 Combination of High Speed AFM with Super–Resolution Optical Techniques for Imaging

The combined techniques of high speed AFM and high-resolution optical microscopy open the door to image the fast-changing biological phenomena, such as DNA methylation, protein folding and unfolding, bacteriolysis and so on, which provide fundamental experimental data and images for further understanding of the fast-changing biological phenomena and verifying the hypothesis. Although high speed AFM [2] and high speed microscopy [16] have been developed, the correlative real-time imaging of live cells *in situ* is still challenging.

A setup of AFM combined with a top view microscope has conflict in acquiring high-resolution images of biological samples in liquids. To acquire high-resolution optical images, the objective with a high NA is required to be close to the sample, while the AFM imaging needs the tip to approach the sample. It is hard to get high-resolution optical images with an AFM cantilever between the objective and the

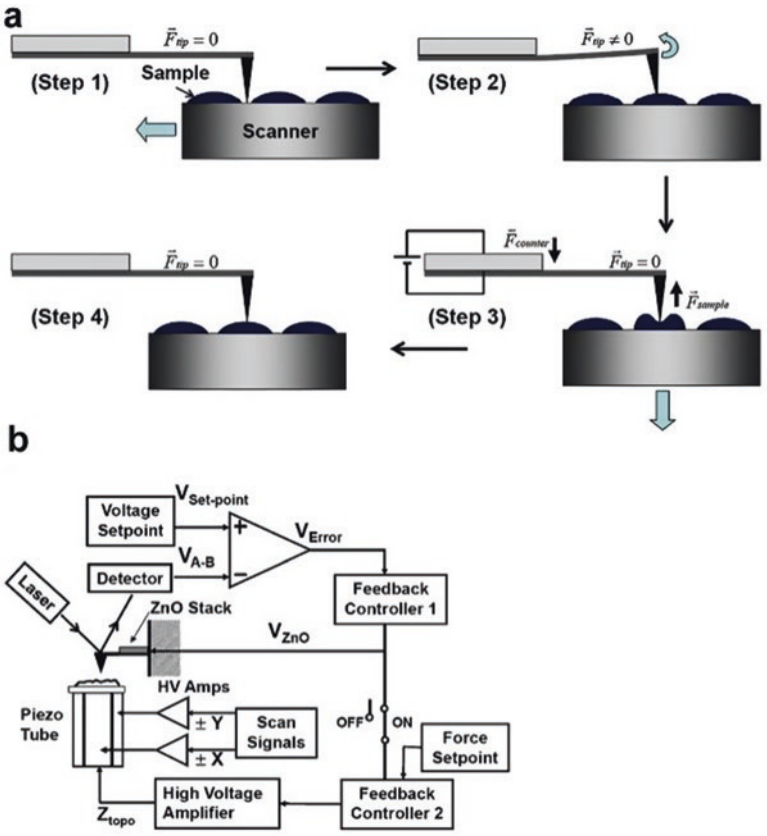

Fig. 6.3 A schematic diagram of the force-feedback high speed AFM. (**a**) Conceptual diagrams. (Step 1) The tip contacts the surface of sample. (Step 2) The cantilever bending occurs when tip encounters the sample. (Step 3) The biological structure was compressed and deformed due to the force-feedback. (Step 4) The activation of a feedback loop involving the piezo tube enables the sample to move down. (**b**) Feedback system. The feedback controller 1 is used for the force-feedback loop involving ZnO stack to obtain force images. The feedback controller 2 is the morphological feedback loop involving the piezo tube. Reprinted with permission from Kim et al. [9] © Elsevier (2016)

sample surfaces. The design of inverted optical microscope coupling with high speed AFM solved this problem. The AFM scan head rests on the top of an inverted microscope providing a platform for any optical access to the sample from below. The setup offers the possibility to integrate any type of fluorescence microscopes, such as epifluorescence, confocal, total internal reflection fluorescence (TIRF) and Fluorescence resonance energy transfer (FRET).

The hybrid high speed AFM/fluorescence microscopy was used to investigate the cell surface structural changes of the living HeLa and 3 T3 fibroblast cell [17]; the cell response to the tip stimulation with soluble agents [18]; the morphological changes of hippocampal neurons at 0.2 fps [19]; the lipid membrane response to

charged polymer nanoparticles [20]; the diffusion of lens cell membrane proteins at the cell surface [21] and mechanical properties of elastomeric proteins [22]. Furthermore, the combination of DNA manipulation and high speed AFM was used to image different biochemical reactions, such as enzymatic reaction and DNA structural changes [23].

The combination of high speed AFM and TIRF microscopy was used to simultaneously image the dynamics of biological samples, such as the effect and mechanism of chitinase A on chitin microfibrils at 3 fps (Fig. 6.4) [19]; rhodamine-labeled actin filaments at 8.3 fps [14]; the morphology changes of *B. subtilis* cell caused by lysozyme [24]; eukaryotic COS-7 and HeLa cell response to insulin [25].

A single chitinase A molecule advancing to the top-right was captured by high speed AFM images at 3 fps with 150 × 35 pixels. The TIRF images (40 × 15 pixels) confirmed the right movement of chitinase A molecule [19]. Several techniques have been developed over the past decades for super-resolution fluorescence microscopy including STED, PALM, and STOM [26, 27]. All these techniques have shown their strength and are promising for biological research. This review demonstrates the current state of high speed AFM development combined with these super-resolution techniques, as well as their application in biomedical research.

3.1 High Speed AFM with STED

STED microscopy generates images with super-resolution through selective deactivation of the fluorophores. As the illumination area at the focal point was minimized, the resolution of target imaging was improved significantly [28]. A typical STED microscope uses a co-aligned scanning pair of laser pulsed beams at the same focus position and controls the fluorescence through the overlap of the point spread functions (PSF) [29]. STED theory was first proposed in 1994 by Hell [30], while the first STED data was published in 2000 [31]. At first, a laser is used to excite the fluorescent molecules to emit the spontaneous fluorescence, which occurs at nanosecond time scale. In the process, an electron is excited into an excited electronic state from the ground state. Before a photon is released, a second laser pulse (STED beam) is introduced to force the excited electron to relax into a dark state,

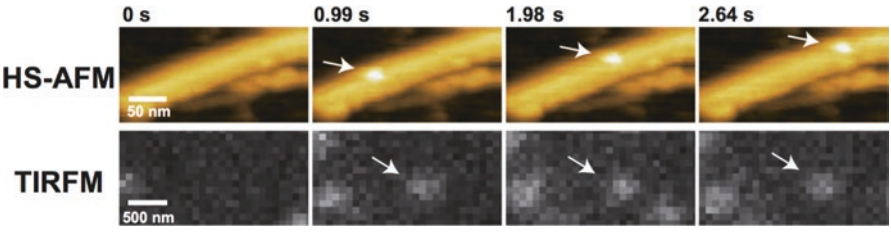

Fig. 6.4 Real-time high speed -AFM/TIRFM imaging of chitinase A labeled with Cy3 moving on a chitin microfibril. Reprinted with permission from Uchihashi et al. [19] © Elsevier (2016)

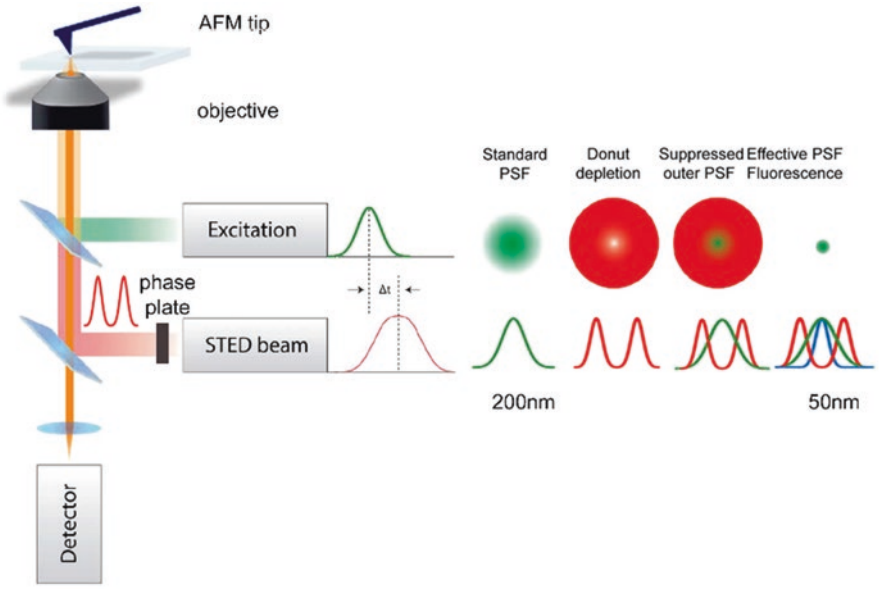

Fig. 6.5 Scheme of an AFM and STED based system showing the major components. The sketch includes the time-shifted pulse of the excitation source and the STED beam, the detector unit, and the AFM placed on an inverted microscope. The layout is adapted from JPK Instruments AG Technical Note: combining AFM with super-resolution STED microscopy system

which depletes the excited state at picosecond time scale [30]. The STED laser has a phase modulation to control the special intensity distribution, resulting in a donut PSF at the focal plane [32]. Overlapping the standard PSF of the first laser and the donut depletion of the second laser results in a suppressed outer PSF (Fig. 6.5). An effective PSF fluorescence is achieved by using a filter to exclude the red-shift fluorescence. Increase the intensity of the STED beam can increase the lateral resolution to less than 50 nm.

Integration of AFM with STED enables high-resolution fluorescence, topographical, and nano-mechanical imaging of biological samples in a physiological environment. This protocol provides fundamental understanding of numerous comprehensive studies in medicine, biology and material science. Using this method, microtubes have been investigated within antibody labeled COS7 cells in PBS solutions [33]. In Fig.6.6, it can be observed that the STED image (Fig. 6.6e), 3D AFM height image (Fig. 6.6c) and a Young's modulus map (Fig. 6.6f) of the same target area on a cell is consistent with each other. Microtubules which are visible in the STED image can be observed in the 3D AFM height image and traced in the Young's modulus map. The combined technology of the fast speed AFM and a high resolute STED can be applied to different kinds of samples and improve the multifunction and versatility of high speed AFM.

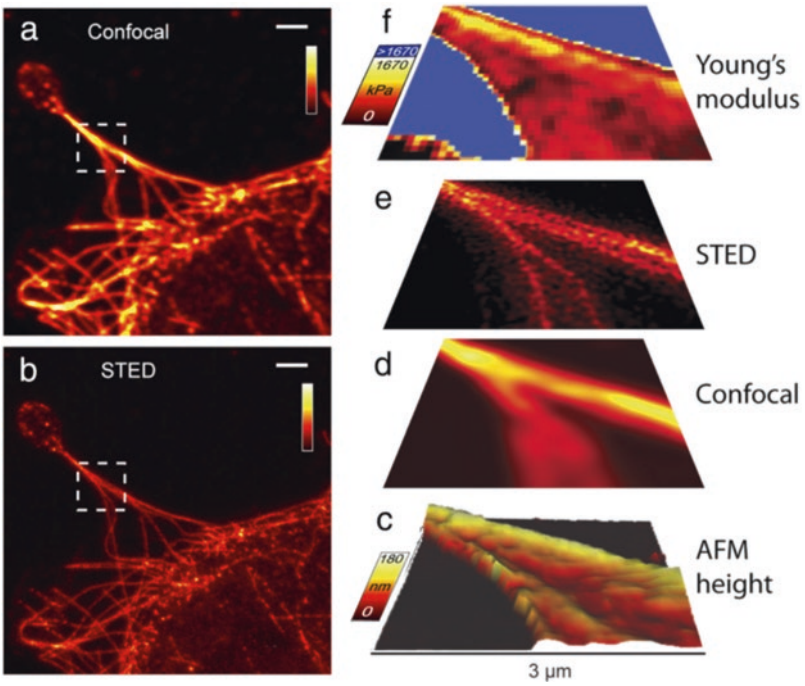

Fig. 6.6 Confocal image (**a**) and STEM image (**b**) of Atto 647 N labeled microtubules in COS7 cells in PBS. 3D height image extracted from AFM mapping (**c**) and calculated elasticity map (**f**) correlated with the STED (**e**) and confocal image (**d**) (both linear deconvolved) collected from the same area. Scale bars in (**a**) and (**b**): 2 µm, axes bars in (**c**)-(**f**): 3 µm. Reprinted with permission from [33] © Harke et al.; Springer Nature (2012)

3.2 High Speed AFM with dSTORM

STORM is a high-resolution imaging technique, which was proposed in 2006 by Zhuang's group to investigate DNA and DNA-protein complexes with a resolution of 20-nm [34]. A fluorescence image is re-constructed from high-accuracy localization of photoswitchable fluorophores. There are a series of imaging cycles involved in the STORM imaging process and system. In each cycle, there are only a small fraction of the fluorophores being switched on. Each of the active fluorophores is separated by a distance exceeding the Abbe diffraction limit, so that it is optically distinguishable from the other fluorophores. This enables the determination of these fluorophores' position with nanometer accuracy. In a repeating imaging cycle, different fluorophores are switched on. The multiple imaging cycles are used to determine the positions of the fluorophores, and are applied to reconstruct the overall image. This method is based on the discovery of the photoactivable molecule (green fluorescent protein) that can be activated and relaxed after emission to a stable dark state that could be re-activated [35].

Integration of AFM with direct STORM holds great potential for conducting correlated nanoscale biomolecular and structural characterization on living samples under physiological conditions [36]. AFM provides exceptional surface resolution, while STORM reveals internal cellular structures at single-molecule level. This combination is particularly useful for actin filaments and microtubules, which are important in intra-cellular transport and cell stability. A hybrid AFM-STORM was used to correlate the density of localizations with the 3D topography along (F-)actin cytoskeletal filament, which is shown in Fig. 6.7 [36]. The combination of high speed AFM and super-resolution optical detection system can provide complementary information, which enables the structural and functional nanoscale characterization of living samples.

Figure 6.7 compared AFM, dSTORM, and total internal reflection fluorescence microscope (TIRF) resolution through correlative imaging the same filaments via AFM, dSTORM, and TIRF respectively. It was found that dSTORM provided

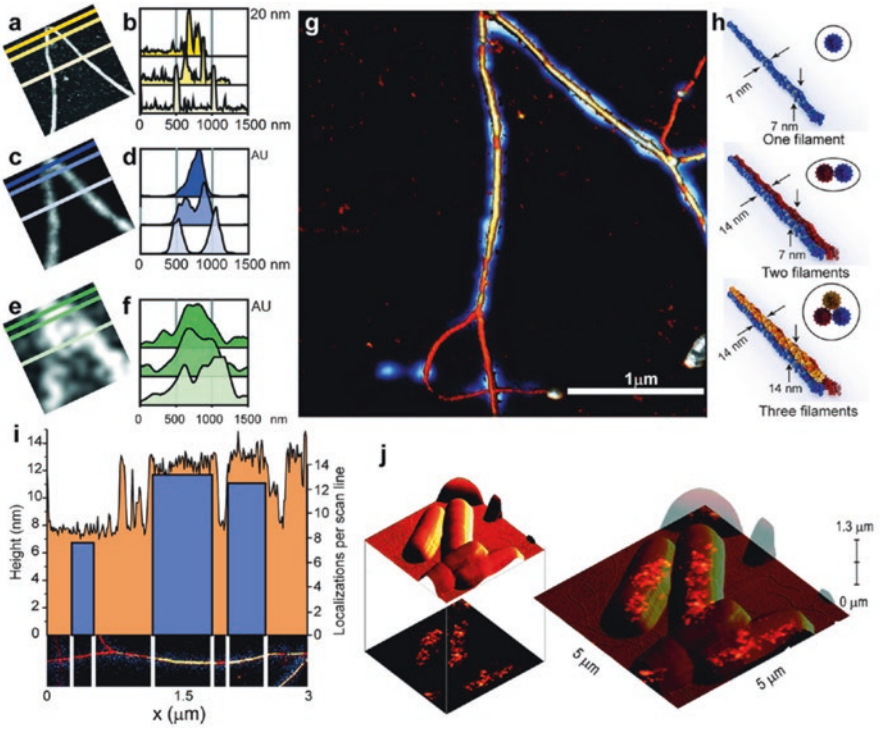

Fig. 6.7 Resolution comparison of AFM (**a**), dSTORM (**c**), and TIRF (**e**) images of correlated filaments. (**b**), (**d**), and (**f**) are the cross-sectional profiles for (**a**), (**c**) and (**e**) respectively. (**g**) Overlap of possible dSTORM map in blue and 3D AFM image in yellow−brown. (**h**) Suggestion of F-actin arrangements based on AFM analysis. (**i**) Maximum height profile of the filament according the AFM image showing below. (**j**) Corresponding AFM/PALM images of *E. coli* expressing RNA polymerase−mEos2. Reprinted with permission from Odermatt et al. [36] © American Chemical Society (2015)

comparable values to AFM when the width of the actin bundles was measured, indicating the comparability of AFM and dSTORM. However, AFM provides more resolute images than dSTORM when the filament diverged (Fig. 6.7a–c).

3.3 High Speed AFM with PALM

PALM and STORM are based on the same principle, using mathematical models to reconstruct a sub-diffraction limit from many sets of images [37]. Numerous sparse subsets of protein molecules which are photoactivatable fluorescent with caged synthetic fluorophores were activated, localized, and then bleached. A small fraction of particular molecules are photoactivated, while the majority of the population remains in the dark state. The new computational algorithm enables fast imaging of cellular structures with 20 nm resolution to be in less than 10 s [38], which is useful for the dynamic imaging of molecules and cells.

The correlative images of bacteria and mammalian cells in aqueous conditions can be obtained through AFM-PALM [36]. Figure 6.8 shows real-time AFM and PALM images of live CHO-K1 cells in a physiological environment. The paxillin-mEos2 cluster changes were monitored by PALM series, while the cell membrane dynamics were shown in AFM images. The upper corner of the entire cell was chosen for real-time analysis, as shown in Fig. 6.8a. Figure 6.8b showed that filopodia extended gradually followed by the extension of the lamellipodium, as the AFM images were obtained every minute. Figure 6.8c shows the PALM images recorded after AFM imaging. Figure 6.8d–g zoomed in to show paxillin clusters in certain regions. In Fig. 6.8d, there were paxillin clusters on the upper left at 28.2 min, while the paxillin clusters disappeared at 31.6 as shown in Fig. 6.8e, while new ones appeared at 30.7 and 33.3 min in Fig. 6.8f, g. In (d) and (e), it was observed that paxillin clusters disappeared from the top left corner (arrow), and new paxillin clusters were generated within 3 min in (f) and (g) (arrows).

The combination of AFM with dSTORM, PALM and STED was used to give complementary information about the same biological sample from different aspects. Chemically fixed bacterial cells (Fig. 6.7j) were imaged using AFM and dSTORM. *E. coli* expressing the fusion protein RNP- mEOS2 was firstly measured by AFM and followed by PALM. PALM was chosen over dSTORM in this case, because PALM can be utilized with lower laser power, which is more suitable for living cell imaging. The PALM provided the level of expression, while AFM provided the 3D bacteria morphology. Interestingly, there was no fusion protein for one bacteria in the PALM image (Fig. 6.7j). In the respective AFM image, it is shown that the bacterium without fusion protein is situated on the top of two other bacteria. This bacterium may be out of the illumination volume, so the respective fusion proteins were not found in the PALM image. This example showed the advantage of the AFM/PALM combination technique, which produced a better interpretation of the microscopy result than AFM or PALM alone.

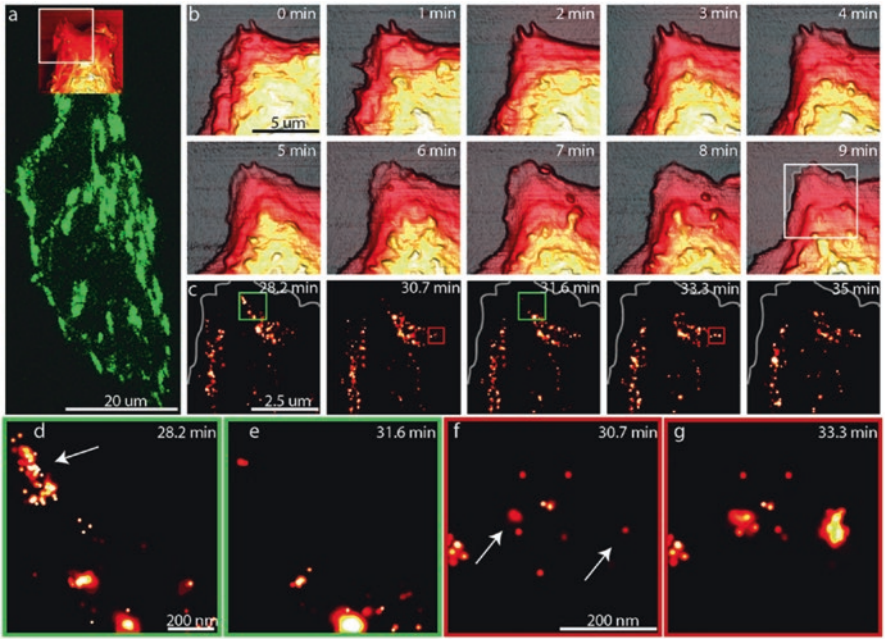

Fig. 6.8 Real-time AFM/PALM images of live mammalian cells. (**a**) Paxillin-mEos2 expression in CHO-K1 cell under TIRF illumination off-state. Overlap part indicates AFM overview of the upper part of CHO-K1 cell. (**b**) Time-resolved AFM images indicating the filopodia protrusion and lamellopodia extension of normal cell at frame rate 1 min^{-1}. (**c**) The paxillin-mEos2 clusters recognized in live-cell by PALM real-time images. The measured area is the same as the white square shown in (a). (**d**) and (**e**) Zoom-in image of the highlighted green square at different time in (**c**). (**f**) and (**g**) Zoom-in image of the highlighted red area in (**c**) at different time. Reprinted with permission from Odermatt et al. [36] © American Chemical Society (2015)

The combination of dSTORM, PALM and STED and AFM techniques to image biologically relevant phenomenon shows the comparison of the two techniques and complement the weaknesses of each technique. In the actin filament imaging and measurement, AFM provided the information of dimension and location, which could be correlated to the labeling density along the actin filament as imaged by the high resolute microscopy.

4 Hyphenated High Speed AFM and Super–Resolution Optical Techniques for Manipulation

4.1 AFM Nanomanipulation

AFM nanomanipulation is utilizing tips to pull, push, scratch and move the object to know the mechanical properties of the targets. Using an AFM tip as a tool, it is able to tailor biological samples at the single-molecule level. Figure 6.9 showed

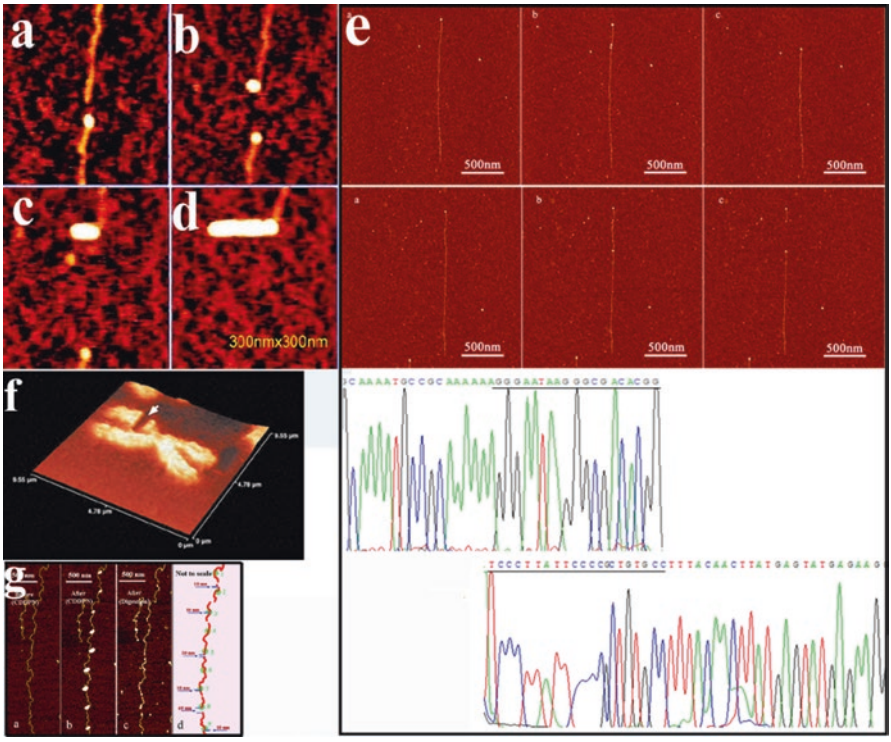

Fig. 6.9 AFM nanomanipulation at the single-molecule level. (**a**)–(**d**), DNA dissection and kneading. Reprinted with permission from Hu et al. [45] © American Chemical Society (2015). (**e**), Dissection of the chromosome. Reprinted with permission from Fotiadis et al. [41] © Elsevier (2002). (**f**), Dip-pen Nanolithography for positioning scission of single DNA molecules with a nonspecific endonuclease. Reprinted with permission from Li et al. [49] © American Chemical Society (2015)

some examples of AFM nanomanipulation. Single-stranded or double-stranded DNA molecules were immobilized on a substrate and then were precisely cut by an AFM tip [39]. The AFM tips are successfully used for DNA pickup from a chromosome [40, 41] or from a substrate by kneading, and then subjected to single-molecule PCR and sequencing [42–45]. AFM also can be used to move virus or nanoparticles to form a pattern on a surface [46]. Cells can be picked up for the study of cell-cell interactions with the assistance of an optical microscope [47]. Apart from mechanical scratching, pulling, or pushing the surface molecules, structures decoration can be made by a method called dip-pen nanolithography, where the tip is used as a pen to directly deposit collections of ink materials onto the substrate [48, 49].

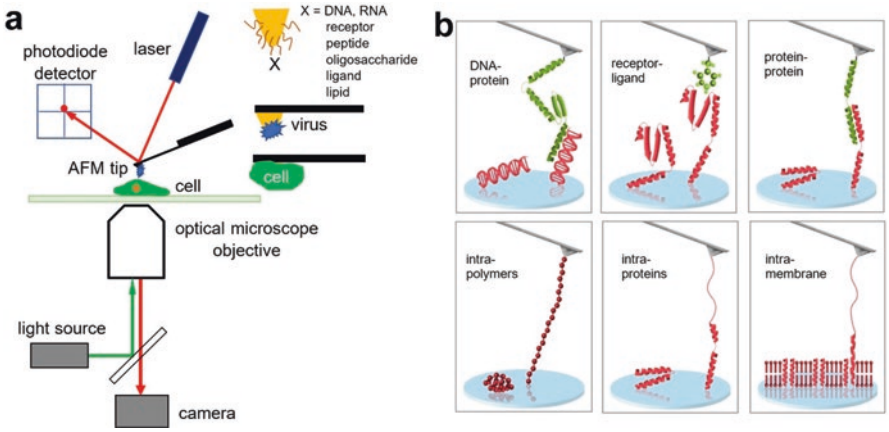

Fig. 6.10 Schematic of AFM resting on an inverted microscope for fast force mapping and force spectroscopy

4.2 Force Spectroscopy

Modification of both the AFM tip and the sample surfaces made AFM very useful in biological applications [50]. Single-molecule force spectroscopy techniques have been used to study the folding/unfolding of proteins [51], the elasticity of polysaccharide [52], DNA base pair interactions [53], interactions between proteins, between DNA and proteins, and between antibody and antigen. Molecular recognitions can be easily done by tagging a molecule (DNA, RNA, ligand, receptor, peptide, lipids, etc), or virus on the AFM tip for imaging or biosensing (Fig. 6.10).

4.3 Fast Force Mapping

For a survey study, force mapping, like Force Volume technique (Bruker), at a large scale usually takes more than 1 h and comes with low-resolution topology image, which presents a big challenge to investigating the short-term changes of living cells under physiological conditions. Long time scanning has problems in drift and time-resolution for *in situ* reactions. Fortunately, new techniques, Peakforce tapping mode AFM (QNM and ScanAsyst, Bruker), QI mode AFM (JPK Instruments AG), and Fast Force Mapping mode AFM (Oxford Instruments), can do fast force mapping in several minutes. The principles are similar to dynamic AFM, which avoids lateral forces by intermittently contacting the sample, and a maximum force is used as feedback. They are able to measure the mechanical properties and to image cells without changing their surface under liquid conditions. Topology, stiffness, adhesion and Youngs' modulus of samples are all obtained at one time scan when

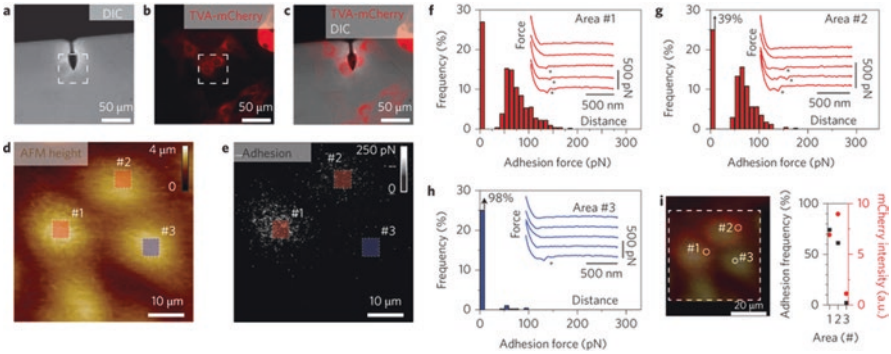

Fig. 6.11 Mapping virus binding to MDCK–TVA cells using correlative confocal microscopy and Peak Force Tapping AFM. Reprinted with permission from Alsteens et al. [56] © Springer Nature (2010)

following the procedure after calibration of the cantilever's spring constant. QI mode AFM is contact mode using contact point to define the height [54]. Small cantilevers are reported to increase the speed of force mapping by 10–100 times to resolve the dynamic process of embryonic fibroblast. With this technique, it is very convenient to study the cell adhesion, dynamics of drug-cell interactions, cell-cell interactions [55].

For the mechanical study, a high-resolution optical microscope helps to localize the AFM tip on the targets. Height image along with mechanical images are collected by fast force mapping over the desired area and then overlaid with the optical image. A modified AFM tip specify the molecules through force mapping to realize double localization. Recently, PeakForce mapping was used to measure the binding step of single viruses over living animal cells [56]. In this case, the confocal laser scanning microscopy was integrated with an AFM to target MDCK cells. The wild-type cell is nonfluorescent, while the TVA-mCherry labeled cells expressed the virus acceptors. The AFM tip was tagged with a single virus and then used to map the cell surfaces. Only cells expressing TVA receptors (mCherry fluorescence channel) were found to interact with the virus, with these binding events appearing as bright pixels in the adhesion image (Fig. 6.11). The combination provides a tool to quantify how molecules interfere with viral entry, and therefore aid the invention of novel drugs against virus infection.

4.4 AFM Manipulation – STED

With the combination of high resolute microscopies, more detailed properties can be discovered. For example, nano-manipulation can be done through combined STED and high speed AFM technology. AFM images can be overlaid with STED

fluorescent image. The STED image can be utilized as a map to target the sample precisely with high-resolution [57]. AFM software was applied to control the tip to the desired bead according to the information provided by STED image. As a result, the AFM tip was manipulated to move a single bead along a designed path and the image was obtained through STED before and after dragging. Thereafter, the STED images are combined together in green and red for analysis (Fig. 6.12b). The red and green colors represent the STED images before and after AFM dragging, respectively. Therefore, the yellow beads indicate the stationary status during the dragging, and the movement path of the dragged bead was observed as the arrows

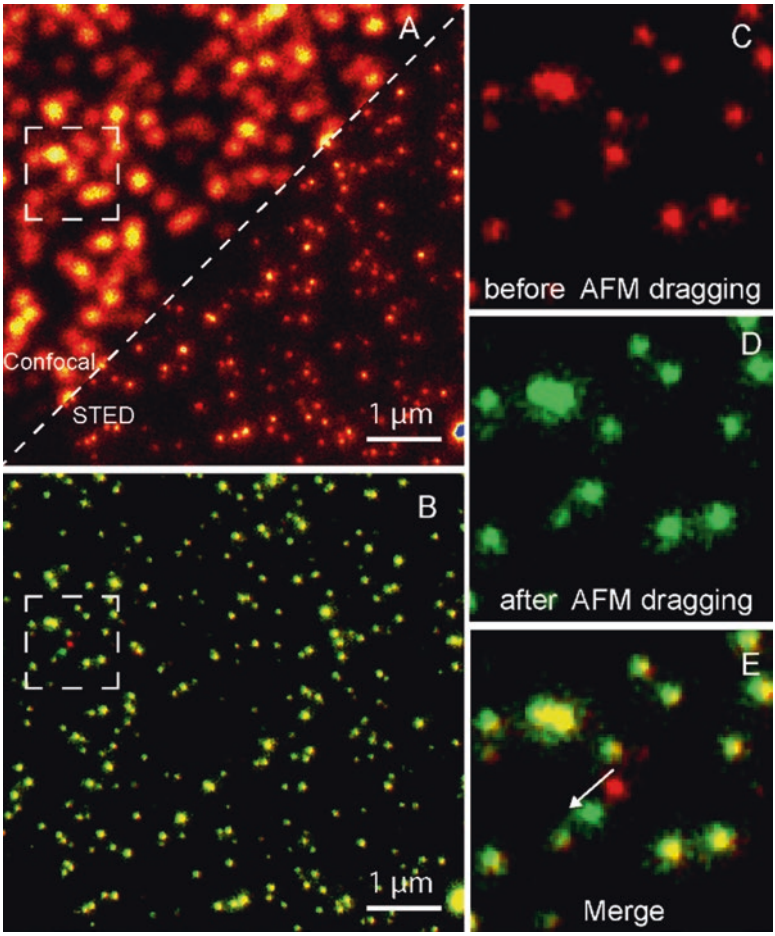

Fig. 6.12 AFM Sub-diffraction Nanomanipulation. STED images show before (**c**, red channel) and after (**d**, green channel) AFM manipulation of a bead. The overlay of images (**b** and **e**) give a yellowish color for unmoved beads, and the dislocation of one bead from red to green position. This is impossible to be distinguished by confocal images. Reprinted with permission from [57] © Chacko et al.; PLOS (2013)

shown in Fig. 6.12e. The fast imaging mode of a STED microscope helps in measuring the nano-manipulation with high-resolution. It can be observed that the AFM manipulation only moved one selected bead while other beads were stationary.

The integration of high speed AFM with high-resolution as STED provides a protocol to study the dynamic process of interactions between a functionalized particle and a target. A dye-labelled enzyme or drug molecules can be easily localized by STED images. Followed by an AFM manipulation push them to a target DNA, protein, or cell. Fast scanning further gain more information happened in short times.

4.5 AFM Nano–Manipulation – Optical Spectroscopy

Combining nano-manipulation with super-resolution optics is crucial for demanding experiments at single-molecule scale. The methodologies for achieving meaningful results with high signal-to-noise ratios in the study of individual molecules or single nanostructures are challenging. Bringing the AFM tip into a laser focus expands the classical spectroscopy to nanoscale with precise location. The integration enables new discoveries and experimental methods for both characterization and fabrication of nanomaterials, such as tip-enhanced near-field optical microscopy and tip-enhanced Raman spectroscopy (TERS). A simple application is to stretch a protein or DNA molecule which is positioned in the laser focus. Both optical and mechanical properties are probed simultaneously.

TERS was introduced and applied to achieve Raman spectroscopy with extraordinarily high spatial resolution [58]. The protocol uses metal-coated tips or solid metal, or tips attached to nanoparticles such as gold, silver, or platinum. The AFM tip is positioned in a laser beam above the sample surface, and manipulated stationary at a z-position, for localized nanoscale enhancement of the Raman signals (Fig. 6.13). With the help of fast force mapping, the spatial resolution is in the single nanometer regime [59]. The experimental and applications can be seen in review [58].

The nanoantenna is usually fabricated by complicated protocols, such as electron beam lithography to have the shape of a small rod or triangle [60]. Plasmonic nanoantennas are able to provide controllable and improved light-matter interactions and strong coupling between localized sources and far-field radiation at the nanoscale [61]. AFM nano-manipulation facilitates the fabrication and the research of nanoantenna. The colloidal nanoparticle can be easily positioned close to another nanoparticle (Fig. 6.13) or coupling to other nanostructures like a waveguide [62]. Bringing the newly formed active nanostructures into the laser focus enables the research of surface plasmon resonance, such as electrical generation of surface plasmon polaritons [63]. The nanoantenna can be used as biosensors for biotechnological applications, such as label-free estimation of DNA hybridization, dynamic quantification of nucleic acid-protein interactions, medical diagnostics, environmental pollution control, insecticide, bacteria, and virus detection [60].

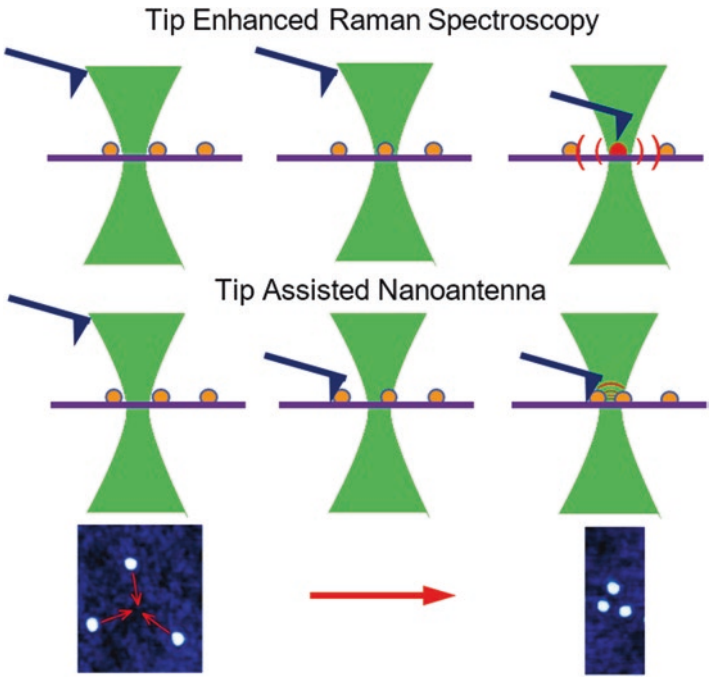

Fig. 6.13 Schematic of the AFM nanomanipulation for tip-enhanced Raman spectroscopy or nanoantenna

4.6 AFM Manipulation – TIRF Microscopy

As aforementioned, the integration of AFM with high-resolution optical techniques has the advantage of dual localization. The localization of the AFM tip in optical microscope view is important for precise specification and controlling the AFM tip for dragging, pushing or pressing an object. The optical microscopy records the process in video rate. The AFM in return gives more information through imaging or fast force mapping. TIRF microscopy enhances image contrast by producing a thin evanescent field in the total internal reflection of excitation light at the glass-sample interface, which has a Z-resolution of 70–200 nm depends on the refractive index [64]. TIRF microscopy is usually used to study the dynamic event in an aqueous environment that is close to a solid substrate. Selective excitation of the surface-bound fluorophores allows TIRF Microscopy to detect single molecule fluorescence.

A recent application example is that Tan et al. use this hyphenated method to resolve the pinning forces of nanobubbles on a substrate [65]. Surface nanobubbles were first generated through a microfluidic channel using solvent exchange protocols (Fig. 6.14a). Nanobubbles were imaged by AFM and TIRF Microscopy simultaneously to assure the location for bubble pulling. After the AFM tip anchored to the

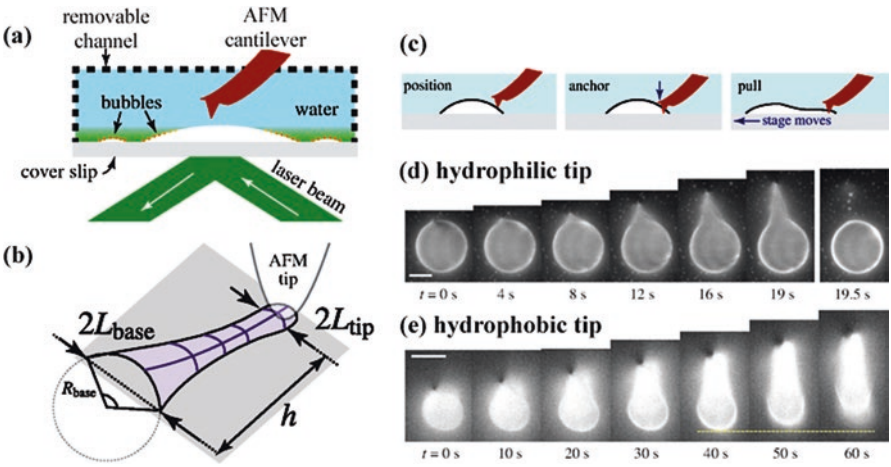

Fig. 6.14 AFM manipulation combined with TIRFM for pulling nanobubbles. (**a**) schematic of setup, bubbles formed inside a microfluidic channel and removed for AFM imaging and manipulation. (**b**) a nanobubble with the stretched neck. (**c**) schematic of AFM manipulation. (**d**) dynamic bubble motion with a hydrophilic tip. (**e**) dynamic bubble motion with a hydrophobic tip. Reprinted with permission from Tan et al. [65] © American Physical Society (2017)

bubble, the bubble-pulling is completed by the stage moving (Fig. 6.14c). Optical images were extracted from the video. The pinning forces can be calculated by a simple equation: $F\,h = \sigma\,\Delta A$, where F is the pinning force, h is the pulling bubble neck, σ is the surface tension, and ΔA is the surface area change due to bubble-pulling. This method opens a window for the study of microbe film, adhesion of cell membrane and biomolecules on the substrates.

5 Prospect and Outlook

The high speed AFM and super-resolution optics combination systems are the experimental setups to fulfil the highest demands on mechanical stability, flexibility, and modularity. A tip scan AFM can be easily combined to inverted optical microscopes. The advantage of the integration is superb time and spatial resolution, and including, but not limited to the aforementioned optics, there are some techniques are under developing and will appeal researchers in the biological research field.

FRET is a highly accurate and sensitive method to determine the nanostructures and interactions between molecules, such as lipids, proteins, DNA, sugars, and other polymers. For experiments at the single-molecule level, donor with fluorophore labelling and acceptor molecules can be bound to a molecular chain. The single molecule can be detected and measured, as both substrate and tip are modified with suitable chemicals. The intramolecular forces and the changes in fluorescence of the donor-acceptor system are measured, when the tip was moved away from the

surface and the molecule was stretched slowly. This combination provides the fundamental information in terms of distance, interactions, structural changes and optical spectroscopy. It has been applied to investigate the morphology of carbon dots and FRET from carbon dots transferred to riboflavin in the biosensor, respectively [66].

Fluorescence Recovery After Photobleaching (FRAP) is a method to determine the diffusion kinetics of a thin molecular film, which contains cells labeled with fluorescent probes through tissue and cells. It is useful in biological studies in protein binding and cell membrane diffusion, and the characterization of surface structure and free energy. High speed AFM can be combined to examine the phase separating structural changes, such as defects, obstructions, lipid condensation and collapse structures of lipid bilayers [67].

Fluorescence-lifetime imaging microscopy (FLIM) is an imaging technology, which is based on the different fluorescence decay rate of a fluorescent sample. Instead of the fluorophore intensity, the lifetime of the signal was used to generate images, which minimized the effect of photon scattering in the thick layers of samples. High speed AFM is combined to obtain the distribution information of biomolecular conformation and structure changes via FRET [68]. For example, FLIM, Fluorescence correlation spectroscopy (FCS) and AFM were applied to characterize the structure of amyloid β protein (Aβ), which is the possible neurotoxic agent in Alzheimer's disease (AD).

Another setup combines the high-resolution of AFM with confocal two-photon fluorescence microscope, which has discriminative power and high sensitivity [69]. This scheme provides the capability of obtaining simultaneous morphology and optical images with high-resolution and sensitivity, and was successfully tested using latex beads loaded with dye. The stacking/unstacking of grana membranes in the envelope-free plant chloroplasts was investigated through this scheme. Furthermore, the combination of AFM and two-photon fluorescence microscope enabled a direct comparison between the signaling protein H-Ras distribution in living cells and the cell morphology, which opens up promising applications in the various research area, such as material and life science.

The combined AFM and optical tweezers (AFM-OT, JPK instruments AG) have high potential in biological studies, molecules manipulation, and nanomechanics. The optical tweezers are able to manipulate small dielectric objects and to measure the extremely small forces in the AFM scanning area [70]. This needs to consider the influence of the AFM laser beam which should be minimized and not affect the laser tweezers. AFM-OT techniques allow dual force measurements and provide a platform to integrate other super-resolution optics STED/PALM/STORM/TIRF or confocal fluorescence microscopy. The new technique achieves more data captured simultaneously and opens up new spectrum applications in dynamic studies of single molecules and living cells. DNA unzipping can be studied using the laser beam to trap a bead attached to DNA hairpin at one end while the AFM tip holding the other end of one strand. If a DNA molecule is attached to two beads at both ends, which are trapped by the laser beams, and the AFM tip is tagged by a DNA enzyme,

the interactions at DNA-enzyme binding can be sensed by both the AFM and the optical tweezer. The AFM-OT techniques can extend to signaling studies. The optical tweezers position a microbead functionalized with signaling molecules close to cells, and the dynamic process is imaged by the AFM tip. On the other hand, the force can be sensed by the optical tweezers when the cell is stimulated or disturbed by the force or temperature from the AFM tip. Using optical tweezers is convenient to manipulate the sample and triggering cellular response, immune response, and infection process. It is reliable to analyze the resulting changes in cellular structure, dynamics, and mechanical properties using fast-scan AFM.

6 Conclusion

The integration of high speed AFM and super-resolution optics provides super spatial and time resolution simultaneous images for biological studies. The combination is more than the sum of the two parts. Both provide complementary information to each other and time resolution is high enough for recording dynamic processes. There is no need to stain, coat, or freeze samples and experiments can be done in ambient or liquids environments. The hyphenated techniques allow fast acquisition of high-resolution morphology, but also obtaining high-resolution optical spectroscopy at the same interested area. Tip-scanning is a preferred choice for the hyphenated techniques for acquiring stable optical images without stress by shaking the cells. Super-resolution optics provide the specific cellular component with a specific individual fluorophore.

Fast force mapping enables probing mechanical properties of cell surfaces and molecular recognition, such as stiffness, elasticity, and adhesion. AFM nanomanipulation and nanolithography assists the fabrications, patterning, and detections at the single-molecule level. The applications of force spectroscopy range from determining intra-interactions by unfolding or stretching of DNA, protein, polysaccharide, and polymers, molecular recognition, to the interactions between DNA-protein, polymer-substrates, and protein-protein.

With the advantage of the precise positioning, the integration of high performance of AFM nanomanipulation and optical spectroscopy pave the way to advanced optical spectroscopy with high spatial resolution. This is important for the fundamental understanding of the fast-changing biological phenomena. These approaches are promising in great applications in a study on a cellular response, immune signaling, drug selection and so on, which significantly further the knowledge about molecular interactions and dynamic processes in living cells. Precise controlling in positioning, high spatial resolution and super time resolution improve the throughput, flexibility, and reproducibility, and attract research interests across the world in the multidisciplinary field.

Acknowledgements H. A. acknowledges the support from the National Key R&D Program of China (2016YFD0400800), and the National Natural Science Foundation of China (NSFC-31470090 and NSFC-31571029). H. Y. acknowledges the financial support by the Singapore Ministry of Education Academic Research Fund Tier 1 (R-143-000-A40-114) and project 31371851 supported by NSFC.

References

1. Huang P, Andersson SB. High speed atomic force microscopy enabled by a sample profile estimator. Appl Phys Lett. 2013;102:213118.
2. Kodera N, Yamamoto D, Ishikawa R, Ando T. Video imaging of walking myosin V by high-speed atomic force microscopy. Nature. 2010;468:72–6.
3. Casuso I, Khao J, Chami M, Paul-Gilloteaux P, Husain M, Duneau J-P, et al. Characterization of the motion of membrane proteins using high-speed atomic force microscopy. Nat Nanotechnol. 2012;7:525–9.
4. Fantner GE, Barbero RJ, Gray DS, Belcher AM. Kinetics of antimicrobial peptide activity measured on individual bacterial cells using high-speed atomic force microscopy. Nat Nanotechnol. 2010;5:280–5.
5. Yang C, Yan J, Dukic M, Hosseini N, Zhao J, Fantner GE. Design of a high-bandwidth tripod scanner for high speed atomic force microscopy. Scanning. 2016;38:889–900.
6. Weisenburger S, Sandoghdar V. Light microscopy: an ongoing contemporary revolution. Contemp Phys. 2015;56:123–43.
7. Fernández-Suárez M, Ting AY. Fluorescent probes for super-resolution imaging in living cells. Nat Rev Mol Cell Biol. 2008;9:929–43.
8. Fantner GE, Schitter G, Kindt JH, Ivanov T, Ivanova K, Patel R, et al. Components for high speed atomic force microscopy. Ultramicroscopy. 2006;106:881–7.
9. Kim BI, Boehm RD. Force-feedback high-speed atomic force microscope for studying large biological systems. Micron. 2012;43:1372–9.
10. Ando T, Uchihashi T, Kodera N. High-speed AFM and applications to biomolecular systems. Annu Rev Biophys. 2013;42:393–414.
11. Mikheikin A, Olsen A, Picco L, Payton O, Mishra B, Gimzewski JK, et al. High-speed atomic force microscopy revealing contamination in DNA purification systems. Anal Chem. 2016;88:2527–32.
12. Sanchez H, Suzuki Y, Yokokawa M, Takeyasu K, Wyman C. Protein–DNA interactions in high speed AFM: single molecule diffusion analysis of human RAD54. Integr Biol. 2011;3:1127–34.
13. Ando T. High-speed atomic force microscopy coming of age. Nanotechnology. 2012;23:062001.
14. Uchihashi T, Iino R, Ando T, Noji H. High-speed atomic force microscopy reveals rotary catalysis of Rotorless F1-ATPase. Science. 2011;333:755–8.
15. Ruan Y, Miyagi A, Wang X, Chami M, Boudker O, Scheuring S. Direct visualization of glutamate transporter elevator mechanism by high-speed AFM. Proc Natl Acad Sci. 2017;114:1584–8.
16. Shim S-H, Xia C, Zhong G, Babcock HP, Vaughan JC, Huang B, et al. Super-resolution fluorescence imaging of organelles in live cells with photoswitchable membrane probes. Proc Natl Acad Sci. 2012;109:13978–83.
17. Suzuki Y, Sakai N, Yoshida A, Uekusa Y, Yagi A, Imaoka Y, et al. High-speed atomic force microscopy combined with inverted optical microscopy for studying cellular events. Sci Rep. 2013;3:2131.

18. Meister A, Gabi M, Behr P, Studer P, Vörös J, Niedermann P, et al. FluidFM: combining atomic force microscopy and Nanofluidics in a universal liquid delivery system for single cell applications and beyond. Nano Lett. 2009;9:2501–7.
19. Uchihashi T, Watanabe H, Fukuda S, Shibata M, Ando T. Functional extension of high-speed AFM for wider biological applications. Ultramicroscopy. 2016;160:182–96.
20. Nievergelt AP, Erickson BW, Hosseini N, Adams JD, Fantner GE. Studying biological membranes with extended range high-speed atomic force microscopy. Sci Rep. 2015;5:11987.
21. Eghiaian F, Rico F, Colom A, Casuso I, Scheuring S. High-speed atomic force microscopy: imaging and force spectroscopy. FEBS Lett. 2014;588:3631–8.
22. Zhou H-T, Gao X, Zheng P, Qin M, Cao Y, Wang W. Mechanical properties of elastomeric proteins studied by single molecule force spectroscopy. Acta Phys Sin. 2016;65:188703.
23. Endo M, Sugiyama H. Single-molecule imaging of dynamic motions of biomolecules in DNA origami nanostructures using high-speed atomic force microscopy. Acc Chem Res. 2014;47:1645–53.
24. Watanabe H, Uchihashi T, Kobashi T, Shibata M, Nishiyama J, Yasuda R, et al. Wide-area scanner for high-speed atomic force microscopy. Rev Sci Instrum. 2013;84:053702.
25. Shibata M, Uchihashi T, Ando T, Yasuda R. Long-tip high-speed atomic force microscopy for nanometer-scale imaging in live cells. Sci Rep. 2015;5:8724.
26. Igarashi K, Uchihashi T, Uchiyama T, Sugimoto H, Wada M, Suzuki K, et al. Two-way traffic of glycoside hydrolase family 18 processive chitinases on crystalline chitin. Nat Commun. 2014;5:3975.
27. Huang B, Bates M, Zhuang X. Super-Resolution Fluorescence Microscopy. Annu Rev Biochem. 2009;78:993–1016.
28. Westphal V, Rizzoli SO, Lauterbach MA, Kamin D, Jahn R, Hell SW. Video-rate far-field optical Nanoscopy dissects synaptic vesicle movement. Science. 2008;320:246–9.
29. Nägerl UV, Willig KI, Hein B, Hell SW, Bonhoeffer T. Live-cell imaging of dendritic spines by STED microscopy. Proc Natl Acad Sci. 2008;105:18982–7.
30. Hell SW, Wichmann J. Breaking the diffraction resolution limit by stimulated emission: stimulated-emission-depletion fluorescence microscopy. Opt Lett. 1994;19:780–2.
31. Klar TA, Jakobs S, Dyba M, Egner A, Hell SW. Fluorescence microscopy with diffraction resolution barrier broken by stimulated emission. Proc Natl Acad Sci. 2000;97:8206–10.
32. Tressler C, Stolle M, Fradin C. Fluorescence correlation spectroscopy with a doughnut-shaped excitation profile as a characterization tool in STED microscopy. Opt Express. 2014;22:31154–66.
33. Harke B, Chacko JV, Haschke H, Canale C, Diaspro A. A novel nanoscopic tool by combining AFM with STED microscopy. Opt Nanosc. 2012;1:3.
34. Rust MJ, Bates M, Zhuang X. Sub-diffraction-limit imaging by stochastic optical reconstruction microscopy (STORM). Nat Methods. 2006;3:793–6.
35. Dickson RM, Cubitt AB, Tsien RY, Moerner WE. On/off blinking and switching behaviour of single molecules of green fluorescent protein. Nature. 1997;388:355.
36. Odermatt PD, Shivanandan A, Deschout H, Jankele R, Nievergelt AP, Feletti L, et al. High-resolution correlative microscopy: bridging the gap between single molecule localization microscopy and atomic force microscopy. Nano Lett. 2015;15:4896–904.
37. Betzig E, Patterson GH, Sougrat R, Lindwasser OW, Olenych S, Bonifacino JS, et al. Imaging intracellular fluorescent proteins at nanometer resolution. Science. 2006;313:1642–5.
38. Wolter S, Schuttpelz M, Tscherepanow M, van de Linde S, Heilemann M, Sauer M. Real-time computation of subdiffraction-resolution fluorescence images. J Microsc. 2010;237:12–22.
39. Hansma HG, Vesenka J, Siegerist C, Kelderman G, Morrett H, Sinsheimer RL, et al. Reproducible imaging and dissection of plasmid DNA under liquid with the atomic force microscope. Science. 1992;256:1180–4.
40. Stark RW, Thalhammer S, Wienberg J, Heckl WM. The AFM as a tool for chromosomal dissection – the influence of physical parameters. Appl Phys A Mater Sci Process. 1998;66:S579–S84.

41. Fotiadis D, Scheuring S, Müller SA, Engel A, Müller DJ. Imaging and manipulation of biological structures with the AFM. Micron. 2002;33:385–97.
42. An H, Guo Y, Zhang X, Zhang Y, Hu J. Nanodissection of single- and double-stranded DNA by atomic force microscopy. J Nanosci Nanotechnol. 2005;5:1656–9.
43. An H, Huang J, Lü M, Li X, Lü J, Li H, et al. Single-base resolution and long-coverage sequencing based on single-molecule nanomanipulation. Nanotechnology. 2007;18:225101.
44. Lü J-h, Li H-k, An H-j, Wang G-h, Wang Y, Li M-q, et al. Positioning isolation and biochemical analysis of single DNA molecules based on Nanomanipulation and single-molecule PCR. J Am Chem Soc. 2004;126:11136–7.
45. Hu J, Zhang Y, Gao H, Li M, Hartmann U. Artificial DNA patterns by mechanical Nanomanipulation. Nano Lett. 2002;2:55–7.
46. Guthold M, Matthews G, Negishi A, Taylor RM, Erie D, Brooks FP, et al. Quantitative manipulation of DNA and viruses with the nanomanipulator scanning force microscope. Surf Interface Anal. 1999;27:437–43.
47. Herman-Bausier P, Formosa-Dague C, Feuillie C, Valotteau C, Dufrêne YF. Forces guiding staphylococcal adhesion. J Struct Biol. 2017;197:65–9.
48. Gould P. Lithography: rewriting the rules. Mater Today. 2003;6:34–9.
49. Li B, Zhang Y, Yan S-H, Lü J-H, Ye M, Li M-q, et al. Positioning scission of single DNA molecules with nonspecific endonuclease based on Nanomanipulation. J Am Chem Soc. 2007;129:6668–9.
50. Neuman KC, Nagy A. Single-molecule force spectroscopy: optical tweezers, magnetic tweezers and atomic force microscopy. Nat Methods. 2008;5:491–505.
51. Hughes ML, Dougan L. The physics of pulling polyproteins: a review of single molecule force spectroscopy using the AFM to study protein unfolding. Rep Prog Phys. 2016;79:076601.
52. Rief M, Oesterhelt F, Heymann B, Gaub HE. Single molecule force spectroscopy on polysaccharides by atomic force microscopy. Science. 1997;275:1295–7.
53. Rief M, Clausen-Schaumann H, Gaub HE. Sequence-dependent mechanics of single DNA molecules. Nat Struct Biol. 1999;6:346–9.
54. Formosa-Dague C, Speziale P, Foster TJ, Geoghegan JA, Dufrêne YF. Zinc-dependent mechanical properties of Staphylococcus aureus biofilm-forming surface protein SasG. Proc Natl Acad Sci. 2016;113:410–5.
55. Eghiaian F, Rigato A, Scheuring S. Structural, mechanical, and dynamical variability of the actin cortex in living cells. Biophys J. 2015;108:1330–40.
56. Alsteens D, Newton R, Schubert R, Martinez-Martin D, Delguste M, Roska B, et al. Nanomechanical mapping of first binding steps of a virus to animal cells. Nat Nanotechnol. 2017;12:177–83.
57. Chacko JV, Canale C, Harke B, Diaspro A. Sub-diffraction Nano manipulation using STED AFM. PLoS One. 2013;8:e66608.
58. Langelüddecke L, Singh P, Deckert V. Exploring the nanoscale: fifteen years of tip-enhanced Raman spectroscopy. Appl Spectrosc. 2015;69:1357–71.
59. Zhang R, Zhang Y, Dong ZC, Jiang S, Zhang C, Chen LG, et al. Chemical mapping of a single molecule by plasmon-enhanced Raman scattering. Nature. 2013;498:82.
60. Sadashivappa G, Sharvari N. Nanoantenna-a review. Int J Renew Energy Technol Res. 2015;4:1–9.
61. Patel SK, Argyropoulos C. Plasmonic nanoantennas: enhancing light-matter interactions at the nanoscale. EPJ Appl Metamater. 2015;2:4.
62. Cohen M, Shavit R, Zalevsky Z. Observing optical Plasmons on a single nanometer scale. Sci Rep. 2014;4:4096.
63. Bigourdan F, Hugonin J-P, Marquier F, Sauvan C, Greffet J-J. Nanoantenna for electrical generation of surface Plasmon Polaritons. Phys Rev Lett. 2016;116:106803.
64. Chan CU, Ohl C-D. Total-internal-reflection-fluorescence microscopy for the study of Nanobubble dynamics. Phys Rev Lett. 2012;109:174501.

65. Tan BH, An H, Ohl C-D. Resolving the pinning force of Nanobubbles with optical microscopy. Phys Rev Lett. 2017;118:054501.
66. Dinç S. A simple and green extraction of carbon dots from sugar beet molasses: biosensor applications. Surg Industry. 2016;141:560–4.
67. Bennun SV, Faller R, Longo ML. Drying and rehydration of DLPC/DSPC symmetric and asymmetric supported lipid bilayers: a combined AFM and fluorescence microscopy study. Langmuir. 2008;24:10371–81.
68. Koh CJ, Lee M. Structural analysis of amyloid aggregates by multifunctional fluorescence nanoscopy. Curr Appl Phys. 2006;6:e257–e60.
69. Gradinaru CC, Martinsson P, Aartsma TJ, Schmidt T. Simultaneous atomic-force and two-photon fluorescence imaging of biological specimens in vivo. Ultramicroscopy. 2004;99:235–45.
70. Pierini F, Zembrzycki K, Nakielski P, Pawłowska S, Kowalewski TA. Atomic force microscopy combined with optical tweezers (AFM/OT). Meas Sci Technol. 2016;27:025904.

Chapter 7
AFM and NSOM/QD Based Direct Molecular Visualization at the Single-Cell Level

Liyun Zhong, Jiye Cai, and Zhengwei Chen

Abstract Cell surface molecules such as receptors play an important role to regulate many essential cellular processes, including cell adhesion, tissue development, cellular communication, inflammation, tumor metastasis, and microbial infection. Specially, these events often involve multimolecular interactions occurring on a nanometer scale, and how to image the distribution and organization of cell surface molecules are becoming increasingly required in Cell and Molecular biology Sciences. By combing atomic force microscopy (AFM), near-field scanning microscopy (NSOM) and quantum dots (QD) labeling, a novel AFM and NSOM/QD-based dual-color nanoscale imaging system is constructed to directly visualize the distribution and organization of these molecules on cell-membrane surface. And this will supply a powerful tool for direct molecular visualization at the single-cell level.

Nanotechnology is emerging as a multidisciplinary tool to advance life science and medicine [1–3]. However, nanoscale imaging or dissecting of functional biologic molecules in cells remain challenging. In the 1980s, the funding of scanning probe microscope, including AFM and NSOM provided an opportunity for imaging single cell on the nanoscale [4, 5]. However, the conventional AFM topographic imaging mode suffers from the lack of biochemical specificity, so single molecule

L. Zhong (✉)
School of Information and Optoelectric Science and Engineering, South China Normal University, Guangzhou, Guangdong, China
e-mail: zhongly@scnu.edu.cn

J. Cai
State Key Laboratory of Quality Research in Chinese Medicines, Macau University of Science and Technology, Macau, China

Department of Chemistry, Jinan University, Jinan, China

Z. Chen
Department of Microbiology and Immunology, Center for Primate Biomedical Research, University of Illinois College of Medicine, Chicago, IL, USA

J. Cai (ed.), *Atomic Force Microscopy in Molecular and Cell Biology*,
https://doi.org/10.1007/978-981-13-1510-7_7

recognition is still difficult. NSOM has proved to be a useful nanotechnology tool for studying hard and flat materials, but its application in biomedical research is limited [6–11]. Complicated natures of cell membranes or biologic molecules make it difficult for NSOM to generate high spatial resolution images. Although NSOM combined with some common fluorescent materials are used for imaging [12, 13], the absence of highly photostable fluorophores for use in NSOM is perhaps one of the major reasons why NSOM has not been reproducibly used for nanoscale imaging of functional cellular molecules.

Recently, researchers have made remarkable progress in the application of NSOM to image the distribution of cell surface molecules [15–22]. Betzig and Trautman first achieved to image nanoscale features of mammalian cell using NSOM in 1992; Enderle et al. directly measured the association of a host and parasite proteins in malaria (Plasmodium falciparum) infected erythrocytes through using dual-color NSOM for the first time [15, 16]. Subsequently, quantum dots (QD) labeling is introduced, and by combing AFM, NSOM and QD labeling, a AFM and NSOM/QD-based nanoscale imaging system was constructed to directly visualize the distribution and organization of these molecules on cell-membrane surface. Specially, this NSOM/QD-based nanoscale imaging can overcome the outstanding problem of photobleaching conventional immune-fluorochromes [23–32] while executing near-field imaging that breaks-through the diffraction limit, and provides highly-reproducible fluorescence imaging with a best optical resolution of 50 nm.

1 AFM and NSOM/QD Based Nanoscale Imaging System

Near-field scanning optical microscopy (NSOM), first developed in the 1980s [6, 7], which and AFM are belong to same scanning probe microscopy family(SPM) in which a small (subwavelength sized) aperture, is placed very close to a fluorescently labeled sample to create a spot of illumination smaller than Rayleigh radius. This spot is then scanned across the sample and fluorescence intensity is recorded as a function of position to produce an image. Since the spot of illumination is very small, the emitted signal correspondingly represents a very small area of the sample and can be resolved much better than the diffraction limit would otherwise allow. In general, the probe consists of a small aperture (30–50 nm in diameter) at the end of a metal-coated tapered optical fiber. And the lateral resolution, down to tens of nanometers, is given by the size of the aperture and the sample-to-probe distance. The probe illuminates the sample with an evanescent field that is strongly localized at the vicinity of the aperture and decreases very rapidly away from the probe's end face. To keep the probe in the near-field region of the sample (<10 nm), an additional feedback loop is required. This is commonly achieved using a shear-force feedback, which in addition generates a topographic image of the sample, the same as AFM, in perfect registry with the optical image.

A NSOM/QD-based dual-color nanoscale imaging is shown in Fig. 7.1 [25]. The continuous wave semiconductor laser is launched into a single mode optical fiber and used as excitation source. Straight, aluminum-coated probe with an aperture

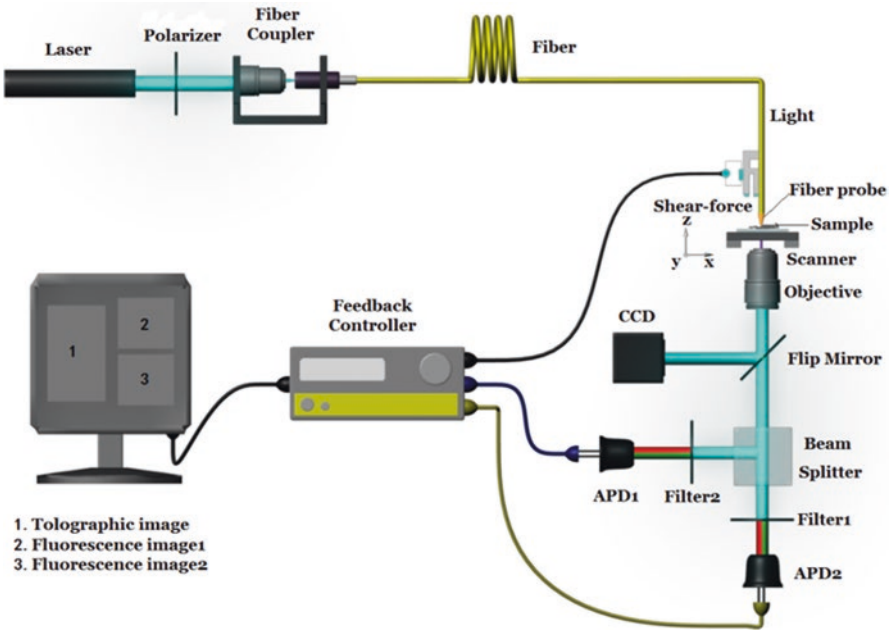

Fig. 7.1 Schematic of dual-color near-field scanning optical microscopy (NSOM). An optical fiber tip with nanoscale aperture is used to scan the sample surface, and then simultaneously generate topographic (AFM) and optical images

diameter of 30–50 nm was used for imaging. It should be noted that no significant difference in full width at the half maximum (FWHM) of fluorescent spots when different probes are used [21, 22]. The probe tip is attached to piezoelectric quartz tuning fork with the resonance frequency of about 90 KHz, and probe-sample distance is maintained constant of 10 nanometers by tuning-fork-based shear-force feedback. This mode of operation will provide simultaneous topographic and optical data, which is collected with an objective and split into two beams by a polarizing cube beam splitter, then detected by two APDs in 0^0 and 90^0, respectively. Two optical filters with different central wavelength are used to separate the fluorescence from the excitation light and the background. The samples are mounted onto the XY stage with full scanning range about 30 um, and a video camera is used to locate the interested regions.

2 Mapping TCRs Nanoclustering and Multimolecular Interactions in T Cell Membranes

T-cell receptors (TCRs) play a crucial role in recognition of antigens and development of immune responses. Whereas immune events for TCR-mediated recognition, signaling, and activation are well described [28–31], nanoscale imaging of

immunobiology of antigenspecific TCR during the in vivo clonal T-cell expansion is still lack. Because TCRs trigger downstream signaling and activation after antigen recognition, some unique TCR nanostructures may develop after TCR contact on Ag/antigen-presenting cell (APC) and thus contribute to selected functions, such as clonal expansion, effector function, contracting (clonal exhaustion), or differentiation. Whereas this presumption can be tested by imaging or visualization of antigen-specific TCR during the in vivo T-cell response, conventional imaging techniques using fluorescent or confocal microscopy do not have nanoscale optical resolution power to reveal individual TCRs and their dynamics during clonal expansion–maturation. Nanotechnology-based imaging may make it possible to reveal TCR nanostructures in the context of T-cell recognition of antigens and therefore provide new insight into T-cell response or ultimately immunity.

The combined NSOM/QD based nanotechnology has been used to perform immunofluorescence imaging of antigen-specific T-cell receptor (TCR) response in an in vivo model of clonal T-cell expansion. Fig. 7.2 presented a NSOM/QD-based single-color nanoscale imaging that Vγ2 Vδ2 TCR arrayed to form high-density TCR nanoclusters, nanodomains and microdomains during the in vivo clonal expansion of Vγ2Vδ2 T cells after HMBPP/IL-2 treatment. It is found that before Ag-induced clonal expansion, those nonstimulating Vγ2Vδ2 TCRs appeared to be distributed differently from their TCR counterparts on the cell surface. Surprisingly, Vγ2Vδ2TCR nanoclusters not only were formed but also sustained on the membrane during an in vivo clonal expansion of Vγ2Vδ2T cells after phosphoantigen treatment or phosphoantigen plus mycobacterial infection. The TCR nanoclusters could array to form nanodomains or microdomains on the membrane of clonally expanded Vγ2Vδ2T cells. Interestingly, the expanded Vγ2Vδ2T cells bearing TCR nanoclusters or nanodomains were able to rerecognize phosphoantigen and to exert better effector function. These studies provided nanoscale insight into the in vivo T-cell immune response.

To further prove that the formation of TCR/CD3 nanodomains was a precondition to induce the immunologic synapse, by using NSOM/QD based dual-color imaging system, Fig. 7.3 showed that CD3, CD4 or CD8 molecules were distinctly distributed as single QD-bound molecules or nano-clusters equivalent to 2–4 QD fluorescence-intensity/size on cell-membrane of un-stimulated primary T cells, and a few CD3 were co-clustering with CD4 or CD8 as nano-clusters without forming nano-domains. The ligation of TCR/CD3 on CD4 or CD8 T cells led to CD3 nanoscale co-clustering or interaction with CD4 or CD8 co-receptors forming nano-domains or micro-domains. Such nano-spatial co-clustering of CD3 and CD4 or CD3 and CD8 appeared to be an intrinsic event of TCR/CD3 ligation, not purely limited to MHC engagement, and be driven by Lck phosphorylation.That is to say, a variety of signalling molecules are recruited to TCR/CD3 nanodomains leading to its signalling amplifies and facilitating T-cell activation.

Also, as shown in Fig. 7.4, it is found that the formation of TCR/CD3 nanodomains wre greatly associated with PKCθ signalling cascades. Since PKCθ was an essential component for inducing TCR/CD3 mediated signalling and IL-2 cytokine production, so the formation of TCR/CD3 nano-domains may involve the cytoskel-

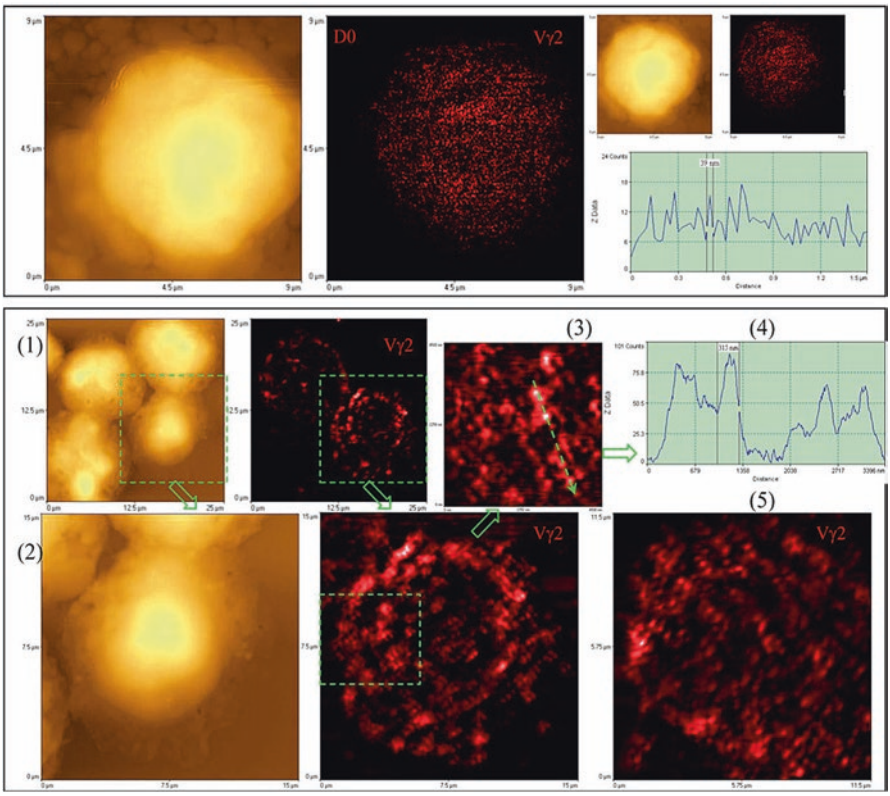

Fig. 7.2 NSOM/QD-based single-color nanoscale imaging showed that Vγ2 Vδ2 TCR arrayed to form high-density TCR nanoclusters, nanodomains and microdomains during the in vivo clonal expansion of Vγ2Vδ2 T cells after HMBPP/IL-2 treatment. Upper panel showed representative NSOM topographic (*left*) and fluorescence (*middle*) images indicating the dominance of non-engaging fluorescence TCR dots on the membrane of unstimulated Vγ2T cells on day 0. The fluorescent intensity profile graph (*right*) was extracted from a random cross section in the fluorescence image (*middle*) showing that predominant fluorescence TCR dots here displayed FWHM of ~50 nm. Lower panel showed representative NSOM images of TCR nanoclusters, nanodomains and microdomains on the membrane of clonally expanded Vγ2 Vδ2 T cells on day 4. (**2**) was enlarged from the boxed area in the low magnification NSOM image (**1**). The fluorescence intensity profile (**4**) is extracted from the cross section part (*dashed arrow*) in (**3**) that is enlarged from the boxed area in (**2**). (**5**) was the NSOM fluorescence image of another activated/expanded Vγ2 Vδ2 T cell collected on day. Reprinted with permission from [24]

etal rearrangement and the recruitment of various signalling molecules into the immunological synapse, and thus would enhance ZAP70 phosphorylation and T cell activation. In contrast, the formation of GM1 nanodomains was associated with PKC$\alpha\beta$ signalling cascades, and while the amount of GM1 nanodomains was decreased, the amount and size of TCR/CD3 nanodomains were remarkably decreased. These findings possibly supported the notion that the formation of GM1 nanodomains indeed served as platforms for the recruitment.

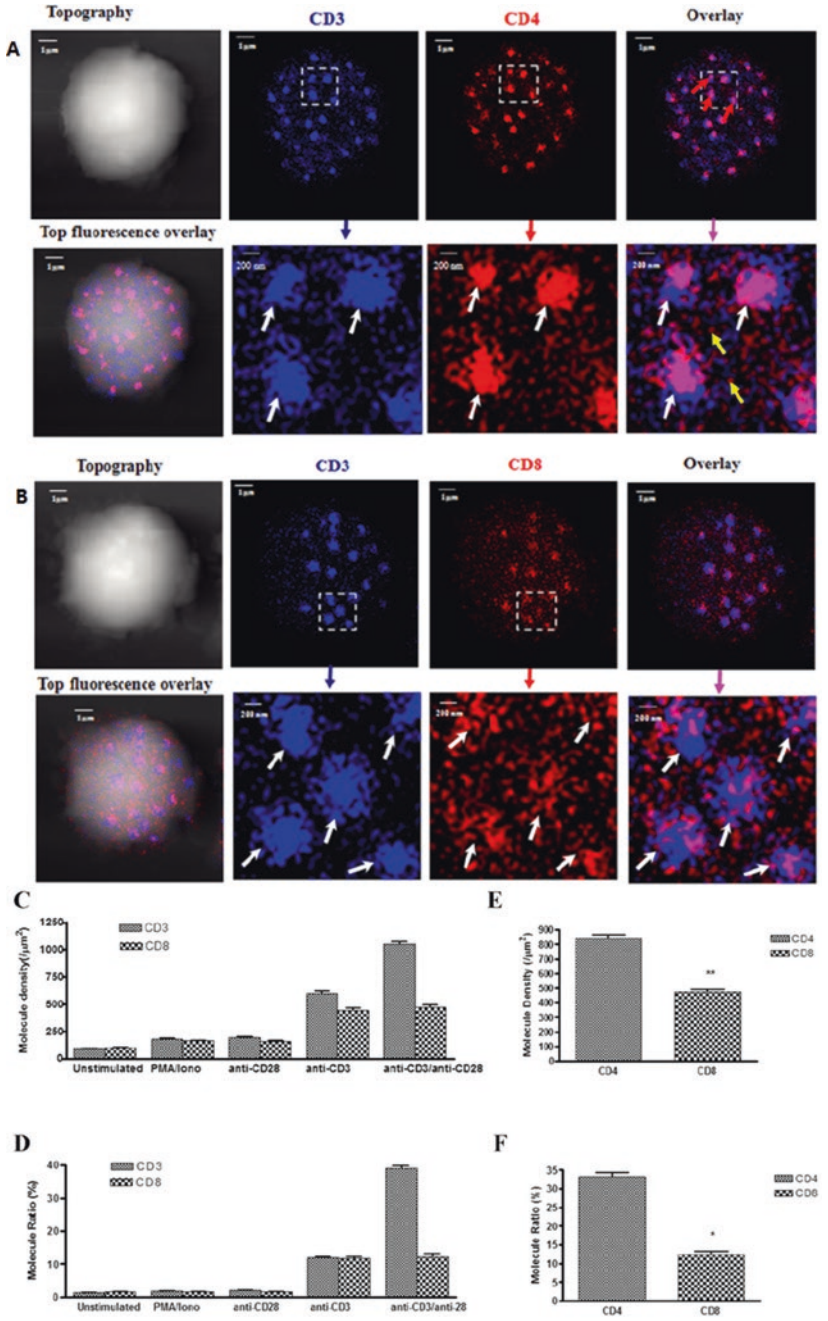

Fig. 7.3 NSOM/QD-based nanoscale two-color imaging directly imaged CD3 co-clustering or interaction with CD4 co-receptor (**a**) or CD8 co-receptor (**b**) after activation of CD4 (or CD8) T cells by anti-CD3/CD28 Ab. Top panel: topographic image of a whole T cell (*left*), two fluorescence images (*middle*); two-color fluorescence overlay images (*right*); Low panel:

3 Visualizing Spatial Distribution of Immunogen Nanoclusters on Vaccine Particles Using NSOM

Moreover, as shown in Fig. 7.5, NSOM/QD-based nanotechnology elucidated nanostructural features of a Y. pestis V immunogen containing particle vaccine capable of eliciting robust response. The obtained result indicated that high-density, high-stability, specific, and immunological pH-responsive loading of immunogen nanoclusters on vaccine particles could readily be presented to the immune system for induction of strong antigen-specific immune responses [26].

4 Nano-Spatial Peak-Valley Polarities of Molecules on Cell-Membrane Fluctuations by Fluorescence-3D Topographic Image Fusion

The activation of T cells involved morphological changes, which included the rearrangement of cell membrane fluctuations relevant to the actin and microtubules cytoskeleton remodeling [33, 34], and the induction of expression for some cell surface molecules such as CD69 (a very early activation antigen, usually regarded as the earliest activation cell surface maker on T cell) and CD71 (a late activation antigen, usually named as membrane glycoprotein transferrin receptor(TfR)). These activation markers participated in cell proliferation and correlate with the degree of immune activation. Recent studies have illustrated that T cells can functionally polarize their actin and microtubules cytoskeleton and some cell surface receptors clustering toward antigen-presenting cells(APCs) to facilitate cell signaling, cell motility and protein uptake [35–40].

An innovated application of NSOM/QD-based nanotechnology through three-dimensional image fusion algorithm to merge the simultaneously-obtained dual-color fluorescence information and three-dimensional topography. This novel imaging system made it possible to visualize nanospatial distribution and organization of early-activation molecules CD69 and late-activation molecules CD71 on cell-membrane fluctuations during T-cell activation. Interestingly, most CD69 molecules were clustered to form 250–500 nm nano-domains polarizing predominantly in the peak of the cell-membrane fluctuations. In contrast, although CD71 molecules

Fig. 7.3 (continued) topography- fluorescence overlay images (*left*), the corresponding zoom images of the areas as indicated by the squares on the top panel (*middle and right*); in which the integration time for all the images was 30 ms with 400*400 scanning lines; (**c**) Molecular-density analysis of CD3, CD8 molecules in stimulated CD8 T cells; (**d**) Molecular number analysis of CD3, CD8 molecules in stimulated CD8 T cells (**e**) Molecule density of CD4 or CD8 in the nano- or micro-domains in the stimulated CD4 or CD8 T cells; (**f**) The percentage numbers of CD4 molecules that arrayed to form nano- or micro-domains in the CD4 T cells or CD8 in the CD8 T cells co-stimulated. Reprinted with permission from [25]

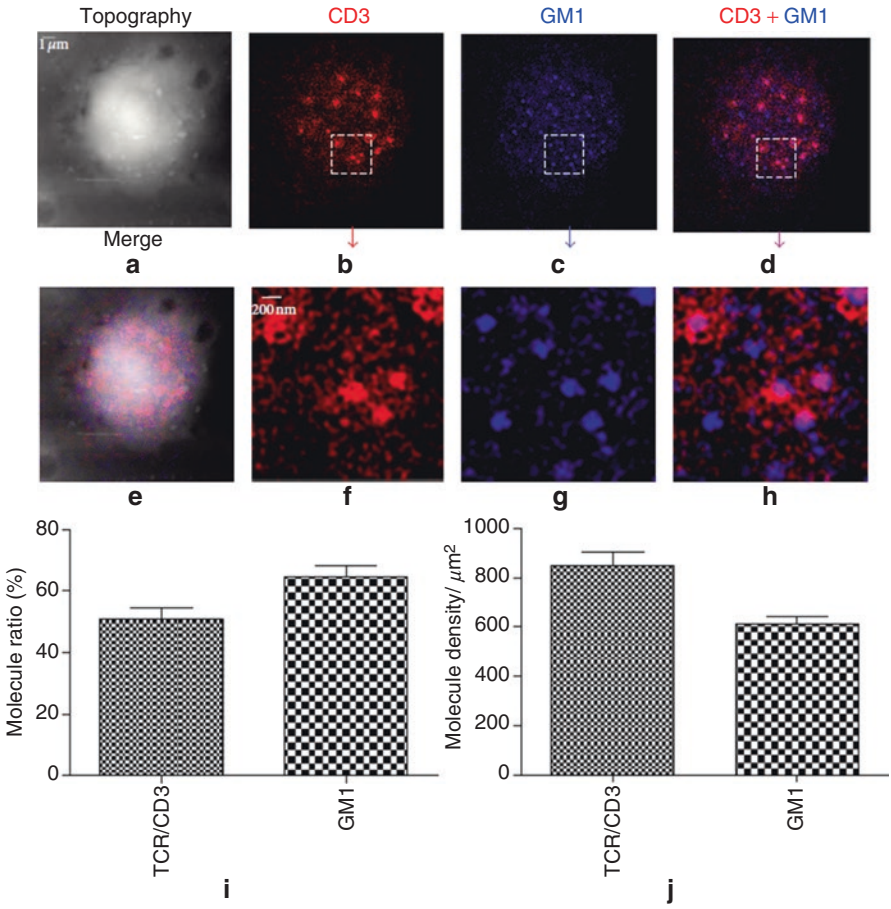

Fig. 7.4 NSOM/QD-based dual-color imaging of CD3 and GM1 for T-cells costimulated with anti-CD3/anti-CD28 Ab. (**a**) T-cell topography; (**b**) fluorescence image of QD-bound CD3 (red); (**c**) fluorescence image of QD-bound GM1 (blue); (**d**) two colour fluorescence merge image; (**e**) Topography-fluorescence merge image; ((**f**), (**g**), (**h**) zoom images of the areas as indicated by the squares on (**b**), (**c**) and (**d**), respectively; (**i**) the percentage numbers of TCR/CD3 or GM1molecules that are arrayed to form nanodomains; (**j**) Molecule density of TCR/CD3 nanodomains or GM1 nanodomains. Scale bars are 1 μm for (**a**), (**b**), (**c**), (**d**) and (**e**) and 200 nm for (**f**), (**g**) and (**h**). Reprinted with permission from [31]

were also clustered as 250–500 nm nano-domains, they polarized dominantly in the valley of the cell-membrane fluctuations. The peak-valley polarities of CD69 nano-domains and CD71 nano-domains implied their different functions. CD69 nano-domains polarizing on membrane-peak fluctuations might serve as transient platforms driving TCR/CD3-induced signaling and activation, whereas CD71 nano-domains distributing in the membrane-valley fluctuations appeared to facilitate iron uptake for increased metabolisms in T-cell activation. Importantly, this NSOM/

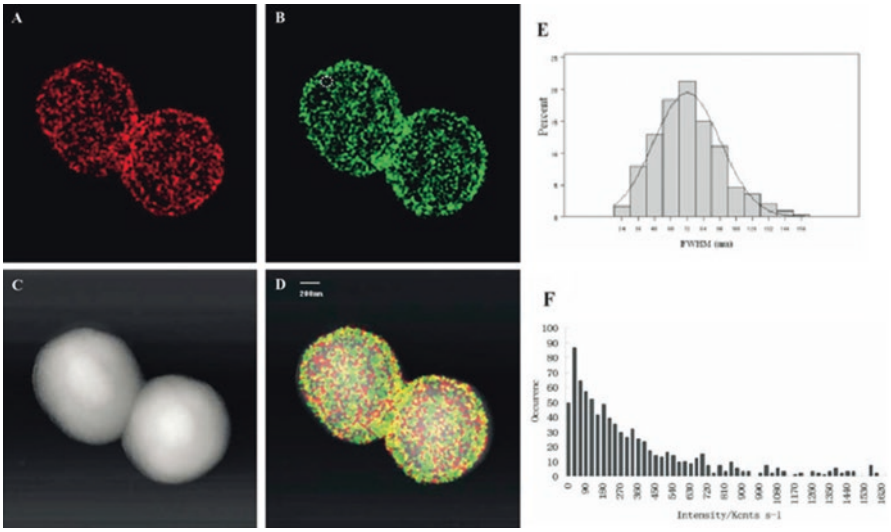

Fig. 7.5 NSOM/QD-based dual-color proteomics imaging shows that majority of V immunogen fused with protein anchor (V-PA) antigen molecules were packed as nanoclusters on the surface of gram positive enhancer matrix (GEM) vaccine particle, (**a**) and (**b**) the 0° versus 90° split emission images for QD-bound V-PA antigen on the surface of GEM particle vaccine, showing the vertical polarization component(0°, **a**) and the horizontal component (90°, **b**); (**c**) topographic imaging of a GEM particle loading V-PA antigen; (**d**) topographic-fluorescent merged image; (**e**) the histogram of FWHM of fluorescent spots; (**f**) the histogram for the intensity distribution of all measured fluorescent spots. Reprinted with permission from [26]

QD-based fluorescence topographic image fusion will provide a powerful tool to visualize nano-spatial distribution of cell surface molecules on cell-membrane fluctuations and enable better understanding of distribution function relationship.

Similarly, NSOM/QD based direct fluorescence-topographic imaging also indicated that GM3 rafts/ nanodomains were localized predominantly on the peaks of microvillus-like protrusions in the apical membrane of GM3 Madin-Darby canine kidney cells, whereas GM1 rafts/nanodomains were distributed mainly on the slope of protrusions or the valleys between protrusions in the plasma membranes of GM1 1 MDCK cells. The data demonstrated that gangliosides polarized not only in a well-known apical-basolateral manner but also in the more microscopic peak-valley manner, implicating unique distribution of GM1 or GM3 in cell-surface fluctuations on the apical membrane of polarized cells. The peak-valley polarities of gangliosides also implicated their different functions relevant to lipid rafts, microvilli, or cellular processes. Importantly, this result demonstrated that the NSOM-based direct fluorescence-topographic imaging is unique and powerful for elucidating nanoscale distribution of specific cell surface molecules in membrane fluctuations.

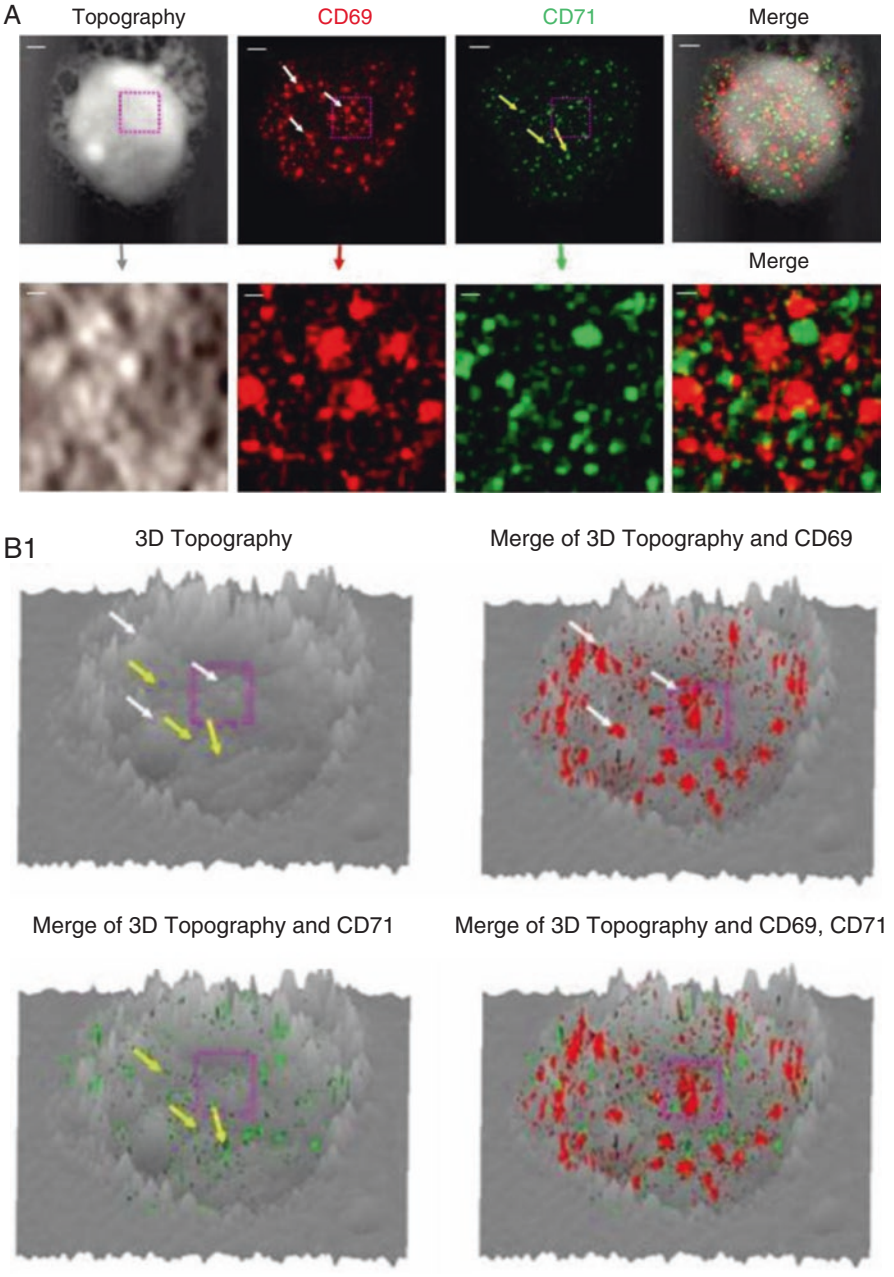

Fig. 7.6 NSOM/QD-based fluorescence-topographic fusion revealed that CD69 were still clustered to form 250–500 nm nanodomains, and polarized predominantly in the peak of the cell membrane fluctuations in medium-term activated T cells, while CD71 were also clustered to form 250–350 nm nano-domains, however polarized predominantly in the valley of the cell membrane fluctuations (**A**) Upper panels showed T cell topography (*left*), fluorescence images of QD-bound CD69 and CD71 (red and green respectively, middle), 2-dimensional topography-fluorescence

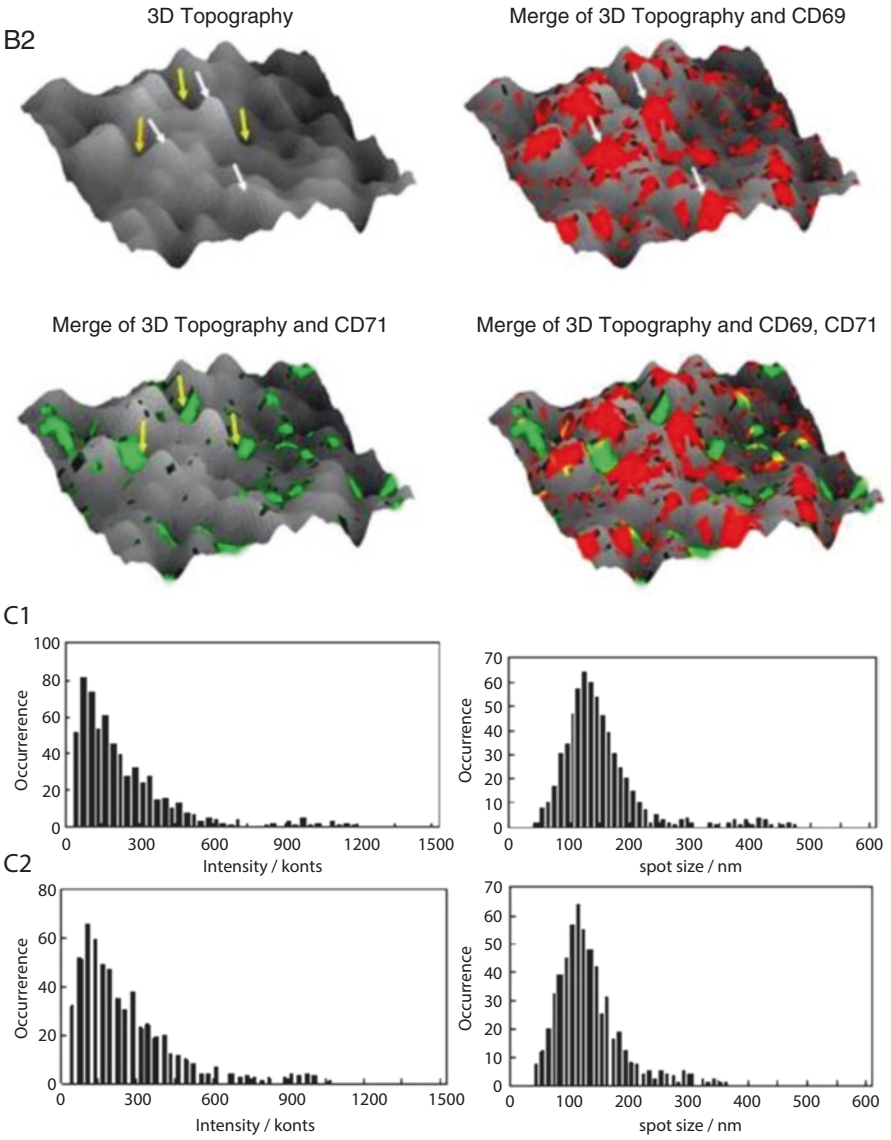

Fig. 7.6 (continued) merge image (*right*). Scale bar 1 μm Lower panels show zoom image of the areas as indicated by the squares on the top panels. Scale bar 200 nm (**B1**) Upper panels showed 3-dimensional images of T cell topography (*left*), CD69 fluorescence-topographic fusion images (*right*); Lower panels showed CD71 fluorescence-topographic fusion images (*left*), dual color of CD69 and CD71fluorescence-topographic fusion image (*right*); (**B2**) Upper panels showed zoom image of the areas as indicated by the squares on the upper panels of **B1**. Lower panels showed zoom image of the areas as indicated by the squares on the lower panels of **B1**. (**C1**) the histograms of frequency distribution of fluorescence intensity (*left*) and size(FWHM) (*right*) of QD-bound CD69 on membrane of T cell; (**C2**) the histogram of frequency distribution of fluorescence intensity (*left*) and size(FWHM) (*right*) of QD-bound CD71 on membrane of T cell. Reprinted with permission from [27]

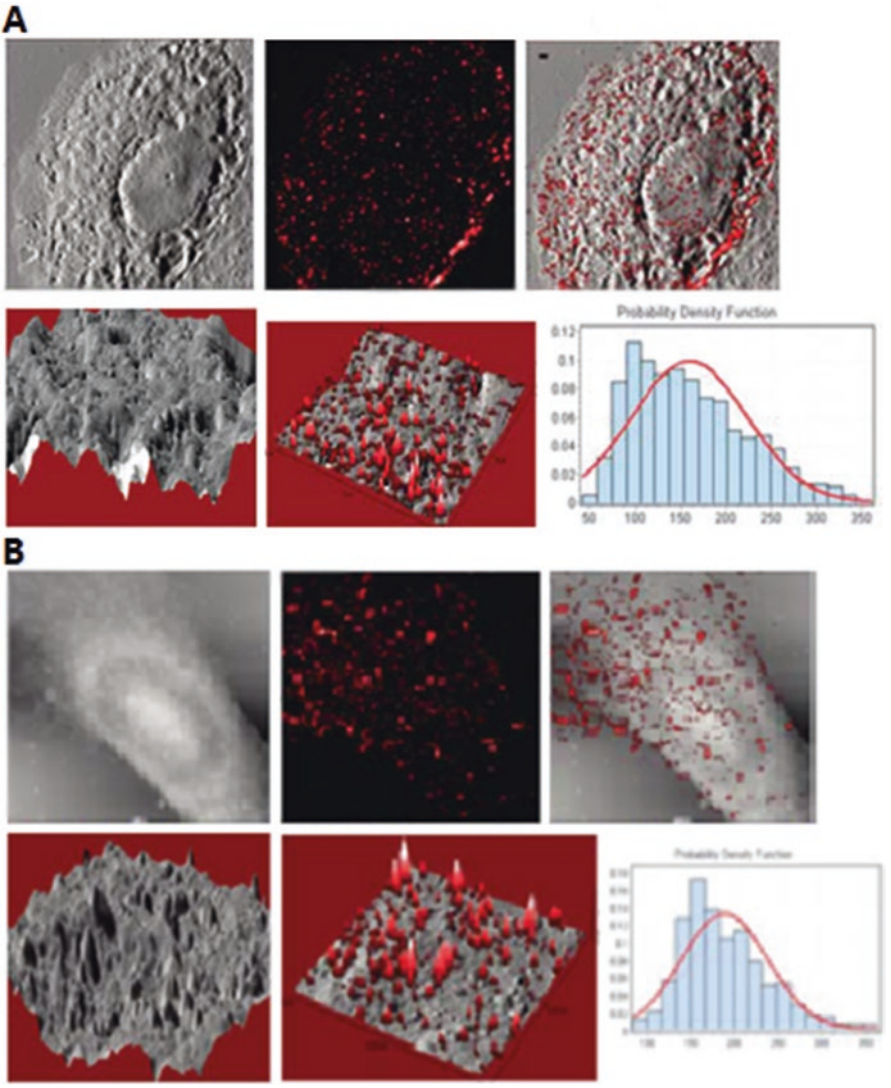

Fig. 7.7 Direct in situ fluorescence-topographic NSOM imaging and quantification of GM1 rafts (**a**) and GM3 rafts (**b**) on cell-membrane fluctuations Top panel: NSOM topographic (*left*), fluorescence (*middle*), and merged images (*right*) of a representative GM11 MDCK cell; Low panel: NSOM topographic three-dimensional (3D) images (left), the NSOM topographic (gray)-fluorescence (red) merged three-dimensional (3D) images (*middle*), the histogram for the diameters of GM1 rafts or GM3 (*right*) Reprinted with permission from [29]

References

1. Delcassian D, Depoil D, Rudnicka D, Liu M, Davis DM, Dustin ML, Dunlop IE. Nanoscale ligand spacing influences receptor triggering in T cells and NK cells. Nano Lett. 2013;13(11):5608–14. https://doi.org/10.1021/nl403252x.
2. Varma R, Campi G, Yokosuka T, Saito T, Dustin ML. T cell receptor-proximal signals are sustained in peripheral microclusters and terminated in the central supramolecular activation cluster. Immunity. 2006;25:117–27.
3. Yokosuka T, Sakata-Sogawa K, Kobayashi W, et al. Newly generated T cell receptor microclusters initiate and sustain T cell activation by recruitment of Zap70 and SLP-76. Nat Immunol. 2005;6:1253–62.
4. Kuo SC, Sheetz MP. Force of single kinesin molecules measured with optical tweezers. Science. 1993;260:232–4.
5. Hu YS, Cang H, Lillemeier BF. Superresolution imaging reveals nanometer- and micrometer-scale spatial distributions of T-cell receptors in lymph nodes. PNAS. 2016;113(26):7201–6. https://doi.org/10.1073/pnas.1512331113.
6. Betzig E., Trautman JK. Near-field optics: microscopy, spectroscopy, and surface modification beyond the diffraction limit. SPIE 1992, 10; 257 (5067):189–195.
7. Betzig E, Trautman JK, Harris TD, Weiner JS, Kostelak RL. Breaking the diffraction barrier: optical microscopy on a nanometric scale. Science. 1991;251(5000):1468–70.
8. Baylis RM, Doak SH, Holton MD, Dunstan PR. Fluorescence imaging and investigations of directly labelled chromosomes using scanning near-field optical microscopy. Ultramicroscopy. 2007;107:308–12.
9. Betzig E, Lewis A, Harootunian A, Isaacson M, Kratschmer E. Near field scanning optical microscopy (NSOM) development and biophysical applications. Biophys J. 1986;49(1):269–79. https://doi.org/10.1016/S0006-3495(86)83640-2.
10. van Zanten TS, Cambi A, Koopman M, Joosten B, Figdor CG, Garcia-Parajo MF. Hotspots of GPI-anchored proteins and integrin nanoclusters function as nucleation sites for cell adhesion. PNAS. 2009;106:18557–62.
11. van Zanten TS, Gomez J, Manzo C, Camb A, Buceta J, Reigada R, Garcia-Parajo MF. Direct mapping of nanoscale compositional connectivity on intact cell membranes. PNAS. 2010;107:15437–41.
12. de Bakker BI, de Lange F, Cambi A, Korterik JP, van Dijk EMHP, van Hulst NF, Figdor CG, García-Parajo MF. Nanoscale organization of the pathogen recognition receptor DC-SIGN mapped by single-molecule high-resolution fluorescence microscopy. ChemPhysChem. 2007;8:1473–80.
13. Herrmann M, Neuberth N, Wissler J, Perez J, Gradl D, Naber A. Near-field optical study of protein transport kinetics at a single nuclear pore. Nano Lett. 2009;9:3330–6.
14. de Bakker BI, Bodnar A, van Dijk EMHP, Vamosi G, Damjanovich S, Waldmann TA, van Hulst NF, Jenei A, Garcia-Parajo MF. Nanometer-scale organization of the alpha subunits of the receptors for IL2 and IL15 in human lymphoma T cells. J Cell Sci. 2008;121:627–33.
15. Enderle T, Ha T, Ogletree DF, Chemla DS, Magowan C, Weiss S. Membrane specific mapping and colocalization of malarial and host skeletal proteins in the Plasmodium falciparum infected erythrocyte by dual-color near-field scanning optical microscopy. PNAS. 1997;94(2):520–5.
16. Enderle T, Ha T, Chemla DS, Weiss S. Near-field fluorescence microscopy of cells. Ultramicroscopy. 1998;71(1–4):303–9.
17. Borger JG, Zamoyska R, Gakamsky DM. Proximity of TCR and its CD8 coreceptor controls sensitivity of T cells. Immunol Lett. 2014;157(1–2):16–22. https://doi.org/10.1016/j.imlet.2013.11.005.
18. Huckabay HA, Armendariz KP, Newhart WH, Wildgen SM, Dunn RC. Near-field scanning optical microscopy for high-resolution membrane studies. Methods Mol Biol. 2013;950:373–94. https://doi.org/10.1007/978-1-62703-137-0_21.

19. Hinterdorfer P, Garcia-Parajo MF, Dufrêne YF. Single-molecule imaging of cell surfaces using near-field nanoscopy. Acc Chem Res. 2012;45(3):327–36. https://doi.org/10.1021/ar2001167.
20. Huckabay HA, Armendariz KP, Newhart WH, Wildgen SM, Dunn RC. Near-field scanning optical microscopy for high-resolution membrane studies. Methods Mol Biol. 2013;950:373–94. https://doi.org/10.1007/978-1-62703-137-0_21.
21. Hinterdorfer P, Garcia-Parajo MF, Dufrene YF. Single-molecule imaging of cell surfaces using near-field nanoscopy. Acc Chem Res. 2012;45(3):327–36. https://doi.org/10.1021/ar2001167.
22. Abeyasinghe N, Kumar S, Sun K, Mansfield JF, Jin R, Goodson T. Enhanced emission from single isolated gold quantum dots investigated using two-photon-excited fluorescence near-field scanning optical microscopy. J Am Chem Soc. 2016;138(50):16299–307. https://doi.org/10.1021/jacs.6b07737.
23. Kelly-Ann DW, Morgan C, Shareen HD, Peter RD. Quantum dots for multiplexed detection and characterisation of prostate cancer cells using a scanning near-field optical microscope. PLoS One. 2013;7(2):e31592. https://doi.org/10.1371/journal.pone.0031592.
24. Chen Y, Shao L, Ali Z, Cai J, Zheng W. ChenNSOM/QD-based nanoscale immunofluorescence imaging of antigen-specific T-cell receptor responses during an in vivo clonal V_2V_2 T-cell expansion. Blood. 2008;11
25. Zhong L, Zeng G, Lu X, Wang RC, Gong G, Yan L, Huang D, Chen ZW. NSOM/QD-based direct visualization of CD3-induced and CD28-enhanced nanospatial coclustering of TCR and coreceptor in nanodomains in T cell activation. PLoS One. 2009;4(6):e5945. https://doi.org/10.1371/journal.pone.0005945.
26. Zeng G, Chen J, Zhong L, Wang R, Jiang L, Cai J, Lin Y, Huang D, Chen CY, Zheng W. Chen1NSOM- and AFM-based nanotechnology elucidates nanostructural and atomic-force features of a Y. pestis V immunogen containing particle vaccine capable of eliciting robust response. Proteomics. 2009;9(6):1538–47. https://doi.org/10.1002/pmic.200800528.
27. Zhong L, Zhang Z, Lu X, Huang D, Chen CY, Wang R, Chen ZW. NSOM/QD-based fluorescence-topographic image fusion directly reveals nano-spatial peak-valley polarities of CD69 and CD71 activation molecules on cell-membrane fluctuations during T-cell activation. Immunol Lett. 2011;140(1–2):44–51. https://doi.org/10.1016/j.imlet.2011.06.003.
28. Fan J, Lu X, Liu S, Zhong L. Nanoscale relationship between CD4 and CD25 of T cells visualized with NSOM/QD-based dual-color imaging system. Nanoscale Res Lett. 2015;10(1):419. https://doi.org/10.1186/s11671-015-1130-x.
29. Chen Y, Qin J, Chen ZW. Fluorescence-topographic NSOM directly visualizes peak-valley polarities of GM1/GM3 rafts in cell membrane fluctuations. J Lipid Res. 2008;49(10):2268–75. https://doi.org/10.1194/jlr.D800031-JLR200.
30. Chen Y, Qin J, Cai J, Chen ZW. Cold induces micro- and nano-scale reorganization of lipid raft markers at mounds of T-cell membrane fluctuations. PLoS One. 2009;4(4):e5386. https://doi.org/10.1371/journal.pone.0005386.
31. Zhong L, Zhang Z, Lu X, Liu S, Chen CY, Chen ZW. NSOM/QD-based visualization of GM1 serving as platforms for TCR/CD3 mediated T-cell activation. Biomed Res Int. 2013;2013:276498. https://doi.org/10.1155/2013/276498.
32. Ke C, Chen J, Guo Y, Chen ZW, Cai J. Migration mechanism of mesenchymal stem cells studied by QD/NSOM. Biochim Biophys Acta. 2015;1848(3):859–68. https://doi.org/10.1016/j.bbamem.2014.12.013.
33. Varma R, Campi G, Yokosuka T, Saito T, Dustin ML. T cell receptor-proximal signals are sustained in peripheral microclusters and terminated in the central supramolecular activation cluster. Immunity. 2006;25:117–27.
34. Yokosuka T, Sakata-Sogawa K, Kobayashi W, et al. Newly generated T cell receptor microclusters initiate and sustain T cell activation by recruitment of Zap70 and SLP-76. Nat Immunol. 2005;6:1253–62.
35. Billadeau DD, Burkhardt JK. Regulation of cytoskeletal dynamics at the immune synapse: new stars join the actin troupe. Traffic. 2006;7:1451–60.

36. Anikeeva N, Lebedeva T, Clapp AR, et al. Quantum dot/peptide-MHC biosensors reveal strong CD8-dependent cooperation between self and viral antigens that augment the T-cell response. PNAS. 2006;103:16846–51.
37. Billadeau DD, Nolz JC, Gomez TS. Regulation of T-cell activation by the cytoskeleton. Nat Rev Immunol. 2007;7:131–43.
38. Tooley AJ, Gilden J, Jacobelli J, Beemiller P, Trimble WS, Kinoshita M, Krummel MF. AmoeboidT lymphocytes require the septin cytoskeleton for cortical integrity and persistent motility. Nat Cell Biol. 2009;11:17–26.
39. Lasserre R, Alcover A. Cytoskeletal cross-talk in the control of T cell antigen receptor signaling. FEBS Lett. 2010;584:4845–50.
40. Manz BN, Groves JT. Spatial organization and signal transduction at intercellular junctions. Nat Rev Mol Cell Biol. 2011;11:342–52.

Chapter 8
Assessment of Pathological or Drug-Dependent Changes in Cell Membrane Morphology and Cell Biomechanical Properties by Atomic Force Microscopy

Hua Jin, Yue Zhao, Wandang Wang, Jinhuan Jiang, Jiye Cai, and Colin E. Evans

Abstract Identification of the nanoscale changes that take place in cell membrane (CM) morphology or cell biomechanical properties (CBPs) in disease states or in response to drug treatment enable for a better understanding of the effects of the drugs on disease pathogenesis and recovery. CM proteins and CBPs have a crucial role in the regulation of many physiological and pathological processes. Direct assessment of the CM and CBPs is therefore useful not only for a better appreciation of cell structure but also for a better understanding of cell pathophysiology. Atomic force microscopy (AFM) is a technique that can be employed to assess CM structure and CBPs at the nanometer scale. In the first part of this chapter, we describe the principles of AFM and appraise its value in the assessment of CM morphology and CBPs. In the second part, we review examples of disease- or drug-dependent changes in CM morphology and CBPs that have been elucidated using AFM.

H. Jin
State Key Laboratory of Quality Research in Chinese Medicines, Macau University of Science and Technology, Macau, China

Feinberg School of Medicine, Northwestern University, Evanston, IL, USA

C. E. Evans
Department of Pediatrics, Feinberg School of Medicine, Northwestern University, Chicago, IL, USA

Y. Zhao · W. Wang · J. Jiang
State Key Laboratory of Quality Research in Chinese Medicines, Macau University of Science and Technology, Macau, China

J. Cai (✉)
State Key Laboratory of Quality Research in Chinese Medicines, Macau University of Science and Technology, Macau, China

Department of Chemistry, Jinan University, Jinan, China
e-mail: tjycai@jnu.edu.cn

J. Cai (ed.), *Atomic Force Microscopy in Molecular and Cell Biology*,
https://doi.org/10.1007/978-981-13-1510-7_8

Keywords Atomic force microscopy · Cell membrane · Nanoscale

1 Introduction

The cell membrane (CM) is the boundary between a cell and its extra-cellular microenvironment. Each membrane contains a variety of proteins that penetrate or span the CM phospholipid bilayer. Multiple protein constituents make up the CM, and these proteins together are suitable for the specialized functions of the cell in its microenvironment [1, 2]. CM plays an important role in not only maintaining cell integrity and controlling the transport of substances in and out of the cell, but also in receiving and sending external chemical signals [3, 4]. Crucially, preserved CM integrity and cell biomechanical properties (CBPs) are basic requirements for the maintenance of a functional cell state. Conversely, CM injury or disruption to CBPs can have immediate and severe consequences [5]. In anoxic injury, for example, the common protein kinase C-mediated cell signaling pathway that triggers damage to the CM, also results in irreversible cell death [6]. Disease-induced disturbance to the CM and its structure can also lead to functional alteration of the membrane, including changes in proliferation, migration, apoptosis, and necrosis. Changes in CM structure [7] and CBPs [8] can directly impair the normal function of healthy cells. Experimental studies have shown, for example, that the morphological and biomechanical properties of cells and CMs are altered in patients with elliptocytosis [9], diabetes [10], or osteoarthritis [11].

Treatments for diseases associated with CM alterations and impaired CBPs will commonly require an effective interaction between the therapeutic agent and the CM, and may aim to induce beneficial changes in the morphological structure of the CM and/or the biomechanical properties of the cell [12]. Changes to the CM morphology and/or CBPs following disease or drug treatment, however, occur at the nanometer level, making reliable assessment of CM integrity and CBPs a non-trivial task. Given that many pathologies are characterized by dysfunctional CM morphology or impaired CBPs, and that some treatments for such diseases aim to restore these variables by directly interacting with the CM, the assessment of disease- or drug-dependent changes in CM morphology and CBPs could aid in the development of novel diagnostic and treatment strategies for diseases associated with CM damage or CBP impairment.

One method that can be used to assess CM morphology and CBPs is atomic force microscopy (AFM), which enables the imaging of biological samples at the nanometer scale [13]. In this chapter, we describe the use of AFM in the assessment of CM morphology and CBPs, which could improve understanding of disease pathologies that involve CM disruption or CBP alteration [14, 15]. We also review examples of AFM studies of disease- or drug-induced alterations in CM morphology and CBPs, which often aim to improve diagnostic and treatment strategies for diseases characterized by aberrant CM morphology or abnormal CBPs.

2 Working Principles and Appraisal of AFM

Traditional microscopic methods to visualize the CM include optical microscopy, scanning electron microscopy (SEM), and transmission electron microscopy (TEM). While these methods can provide detailed information regarding cell structure, they also have their disadvantages [16, 17]. The common optical microscope, for example, is unable to obtain high resolution at a subcellular or nanoscale level. Furthermore, scanning and transmission electron microscopes are suitable for imaging conductive samples, but non-conductive biological samples require coating with conductive materials, which can complicate sample preparation procedures [18, 19].

The advent of AFM in 1986 extended imaging capabilities beyond these techniques, offering new possibilities for visualizing the molecular organization of CM in real time [20, 21]. The atomic force microscope (Fig. 8.1) is in the scanning probe family of microscopes, and consists of a cantilever, a sample stage, and an optical deflection system. The cantilever tip is used to scan the surface of biological samples, which can include tissue or cells in suspension or fixed cells. These tips are typically microfabricated from silicon, silicon nitride, or gold, with a radius of curvature in the order of nanometers (4-20 nm). When the tip approaches the sample surface, adhesion forces between the tip and the sample result in deflection of the cantilever and mounted laser, the signal from which is collected by a photodetector. AFM imaging can be performed in contact or dynamic/intermittent modes. The

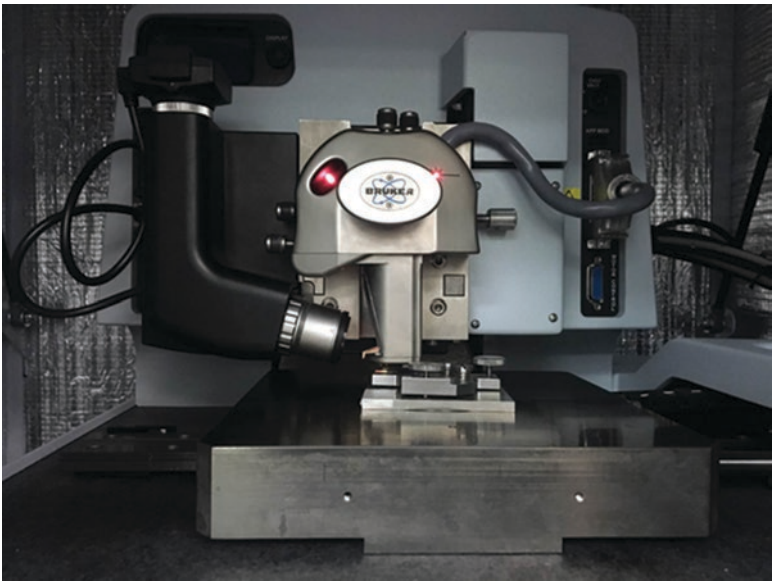

Fig. 8.1 The atomic force microscope
Photograph of an atomic force microscope (Bruker, USA)

most commonly used mode is contact mode, in which force produced by the tip is minimized to prevent sample damage. This can be achieved by adjusting sample height to keep the deflection of the cantilever constant. In dynamic or intermittent mode, an oscillating tip is scanned over the sample surface, meaning interactions between tip and sample vary the cantilever feedback amplitude.

In chemical force microscopy (CFM), single molecular force spectroscopy (SMFS), molecular recognition mapping (MRM), and single-cell force spectroscopy (SCFS), the tip of the atomic force microscope is functionalized by the addition or conjugation of biological molecules or viruses, chemical groups, or even replaced with a living cell. The modified tip is moved towards and away from the biological sample, and the cantilever deflection provides a measurement of interaction force, through generation of force–distance curves (Fig. 8.2). The characteristic adhesion and unbinding forces observed during tip approach and retraction respectively are key parameters that can provide information regarding: spatial distribution of chemical groups (e.g. in CFM); forces involved in cell–cell and cell–substrate interactions (e.g. in SCFS); specific receptor–ligand interactions (e.g. in SMFS); or individual receptors (e.g. in MRM). Lastly, topography and recognition (TREC) imaging is a recently described MRM mode, in which molecular recognition signals are detected during dynamic force microscopy imaging, rather than through the recording of force-distance curves. Importantly, these AFM-based methods can all be used simultaneously with fluorescence microscopes and to assess samples under various physiological conditions.

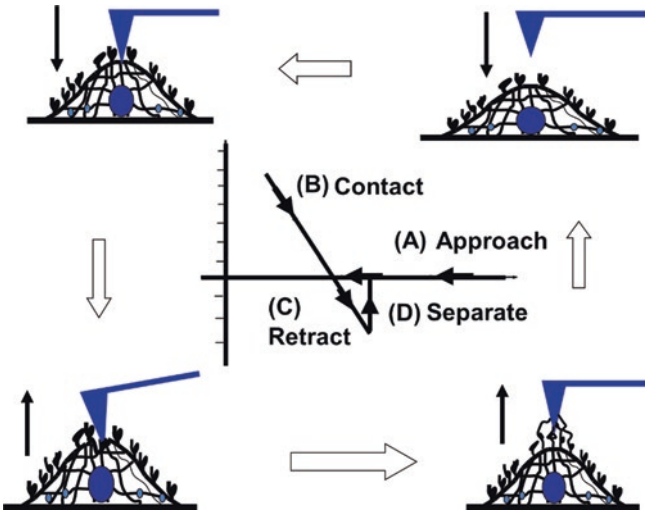

Fig. 8.2 Generation of force-distances curves by AFM
A force–distance curve can be generated by AFM approach-retraction cycles: (**a**) the tip approaches the sample; (**b**) the tip and sample connect; (**c**) the tip retracts from the sample; and (**d**) the tip-sample contact is ruptured. In the schematic curve (middle image), the slope demonstrates the elasticity/stiffness of the cell surface, and the interaction between the sample and the tip surface provides a measurement of the cellular adhesive force

AFM allows high resolution imaging of biological samples in a hydrated environment, enabling real-time investigation of cell structural, interactive, and biomechanical changes [13]. AFM can yield high-resolution information of the 2D and 3D topographic view of cell or tissue specimens with a lateral resolution of 0.5–1.0 nm and a vertical resolution of 0.1–0.2 nm. As such, AFM is a powerful method for visualizing CM structure and CBPs to the level of single nanoscale structures including the cell nuclear pore, CM ion channels, and cell cytoskeletal fibers [22–24]. AFM can also be used to measure intra/intermolecular interactions and structures ([25]). Along with the generation of detailed images of CM and cell structure, the open architecture of AFM allows for integration with complementary assessment tools, and operation under physiologically-relevant environments that can be readily manipulated.

Although AFM has many merits in the investigation of CM and CBPs, still there are some disadvantages that could be addressed in the future. Firstly, AFM can only image a maximum scanning area of ~150x150μm, and a maximum depth of 10-20 μm. Secondly, each scan typically takes 5–30 min to complete, and this relatively slow scanning rate can result in thermal drift, potentially leading to inaccurate measurement of distances between topographical features. Thirdly, AFM images can be affected by nonlinearity, hysteresis, and creep of the piezoelectric material, along with cross-talk between the x, y, and z axes. These caveats may require software enhancement, filtering, real-time correction, and/or the use of closed-loop scanners. Finally, AFM users must be aware of the potential for image artefacts resulting from unsuitable or worn tips or from sub-optimal operating environments.

3 Pathological and Pharmacological Studies Using AFM

AFM enables for the assessment of numerous parameters at nanoscale resolution (Table 8.1), such as cell topography, CM nanostructures [26, 27] and CBPs (e.g., cell surface adhesion force and cell surface elasticity) [7]. In endothelial cells, AFM has been used to assess topographical CM features [28], CM surface receptors [29–31], and CBPs [32, 33], showing the potential of AFM to qualitatively and

Table 8.1 Biological and biomechanical parameters derived by AFM. AFM can be used to obtain a variety of measurements related to CM morphology or CBPs

Category	Parameter	References
CM morphology	CM integrity (e.g. level of CM digestion)	[9, 43]
	Cell size and shape (e.g. elliptical or bi-concave)	[9, 34]
	CM topography (e.g. surface deformations or microridges)	[9, 35]
	CM components (e.g. receptors or microvilli)	[35, 42, 51, 54]
CBPs	Cell surface adhesion	[34, 45, 56, 57]
	Cell surface elasticity/stiffness/softness	[45, 47, 57]

quantitatively study cell structures and biomechanics *ex vivo*. The following part of this chapter describes examples of AFM studies that have been used to assess disease- and drug-dependent alterations in CM morphology and CBPs (for further reading, please see accompanying chapter by Cai et al.).

Evaluation of pathological or drug-induced changes in CM morphology by AFM AFM can be used to visualize CM topography, which enables for spatial characterization of healthy and unhealthy cell types. Such information could be vital from a diagnostic standpoint. Xing et al. [9], for example, observed dramatic surface deformations in the cell surface of erythrocytes from patients with elliptocytosis, despite retention of their typical gross elliptocyte shape. Erythrocytes from patients with anemia are transformed into oval shapes [34], but following therapy, the irregular oval erythrocytes could be seen by AFM to be returned to their regular bi-concave shape. Jin et al. also used AFM to detect erythrocytes that were influence by type II diabetes or aging [10] (e.g., Fig. 8.3). Iyer et al. [35] reported quantitative and qualitative differences between normal and cancerous human cervical epithelial cells by assessing the cell surface microvilli and microridges. Based on these data, a novel AFM method for the *in vitro* detection of cancer cells was proposed [36].

Drug-induced changes in CM morphology can also be assessed using AFM. Fig. 8.4 shows contact mode AFM images of A549 (human lung carcinoma) cell morphology and structure at the nanoscale level. CM structure was visualized before and after drug treatment, to assess alterations in CM topography; in this instance, cells were treated with oridonin, an anti-tumor drug that induces tumor cell apoptosis. Using AFM, Jiye Cai's research team have demonstrated that the morphology of MCF-7 breast cancer cells is markedly altered compared with non-cancer MCF-10A breast cells or following treatment with another anti-tumor and apoptosis-inducing drug, apigenin [37]. Elasticity and non-specific adhesion force of the CM were also decreased, but to a lesser extent. Many drugs need to pass through the CM to reach their site of action. In biomedicine, real-time imaging of drug-dependent changes in CM or CBPs could improve understanding of drug delivery and efficacy, and advance screening programs for the identification of potential therapeutic agents [38, 39]. A comprehensive review of the use of AFM in drug discovery can be found elsewhere [40].

Drug-induced changes in CM morphology have been studied using AFM in a variety of disease states, ranging from cancer to *Pseudomonas aeruginosa* infection [41]. Incubation of mycobacteria with a series of anti-bacterial drugs induced major alterations in cell/CM structure that reflected an inhibition of the synthesis of major cell wall constituents including mycolic acids, arabinans, and structural proteins [42]. Also, time-lapse AFM images of *Staphylococcus aureus* exposed to lysostaphin (an enzyme that cleaves peptidoglycan) revealed a progressive digestion of the cell wall, leading to formation of osmotically-fragile cell types [43].

Identification of pathological or drug-induced alterations in CBPs by AFM CBPs including cell surface adhesion force and cell surface elasticity can be assessed using AFM (Fig. 8.5) [44]. Using AFM, Cross et al. [45] measured CBPs of meta-

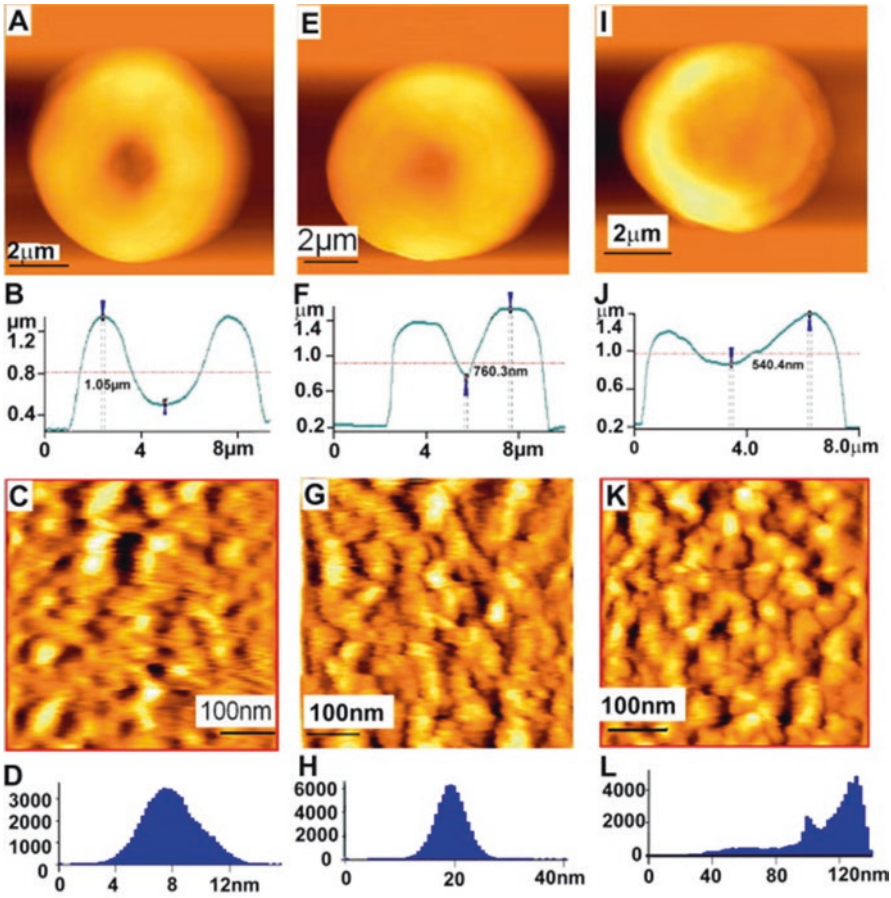

Fig. 8.3 AFM topographic data of young, aged, and diabetic erythrocytes
AFM data of erythrocytes from young (**a**–**d**), aged (**e**–**h**) and diabetic (**i**–**l**) people. Single erythrocytes (**a**, **e**, **i**); height profiles (**b**, **f**, **j**); surface ultrastructures (**c**, **g**, **k**); and histograms of the particle size (**d**, **h**, **l**). Scanning areas: 8 × 8 μm^2 (**a**, **e**, **i**); 500 × 500 nm^2 (**c**, **g**, **k**). Reproduced with permission from Jin et al. [10]

static cancer cells and normal non-cancerous counterparts, and showed that metastatic tumor cells were > 80% softer than benign cells. Cross et al. [45] also quantitatively distinguished cancer cells from normal cells in the same specimen using AFM, by showing that cancer cells were softer than normal cells. Furthermore, the surface adhesion of cancer cells was ~30% lower than normal cells. Zhao et al. [46] used AFM to study the adhesion of single silica beads to normal or malignant cells isolated from human cervix, and found that cell surface adhesion was reduced in malignant versus normal cells. Li et al. [47] measured the elasticity of benign and cancerous human breast epithelial cells using AFM. In their study, elasticity of malignant cells was ~1.5-fold lower than that of non-malignant cells; these authors also showed that elasticity was dependent upon sub-membrane actin organization.

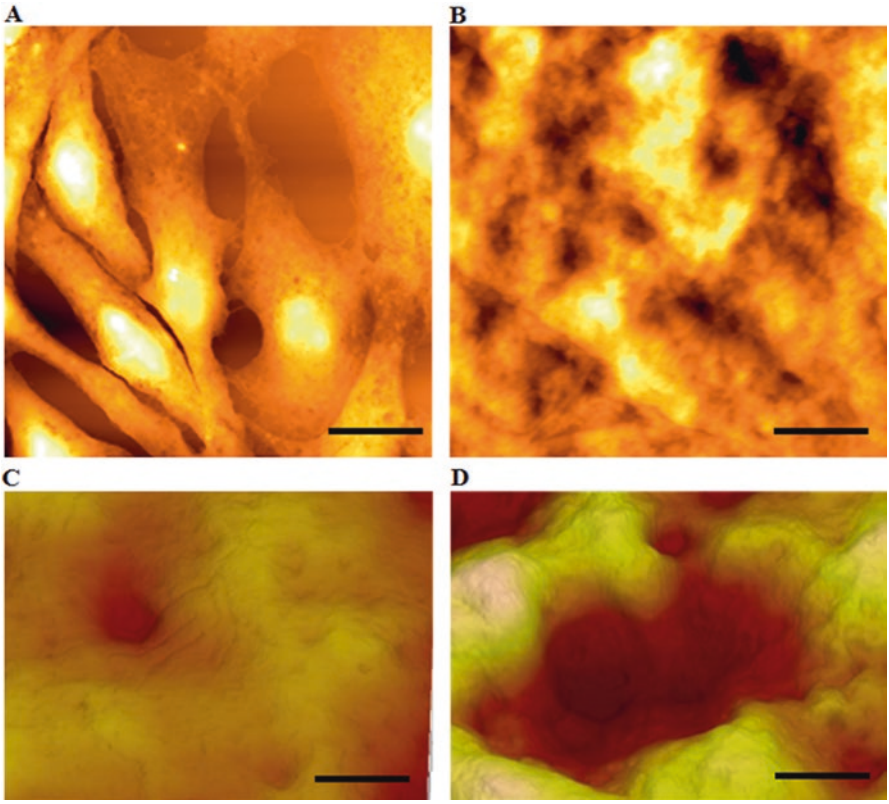

Fig. 8.4 Assessment of cell structure and CM morphology by AFM
Human A549 lung carcinoma cells imaged by AFM at basal state (**a**-**c**) and following treatment with the anti-tumor drug, oridonin (**d**, 50 μm for 24 hrs). Scale bars: (**a**) 20 μm; (**b**) 1 μm; and (**c**, **d**) 0.6 μm

These data together suggest that AFM could be used as a diagnostic tool, given that the ultrastructural and biomechanical parameters measured by AFM often differ between normal and malignant cell types.

As well as cancer diagnosis, authors have suggested that AFM could be used to diagnose viral infections [9] or early stage osteoarthritis [11]. AFM can be used, for instance, to construct force maps that characterize the nanomechanical stiffness of bacterial microorganisms [48]. Furthermore, AFM can be used to observe chemical species [49] or specific receptors [50] on the CM of bacteria, and to assess real-time interactions between antimicrobial agents and bacteria [51]. Using indentation-type AFM, Stolz et al. [11] measured the age-related morphological and biomechanical changes (i.e. cell adhesion force and elasticity) in the hip cartilage of normal and osteoarthritic mice and humans. These authors also speculated that AFM could be developed into a minimally-invasive arthroscopic tool to diagnose the early onset of osteoarthritis by *in situ* assessment.

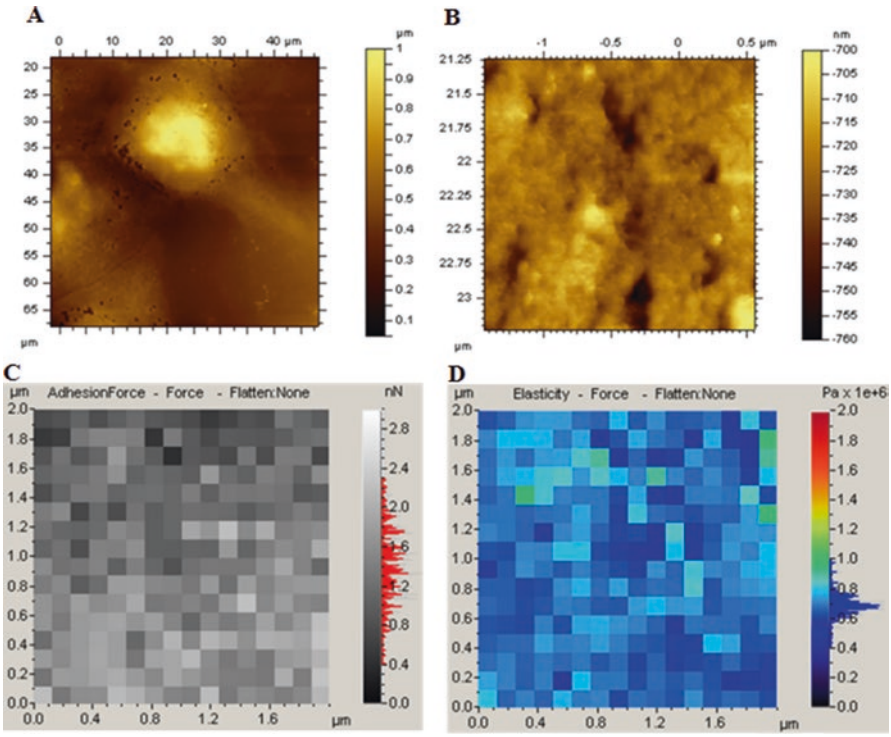

Fig. 8.5 Assessment of CBPs by AFM
Human A549 lung carcinoma cells imaged by AFM at basal state (**a**, **b**) can be used to generate distribution histograms of cell surface adhesion force (**c**) and cell surface elasticity (**d**). For detailed methodological descriptions, see references in Table 8.1 and main text

As mentioned above, morphological, biomechanical, and cytoskeletal changes in cells following drug treatment can be detected using AFM [52, 53] (e.g., Figs 8.6 and 8.7). Furthermore, AFM can be used to explore the potential cytotoxic side effects of drugs in cultured cell lines, cells extracted from patient blood, or cells isolated from patient biopsies [41]. Regarding drug-dependent changes in CBPs, Zuk et al. [32] measured the elasticity of untreated erythrocytes or erythrocytes incubated with aminophylline, which acts through the CM. This study showed that the elasticity of aminophylline-treated erythrocytes was substantially higher compared with untreated cells. Increased elasticity can reduce cell binding to oxygen and impair its transport through capillaries [32]. These data demonstrated that AFM could be used as a nanotool to evaluate the effects or side effects of different therapeutic agents. Other researchers have also investigated the effect of biomaterials or drugs on morphological and biomechanical changes in erythrocytes following treatment with vehicle or drug. Scheuring et al. [31], for instance, imaged the nanoscale morphology of erythrocytes and quantitatively mapped erythrocyte viscosity, which is crucial for cell integrity and function. These authors showed that structural and

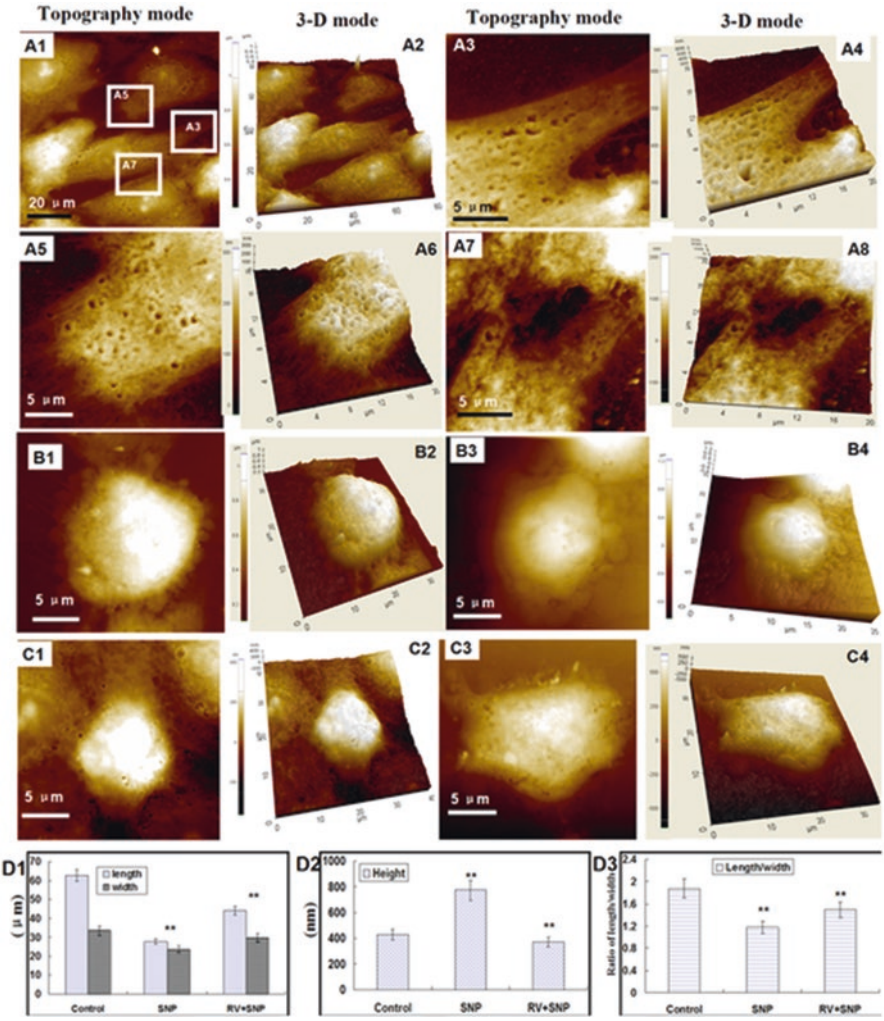

Fig. 8.6 Morphological data of chondrocytes
Control chondrocytes (**A1**–**A2**) with enlargement images of white panes in **A1** (**A3**–**A8**). Chondrocytes treated with 1.5 mM sodium nitroprusside (SNP) for 12 h (**B1**–**B4**). Chondrocytes pretreated with 100 mM of resveratrol (RV) for 24 h, then treated with 1.5 mM of SNP for 12 h (**C1**–**C5**). Histograms of average length and width (**D1**), height (**D2**) and length/width ratio (**D3**). Reproduced with permission from Jin et al. [53]

biomechanical properties of the erythrocyte membrane were indicative of membrane stability.

Changes in CM morphology and cell elasticity/stiffness can be indicative of drug-dependent cell growth. Wang et al. [54] suggested that AFM could represent a rapid and sensitive visual method for studying the impact of different drugs on isolated cancer cells. These authors showed that the anti-cancer drugs, colchicine or

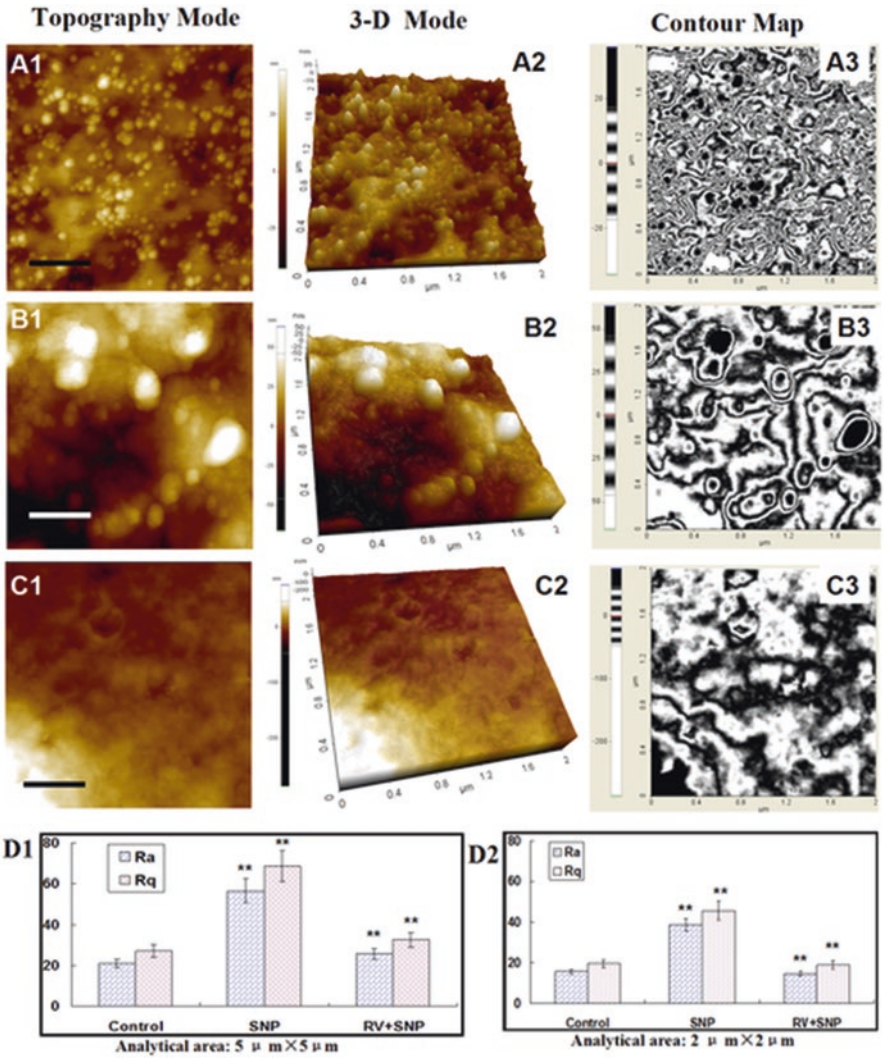

Fig. 8.7 AFM ultrastructural data of chondrocytes
Control chondrocytes (**A1**–**A3**) or chondrocytes treated with 1.5 mM sodium nitroprusside (SNP) for 12 h (**B1**–**B3**). Chondrocytes pretreated with 100 μM of resveratrol (RV) for 24 h, then treated with 1.5 mM of SNP for 12 h (**C1**–**C3**). Scanning area: 2 × 2 μm^2. Topography mode (**A1**, **B1**, **C1**); 3-D mode of **A1**, **B1**, and **C1**, respectively (**A2**, **B2**, **C2**); contour map of **A1**, **B1**, and **C1**, respectively (**A3**, **B3**, **C3**). Histograms of average roughness (Ra) of chondrocytes analyzed in 5 × 5 μm^2 and 2 × 2 μm^2, respectively (**D1**, **D2**). Reproduced with permission from Jin et al. [53]

cytarabine, resulted in changes in the CBPs of liver and cervical cancer cells, including increases in the fluctuation of surface components of the CM and decreases in cell/CM surface components [54], suggesting that drug-dependent early stage apoptosis can be visualized in tumor cells in response to anti-cancer drugs. Cai et al. [55]

employed AFM to detect morphological changes and alterations in adhesion force, elasticity, and stiffness of Jurkat cells exposed to artesunate, and concluded that AFM can be used to estimate the efficacy of this anti-tumor drug.

4 Future Directions and Conclusions

Areas of future research that utilize AFM could include: (i) electrical recording; (ii) microfluidics; (iii) protein misfolding; (iv) parallel integrated cantilevers; (v) identification of target molecules and structures; (vi) comparisons of normal versus diseased cells and tissues; (vii) assessment of therapeutic efficacy; and (viii) development of novel drug nanocarriers [40]. In summary, AFM can be used to measure CBPs and to observe cell/CM structure at the nanometer scale. As a powerful complement to fluorescence and electron microscopy, AFM provides a useful nanotool for the assessment of changes in CM morphology and CBPs that are induced by disease or pharmacological treatment.

References

1. Robertson DS. The physical chemistry of brain and neural cell membranes: an overview. Neurochem Res. 2010;35:681–7.
2. Glushkov VS, Storozhok LF, Panchenko LF, Silina EG. Role of membrane deformations in regulation of functions of cells. Biomed Khim. 2005;51:473–80.
3. Chitemerere TA, Mukanganyama S. Evaluation of cell membrane integrity as a potential antimicrobial target for plant products. BMC Complement Altern Med. 2014;14:278.
4. Klingstrom J, Hardestam J, Stoltz M, Zuber B, Lundkvist A, Linder S, et al. Loss of cell membrane integrity in puumala hantavirus-infected patients correlates with levels of epithelial cell apoptosis and perforin. J Virol. 2006;80:8279–82.
5. Defour A, Sreetama SC, Jaiswal JK. Imaging cell membrane injury and subcellular processes involved in repair. J Vis Exp. 2014**.**
6. Grammas P, Moore P, Cashman RE, Floyd RA. Anoxic injury of endothelial cells causes divergent changes in protein kinase C and protein kinase a signaling pathways. Mol Chem Neuropathol. 1998;33:113–24.
7. Shan Y, Wang H. The structure and function of cell membranes examined by atomic force microscopy and single-molecule force spectroscopy. Chem Soc Rev. 2015;44:3617–38.
8. Dufrene YF, Pelling AE. Force nanoscopy of cell mechanics and cell adhesion. Nanoscale. 2013;5:4094–104.
9. Xing X, Jin H, Lu Y, Wang Q, Pan Y, Cai J, et al. Detection of erythrocytes in patient with elliptocytosis complicating ITP using atomic force microscopy. Micron (Oxford, England: 1993). 2011;42:42–6.
10. Jin H, Xing X, Zhao H, Chen Y, Huang X, Ma S, et al. Detection of erythrocytes influenced by aging and type 2 diabetes using atomic force microscope. Biochem Biophys Res Commun. 2010;391:1698–702.
11. Stolz M, Gottardi R, Raiteri R, Miot S, Martin I, Imer R, et al. Early detection of aging cartilage and osteoarthritis in mice and patient samples using atomic force microscopy. Nat Nanotechnol. 2009;4:186–92.

12. Peng Z, Baena JC, Wang M. Investigations of micron and submicron wear features of diseased human cartilage surfaces. Proc Inst Mech Eng H J Eng Med. 2015;229:164–74.
13. Muller DJ, Dufrene YF. Atomic force microscopy: a nanoscopic window on the cell surface. Trends Cell Biol. 2011;21:461–9.
14. Varady NH, Grodzinsky AJ. Osteoarthritis year in review 2015: mechanics. Osteoarthr Cartil. 2016;24:27–35.
15. Desrochers J, Amrein MA, Matyas JR. Structural and functional changes of the articular surface in a post-traumatic model of early osteoarthritis measured by atomic force microscopy. J Biomech. 2010;43:3091–8.
16. Southam G, Firtel M, Blackford BL, Jericho MH, Xu W, Mulhern PJ, et al. Transmission electron microscopy, scanning tunneling microscopy, and atomic force microscopy of the cell envelope layers of the archaeobacterium Methanospirillum hungatei GP1. J Bacteriol. 1993;175:1946–55.
17. Engel A. Biological applications of scanning probe microscopes. Annu Rev Biophys Biophys Chem. 1991;20:79–108.
18. Francis LW, Gonzalez D, Ryder T, Baer K, Rees M, White JO, et al. Optimized sample preparation for high-resolution AFM characterization of fixed human cells. J Microsc. 2010;240:111–21.
19. Ruozi B, Belletti D, Tombesi A, Tosi G, Bondioli L, Forni F, et al. AFM, ESEM, TEM, and CLSM in liposomal characterization: a comparative study. Int J Nanomedicine. 2011;6:557–63.
20. Radmacher M, Tillamnn RW, Fritz M, Gaub HE. From molecules to cells: imaging soft samples with the atomic force microscope. Science. 1992;257:1900–5.
21. Le Grimellec C, Lesniewska E, Cachia C, Schreiber JP, de Fornel F, Goudonnet JP. Imaging of the membrane surface of MDCK cells by atomic force microscopy. Biophys J. 1994;67:36–41.
22. Usukura E, Narita A, Yagi A, Ito S, Usukura J. An Unroofing method to observe the cytoskeleton directly at molecular resolution using atomic force microscopy. Sci Rep. 2016;6:27472.
23. Hamon L, Curmi PA, Pastre D. High-resolution imaging of microtubules and cytoskeleton structures by atomic force microscopy. Methods Cell Biol. 2010;95:157–74.
24. Berdyyeva T, Woodworth CD, Sokolov I. Visualization of cytoskeletal elements by the atomic force microscope. Ultramicroscopy. 2005;102:189–98.
25. Jarvis SP. Resolving intra- and inter-molecular structure with non-contact atomic force microscopy. Int J Mol Sci. 2015;16:19936–59.
26. Morkvenaite-Vilkonciene I, Ramanaviciene A, Ramanavicius A. Atomic force microscopy as a tool for the investigation of living cells. Medicina (Kaunas, Lithuania). 2013;49:155–64.
27. Kilpatrick JI, Revenko I, Rodriguez BJ. Nanomechanics of cells and biomaterials studied by atomic force microscopy. Adv Healthc Mater. 2015;4:2456–74.
28. Kim KS, Cho CH, Park EK, Jung MH, Yoon KS, Park HK. AFM-detected apoptotic changes in morphology and biophysical property caused by paclitaxel in Ishikawa and HeLa cells. PLoS One. 2012;7:e30066.
29. Liu Z, Jiao Y, Wang T, Zhang Y, Xue W. Interactions between solubilized polymer molecules and blood components. J Control Release. 2012;160:14–24.
30. Liu Z, Janzen J, Brooks DE. Adsorption of amphiphilic hyperbranched polyglycerol derivatives onto human red blood cells. Biomaterials. 2010;31:3364–73.
31. Picas L, Rico F, Deforet M, Scheuring S. Structural and mechanical heterogeneity of the erythrocyte membrane reveals hallmarks of membrane stability. ACS Nano. 2013;7:1054–63.
32. Zuk A, Targosz-Korecka M, Szymonski M. Effect of selected drugs used in asthma treatment on morphology and elastic properties of red blood cells. Int J Nanomedicine. 2011;6:249–57.
33. Zhong D, Jiao Y, Zhang Y, Zhang W, Li N, Zuo Q, et al. Effects of the gene carrier polyethyleneimines on structure and function of blood components. Biomaterials. 2013;34:294–305.
34. Zhang Y, Zhang W, Wang S, Wang C, Xie J, Chen X, et al. Detection of erythrocytes in patient with iron deficiency anemia using atomic force microscopy. Scanning. 2012;34:215–20.

35. Iyer S, Gaikwad RM, Subba-Rao V, Woodworth CD, Sokolov I. Atomic force microscopy detects differences in the surface brush of normal and cancerous cells. Nat Nanotechnol. 2009;4:389–93.
36. Iyer S, Woodworth CD, Gaikwad RM, Kievsky YY, Sokolov I. Towards nonspecific detection of malignant cervical cells with fluorescent silica beads. Small (Weinheim an der Bergstrasse, Germany). 2009;5:2277–84.
37. Bai H, Jin H, Yang F, Zhu H, Cai J. Apigenin induced MCF-7 cell apoptosis-associated reactive oxygen species. Scanning. 2014;36:622–31.
38. Ushiki T. Atomic force microscopy and its related techniques in biomedicine. Ital J Anat Embryol = Archivio italiano di anatomia ed embriologia. 2001;106:3–8.
39. Choi S, Jung GB, Kim KS, Lee GJ, Park HK. Medical applications of atomic force microscopy and Raman spectroscopy. J Nanosci Nanotechnol. 2014;14:71–97.
40. Lal R, Arnsdorf MF. Multidimensional atomic force microscopy for drug discovery: a versatile tool for defining targets, designing therapeutics and monitoring their efficacy. Life Sci. 2010;86:545–62.
41. Pillet F, Chopinet L, Formosa C, Dague E. Atomic force microscopy and pharmacology: from microbiology to cancerology. Biochim Biophys Acta. 1840;2014:1028–50.
42. Alsteens D, Verbelen C, Dague E, Raze D, Baulard AR, Dufrene YF. Organization of the mycobacterial cell wall: a nanoscale view. Pflugers Arch. 2008;456:117–25.
43. Francius G, Domenech O, Mingeot-Leclercq MP, Dufrene YF. Direct observation of Staphylococcus aureus cell wall digestion by lysostaphin. J Bacteriol. 2008;190:7904–9.
44. Haase K, Pelling AE. Investigating cell mechanics with atomic force microscopy. J R Soc Interface. 2015;12:20140970.
45. Cross SE, Jin YS, Tondre J, Wong R, Rao J, Gimzewski JK. AFM-based analysis of human metastatic cancer cells. Nanotechnology. 2008;19:384003.
46. Zhao X, Zhong Y, Ye T, Wang D, Mao B. Discrimination between cervical Cancer cells and normal cervical cells based on longitudinal elasticity using atomic force microscopy. Nanoscale Res Lett. 2015;10:482.
47. Li QS, Lee GY, Ong CN, Lim CT. AFM indentation study of breast cancer cells. Biochem Biophys Res Commun. 2008;374:609–13.
48. Dufrene YF. Towards nanomicrobiology using atomic force microscopy. Nat Rev Microbiol. 2008;6:674–80.
49. Sugimoto Y, Pou P, Abe M, Jelinek P, Perez R, Morita S, et al. Chemical identification of individual surface atoms by atomic force microscopy. Nature. 2007;446:64–7.
50. Whited AM, Park PS. Atomic force microscopy: a multifaceted tool to study membrane proteins and their interactions with ligands. Biochim Biophys Acta. 1838;2014:56–68.
51. Longo G, Kasas S. Effects of antibacterial agents and drugs monitored by atomic force microscopy. Wiley Interdiscip Rev Nanomed Nanobiotechnol. 2014;6:230–44.
52. Jung SH, Park JY, Yoo JO, Shin I, Kim YM, Ha KS. Identification and ultrastructural imaging of photodynamic therapy-induced microfilaments by atomic force microscopy. Ultramicroscopy. 2009;109:1428–34.
53. Jin H, Liang Q, Chen T, Wang X. Resveratrol protects chondrocytes from apoptosis via altering the ultrastructural and biomechanical properties: an AFM study. PLoS One. 2014;9:e91611.
54. Wang J, Wan Z, Liu W, Li L, Ren L, Wang X, et al. Atomic force microscope study of tumor cell membranes following treatment with anti-cancer drugs. Biosens Bioelectron. 2009;25:721–7.
55. Cai X, Gao S, Cai J, Wu Y, Deng H. Artesunate induced morphological and mechanical changes of Jurkat cell studied by AFM. Scanning. 2009;31:83–9.
56. Muller DJ, Dufrene YF. Atomic force microscopy as a multifunctional molecular toolbox in nanobiotechnology. Nat Nanotechnol. 2008;3:261–9.
57. Zemla J, Danilkiewicz J, Orzechowska B, Pabijan J, Seweryn S. Lekka M. Semin Cell Dev Biol: Atomic force microscopy as a tool for assessing the cellular elasticity and adhesiveness to identify cancer cells and tissues; 2017.

Chapter 9
In Situ Measuring Mechanical Properties of Normal and Disease Cells

Sui-Ping Deng, Yi-Li Yang, Xing-Xing Cheng, Wen-Rong Li, and Jiye Cai

Abstract Atomic force microscopy (AFM) has recently made great progress in mapping local mechanical properties of a single cell including living cell. These mechanical properties can provide not only cellular nano- and micro-structure, but also physiological and pathological information of cells. Here, the recent applications of AFM for the study of mechanical characteristics of normal cells and disease cells are reviewed.

Recently, the mechanical characteristics of cells have gained increasing attention. Cell mechanics can contribute a more detailed understanding of how underlying molecular and architectural changes evolve with cell-state and disease processes at the single cell level [1–4]. The mechanical properties correlate with extensive biological processes such as cell adherence, migration, differentiation and proliferation, etc. [5–9]. Any abnormal changes in the mechanical properties of cells may lead to diseases via alterations of cell physiology [10, 11]. Thus, these mechanical characteristics have promising biomedical applications for recognizing cellular conditions and clinical diagnosis of human health.

Cell mechanics may also serve as a marker for diseases. A recent evidence shows that changes in the mechanical properties of living cells are associated with disease development, such as inflammation, cancer [12] and muscular dystrophies [13], though the exact underlying mechanisms remain to be uncovered.

Elasticity and stiffness are typical mechanical properties of a single cell. The elasticity of a material is its ability to recover to its original size, shape and condition from stress. Stiffness is the rigidity of a substance in response to an applied force. Elasticity and stiffness are important factors in modulating cell functions [14,

S.-P. Deng (✉) · Y.-L. Yang · X.-X. Cheng · W.-R. Li
Department of Chemistry, College of Chemistry and Materials Science, Jinan University, Guangzhou, People's Republic of China
e-mail: tspdeng@jnu.edu.cn

J. Cai (✉)
State Key Laboratory of Quality Research in Chinese Medicines, Macau University of Science and Technology, Macau, China

Department of Chemistry, Jinan University, Jinan, China
e-mail: tjycai@jnu.edu.cn

J. Cai (ed.), *Atomic Force Microscopy in Molecular and Cell Biology*,
https://doi.org/10.1007/978-981-13-1510-7_9

15]. The modulus of elasticity (E) is also called Young's modulus. Young's modulus is the measurement of a material's stiffness, and it is used to compare the stiffness of different biological samples.

In the last several years, atomic force microscopy (AFM) is applied to measure the mechanical properties of a single cell in physiological state. The AFM technique has some outstanding benefits for biological research. First, AFM can observe nano- and microstructures of living cells and cell organelles in their physiological environment, that is, in buffer solutions and at room temperature. It is a vital advantage over the light microscopy and electron microscopy [16, 17]. Second, AFM can be used to simultaneously evaluate the surface morphology and local nanomechanical properties of living cells with high resolutions [16, 18]. Third, after functioning with specific molecules, the tip of AFM can be used to quantify the interaction force between single ligand and its receptor on cell surface, either in vitro or in vivo [19, 20].

Here, some mechanical research by AFM on normal cells and disease cells from several kinds of human diseases, such as cancer, erythrocyte-related diseases, are reviewed. The results may help shed light on the pathogenesis mechanisms of such diseases, and contribute to early diagnosis and clinical treatment.

1 Cancer

By AFM characterization of normal and cancer cells, the mechanical measurements of AFM have shown that normal cells are stiffer than cancer cells (Table 9.1). In spite of cancer types, it seems that this conclusion is commonly found in many studies [21]. It's suggested that the difference in cell elasticity is due to different organization of membrane actin structures. And these measurements can also identify the different cancerous stage. However, few clinical doctors regard AFM technique as an alternative way to assess pre-cancerous and cancerous changes. This is due to the complicated structures and heterogeneous properties of tumours.

Lim et al. [22] have shown clear stiffness of human breast biopsies under physiological conditions by using AFM. The results disclose distinct mechanical profiles that help define the different process of cancer. Compared with normal cells, relevant stiffness maps of cancer cells reveal that the transformation from healthy tissue to malignant tumor is accompanied by notable cell softening. In Fig. 9.1, heterogeneous stiffness distribution is shown for malignant tumour tissue, and the predominant peak of Young's modulus is 0.6 kPa, which is lower than that for normal tissue (1.1 kPa). Moreover, it was further proved by the later report about the Young's modulus among healthy and cancerous tissues of breast. Tafazzoli-Shadpour et al. [23] demonstrated that cancerous tissues are almost twice softer than healthy tissues at the center of tissue samples. They assumed these centers were related to the cellular zone of breast tissue. But there was no significant difference on stiffness between healthy and cancerous tissues ($P > 0.05$) when intermediate and fibrous regions of tissue samples were taken into account. However, the relevant mechanisms

Table 9.1 Difference in mechanical properties between normal and cancer cells

Organ	Normal cell	Average Young's modulus (kPa)	Cancer cell	Average Young's modulus (kPa)	Refs.
Breast	Normal tissue	1.1–1.8	Malignant tissue	0.6, 2.0, 5.8	[22]
	Normal tissue	1.427[a]	Malignant tissue	0.709[a]	[23]
	MCF-10A	0.5–1.16	MCF-7	0.31–0.61	[26]
	MCF-10A	0.7[b]	MCF-7	0.5[b]	[25]
			MDA-MB-231	0.3[b]	[25]
	MCF-10A	250[c]	MCF-7	28[c]	[25]
			MDA-MB-231	25[c]	[25]
Ovary	IOSE	2.472	HEY HEY A8 OVCAR-3 OVCAR-4	0.884 0.494 0.576 1.120	[29] [29] [29] [29]
Thyroid	S748(primary)	2.211–6.879	S277(primary)	1.189–1.365	[28]
			FTC-133 LRP-1(−) FTC-133 LRP-1(+)	13.39 5.26	[32] [32]
	S747(primary)	1.2–2.6	S277(anaplastic)	1.3	[37]
Osteogen	NHOst	2.42	MG-63	0.82	[66]
			U-2 OS	2.0–2.8(nucleus) 3.5–4.4(periphery)	[7] [7]
Cervix	Primary cell	2.05	Primary cell	2.8	[35]
Kidney	RC-124	1.2–2.1[d]	A498	1–1.2[d]	[36]
			ACHN	1–1.9[d]	[36]
Blood	Lymphocyte	1.24 ± 0.09	Jurkat	0.51 ± 0.06	[33, 34]

[a]Values obtained at the center of tissue samples
[b]Low loading-rate indentation at 1 Hz
[c]High loading-rate indentation at 250 Hz
[d]Cells on soft hydrogel instead of hard substrate

of these changes in stiffness remain to be elucidated. It could be in connection with high density of collagen fibers in the breast tissue [24]. Furthermore, such results are in agreement with other reports. The mean moduli of non-malignant breast cells (MCF-10A), malignant breast cells (MCF-7 and MDA-MB-231) are 0.7, 0.5, 0.3 kPa repectively, when AFM was operated with a low loading-rate indentation at 1 Hz. Yet these moduli increased to 250, 28, 25 kPa repectively, when AFM was operated with a high loading-rate indentation at 250 Hz in Fig. 9.2 [25]. Notably, earlier report also showed different values that the Young's modulus of MCF-7 were significantly lower (1.4–1.8 folds) than that of MCF-10A [26]. All of these measurements were done with living breast cells at a single cell level and in a natural environment. The reason for the inconsistent values is due largely to the diverse conditions of measurement and sample preparations in each research group. For example, the cells in different numbers of passage [27] or different cultivation peri-

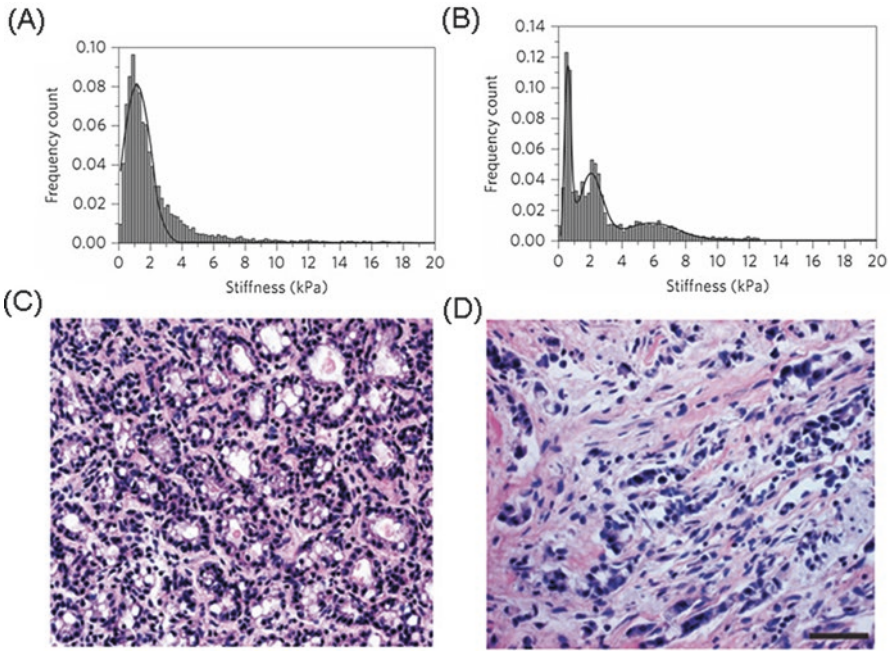

Fig. 9.1 Stiffness of normal mammary gland tissue (**a**) and malignant tumour tissue (**b**). H&E-stained section of normal mammary gland tissue (**c**) and malignant tumour tissue (**d**). Scale bar: 50 μm [22]

ods [28] have various mechanical properties. Although the moduli are not completely identical, the general trend is unalterable that normal cells have higher modulus. Therefore, it is suggested that Young's modulus can be regarded as a promising indicator for cancer diagnosis.

It is remarkable that breast tissue has characteristic nanomechanical behaviours. Therefore, similar mechanical properties may be found in other cancers. In Fig. 9.3, Prabhune et al. [28] reported that cancerous thyroid cells are 3- to 5-times softer than normal thyroid cells because of the different organization of actin cytoskeleton in malignant cells.

And cell stiffness could be considered as an indicator for the relative metastatic potential of cancerous cells. It's suggested that relative stiffness is in inverse relation to the migratory potential. The changes of overall mechanical properties of cells could reflect cancer metastasis. Sulchek et al. [29] measured the Young's modulus for a series of ovarian epithelial cell lines. The results showed that normal ovarian epithelial cells (IOSE) were the stiffest compared with other ovarian cancer cell lines (HEY, HEY A8, OVCAR-3 and OVCAR-4). The mean stiffness values for these cell lines are 2.472, 0.884, 0.494, 0.576, 1.120 kPa, respectively. And less stiffer cells exhibited high invasiveness. Such tendency is proved by the studies using other types of epithelial cancer cells [30, 31]. It's due to actin cytoskeleton reorganization and/or disruption, and in relation to low-density lipoprotein

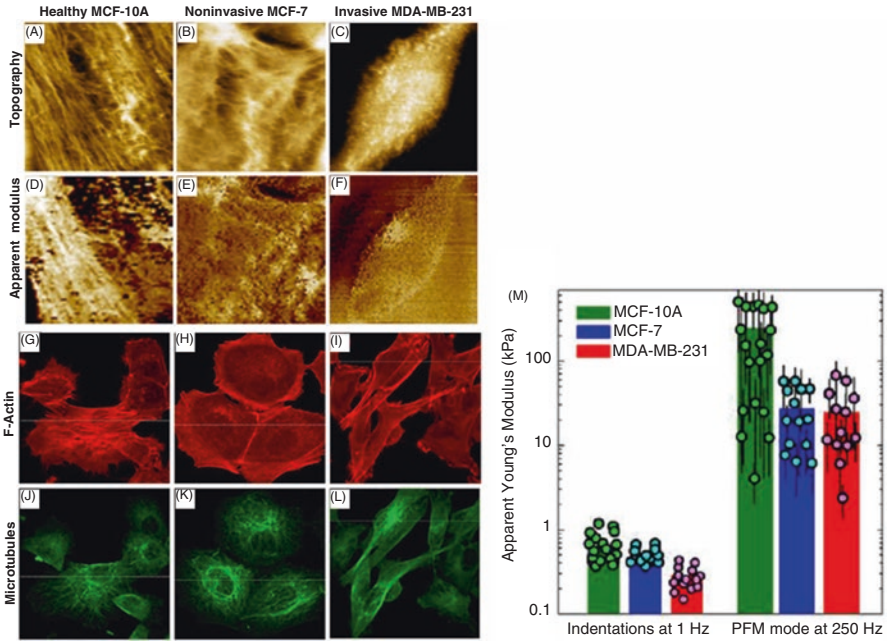

Fig. 9.2 Morphology (**a**–**c**), apparent modulus (**d**–**f**) from 2.5 to 250 kPa, F-actin (**g**–**i**) and microtubules (**j**–**l**) of three cell lines. First column for healthy MCF-10A cells, second column for noninvasive MCF-7 cancer cells, and third column for invasive MDA-MB-231 cancer cells. AFM image size is 25 × 25 μm (**a**–**f**). Confocal fluorescence image size is 80 × 80 μm (**g**–**l**). Average values of apparent Young's modulus for single cells at 1 Hz or at 250 Hz loading rate (**m**) [25]

receptor-related protein 1 (LRP-1), which is a member of a superfamily of transmembrane receptors. LRP-1 can affect the endocytosis of membrane-anchored proteins. Molinari et al. [32] showed that after LRP-1 silencing in a human thyroid follicular carcinoma cell line (FTC-133), Young's modulus and adhesion force increased, and cancer cell invasiveness weakened. These changes were due to an alteration of integrin clustering in the LRP-1(−) cells. Moreover, similar behaviors also exist in suspension cells. Cai et al. [33, 34] demonstrated the differences of morphology and stiffness between normal lymphocyte and Jurkat cell, an acute lymphoid leukemia cell. In Fig. 9.4, Jurkat cells exhibited much rougher cell surface and lower modulus. The average Young's modulus of Jurkat cell is 0.51 ± 0.06 kPa, which is about 2-times lower than that of normal lymphocyte (1.24 ± 0.09 kPa).

However, the above-mentioned regular mechanical alterations between normal and cancer cells are exceptional when Sokolov et al. [35] measured the mechanics of primary human cervical epithelial cells, including normal and cancerous cells, when considering the brush layer on the cell surface. In this case, the primary cancerous cells have higher Young's modulus (2.8 ± 1.7 kPa) than normal cells (2.05 ± 0.48 kPa). Because cancerous cells have longer brush and larger variability in brush size, the brush layers should be taken into consideration when measuring

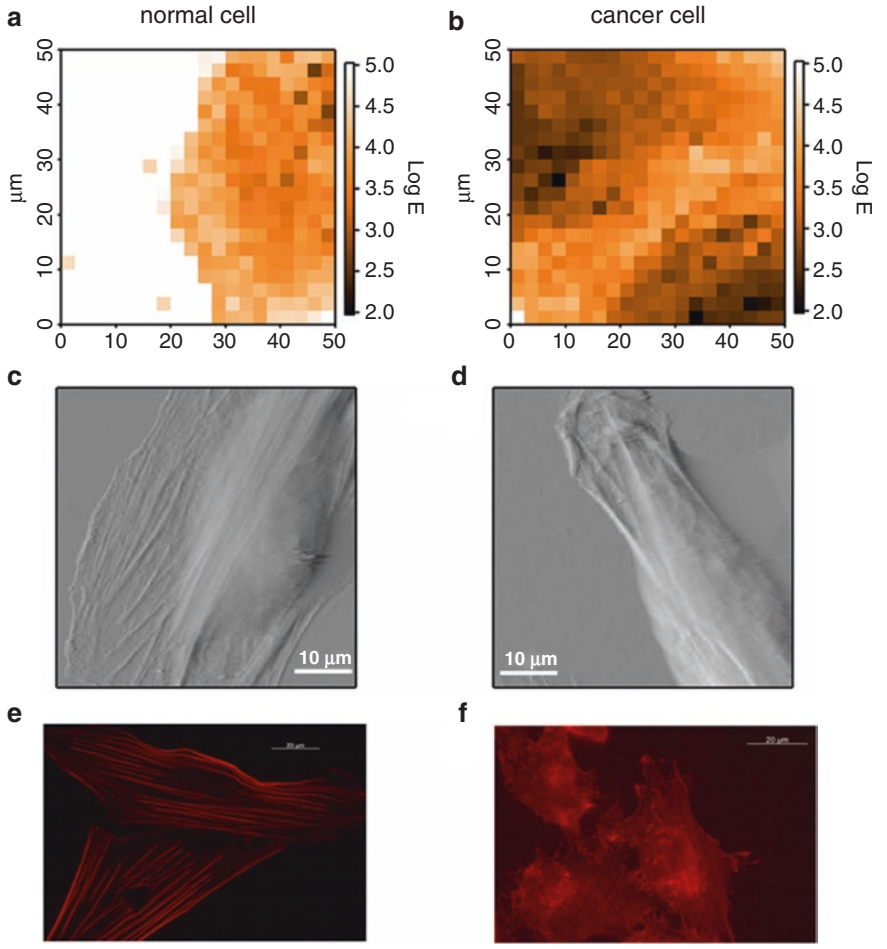

Fig. 9.3 Elasticity maps (**a**, **b**), deflection AFM images (**c**, **d**) and F-action labelled with rhodamine phalloidin of normal thyroid cells and cancerous thyroid cells. First column for healthy normal cells, second column for cancer cells. The cancer cells showed fewer actin stress fibres and are thicker than the normal cells. Elasticity map size is 50 × 50 μm (**a**, **b**). Scale bars: 10 μm (**c**, **d**), 20 μm (**e**, **f**) [28]

the cell surface mechanics [35]. Moreover, metastatic renal cells showed a higher values of Young's modulus with respect to normal renal cells when the cells were on the very soft gels instead of harder substrates [36]. Similar phenomenon was observed for elastic properties of cancer and normal thyroid cells on softer gels [37]. This is unlike the general trend that normal cells are stiffer than cancer cells. It is indicated that further detections on cell mechanical properties by AFM still need careful considerations.

On the other side, the changes in mechanical properties, binding force between ligand-receptor and morphology of cells can be used to screen some potential

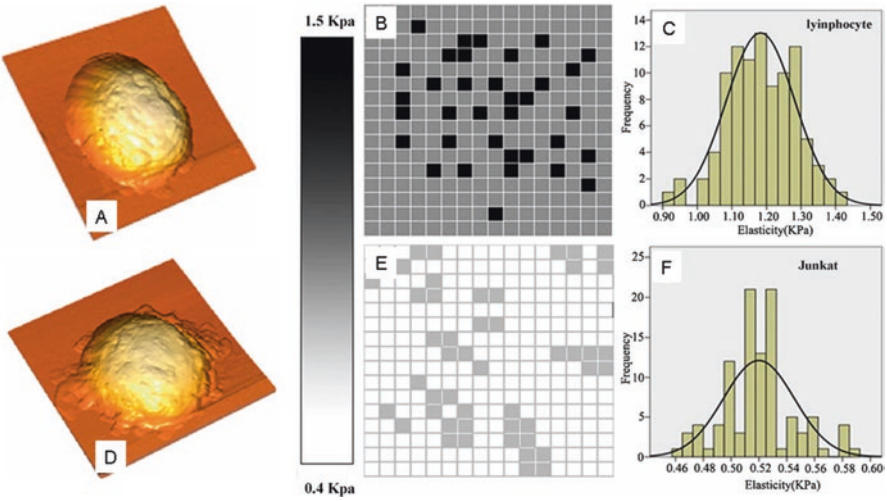

Fig. 9.4 3D morphology and Young's modulus of normal lymphocyte (**a**–**c**) and Jurkat cell (**d**–**f**) [33, 34]. The average Young's modulus of normal lymphocyte is 1.24 ± 0.09 kPa, and that of Jurkat cell is 0.51 ± 0.06 kPa

anti-cancer drugs or illuminate some cytoactivators to reveal the mechanisms of these agents. In order to assess anti-cancer effects of oridonin, single molecule force spectroscopy based on AFM was used to detect EGF-EGFR interactions and Young's modulus of living esophageal cancer cells (KYSE-150) [38, 39]. The results showed that oridonin could reduce the unbinding force and binding probability of EGF-EGFR with respect to intracellular ROS level (Fig. 9.5), and increase Young's modulus of KYSE-150 cells (Fig. 9.6). Moreover, a decreased energy barrier width, an increase dissociation off rate constant, and a decreased activation energy of EGF-EGFR complexes in ROS dependent way were shown after KYSE-150 cells were treated by oridonin. Similarly, the effects of resveratrol on unbinding forces between EGF-EGFR of living MCF-7 cells [40], the effects of quercetin on Young's modulus of HepG2 cells [41], the effects of curcumin on binding forces between CD44/CD44 antibody of HepG2 cell [42] were also reported.

RBL-2H3 is basophilic leukemia cell line. Stimulated by ionomycin, RBL-2H3 cells exhibited degranulation and morphological changes (Fig. 9.7) [43]. Some peculiar vesicles and some pores appeared in the cytoplasm area. These vesicles would disintegrate to release a lot of granules surrounding the cells by the controlling of F-actin. RAW264.7 cells, a macrophage cell line, also showed the changes of morphology, larger adhesion force and greater Young's modulus after lipopolysaccharide (LPS) stimulation (Fig. 9.8) [44].

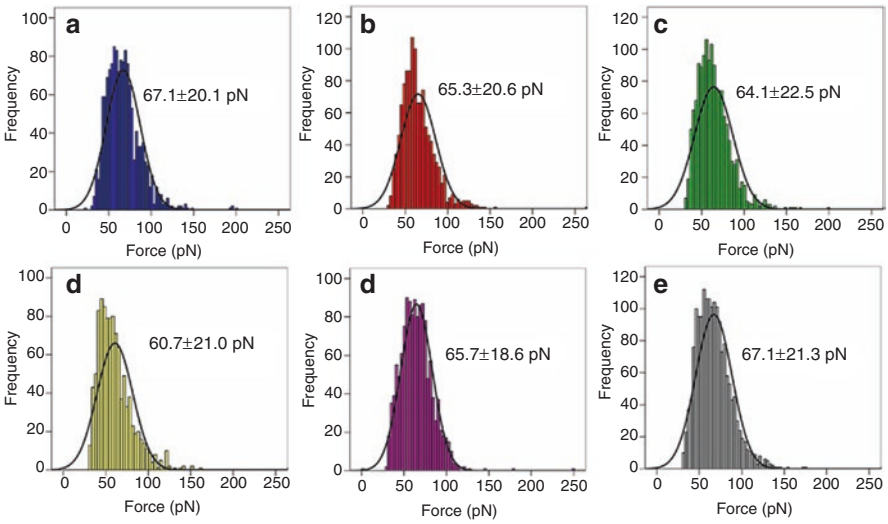

Fig. 9.5 Unbinding forces of EGF-EGFR complexes of KYSE-150 cells treated by different concentrations of oridonin. (**a**) 0, (**b**) 10, (**c**) 30, (**d**) 50 μmol/L, (**e**) 50 μmol/L + 2.5 mmol/L N-acetyl-L-cysteine (NAC), (**f**) 2.5 mmol/L NAC [38]

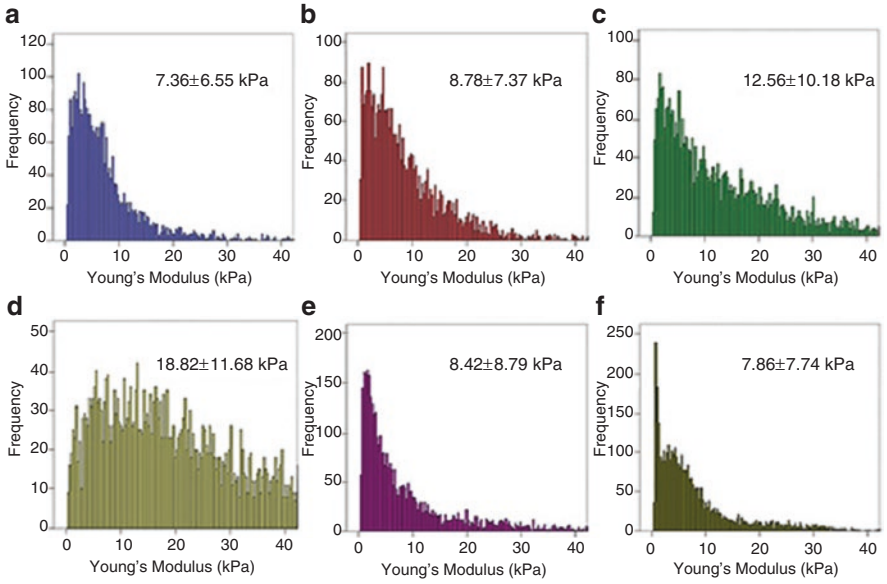

Fig. 9.6 Young's modulus of KYSE-150 cells treated by different concentrations of oridonin. (**a**) 0, (**b**) 10, (**c**) 30, (**d**) 50 μmol/L, (**e**) 50 μmol/L + 2.5 mmol/L NAC, (**f**) 2.5 mmol/L NAC [39]

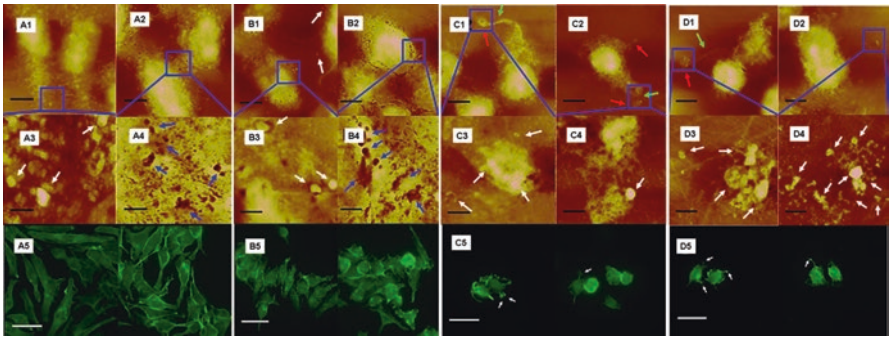

Fig. 9.7 AFM images of RBL-2H3 cell morphology (first and second panels) with white arrows showing granule location, and blue arrows showing the emergence of pores in the cell membrane. Fuorescence images of F-actin cytoskeleton (third panel) with white arrows showing the formation of unknown vesicles. Control cells (**A1**–**A5**), and cells treated by ionomycin for 5 min (**B1**–**B5**), 10 min (**C1**–**C5**), and 30 min (**D1**–**D5**), respectively. Scale bars: (first panel): 10 μm, (second panel): 2 μm, (third panel): 50 μm [43]

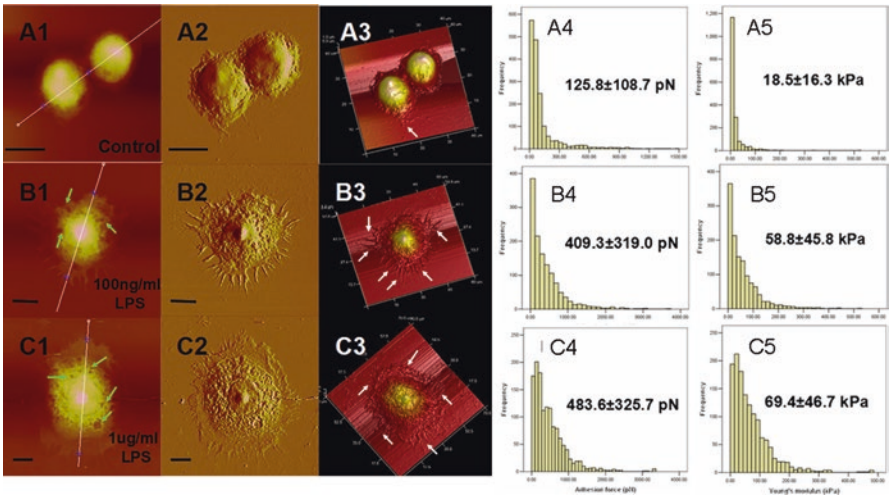

Fig. 9.8 Morphology (**A1**–**A3**, **B1**–**B3**, **C1**–**C3**), adhesion force (**A4**, **B4**, **C4**) and Young's modulus (**A5**, **B5**, **C5**) of RAW264.7 macrophages induced by LPS. Control cells (**A1**–**A5**), and cells treated by 100 ng/mL LPS (**B1**–**B5**), 1 μg/mL LPS (**C1**–**C5**), respectively. The green arrows showed some holes on cell membrane, and white arrows showed the pseudopod structures. Scale bars: 10 μm [44]

2 Erythrocyte–Related Diseases

Because red blood cell (RBC) membrane is composed of junctional complexes, spectrin network and lipid molecules, RBCs are able to change shape and recover to the original shape, which is called deformability. Deformability is an important

Table 9.2 Average Young's modulus (kPa) of healthy and diseased erythrocytes

Healthy erythrocytes	Diseases			Refs.
	Types of diseases	Diseased erythrocytes		
26 ± 7[a]	Hereditary spherocytosis	43 ± 21[a]		[53]
	Thalassemia	40 ± 24[a]		[53]
	G6PD deficiency	90 ± 20[a]		[53]
1.1 ± 0.4	Genotypic sickle cell trait	3.05 ± 1.09		[54, 55]
	Sickle cell disease	1.0 ± 1.1, 3.0 ± 2.7		[55]
1.82 ± 0.20	Diabetes mellitus II	2.52 ± 0.58		[57]
26 ± 12[a]	Diabetes I ketoacidosis	300 ± 98[a]		[59]
104 ± 19[a]	Diabetes mellitus II	178 ± 39[a]		[67]
4.9 ± 0.5	Diabetes mellitus	2~19	Average	[58]
	Hypertension	2~19	8.6 ± 0.8	[58]
	Coronary disease	2~19		[58]
1.205 ± 0.0142	Non-ischemic CHF	1.248 ± 0.0108		[2]
	Ischemic CHF	1.142 ± 0.0108		[2]
16 ± 5 kPa (<20 days)	Aging	34 (33[d] day)		[65]
104 ± 19[a]	Aging	153 ± 41[a]		[67]
75–85 (center)[b] 105–127 (external)[b]	Aging Aging	177–178 (center)[b] 178–180 (external)[b]		[64] [64]

[a]Erythrocytes were pretreated by fixation
[b]Erythrocytes were dried before measurement

mechanical property of normal RBCs linking to their physiological functions [45]. Reduced deformability of RBC is occurred in many diseases, and it is in direct relation to stiffness and elasticity of RBC membrane [46]. Reduced deformability is corresponding to enhanced stiffness, in term of larger values of Young's modulus. However, the biconcave shape of erythrocyte implied heterogeneous distribution of mechanical properties. Obviously, AFM is an appropriate tool to be used for quantitatively nanomechanical mapping of erythrocyte. It can link the structure of key components of erythrocyte membrane to cell mechanics and function. In Table 9.2, the Young's modulus of healthy and pathological erythrocytes was shown for comparison.

2.1 Malaria

Malaria is caused by parasites, called Plasmodium, which is transferred through infected mosquitoes bites. Although a significant decline in mortality is observed now with the aid of developed treatment including some new drugs and vaccines, malaria is still the most important parasitic infection disease. And new methods for treatment, prevention and rapid diagnostic testing are needed [47–49].

The disease-associated malaria parasite is confined to human red blood cells (RBC), leading to mechanical deformability and biorheological changes in RBC. It

will then affect organ functions, states of overall health and disease. The dramatic changes of membrane and cytoskeletal structure during the advancing stage of malaria infection should be considered in the loss of deformability of the infected cells [50]. But, seen from another point of view, it may be seen as the innate defense response of RBCs against the infection. Recent study [51] showed that Plasmodium alciparum could not penetrate through the RBCs which have damaged cytoskeleton and stiffer membranes under oxidative stress.

Similarly, Fernàndez-Busquets et al. [52] quantitatively evaluated the binding force between heparin and Plasmodiumfalciparum-infected red blood cells (pRBCs) by AFM. The results showed that heparin-pRBC binding force was 28~46 pN at different loading rates. However, no significant binding force was observed for non-infected RBCs.

2.2 Anemia

Lekka et al. [53] showed the stiffness of erythrocytes from healthy persons and patients with hemolytic anemia, respectively. The Young's modulus was 26 ± 7 kPa of healthy erythrocytes, less than that of diseased erythrocytes. The Young's moduli were 43 ± 21 kPa, 40 ± 24 kPa and 90 ± 20 kPa for hereditary spherocytosis, thalassemia and glucose-6-phosphate-dehydrogenase (G6PD) deficiency patients, respectively. It's worth noting that these values of Young's modulus were a little larger because the erythrocyte samples were fixed by 0.5% glutaraldehyde for 1 min.

Lykotrafitis et al. [54] measured the Young's modulus of human RBCs from healthy subjects and that from persons with genotypic sickle cell trait under physiological conditions. The results showed that normal cells are more elastic. The Young's modulus of normal cells (1.1 ± 0.4) was approximately three-folds lower than that of abnormal cells (3.05 ± 1.09). It's suggested that the sickle cell trait is associated with the polymerization of sickle hemoglobin and changed organization of cell cytoskeleton. Moreover, Lykotrafitis et al. [55] pointed out that normal RBCs are softer than those from patients with sickle cell disease in the oxygenated or deoxygenated state, providing further confirmation of the relationship between the polymerization of sickle hemoglobin and sickle cell disease.

2.3 Diabetes Mellitus

Deformability reduction of RBC is observed in diabetes mellitus. By using AFM, Papi et al. [56] measured the Young's modulus of living red blood cells, including healthy cells from volunteers and pathological cells from diabetes mellitus II patients. The results showed that the stiffness of RBC is heterogeneous, stiffer at the centre and softer at the periphery. For healthy cells, the average Young's modulus of the whole RBC is 1.82 ± 0.20 kPa while for pathological cells, 2.52 ± 0.58 kPa. It

is indicated that healthy RBCs are softer and deformed more easily. In diabetic patients, the membrane roughness and ultrastructure of RBC changed, and elongated shape and fibrin fibers around were seen [57]. These changes may affect erythrocyte deformability.

Lekka et al. [58] compared the stiffness of RBCs in healthy group with that in patients suffering from diabetes mellitus, hypertension and coronary disease. The measurements were carried out in physiological conditions. The results showed that RBCs in diabetes mellitus patients had higher average Young's modulus (8.6 ± 0.8 kPa) than healthy persons (4.9 ± 0.5 kPa). It is attributed to different structures of glycocalix, lipid bilayer and actin cytoskeleton between two groups.

The in situ single molecule detection of local stiffness, ultrastructures and ligand-receptor interactions between healthy and diseased erythrocytes, respectively, are beneficial to understand the pathology of diabetes. Zhang et al. [59] reported the morphology, ultrastructures, stiffness, single molecule binding force between insulin–insulin receptor of healthy erythrocytes and diseased erythrocytes from type 1 diabetes ketoacidosis (T1-DKA), respectively. A decreased roughness and an increased stiffness in T1-DKA erythrocytes were shown in Fig. 9.9, as well as decreased binding force and binding probability between insulin–insulin receptor in T1-DKA erythrocytes in Fig. 9.10. It indicated decreasingly functional and less stable insulin–insulin receptor complexes on T1-DKA erythrocytes than those on healthy erythrocytes.

Oxidative stress is related to diabetes. After oxidative stress, the stiffness and morphology of erythrocytes have changed. As shown in Fig. 9.11, after hydroxyl radicals treatment, the typical morphology of erythrocytes disappeared and the adhesion force increased. Besides, the erythrocytes became stiffer after treatment with hydroxyl radicals. However, the erythrocytes recover to normal status after treatment by quercetin-germanium (IV) complex, a radical scavenging compound [60].

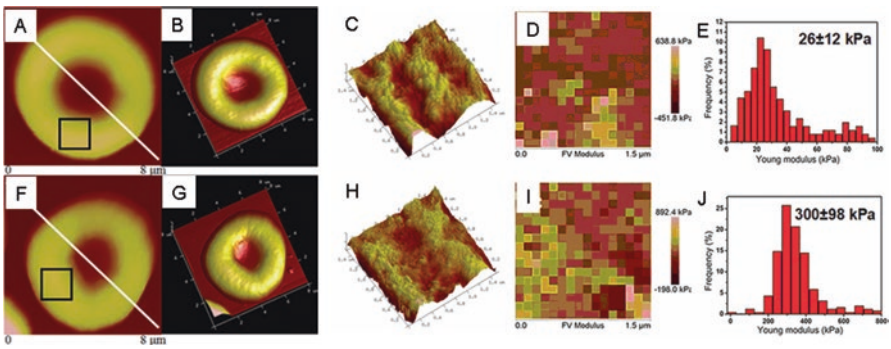

Fig. 9.9 Healthy erythrocyte (**a**–**e**) and T1-DKA erythrocyte (**f**–**j**). Typical morphology (**a**, **f**), corresponding 3D image (**b**, **g**), ultrastructures (**c**, **h**), force volume modulus (**d**, **i**) and histogram distribution of modulus (**e**, **j**) [59]

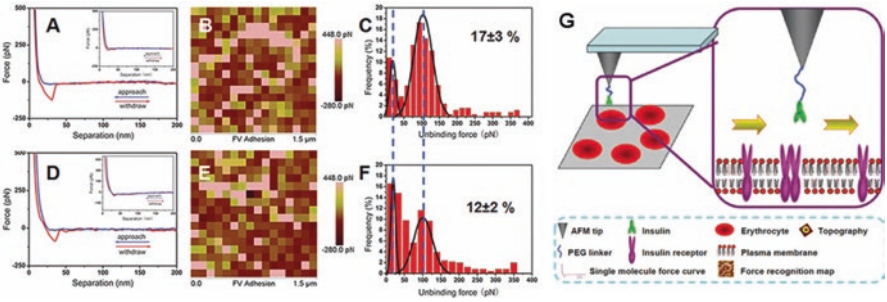

Fig. 9.10 Binding force and binding probability between insulin–insulin receptor of erythrocytes (**a**–**f**, *left panel*), and scheme for tip modification (**g**, *right panel*). Healthy erythrocyte (**a**–**c**) and T1-DKA erythrocyte (**d**–**f**) [59]

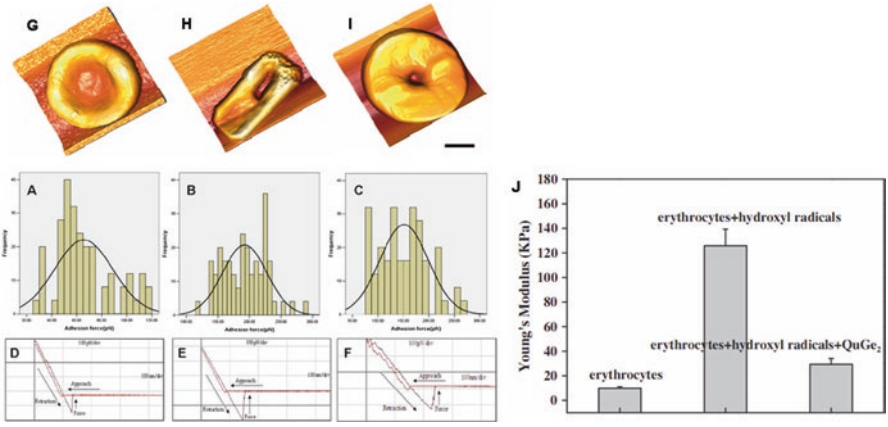

Fig. 9.11 Normal erythrocytes (**g**, **a**, **d**), erythrocytes treated by hydroxyl radicals (**h**, **b**, **e**) and after treatment with quercetin-germanium (IV) (**i**, **c**, **f**). AFM images of cell morphology (**g**–**i**), force histograms (**a**–**c**), force-distance curves (**d**–**f**), and Young's modulus (**j**). Scale bar: 12 μm [60]

2.4 Cardiovascular Disease

At present, there are few biomarkers to evaluate the risk of cardiovascular diseases. High fibrinogen concentration is a risk factor, however, the underlying mechanisms remain unidentified. Recently, cell stiffness, and binding forces between fibrinogen and erythrocyte measured by AFM are being prospective factors to identify increased risk for patients with cardiovascular diseases.

By using AFM, Santos et al. [2] showed increased fibrinogen-erythrocytes binding force in ischaemic chronic heart failure (CHF) patients (74.9 ± 10.7 pN) with respect to non-ischaemic CHF patients (45.4 ± 5.6 pN). The values of Young's modulus of erythrocytes for non-ischemic CHF group and ischemic CHF patients were

1.248 ± 0.0108 kPa and 1.142 ± 0.0108 kPa, respectively, and that of healthy control group was1.205 ± 0.0142 kPa. It is indicated that cell stiffness in both patient groups were changed.

2.5 Essential Hypertension

Essential arterial hypertension (EAH) is a clinical complication. It is one of the major risk factors for heart failure, heart attack or stroke. Many patients with essential hypertension showed reduced deformability of RBCs by some studies. Decreased RBC deformability is related to different patterns of membrane skeleton between healthy donors and patients with essential hypertension and/or hypercholesterolemia [61]. Hence, the lower RBC deformability may be regarded as a marker for endothelial dysfunction in hypertensive patients.

Increased aggregation of erythrocytes by high plasma fibrinogen level has been linked to EAH. Santos et al. [62] demonstrated the effects of fibrinogen on erythrocyte aggregation in essential arterial hypertension by AFM. The results showed that erythrocyte–erythrocyte detachment force is higher for patients than that for healthy persons. The force for both groups is increased with higher fibrinogen concentrations. In other words, erythrocyte bridging by fibrinogen is powerful in patients. So higher levels of γ' fibrinogen in EAH patients contributed to increased risk of EAH.

2.6 Aging

The ageing of erythrocytes plays an important role in promoting the removal of malfunctioning RBCs. Changes in RBC deformability were observed in aging or storage [63].

During the aging process, the mechanical properties of erythrocytes have changed. Girasole et al. [64] demonstrated the nanomechanical properties of cell plasma membrane in the intermediate states along the ageing of erythrocytes. When the aging proceeded, the Young's modulus of the cells became larger than that of normal cells. It is indicating the cells became more rigid. And the spatial distribution of Young's modulus also became more uniform in the whole cell together with the lose of asymmetry in the cell external and center. It is suggested that the cytoskeleton structure had changed, especially at the center.

During storage, structural and morphological changes appeared in RBCs. Kozlova et al. [65] showed the mechanical properties of RBCs during 40 days of storage by using AFM. At a transition period (20–26 days), the Young's modulus of the cell membranes was 1.6–2 folds than that at the beginning. And cells changed to irreversible forms with nanodefects on cell surface.

In brief, a lot of evidence showed that the Young's modulus of pathological erythrocytes was higher than that in normal cells. It is suggested that the pathologi-

cal erythrocytes became stiffer (i.e. more rigid and less elastic). The cell deformability changed with the variation of pathological conditions. Generally, the changes in cell mechanics and deformability were often accompanied by cytoskeleton variation, thus erythrocyte functions and blood flow were affected and it would be connected to pathological implications and various diseases. Therefore, the mechanical properties of erythrocytes could be developed into a novel biomarker for diseases.

3 Conclusion

Atomic force microscope is a very sensitive tool for directly evaluating mechanical properties of single cells. Moreover, AFM measurements can be carried out in conjunction with other more commonly used techniques such as optical microscope observation, and histological stain. Based on these considerations, cell stiffness may be served as a potential diagnostic indicator in quantitatively analyzing the pathological and physiological states of cells by using AFM, and may provide new approaches to human diseases, though several challenges remain to be solved before clinical implementation of these approaches. Up to now, many questions have remained to be the cause for the observed changes in stiffness. Furthermore, because human physiological environment is highly complex, a deeper knowledge of stiffness-related changes of cells is still required for diagnosing human diseases. AFM, a promising tool, can help to obtain a more reliable diagnosis in future research.

Acknowledgement This work was supported by Guangdong Natural Science Foundation, China (No. 2016A030313078), the Fundamental Research Funds for the Central Universities, China (No. 21617430), Foundation for Distinguished Young Talents in Higher Education of Guangdong, China (No. LYM11020), and Macau FDCT (No. 028/2014/A1).

References

1. Montell DJ. Morphogenetic cell movements: diversity from modular mechanical properties. Science. 2008;322:1502–5.
2. Guedes AF, Carvalho FA, Malho I, Lousada N, Sargento L, Santos NC. Atomic force microscopy as a tool to evaluate the risk of cardiovascular diseases in patients. Nat Nanotechnol. 2016;11:687–92.
3. Gardel ML, Schneider IC, Aratyn-Schaus Y, Waterman CM. Mechanical integration of actin and adhesion dynamics in cell migration. In: Schekman R, Goldstein L, Lehmann R, editors. Annual review of cell and developmental biology, vol. 26. Palo Alto: Annual Reviews; 2010. p. 315–33.
4. Chen W, Zhu C. Mechanical regulation of T-cell functions. Immunol Rev. 2013;256:160–76.
5. Discher DE, Janmey P, Wang YL. Tissue cells feel and respond to the stiffness of their substrate. Science. 2005;310:1139–43.

6. Parsons JT, Horwitz AR, Schwartz MA. Cell adhesion: integrating cytoskeletal dynamics and cellular tension. Nat Rev Mol Cell Biol. 2010;11:633–43.
7. Zhang GC, Fan N, Lv XY, Liu YY, Guo J, Yang LX, et al. Investigation of the mechanical properties of the human osteosarcoma cell at different cell cycle stages. Micromachines. 2017;8.
8. Fletcher DA, Mullins D. Cell mechanics and the cytoskeleton. Nature. 2010;463:485–92.
9. Friedl P, Alexander S. Cancer invasion and the microenvironment: plasticity and reciprocity. Cell. 2011;147:992–1009.
10. Schroeder MC, Halder G. Regulation of the hippo pathway by cell architecture and mechanical signals. Semin Cell Dev Biol. 2012;23:803–11.
11. Hoffman BD, Grashoff C, Schwartz MA. Dynamic molecular processes mediate cellular mechanotransduction. Nature. 2011;475:316–23.
12. Mierke CT. The fundamental role of mechanical properties in the progression of cancer disease and inflammation. Rep Prog Phys. 2014;77:076602.
13. Hu HY, Candiello J, Zhang P, Ball SL, Cameron DA, Halfter W. Retinal ectopias and mechanically weakened basement membrane in a mouse model of muscle-eye-brain (MEB) disease congenital muscular dystrophy. Mol Vis. 2010;16:1415–28.
14. Humphrey JD, Dufresne ER, Schwartz MA. Mechanotransduction and extracellular matrix homeostasis. Nat Rev Mol Cell Biol. 2014;15:802–12.
15. Patel NR, Bole M, Chen C, Hardin CC, Kho AT, Mih J, et al. Cell elasticity determines macrophage function. PLoS One. 2012;7:e41024.
16. Muller DJ, Dufrene YF. Atomic force microscopy: a nanoscopic window on the cell surface. Trends Cell Biol. 2011;21:461–9.
17. Dufrene YF, Ando T, Garcia R, Alsteens D, Martinez-Martin D, Engel A, et al. Imaging modes of atomic force microscopy for application in molecular and cell biology. Nat Nanotechnol. 2017;12:295–307.
18. Raman A, Trigueros S, Cartagena A, Stevenson APZ, Susilo M, Nauman E, et al. Mapping nanomechanical properties of live cells using multi-harmonic atomic force microscopy. Nat Nanotechnol. 2011;6:809–14.
19. Alsteens D, Muller DJ, Dufrene YF. Multiparametric atomic force microscopy imaging of biomolecular and cellular systems. Acc Chem Res. 2017;50:924–31.
20. Alsteens D, Beaussart A, El-Kirat-Chatel S, Sullan RMA, Dufrene YF. Atomic force microscopy: a new look at pathogens. PLoS Pathog. 2013;9:e1003516.
21. Lekka M, Pogoda K, Gostek J, Klymenko O, Prauzner-Bechcicki S, Wiltowska-Zuber J, et al. Cancer cell recognition - mechanical phenotype. Micron. 2012;43:1259–66.
22. Plodinec M, Loparic M, Monnier CA, Obermann EC, Zanetti-Dallenbach R, Oertle P, et al. The nanomechanical signature of breast cancer. Nat Nanotechnol. 2012;7:757–65.
23. Ansardamavandi A, Tafazzoli-Shadpour M, Omidvar R, Jahanzad I. Quantification of effects of cancer on elastic properties of breast tissue by atomic force microscopy. J Mech Behav Biomed Mater. 2016;60:234–42.
24. Esbona K, Inman D, Saha S, Jeffery J, Schedin P, Wilke L, et al. COX-2 modulates mammary tumor progression in response to collagen density. Breast Cancer Res. 2016;18:35.
25. Calzado-Martin A, Encinar M, Tamayo J, Calleja M, Paulo AS. Effect of actin organization on the stiffness of living breast Cancer cells revealed by peak-force modulation atomic force microscopy. ACS Nano. 2016;10:3365–74.
26. Li QS, Lee GYH, Ong CN, Lim CT. AFM indentation study of breast cancer cells. Biochem Biophys Res Commun. 2008;374:609–13.
27. Dokukin ME, Guz NV, Sokolov I. Mechanical properties of cancer cells depend on number of passages: atomic force microscopy indentation study. Jpn J Appl Phys. 2017;56:08LB01.
28. Prabhune M, Belge G, Dotzauer A, Bullerdiek J, Radmacher M. Comparison of mechanical properties of normal and malignant thyroid cells. Micron. 2012;43:1267–72.
29. Xu WW, Mezencev R, Kim B, Wang LJ, Mcdonald J, Sulchek T. Cell stiffness is a biomarker of the metastatic potential of ovarian Cancer cells. PLoS One. 2012;7.

30. Quan FS, Kim KS. Medical applications of the intrinsic mechanical properties of single cells. Acta Biochim Biophys Sin. 2016;48:865–71.
31. Andolfi L, Bourkoula E, Migliorini E, Palma A, Pucer A, Skrap M, et al. Investigation of adhesion and mechanical properties of human glioma cells by single cell force spectroscopy and atomic force microscopy. PLoS One. 2014;9:e112582.
32. Le Cigne A, Chieze L, Beaussart A, El-Kirat-Chatel S, Dufrene YF, Dedieu S, et al. Analysis of the effect of LRP-1 silencing on the invasive potential of cancer cells by nanomechanical probing and adhesion force measurements using atomic force microscopy. Nanoscale. 2016;8:7144–54.
33. Cai X, Gao S, Cai J, Wu Y, Deng H. Artesunate induced morphological and mechanical changes of Jurkat cell studied by AFM. Scanning. 2009;31:83–9.
34. Cai X, Xing X, Cai J, Chen Q, Wu S, Huang F. Connection between biomechanics and cytoskeleton structure of lymphocyte and Jurkat cells: an AFM study. Micron. 2010;41:257–62.
35. Iyer S, Gaikwad RM, Subba-Rao V, Woodworth CD, Sokolov I. Atomic force microscopy detects differences in the surface brush of normal and cancerous cells. Nat Nanotechnol. 2009;4:389–93.
36. Rianna C, Radmacher M. Influence of microenvironment topography and stiffness on the mechanics and motility of normal and cancer renal cells. Nanoscale. 2017;9:11222–30.
37. Rianna C, Radmacher M. Comparison of viscoelastic properties of cancer and normal thyroid cells on different stiffness substrates. Eur Biophys J Biophys Lett. 2017;46:309–24.
38. Pi J, Jin H, Jiang J, Yang F, Cai H, Yang P, et al. Single molecule force spectroscopy for in-situ probing oridonin inhibited ROS-mediated EGF-EGFR interactions in living KYSE-150 cells. Pharmacol Res. 2017;119:479–89.
39. Pi J, Cai H, Jin H, Yang F, Jiang J, Wu A, et al. Qualitative and quantitative analysis of ROS-mediated Oridonin-induced Oesophageal Cancer KYSE-150 cell apoptosis by atomic force microscopy. PLoS One. 2015;10:e0140935.
40. Zhang L, Yang F, Cai J-Y, Yang P-H, Liang Z-H. In-situ detection of resveratrol inhibition effect on epidermal growth factor receptor of living MCF-7 cells by atomic force microscopy. Biosens Bioelectron. 2014;56:271–7.
41. Pi J, Li B, Tu L, Zhu H, Jin H, Yang F, et al. Investigation of quercetin-induced HepG2 cell apoptosis-associated cellular biophysical alterations by atomic force microscopy. Scanning. 2016;38:100–12.
42. Wang M, Ruan Y, Xing X, Chen Q, Peng Y, Cai J. Curcumin induced nanoscale CD44 molecular redistribution and antigen-antibody interaction on HepG2 cell surface. Anal Chim Acta. 2011;697:83–9.
43. Pi J, Huang L, Yang F, Jiang J, Jin H, Liu J, et al. Atomic force microscopy study of ionomycin-induced degranulation in RBL-2H3 cells. Scanning. 2016;38:525–34.
44. Pi J, Li T, Liu J, Su X, Wang R, Yang F, et al. Detection of lipopolysaccharide induced inflammatory responses in RAW264.7 macrophages using atomic force microscope. Micron. 2014;65:1–9.
45. Minetti G, Egee S, Morsdorf D, Steffen P, Makhro A, Achilli C, et al. Red cell investigations: art and artefacts. Blood Rev. 2013;27:91–101.
46. Szablewski L, Sulima A. The structural and functional changes of blood cells and molecular components in diabetes mellitus. Biol Chem. 2017;398:411–23.
47. Greenwood BM, Bojang K, Whitty CJM, Targett GAT. Malaria. Lancet. 2005;365:1487–98.
48. Agnandji ST, Lell B, Soulanoudjingar SS, Fernandes JF, Abossolo BP, Conzelmann C, et al. First results of phase 3 trial of RTS,S/AS01 malaria vaccine in African children. N Engl J Med. 2011;365:1863–75.
49. Rossi G, De Smet M, Khim N, Kindermans JM, Menard D. Performance of rapid diagnostic testing in patients with suspected malaria in Cambodia, a low-Endemicity country aiming for malaria elimination. Clin Infect Dis. 2017;65:1769–70.
50. Shi H, Liu Z, Li A, Yin J, Chong AGL, Tan KSW, et al. Life cycle-dependent cytoskeletal modifications in Plasmodium falciparum infected erythrocytes. PLoS One. 2013;8.

51. Sinha A, Chu TTT, Dao M, Chandramohanadas R. Single-cell evaluation of red blood cell biomechanical and nano-structural alterations upon chemically induced oxidative stress. Sci Rep. 2015;5.
52. Valle-Delgado JJ, Urban P, Fernandez-Busquets X. Demonstration of specific binding of heparin to Plasmodium falciparum-infected vs non-infected red blood cells by single-molecule force spectroscopy. Nanoscale. 2013;5:3673–80.
53. Dulinska I, Targosz M, Strojny W, Lekka M, Czuba P, Balwierz W, et al. Stiffness of normal and pathological erythrocytes studied by means of atomic force microscopy. J Biochem Biophys Methods. 2006;66:1–11.
54. Maciaszek JL, Lykotrafitis G. Sickle cell trait human erythrocytes are significantly stiffer than normal. J Biomech. 2011;44:657–61.
55. Maciaszek JL, Andemariam B, Lykotrafitis G. Microelasticity of red blood cells in sickle cell disease. J Strain Anal Eng Des. 2011;46:368–79.
56. Ciasca G, Papi M, Di Claudio S, Chiarpotto M, Palmieri V, Maulucci G, et al. Mapping viscoelastic properties of healthy and pathological red blood cells at the nanoscale level. Nanoscale. 2015;7:17030–7.
57. Buys AV, Van Rooy MJ, Soma P, Van Papendorp D, Lipinski B, Pretorius E. Changes in red blood cell membrane structure in type 2 diabetes: a scanning electron and atomic force microscopy study. Cardiovasc Diabetol. 2013;12:25.
58. Lekka M, Fornal M, Pyka-Fosciak G, Lebed K, Wizner B, Grodzicki T, et al. Erythrocyte stiffness probed using atomic force microscope. Biorheology. 2005;42:307–17.
59. Zhang L, Pi J, Shi Q, Cai J, Yang P, Liang Z. In situ single molecule detection of insulin receptors on erythrocytes from a type 1 diabetes ketoacidosis patient by atomic force microscopy. Analyst. 2015;140:7407–16.
60. Li S-P, Xie W-L, Cai H-H, Cai J-Y, Yang P-H. Hydroxyl radical scavenging mechanism of human erythrocytes by quercetin-germanium (IV) complex. Eur J Pharm Sci. 2012;47:28–34.
61. Kaczmarska M, Fornal M, Messerli FH, Korecki J, Grodzicki T, Burda K. Erythrocyte membrane properties in patients with essential hypertension. Cell Biochem Biophys. 2013;67:1089–102.
62. Guedes AF, Carvalho FA, Moreira C, Nogueira JB, Santos NC. Essential arterial hypertension patients present higher cell adhesion forces, contributing to fibrinogen-dependent cardiovascular risk. Nanoscale. 2017;9:14897–906.
63. Cluitmans JCA, Hardeman MR, Dinkla S, Brock R, Bosman G. Red blood cell deformability during storage: towards functional proteomics and metabolomics in the blood Bank. Blood Transf. 2012;10:S12–S8.
64. Girasole M, Dinarelli S, Boumis G. Structural, morphological and nanomechanical characterisation of intermediate states in the ageing of erythrocytes. J Mol Recognit. 2012;25:285–91.
65. Kozlova E, Chernysh A, Moroz V, Sergunova V, Gudkova O, Manchenko E. Morphology, membrane nanostructure and stiffness for quality assessment of packed red blood cells. Sci Rep. 2017;7:7846.
66. Wang XL, Yang YJ, Hu XH, Kawazoe N, Yang YN, Chen GP. Morphological and mechanical properties of osteosarcoma microenvironment cells explored by atomic force microscopy. Anal Sci. 2016;32:1177–82.
67. Jin H, Xing XB, Zhao HX, Chen Y, Huang X, Ma SY, et al. Detection of erythrocytes influenced by aging and type 2 diabetes using atomic force microscope. Biochem Biophys Res Commun. 2010;391:1698–702.

Chapter 10
High Resolution AFM and Its Applications

Hao Sun, Ming Ye, and Wanxin Sun

Abstract Imaging fine structures of molecules and cells under controlled conditions, and early detection of subtle changes in material properties are very important for understanding the mechanism of many biological processes. In the past decades, scientists made extensive efforts in exploring and developing new imaging technologies to improve the resolution and sensitivity of detection. AFM is not an exception, improving the resolution of measurements is a long-lasting effort for both users and instrument makers. It is even more challenging for soft materials, such as biological molecules, cells and biomaterials, as the force control in soft material measurement is more critical and difficult. In this chapter, we will first review the applications of high resolution AFM, discuss the challenges for high resolution in different aspects and followed by solutions to achieve high resolution for different applications, including AFM system optimization and sample-probe interaction optimization by probe design and control algorithm. A series of examples will be used as case studies to illustrate how to achieve high resolution in AFM experiments. At the end of this chapter, we will provide our prospective view on future developments in AFM technology.

1 Review of High Resolution AFM Applications

There are already several good review papers discussing about the applications of high-resolution AFM [1–10]. Raigoza A. F. et al. reviewed some important innovations in AFM techniques for biological molecules studies, and highlighted the challenges to gain atomic- and molecular-level information of complex biomolecular structures [3]. Alsteens D. et al. also discussed the high-resolution imaging of biomolecular and cellular systems by force-distance curve based AFM technologies in details [4]. For sub-nanometer resolution on biological samples, Dufrene Y. F. et al.

H. Sun · M. Ye · W. Sun (✉)
Bruker Nano Surface, Singapore, Singapore
e-mail: wanxin.sun@bruker.com

J. Cai (ed.), *Atomic Force Microscopy in Molecular and Cell Biology*,
https://doi.org/10.1007/978-981-13-1510-7_10

reviewed the basic principles, advantages and limitations of the most commonly used AFM bioimaging modes, including the popular contact and dynamic modes, as well as recently developed modes such as multiparametric, molecular recognition, multifrequency and high-speed imaging [5]. In these papers, many techniques are discussed for high-resolution AFM imaging. These techniques combined with functionalized probes were used to measure the mechanical and chemical properties of single proteins in purple membranes, observe structurally localized chemical groups of water-soluble proteins, map and analyze nanomechanically individual sensors on yeast cells, image the sites of assembly and extrusion of single filamentous bacteriophages in live bacteria, unravel the adhesive properties of biofilm-forming microbial pathogens, map the ligand binding free energy landscape of human membrane receptors in proteoliposomes, and map nanomechanically the first binding events of viruses to animal cells [4]. For further information, readers are advised to refer to the references.

In this section, we will review some representative high-resolution works, including biomolecules, and cells. With necessary knowledge in engineering and life sciences, these examples can be readily extended to other applications.

1.1 DNA

The DNA double helix structure was first investigated by X ray diffraction method in 1953 [11]. Besides this well-known right-handed helix structure with 10~10.5 base pairs per turn, many different secondary structures were discovered in last century. For example, DNA with guanine-rich sequences could fold into quadruple-stranded helical structures, called 'G-quadruplexes'. These nucleic acids assembling structures play complex roles in gene expression, translation, telomere-end maintenance, recombination and replication [12]. X ray diffraction method generally relies on ensemble-averaging of the DNA molecules. It is less sensitive to single mutant as the mutant's structural information will be buried in the ensemble average. Furthermore, it is not always possible to get molecules crystallization which is required by X ray measurement. However, local deformations of the DNA double helix are important in mediating protein-DNA binding specificity [13]. Therefore, it is highly desirable to develop a new technique that can convey the information of detailed structure and mechanical properties of single DNA molecule under controlled environment, including temperature, pH, ion strength etc.

Immediately after its invention in late 1980s, AFM was quickly adopted in biomolecular researches, especially DNA [14]. To date, AFM is the only tool for human to "see" the secondary structure of a DNA molecule directly in real-space. However, most of AFM images typically show DNA molecules as featureless strands. This is because DNA is a highly dynamic molecule, having both translational and rotational movements. DNA is usually adsorbed on positively charged surfaces for AFM imaging, like APTES and APS. This light adsorption maintains its native conformation, and its high degree of mobility as well. This mobility, in conjunction

with the DNA structure constantly changing, makes it difficult to resolve the double helical structure on the time scale of AFM imaging.

The first observation of DNA helical period was achieved in contact mode AFM in 1995 [15]. In this work, the pitch of B-DNA was measured by AFM with a reported periodical modulation of 3.4 ± 0.4 nm. The DNA molecules were immobilized onto a positively charged lipid bilayer. It is important to note that the DNA pitch was only observed when the DNA strands were densely and uniformly packed on the bilayer surface and the isolated DNA strands did not show any periodical structure. The possible reason is that the close packing of DNA limits its movement, thereby enhancing the stability of DNA strands and making the pitch of DNA strands resolved.

In addition to contact mode, several groups had reported that the major and minor groove can be resolved on conjugated and circular DNA by tapping mode and PeakForce tapping mode [16–19]. Figure 10.1 shows the DNA double helix high-resolution images obtained with PeakForce tapping on Bruker MultiMode 8 system. The probe used is AC40 (Olympus, Tokyo, Japan). As discussed in Chap. 1, the imaging force can be precisely controlled to a very low level in PeakForce taping mode. In this study, the imaging force was controlled from several tens of pN to over 100 pN by using small PeakForce Amplitude ~5 nm. At low imaging force, shown in Figs.10.1a, b, direct visualization of the helical structure and accurate measurement of the ~2 nm diameter of B-DNA were realized on loosely bound DNA sample. With increase in imaging force, the DNA strand is compressed and the major and minor grooves disappear, shown in Figs. 10.1e, f.

The applications of AFM in DNA research are mainly in two aspects. One is to use AFM to understand the fundamental bio-physical properties of DNA as the

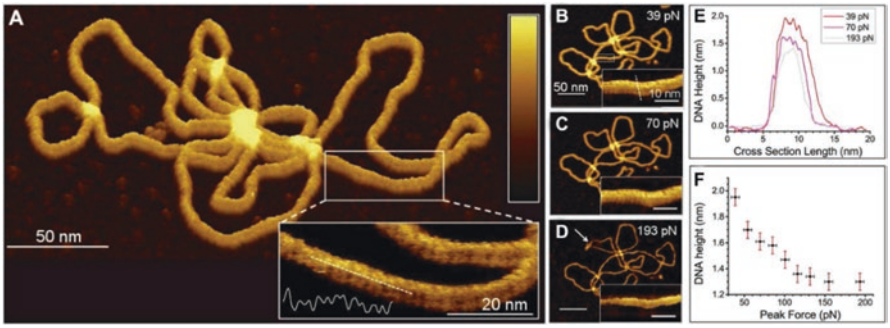

Fig. 10.1 DNA double helix high-resolution images obtained on Bruker MultiMode 8 System under PeakForce tapping with AC40 probe. (**a**) DNA imaged at a peak force of 49 pN. Inset: High resolution image of DNA, and a height profile taken along the dashed line, showing major and minor grooves. Color scale: 3.5 nm; (**b**)–(**d**) DNA imaged at peak forces of 39, 70, and 193 pN, respectively. Insets: Major and minor grooves of the DNA double helix. (**e**) Height profiles measured across the DNA under different peak forces, the dashed line in B inset marks the location of the height profiles. (**f**) Measured height as a function of peak force, measured along the same section across the DNA (as E). (Reprinted with permission from 19, Copyright (2014) John Wiley and Sons.)

cornerstone of genetic science [19, 20]. The other is to use DNA as a basic programmable nano-construction material and AFM as an imaging tool to visualize the designed 2D or 3D smart devices [21]. In both aspects, the core technical challenges are still optimizing immobilization method and controlling the imaging force. In general, a stronger immobilization would lead to a better quality in AFM imaging. However, the strong immobilization achieved by divalent ions could also bend DNA molecules in an unnatural way. Furthermore, the binding efficiencies between proteins and DNA molecules could be also strongly influenced by the immobilization of DNA molecules on the substrate. Usually, for DNA self-assembling structures, like DNA origami, double helix resolution cannot be achieved on their densely packaged DNA molecular chains. But the details for the DNA hybridization could be identified easily [22–24]. Therefore, optimizing immobilization strength and imaging force control are the tricky parts in the whole experiment [25].

Although there were quite a few reports of DNA double helix imaging, the high-resolution imaging of RNA by AFM has not been reported yet. This might be because of the lack of effective ways to equilibrate RNA on flat surfaces [26]. Ares P. et al. imaged double-stranded RNA (dsRNA) for the first time with a lateral resolution sufficient to resolve a ~1.5 nm periodicity under near physiological conditions, compatible with the A-form of dsRNA [27]. Less than 1 nm oscillation amplitude was used to keep the imaging force at tens of pN level.

1.2 Proteins

Proteins studied by AFM high resolution imaging are mainly membrane-related proteins and amyloid disease related peptides/proteins. Both native membrane proteins and toxin proteins that attack cell membrane have been studied with AFM, where sub-molecular resolution morphologies were obtained in aqueous solution and at physiological temperature. Time-lapse imaging provides the information about how these proteins work, rotate, self-assemble in lipids [28]. The dynamic behavior of the KcsA channel on the lipid membrane was studied with high-resolution AFM [29], where the functional open and closed gates of the KcsA channel under the membrane-embedded condition were resolved. However, with the rapid developments in cryo-electron microscopy (Cryo-EM), some high resolution morphological measurements for protein used to be done by AFM were achieved by Cryo-EM [30].

The recent developments in high-resolution mechanical properties mapping by AFM, i.e. PeakForce Quantitative Nano-mechanical Mapping (PFQNM) [31], achieved single hydrogen bond level energy resolution in membrane protein physical properties research [9]. In cooperation with high resolution morphology imaging, PFQNM provides additional information in understanding protein dynamics. This technique is based on the PeakForce tapping technology discussed in Chap. 1. With carefully controlled interaction force, force-distance curves were recorded at every pixel. Derived from the force-distance curves, difference in elastic modulus at

the subunits of protein molecules was observed. Through energy dissipation calculation on each probe-sample interaction, the energy to open a specific loop structure could be determined. Such kind of results could be used as reference and validation for molecular dynamics simulation to understand the functions of the membrane proteins [32]. As an example, the work done by Rico F. et al. is highlighted here, where PFQNM was used to map quantitatively the flexibility of individual membrane proteins in native, folded state at unprecedented sub-molecular resolution [33]. In this work, protein flexibility was correlated with crystal structure, and the results support the hypothesis that flexible interhelical loops of bacteriorhodopsin (bR) allow conformational changes related to functions, while stiff protruding α-helices provide molecular stability. Figure 10.2a, b show the topography image and stiffness image, respectively, which were calculated with 3-fold symmetrized correlation average from 13 bR trimers and overlaid with the atomic structure. Figure 10.2c sketches the structure of the membrane. Stiffness mapping across individual bR monomers revealed two major different areas: the areas with high

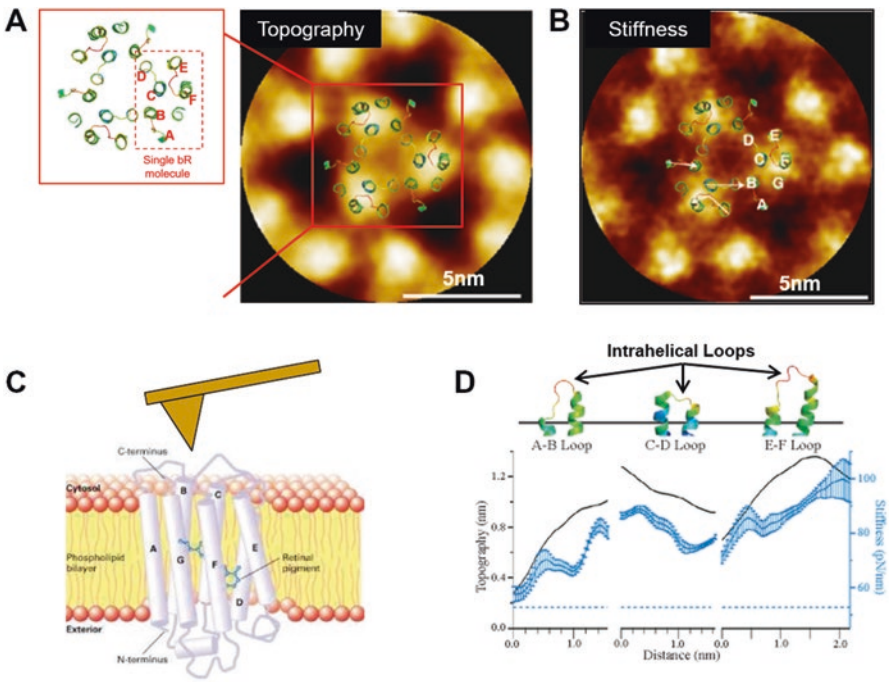

Fig. 10.2 High-resolution imaging of bacteriorhodopsin. The 3-fold symmetrized correlation average (**a**) Topography image and (**b**) Stiffness image were calculated from 13 bR trimers and overlaid with the atomic structure. (**c**) Sketch of the membrane structure. (**d**) Lateral view of the atomic structure (*top*) of each intrahelical loop, and cross-sectional profiles (*bottom*) of topography (black) and stiffness (blue) along the arrows shown in (**b**). The blue dashed line shows the average stiffness of the lipidic region in (**b**). (Reprinted with permission from 33, Copyright (2011) American Chemical Society)

stiffness, which means low flexibility, are α-helices, while the areas with low stiffness, which means high flexibility, are the intrahelical loops. Figure 10.2d shows the E-F loop is the most rigid structure at low force and collapses at ~125 pN.

Besides elastic modulus mapping, with functionalized tips, PFQNM has been successfully used to recognize chemical groups in single protein molecules under physiological condition. A sub-nanometer resolution recognition map could be constructed in less than 30 min by 250 or 500 Hz ramp rate in PFQNM mode [34]. During each ramp cycle, the total force acting on the probe has three different components: the interaction, the hydrodynamic, and the inertial. With the increase in ramp rate, the hydrodynamic force and cantilever inertia contribute more, affecting the unbinding force measurement results. The ratio of cantilever resonance frequency and ramp rate should be at least 50 to make the contribution of hydrodynamic force and cantilever inertia negligible [35].

Similar to the situation of membrane proteins, the research on amyloid disease related proteins/peptides also requires more than high resolution morphology. High resolution mechanical mapping provides significant distinction between amyloid fibers with similar diameter but different internal assembling structure [36]. As the amyloid fibers are usually several nanometers in dimeter, additional care should be taken about elastic modulus fitting model. When doing the mechanical mapping, a spherical indenter on cylinder model may be better than the usually used spherical indenter on flat surface model [37].

1.3 Live Cells

It has been a dream for molecular cell biologists since the invention of AFM to achieve molecular resolution on cell surface under physiological condition. This ambitious task has been achieved on bacteria surfaces [38], where nanoscale net-like structures were revealed by AFM. However, direct “seeing” single proteins on a eukaryotic cell surface is still a challenge for AFM. The best reported result is the direct observation of the microvilli structure on live MDCK cell [39]. Microvilli are microscopic cellular membrane protrusions that increase the surface area of cells and minimize any increase in volume, and are involved in a wide variety of functions, including absorption, secretion, cellular adhesion, and mechanotransduction. Microvilli are very soft and are prone to damage even under sub-nN imaging force. With PeakForce tapping, microvilli on live cell were imaged for the first time. By using less than 100 pN imaging force, a lateral resolution better than 50 nm could be achieved on these soft and flexible structures. Figure 10.3 shows AFM images of a MDCK C11 cell by PeakForce tapping. Different imaging force and scan rate lead to different resolution of the microvilli.

The cell-wall peptidoglycan (PG) structure of Gram-positive bacteria is another topic attracting extensive attentions. The strong and elastic multi-layer PG is known to resist turgor pressure and determine the cell shape and growth; however, its architecture remains largely unknown. Dover R. S. et al. utilized high-resolution

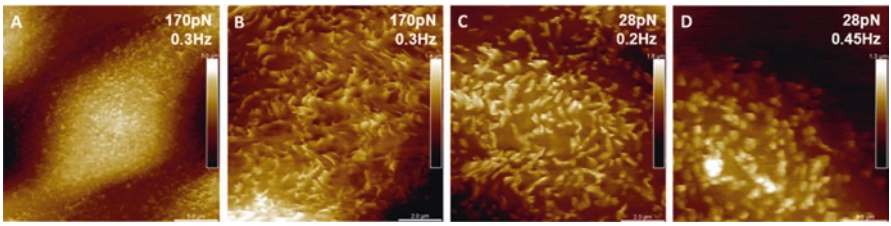

Fig. 10.3 Microvilli images of a MDCK C11 cell obtained with PeakForce tapping (Bruker Bioscope Resolve, PFQNM-LC probe). Individual microvilli were resolved on the cell surface. (**a**) Imaging force 170 pN, scan rate 0.3 Hz, 25 μm scan size. (**b**) Imaging force 170 pN, scan rage 0.3 Hz, 10 μm scan size. (**c**) Imaging force 28 pN, scan rate 0.2 Hz, 10 μm scan size. (**d**) Imaging force 28 pN, scan rate 0.45 Hz, 10 μm scan size. (Reprinted with permission from 39, Copyright (2015) John Wiley and Sons)

AFM to reveal how the structure and elasticity of PG change when subjected to increasing turgor pressure in live Group B Streptococcus (GBS) [38]. To respond the osmotic challenge, the net-like arrangement of PG stretches and stiffens.

Another example to study cell wall structure with PFQNM is the water sample from the Adriatic Sea [40]. Some cell wall remnants were found in this suspension. Figure 10.4 shows the structure and mechanical properties of this sample.

Besides the works on high resolution imaging of cell surface structures, many efforts have been made to observe internal structures of cells. For example, Usukura E. et al. developed an unroofing method which enabled the cantilever of AFM to directly reach into a cell to observe intracellular structure [41]. With this method, the intracellular cytoskeletal actin filaments, microtubules, clathrin coats, and caveolae were directly observed with high resolution in phosphate-buffered saline (PBS). Kumar S. et al. used small amplitude tapping mode in buffer conditions to image the membrane organization of intact vesicular bacterial photosynthetic "organelles", chromatophores, prepared from photosynthetically grown cells of Rba. Sphaeroides [42]. In this experiment, small cantilever was used to obtain faster response and lower thermal noise. Small tapping amplitude around 1 nm was adopted to minimize the imaging force in both vertical and lateral. With properly optimized imaging parameters, this approach provided sufficiently high resolution to allow proteins to be identified by their tertiary and quaternary structure, enabling the native organization of the proteins in a largely undeformed organelle to be studied.

In addition to high resolution morphological imaging and high resolution mechanical properties mapping, using functionalized probes to identify target molecules on live cell surface [43–45] and integrating AFM with advanced fluorescence techniques are two major trends in AFM developments for cell biology. For example, Alsteens D. et al. combined AFM and confocal microscopy to image the surface receptor landscape on cells and map the virus binding events within the first millisecond of contact with the cell at high resolution (better than 50 nm) [45]. Furthermore, by integrating AFM with inverted optical microscopy (IOM), the two coordinates can be linked together, i.e., fluorescently labeled bio-molecules could

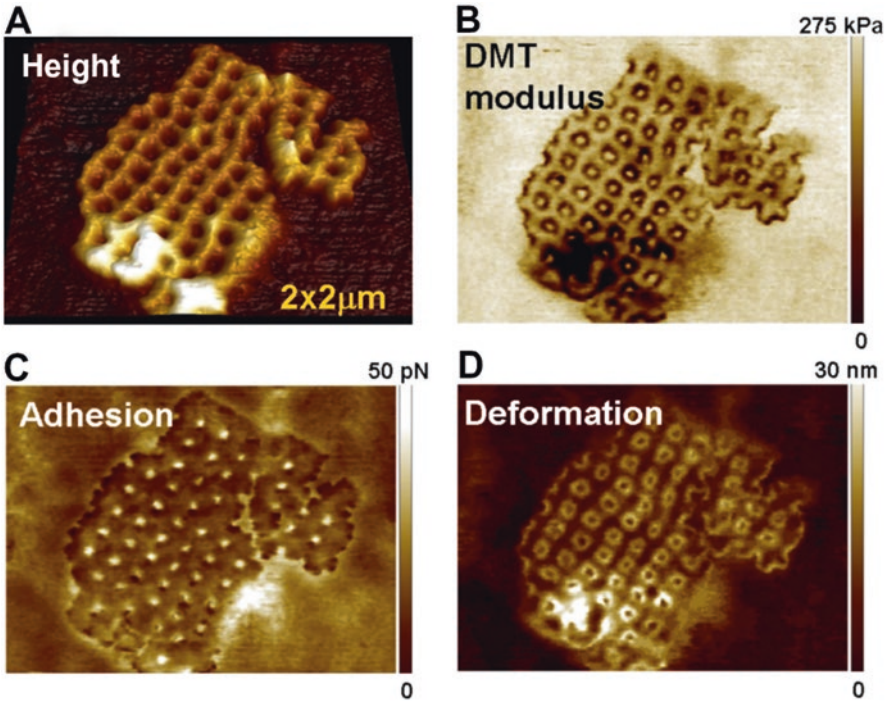

Fig. 10.4 PFQNM imaging of phytoplankton cell wall obtained on Bruker BioScope Catalyst system. (**a**) Topography image, (**b**) Young's modulus mapping, (**c**) Adhesion mapping, (**d**) Deformation mapping. (**b**) (**c**) (**d**) provide a remarkable contrast and high-resolution features. (Sample courtesy of Dennis Kunkel, Astrographics)

guide AFM measurement and their data could be fused together. Figure 10.5 shows an example to examine the differences in the mechanical properties of live and dead E. coli bacteria cells. In this study, a Bruker BioScope Catalyst (Santa Barbara, CA) was operated in PFQNM mode to image the cell surface while the Microscope Image Registration and Overlay (MIRO) function [40] was used to register epifluorescence images with the AFM images. By AFM topography image alone, a live and a dead bacteria cell cannot be easily distinguished. However, with the fluorescence images (Fig. 10.5c) we can easily and definitively identify the red-fluorescing dead cell at the top of the image from the two live cells – that are fluorescing green - at the bottom of the image. The deformation data (Fig. 10.5a) measure the deformation of the sample surface under the applied force by the AFM tip. Here, the deformation image reveals the live cells to have a fairly uniform deformation across the surface of the cell. The dead cell, however, appears more heterogeneous in deformation with definitive areas of increased deformation which indicate softer or less elastic surfaces. But in adhesion data (Fig. 10.5b), there is no difference. Fluorescence images can also be used to navigate the AFM probe to specific points on a surface to conduct force-distance curve measurements, which are shown in Fig. 10.5d.

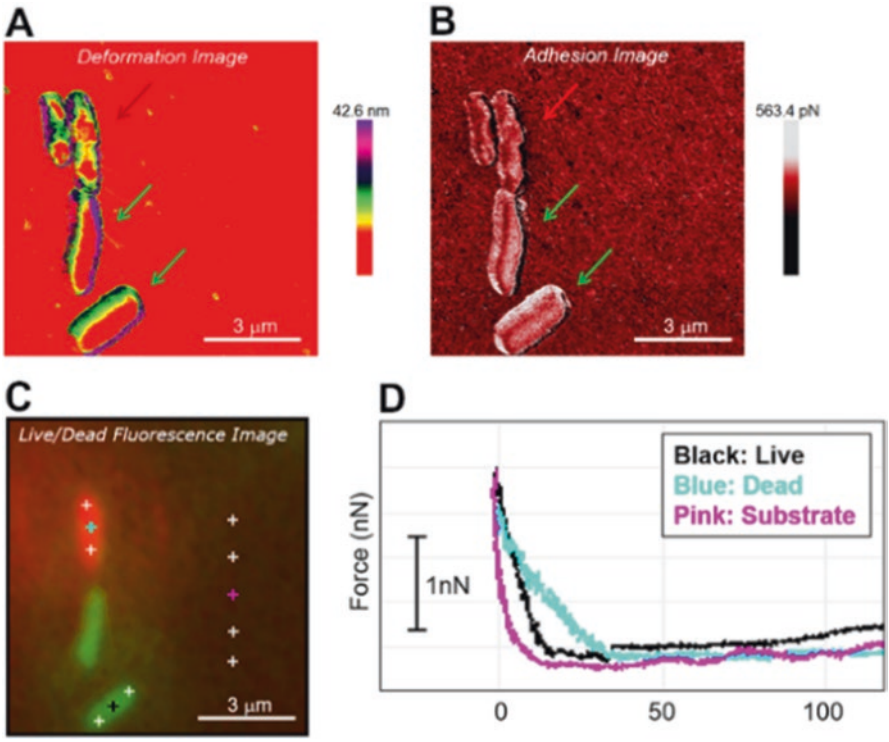

Fig. 10.5 Differences in the mechanical properties of live and dead E. Coli bacteria. (**a**) Deformation image shows dead cell is softer than live cell. (**b**) No obvious difference in adhesion image. (**c**) Fluorescence image can distinguish live (green) and dead (red) cells. The bacteria were labeled with a fluorescent live/dead assay. This image can be used to navigate the AFM probe to specific points to do force-distance curves. (**d**) Force curves measured at different locations. The result shows the stiffness order: substrate > live cells > dead cells

With the advances in AFM technology and experimental methods, researchers can now identify the binding steps of virus to animal cells through a single virus modified AFM tip [45], locate membrane sensor protein Mid2 on yeast cells by Ni^{2+}-nitrilotriacetate(NTA) groups modified tip [43], identify knob structures on P. falciparum infected erythrocytes by CD36 modified tip [44].

2 Challenges and Solutions in High Resolution AFM Imaging

AFMs usually use a feedback system to ensure that the probe accurately tracks the surface topography. The feedback system will continually compare the detector signal with the setpoint at real time. If they are not equal, a voltage is applied to the

scanner to move the probe either closer to or farther from the sample surface to bring the error signal back to zero. This applied voltage is usually used as the signal to generate an AFM image. Based on different feedback signals, there are 4 primary imaging modes of AFM, i.e. contact mode (or DC mode, static mode), amplitude modulation (AM) mode (or tapping mode, intermittent contact mode), frequency modulation (FM) mode (or non-contact mode) and PeakForce tapping (PFT) mode. FM mode is mainly used to image in vacuum environment, and will not be discussed in this chapter. Force control in the rest three imaging modes will be discussed in detail in this chapter.

2.1 Definition of "Resolution" in AFM Imaging

"Resolution" is one of the basic concepts in AFM imaging. AFM users and manufacturers always pursue high resolution imaging, but "resolution" is perhaps the most ambiguous term when people talk about it. Sometimes it is used to describe "the smallest feature one can observe", and sometimes it means "the smallest difference one can observe", sometimes "resolution" is used to describe pixel spacing or imaging size [46]. Some instrument manufacturers define "resolution" as "bit resolution", which means how many nanometers (or volts, pico-newton, etc.) 1 bit in digital-analog converter (DAC) corresponds to. Therefore, more attentions should be paid whenever "resolution" is discussed. In this chapter, "resolution" is defined as "the minimum distance by which two points must be separated for them to be recognized as separate".

2.2 Vertical Resolution of AFM

The vertical resolution of AFM is defined as the minimum step height that can still be recognized as two surfaces. Generally, the vertical resolution is equivalent to the noise floor of the AFM system, consisting of cantilever vertical deflection noise, Z scanner noise, environment acoustic and seismic noise. Environmental acoustic and seismic noise can be reduced by choosing quiet environment and implementing proper isolation. The vertical deflection noise can be plotted as a noise density spectrum. At low frequency range, the relationship of noise density versus frequency shows *1/f* trend. The lower the frequency, the higher the noise density. At high frequency range, the noise density is a constant (white noise) [6]. Figure 10.6 illustrate this relationship schematically. As a result, the imaging signal is subject to 1/*f* noise in contact mode while the low frequency noise has less effect in dynamic AFM if the drive frequency is higher than the *1/f* corner frequency (usually at several hundreds to thousands Hz).

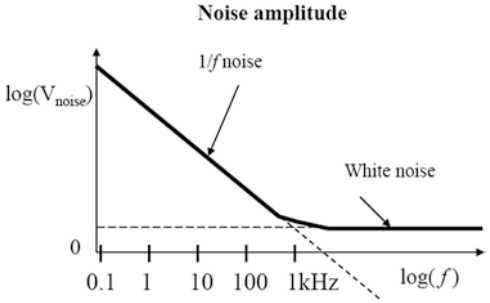

Fig. 10.6 Schematic diagram of noise density versus frequency. The noise density depends strongly on signal frequency. At DC and low frequency, the noise density is inversely proportional to the frequency; and at high frequency, the noise density is constant, called white noise

The vertical deflection noise includes two major components: one is the detector noise, which is also known as laser pointing noise, the other is thermal noise. The vertical deflection noise determines the detectable smallest change in vertical deflection, i.e. the ultimate resolution limit of an AFM. The power spectral density (PSD) of the vertical deflection noise is typically 100–1000 fm/$\sqrt{\text{Hz}}$. Many efforts were made to reduce this kind of noise, on some AFMs, even <10 fm/$\sqrt{\text{Hz}}$ PSD can be achieved in both air and liquid [47–51].

In dynamic AFM, thermal noise δz_{th} at frequency f_0 with detection bandwidth B can be calculated by following equation [52]:

$$\delta z_{th} = \sqrt{\frac{4k_B TQB}{\pi f_0 k}} \tag{10.1}$$

where k_B is the Boltzmann constant, T the absolute temperature, Q the quality factor, k the spring constant of cantilever. In general, cantilevers with higher spring constant and resonance frequency has less thermal noise. For the typical imaging bandwidth of 1 kHz, a typical cantilever for tapping mode (for example, $k = 28$ N/m, $Q = 400$, $f = 318$ kHz) has ~0.015 nm thermal noise at room temperature.

Z scanner noise is another factor affecting vertical resolution of an AFM. This noise is caused by the electronic noise in the high voltage applied to the scanner and the bit resolution of z drive DAC. The z scanner can be extended or retracted by applying a DC voltage on it, and this DC is applied via a z drive DAC. The bit resolution of the DAC determines the smallest step of the voltage. The electronic noise can be managed through optimizing electronic design and choosing proper bandwidth. Narrow bandwidth can reduce the electronics noise, but also limit the imaging speed. Therefore, a tradeoff between noise level and imaging speed must be made. If the Z scanner has the option to reduce z range, it will help on noise control for both sources.

2.3 *Lateral Resolution of AFM*

The "Lateral Resolution" of AFM is defined as the minimum separation for which the dimple depth Δz arising from the intersection of the individual images of two sample features is larger than the noise [53]. Reference [54] derived AFM lateral resolution based on the convolution between probe and sample features in details. Here we just illustrate the principle briefly. During AFM imaging, both the tip and sample are assumed undeformable. Figure 10.7a illustrates the dilation in AFM image due to the convolution between the tip and a sharp spike. Figure 10.7b shows the dimple depth formed by overlapping the dilated AFM images of two sharp spikes with the same height. In case that the sharp spikes have different height, the

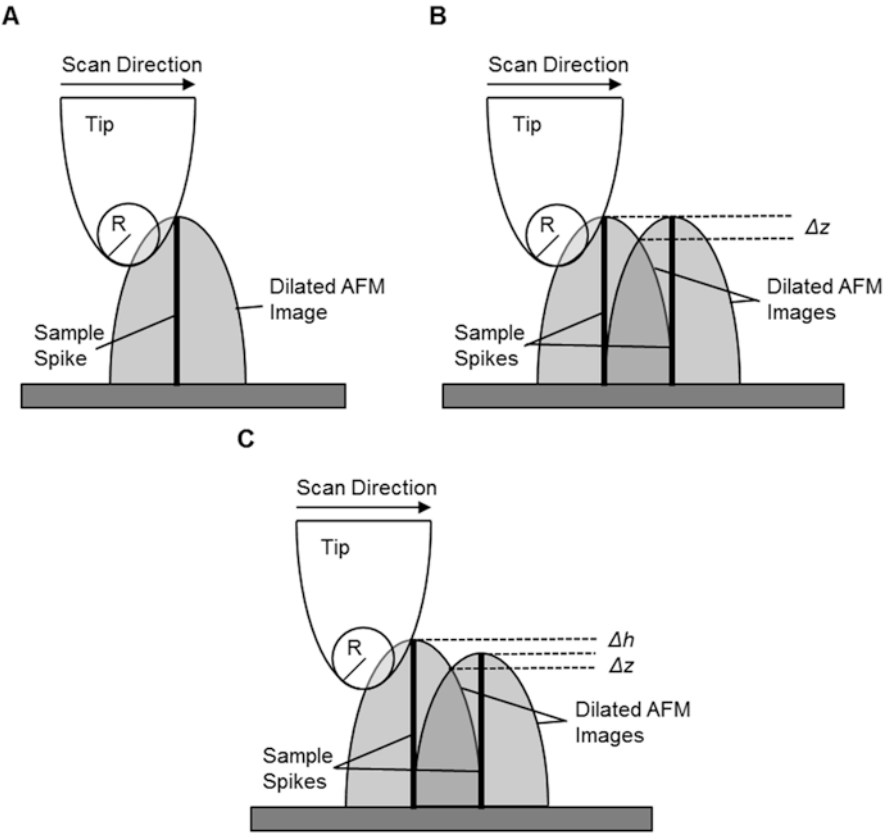

Fig. 10.7 Schematic of the convolution between AFM probe and sample features. (**a**) a sharp spike is dilated in AFM image due to the finite size of probe. (**b**) Overlap of the dilated AFM images of two sharp spikes with the same height. (**c**) Overlap of the dilated AFM images of two sharp spikes with different heights. R, Δz, Δh, and d are the tip radius, depth of the dimple, height difference between the spikes, and separation between two spikes respectively

dimple depth becomes less, as shown in Fig. 10.7c. If we define the lateral distance between the adjacent features as d, and the height difference between the adjacent features as Δh, tip radius as R, the minimum separation, i.e. the lateral resolution can be given by following equation when Δz converge towards vertical noise:

$$d = \sqrt{2R}\left(\sqrt{\Delta z} + \sqrt{\Delta z + \Delta h}\right)(d > \sqrt{2R\Delta h}) \tag{10.2}$$

From the above equation, if the surface is perfectly flat ($\Delta h = 0$), which is shown in Fig. 10.7b, the smallest d is achieved. As the height difference between the adjacent features increases, which is shown in Fig. 10.7c, the value of d increases, so the lateral resolution becomes worse. Therefore, flatter surface and sharper tip can lead to higher lateral resolution if the deformation of the tip and sample are negligible.

In case that the tip deforms the sample surface, the lateral resolution predicted by the above model might be inaccurate. Under such situation, the applied force increases the contact area, thus decreases the lateral resolution. A common rule here is that the lateral resolution cannot be better than the real or effective tip-surface contact area [54]. When the applied force is small, the deformation of the sample surface is usually elastic, so the surface can recover after the applied force is released. But for large applied force, the deformation of the surface may be plastic and irreversible, in such case, high resolution cannot be achieved. Therefore, the applied force should be small enough to make the tip-sample contact area smaller than the feature to be resolved. In case of true atomic resolution, the tip-sample contact area should be smaller than a single atom size. Some calculations have been done to find out the relationship between lateral resolution and applied force. If Hertz contact mechanism is applied on the tip-sample system, the lateral resolution l can be expressed as following equation [54]:

$$l = 2\sqrt[3]{\frac{3RF}{4E_{eff}}} \tag{10.3}$$

where R is the effective tip radius, F the applied force and E_{eff} the effective Young's modulus of the tip-sample system. According to this equation, high resolution is easier to achieve on stiffer sample. Sharp tip and low applied force are also vital for high resolution. The radius of curvature of the tip end will determine the highest lateral resolution obtainable with a specific tip. The sidewall angles of the tip will determine its ability to probe high aspect ratio features. Based on the above analysis, proper probe selection and good force control are the core issues in high resolution AFM imaging, and will be discussed in detail later in this chapter. In order to get high-resolution imaging on soft biological samples or polymer samples, force control is of paramount importance. Generally, less than 1 nN force is required for this kind of applications.

It should be noted that the above discussion is based on the sample deformation is less than the radius of curvature of the tip end. In case that the sample deformation is larger than the tip radius, the resolution achieved is poorer than that predicted by

Eq. 10.3. That is why sharper tip may not always lead to better resolution. If force control cannot be improved further to reduce sample deformation, a little bit blunter probe is worth a try.

The lateral resolution can also be affected by the number of pixels. According to Nyquist–Shannon sampling theorem [55], the pixel spacing should be less than half of the lateral resolution. For an image of a lateral size Δx with pixel number N, the lateral resolution cannot be better than $2\Delta x/N$. For high resolution imaging, number of pixels should be sufficient to make the tip-sample contact area as the limiting factor.

Atomic resolution is a frequently mentioned term when high resolution AFM imaging is discussed. However, atomic resolution is often confused with atomic lattice resolution. Atomic resolution of AFM is defined as the capability of AFM to resolve single or multiple atomic-scale entities separated by an atomic-scale distance. Atomic-scale entities include surface atoms, molecules, complexes, point defects, dislocations, and grain boundaries [1]. It is also called "true atomic resolution" [56]. On contrast, atomic lattice resolution refers to the AFM capability of revealing crystal lattice structure. Atomic lattice resolution is usually achieved in contact mode, and cannot show atomic defects in the image. Atomic lattice resolution is in general much easier to achieve than atomic resolution.

2.4 Key Elements in High Resolution Imaging on AFM

There are substantial number of factors affecting the final resolution of AFM imaging. In this section, four key elements will be discussed. If all of them are taken care carefully, high resolution imaging should be achieved most of time.

2.5 AFM System

A good system design is the foundation for high resolution imaging. To achieve high resolution, the AFM must have low noise, good scanner performance, low drift, and isolation from environmental noise and interference. Noise analysis and control have been discussed previously, and will not be covered in this section.

Drift is the undesired motion of the tip relative to the sample. If the AFM system is continuously drifting, the image will be distorted and it will be challenging to achieve high-resolution imaging. Drift control is an important task for AFM design and operation. When temperature changes, the thermal expansion of mechanical parts in AFM may cause relative motion between the tip and sample, called thermal drift. Typical values of expansion coefficients are in the range of 10^{-5} – 10^{-6} K^{-1}. For example, 1 °C temperature change in a 10 cm body will cause 1 μm change in its length. To obtain stable high resolution, a drift less than 0.2 Å/s is desirable [56]. A good AFM system can achieve 0.2 nm/min thermal drift or better. The thermal

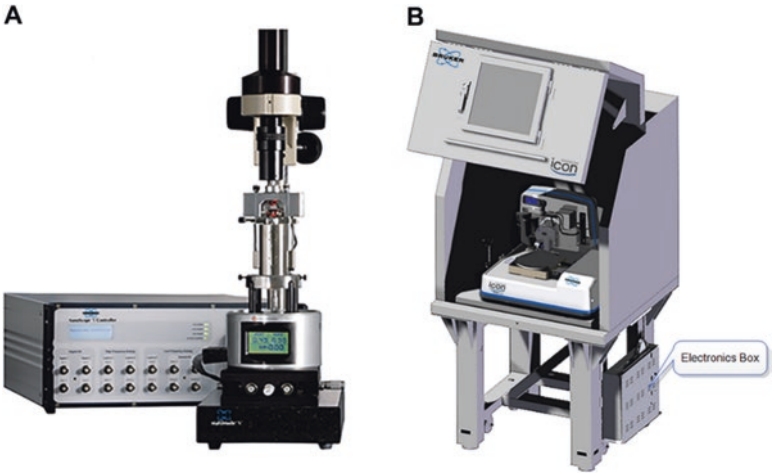

Fig. 10.8 Two examples of AFM designs to minimize thermal drift. (**a**) Bruker MultiMode system with a highly symmetrical structure. (**b**) Bruker Dimension Icon system with a remote electronics box to reduce heat generation in the acoustic enclosure

drift control is often achieved by both hardware and software. Symmetric design, choosing smart materials to match the thermal expansion of different components, and relocating heat generating components out of the acoustic enclosure are the commonly used approaches to minimize thermal drift. Figure 10.8 shows some AFM designs to reduce the thermal drift. In addition to hardware design, software is also used to compensate thermal drift, where software tracks features on the sample surface and calculates the drift direction and speed, then apply proper voltages to the XY scanner to correct the drift. One example is the "NanoTrack" function on Bruker Dimension Fastscan Bio system. With proper compensation, sub-pixel accuracy can be achieved with NanoTrack. Besides the hardware and software designs, temperature should be kept at constant during operation. Before high-resolution imaging, warm up and stabilizing the system at least half an hour is highly recommended. Increasing the scan speed is another commonly used approach to minimize the effect of thermal drift.

Environmental noise and interference also have deleterious effect on high resolution imaging. The environmental noise often contains seismic vibration from the floor and acoustic noise. The noise caused by seismic vibration is usually at low frequency. Figure 10.9 shows 2 Hz seismic vibration measured by AFM. The common vibration sources include large pumps, big fans, ventilation ducts, and so on. Removing the vibration sources around the system and high-performance vibration isolation table are necessary for high resolution imaging. Ideally, the vibration level in any direction should be better than vibration criteria D. Acoustic waves can couple into mechanical parts of the AFM system, causing noise in images. Even with proper acoustic enclosure, the environment acoustic noise should be less than 85 dBC (C weighting).

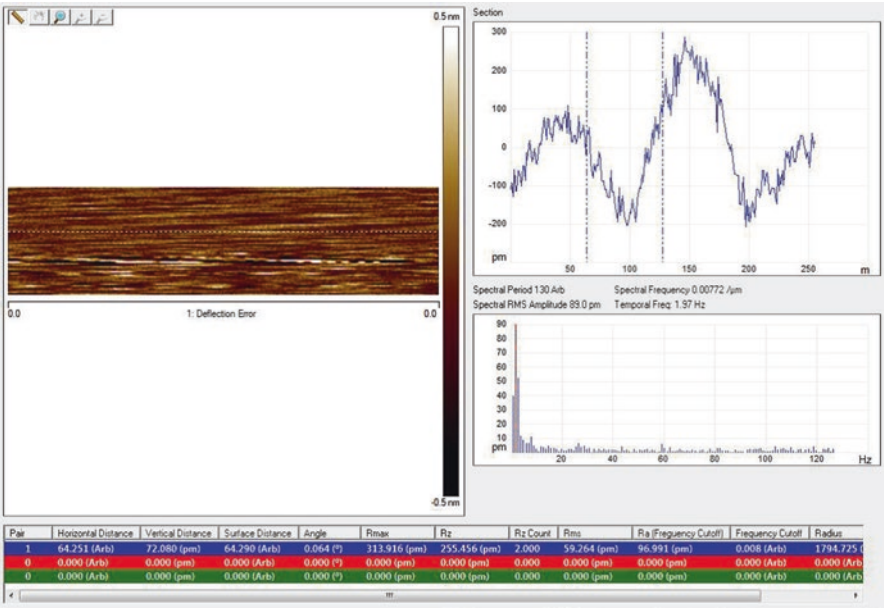

Fig. 10.9 AFM image shows 2 Hz seismic vibration

2.6 Probe

Probe is one of the major parts in AFM. It consists of three components: substrate, cantilever and tip. Substrate is used to hold the whole probe in a probe holder, cantilever is the force sensor and tip is used to interact with sample surface to form images. Both cantilever and tip affect image quality significantly.

Resonance frequency and spring constant are two critical properties of a cantilever. The resonance frequency affects the response time of the cantilever. In tapping mode, the change of amplitude with a change in tip-sample interaction is on a time scale $2Q/f_0$, where Q is the quality factor of the cantilever, while in frequency modulation, the change in frequency occurs within a single oscillation cycle on a time scale of $1/f_0$ [7]. So higher resonance frequency leads to faster response of a cantilever. If the AFM system is operated in vacuum environment, where Q is typically in the range of 10^4~10^5, tapping mode cannot work properly because it takes long time for the cantilever to respond to surface topography, while frequency modulation works in vacuum as the cantilever response time is independent of Q. Operating tapping mode in liquid allows faster scan due to the lowered Q factor in liquid. To reduce the deleterious effect of thermal drift, higher scan speed is always preferred, so cantilevers with high resonance frequency are usually used.

The spring constant affects the imaging force. In contact mode and PeakForce tapping mode, the operating frequency is far below the cantilever resonance frequency, the imaging force is proportional to the spring constant; while in dynamic AFM, the

operating frequency is near the resonance frequency, the imaging force is proportional to k/Q. As discussed previously, force control is one of the core issues in high-resolution imaging. Large imaging force may deform the sample too much and lead to tip wear. According to Eq. (10.3), large force and large tip end radius result in low lateral resolution. Therefore, cantilever with low k is preferred in high-resolution imaging. However, if the k is too low, the attractive force between tip and sample may pull the cantilever to jump to contact the surface in dynamic AFM modes. The tip crush may blunt the sharp tip end, or/and damage samples, lowering the image resolution as a result. In case of strong adhesion force between tip and sample, the cantilever may stop oscillation as it is stuck to the sample surface. For high resolution imaging, to avoid the "jump to contact", the following conditions must be fulfilled for stable operations [57]:

$$\left| \frac{d^2 V_{ts}}{dz^2} \right| < k \left| -\frac{dV_{ts}}{dz} \right| < kA_0 \tag{10.4}$$

where V_{ts} is the tip-sample potential and A_0 is the amplitude of the cantilever.

Another important parameter is "deflection sensitivity" (DS), with a unit of nm/V, which is the conversion factor describing how many nm in cantilever deflection corresponds to 1 V in PSPD output. As discussed in Chap. 1, shorter cantilever has better deflection sensitivity. In high resolution imaging, short cantilever is preferred. It should be noted that the cantilever length discussed above is the effective length. When the laser spot position on cantilever changes, the effective length changes accordingly.

In summary, cantilevers with short length, high resonance frequency and low spring constant are preferred for high resolution imaging. To meet all these requirements, the cantilevers should be small and thin. In addition, small cantilevers suffer less hydrodynamic damping when operated in fluid.

Since AFM tip physically scans on the sample surface, the image obtained is always the convolution of tip shape and the actual sample surface topography. Therefore, tip shape and size play significant roles in image quality. If the tip goes bad, the image quality will degrade. The bad tip could be caused by tip contamination, double tip, or tip wearing. Figure 10.10 shows the typical situations of tip-sample convolution.

Based on the previous discussion, the end radius of a tip intensively affects the lateral resolution. But more attention should be paid when specific situation is discussed. The same probe may have different tip end radii under different applications. As shown in Fig. 10.11a, different indentation has different effective end radius for a conical tip. For soft samples, the small load force may lead to large indentation, which means, even the very end of the tip may be very sharp, the effective end radius may not be suitable for high resolution imaging. Conversely, the tip with large nominal end radius may have irregularities or sharp spikes on the tip surface, as shown in Fig. 10.11b. One of the sharp features can be used for high resolution imaging if the imaging force is controlled properly.

In summary, for high resolution imaging applications, a probe with smaller and softer cantilever, higher resonance frequency, and sharp tip should be chosen for higher sensitivity in detecting tiny change in topography and better force control.

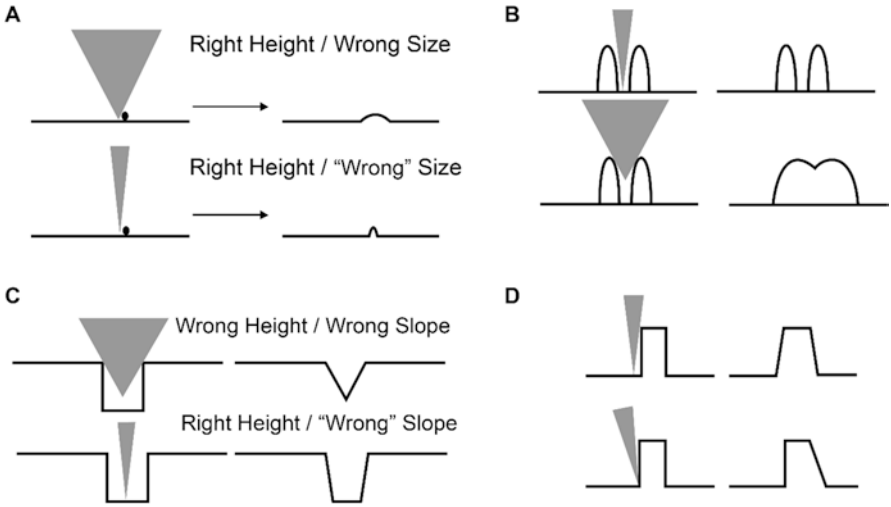

Fig. 10.10 Typical situations of tip-sample convolution. (**a**) Both tips with large and small end radius can get right height but wrong size of the particles on flat surface. The size of the particle is closer to its real value if the tip end radius is smaller. (**b**) Tip with smaller end radius can resolve two hills but the one with big end radius cannot. (**c**) Tip with smaller end radius can resolve right height of a valley but the one with large end radius cannot. Both of them cannot get right slope. (**d**) The tip side angle also affects the slope measurement

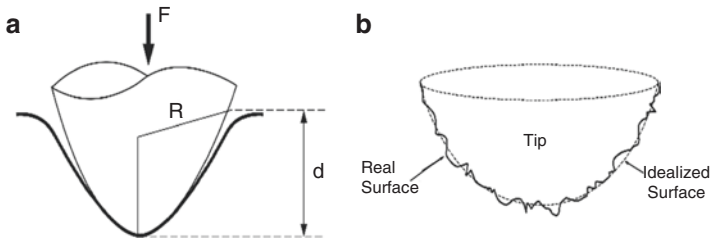

Fig. 10.11 The definition of the tip end radius. (**a**) A cone tip has different end radius at different indentation depth. (**b**) A tip with large end radius may have some irregularities on the very end, enabling high-resolution imaging

2.7 Force Control

In the lateral resolution section, the relationship between lateral resolution and applied force was discussed, showing that sample deformation increases with the increase in applied force and it leads to poor lateral resolution. Therefore, it is vital for high resolution imaging to use minimal imaging force. The interactions between tip and sample are very complex, especially in liquid environment. This topic has been reviewed in detail [1, 55, 58]. For simplicity, only the aspects affecting

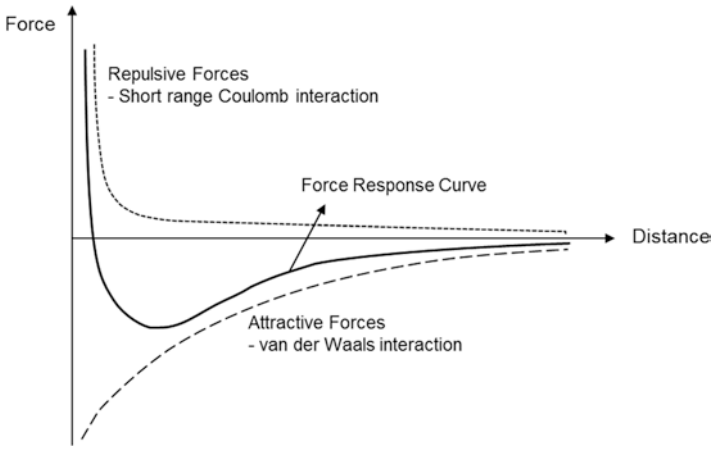

Fig. 10.12 Schematic diagram to illustrate the interaction between two objects versus distance. The short-range repulsive force originates from Coulomb repulsion at short ranges due to electron orbital overlapping, and the long-range attractive is from the van der Waals interaction at long ranges. The solid line indicates the total force

imaging resolution will be discussed in this chapter. Figure 10.12 shows the relationship between the total force and tip-sample separation. The total force is considered as the sum of repulsive and attractive forces. The repulsive force is typically short-range, mainly comes from coulomb repulsion induced by electron orbital overlapping, which can be well described by various contact mechanics models. Attractive force is typically long-range, mainly comes from Van der Waals interaction. In ambient environment, a meniscus is formed between probe and sample by spontaneous condensation, resulting in capillary force with a magnitude ranging from 1nN to 100nN. The meniscus formation between AFM tip and sample was directly observed with Environmental Scanning Electron Microscopy (ESEM) by Weeks B. L. et al. [59]. The capillary force could dominate all other tip-sample interactions [54] in ambient environment. It will be eliminated in liquid. While capillary force is eliminated in liquid, the electrostatic double-layer (EDL) generates repulsive force between tip and sample. The EDL force can be long-ranged or short-ranged, which can be fine-tuned by adjusting the ion concentration, pH, temperature and the type of solutions [1]. The electrostatic force has been used to balance the attractive force between tip and sample and reduce the net tip-sample interactions [60, 61]. Figure 10.13 shows the balancing effect of electrostatic force.

Previous studies show that repulsive force is more localized [6, 62, 63], thus, using minimal short-range tip-sample interaction is preferred for high resolution imaging. A good force control means the imaging force is controlled instantaneously and intuitively at the minimal short-range tip-sample interaction. In this section the force control for different AFM working modes will be discussed in detail.

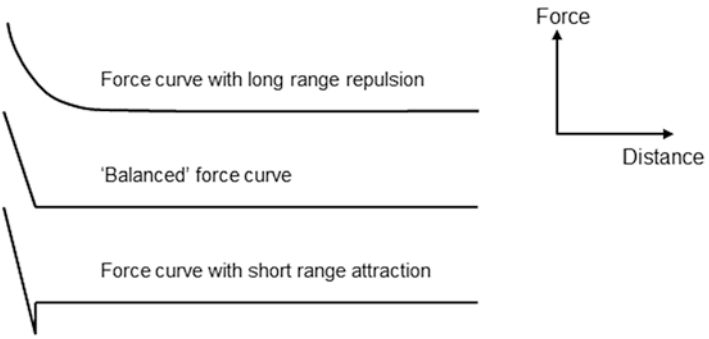

Fig. 10.13 Force distance curves to illustrate different states of force balancing. When the forces are well balanced, the net tip-sample interaction is minimized, shown in the middle curve. The top and bottom curves show the situations that long-range repulsive force dominates and short-range attractive force dominates respectively. In the bottom curve, "jump to contact" or "snap in" happened

2.7.1 Contact Mode

In contact mode, AFM uses a static cantilever deflection as the feedback signal. In this mode, the tip is in perpetual contact with the sample surface. During a scan, the changes of surface topography causes changes in cantilever deflection. The feedback loop maintains a constant deflection by vertically moving the scanner at each location. The constant deflection is called deflection setpoint. As discussed in Chap. 1, the force applied by cantilever is proportional to its spring constant and thus cantilevers with low spring constant are preferred for high resolution imaging [6].

It seems that force control in contact mode is easy and intuitive, however, it is much more than choosing soft cantilevers. In ambient environment, capillary force can cause strong interaction force between probe and sample, even the force applied by cantilever deflection is small. In addition to the large normal force, the shear force in lateral direction always exists, which can cause the image distortion, sample scratch, and tip wear. Due to the issues caused by capillary force, true atomic resolution achieved by contact mode has rarely been reported. The classic work on true atomic resolution by contact mode was achieved by Ohnesorge F. et al. in 1993 [56]. In this work, the true atomic resolution of the (10$\underline{1}$4) cleavage plane of calcite was obtained by immersing tip and sample in liquid. To compensate the attractive forces on the cantilever and resist "jump to contact", a magnetically controlled feedback mechanism was designed by Jarvis S. P. et al. [64]. In addition to these experimental achievements, theory study was also carried to answer the question "can contact mode achieve true atomic resolution?" [65]. Total-energy pseudopotential calculations show that in the case of a diamond tip and a diamond surface, it is possible for a tip terminated by a single atom to sustain forces more than 30 nN, enabling true atomic resolution, but imaging at true atomic resolution may be limited by the blunting of the tip during lateral scanning.

Cantilever deflection drift is another challenge for contact mode imaging, especially for soft cantilever in liquid. As discussed in Chap. 1, the deflection drift prevents users from using minimal setpoint. To overcome this issue, warming up AFM till thermal equilibrium and increasing scan speed are commonly used approaches.

Instead of atomic resolution, contact mode is often used for atomic lattice resolution imaging. As early as 1987, atomic lattices of graphite and boron nitride were reported [66–68]. These images are pseudo atomic images, which show lattice periodicity only, and no atomic defect is observed. The atomic lattice resolution usually does not require minimal normal force and sharp probes, where both tip and sample are deformed by the repulsive force. The tip-sample contact area is much larger than that required by atomic resolution. Morita S. et al. proposed a 2D stick-slip model to explain the lattice periodicity obtained in contact mode [8]. Figure 10.14 shows several examples of atomic lattice resolution achieved by contact mode.

Biological and polymer samples usually do not require atomic resolution, where molecular or sub-molecular resolution is of great interest. Molecular sub-units on purple membranes adsorbed on mica were imaged in buffer solution with contact mode on Bruker Nanoscope III system by Muller D. J. et al. [61]. In this work, to obtain sub-nanometer resolution on purple membrane, the EDL force was carefully controlled by adjusting pH, ionic concentration and buffer solution types. The forces acting on tip were partly canceled and the net tip-sample interaction decreased to ~100 pN. One example of overcoming cantilever drift to achieve high resolution imaging was reported by Czajkowsky D. M. et al., where perfect sub-nanometer images of Perfringolysin O (PFO) prepore complex associated with support, cholesterol containing lipid bilayers were obtained in contact mode on Bruker MultiMode system [69]. In this work, imaging force was controlled at ~100 pN by a cantilever

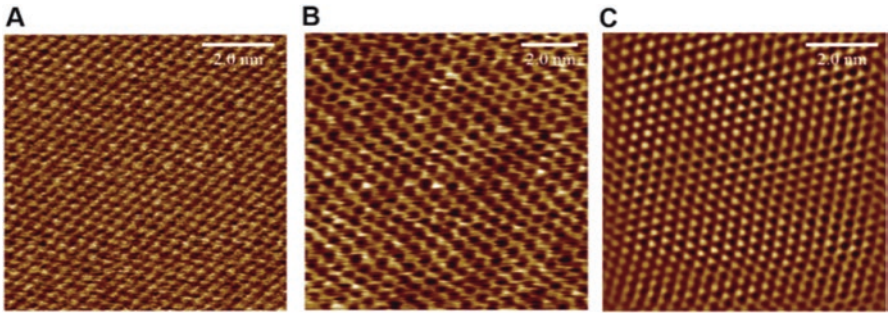

Fig. 10.14 Atomic lattice resolution images obtained under contact mode, friction channel. (**a**) HOPG atomic lattice resolution obtained on Bruker Dimension Icon system with SNL-A probe at 6 Hz scan rate. (**b**) Mica atomic lattice resolution obtained on Bruker MultiMode 8 system with SNL-C probe at 60 Hz scan rate. (**c**) MoS_2 atomic lattice resolution obtained on Bruker Dimension Icon system with MLCT-F probe at 10 Hz scan rate

with a spring constant of 0.06 N/m, which corresponds to 0.024 V in deflection setpoint. It is a challenge in contact mode as the vertical deflection may drift more than 0.05 V/min in case of soft cantilever in liquid. That is why the sub-nanometer resolution images were obtained at 9 Hz scan rate in this work.

In summary, contact mode AFM can achieve true atomic resolution and sub-nanometer resolution, but capillary force, EDL force, and cantilever deflection drift must be taken care in addition to choosing proper cantilevers.

2.7.2 Tapping Mode

In tapping mode, AFM uses cantilever oscillation amplitude as the feedback signal. In this mode, the cantilever oscillates at a frequency close to its resonance. During a scan, the changes in surface topography cause changes in cantilever oscillation amplitude. The feedback loop maintains a constant amplitude by vertically moving the scanner at each location. The maintained constant amplitude is called amplitude setpoint. This mode eliminates lateral force, generates less damage on sample and less tip wear. The imaging force is controlled by amplitude, which is not a direct measurement of tapping force, but a force average during each tapping cycle. Therefore, force control in tapping mode is not instantaneous, making force control in tapping mode more complicating than contact mode.

Since the invention of tapping mode, the efforts to understand the cantilever dynamics have never stopped. The peak force in each tapping cycle plays a critical role in imaging resolution and tip wear. To understand the peak force, Hu S. et al. derived analytical expressions of peak attractive and repulsive forces by using nonlinear asymptotic theory and proved that the peak force in tapping mode is closely related to the ratio of amplitude setpoint to its free amplitude [70]. For illustration purpose, the relationship is shown in Fig. 10.15. It is easily seen that 1) Smaller free amplitude leads to smaller peak force; 2) For constant free amplitude, with the decrease in amplitude setpoint, the tip-sample interaction force first increases, then decreases. The maximum force is reached at the relative setpoint of about 0.5. To control tapping force for high resolution, small free amplitude and optimized setpoint should be used to avoid tip wear and sample damage.

The experimental verification of the relationship discussed above was done by Su C. et al. [71], where the tip wear under different amplitude setpoint was studied. In this work, an OTESPA probe (Bruker, Santa Barbara, CA) with a spring constant of about 40 N/m was used to image a Tip Check RS sample (Bruker, Santa Barbara, CA). In all scans, the free amplitude was set to 44 nm, the scan size was 1.5 μm and scan rate was 0.3 Hz. Feedback gains were optimized to make the tip track the surface properly. The results are shown in Fig. 10.16, where (**a**)–(**c**) are three topography images obtained in succession at ~4.4 nm amplitude setpoint, (**d**)–(**f**) and (**g**)–(**i**) are topography images obtained at amplitude setpoint of ~22 nm and 35.2 nm, respectively. For each amplitude setpoint, a new probe was used to image the sample several times, and the image degradation was then compared. The results prove that at low (10%) (Figs. 10.16a, b, c) and high (80%) (Figs. 10.16g, h, i)) amplitude

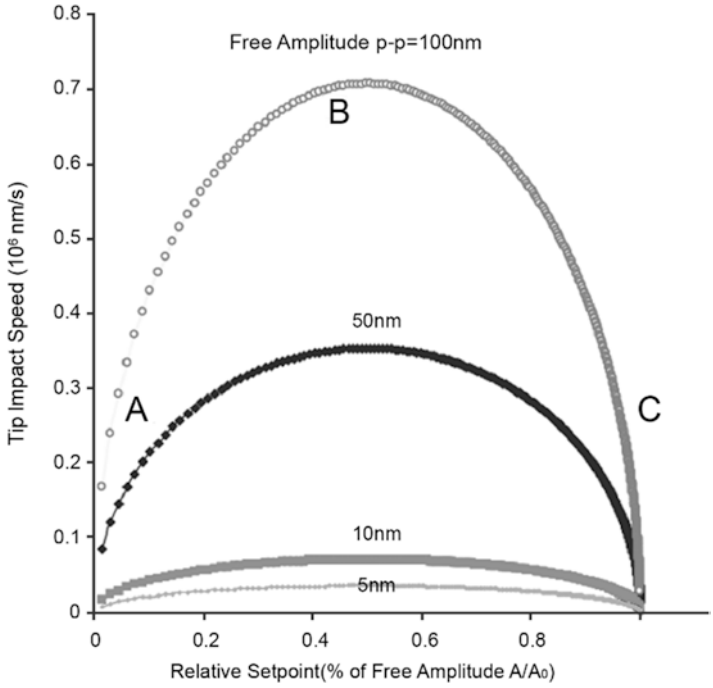

Fig. 10.15 The relationship between the tip impact speed and relative setpoint (amplitude setpoint divided by free amplitude). The tip impact speed is in general proportional to the impact force

ratio, the imaging force is relative small and the tip sharpness is maintained but at medial (50%) (Figs. 10.16d, e, f) amplitude ratio, the imaging force is large enough to blunt the tip quickly.

Based on the relationship between tapping force and amplitude ratio, low imaging force can be achieved at both high and low amplitude settings. In routine tapping mode operation, high amplitude ratio (~60%–80%) is commonly used, but for very flat sample, low amplitude ratio can produce higher resolution. Su C. et al. used low amplitude ratio to image flat samples, this kind of operation is also called "low force tapping", compared with "normal tapping" [71]. In low force tapping, low amplitude setpoint results in much faster error generation, allowing feedback loop to run at higher bandwidth. This makes tip track surface better and faster. A polysilicon surface was imaged by normal tapping mode and low force tapping on Bruker Dimension V system with OTESPA probe (Bruker, Santa Barbara, CA). The images obtained by "normal tapping" and "low force tapping" are shown in Fig. 10.17. The image obtained by normal tapping produces a Root Mean Square Roughness (R_q) of 0.349 nm, while 0.618 nm for low force tapping. Obviously, low force tapping produces higher resolution. However, it's noteworthy that the low amplitude operation may reach zero tapping amplitude at some points if the sample height variation is too much and scan speed is too high. Zero tapping amplitude means tapping mode

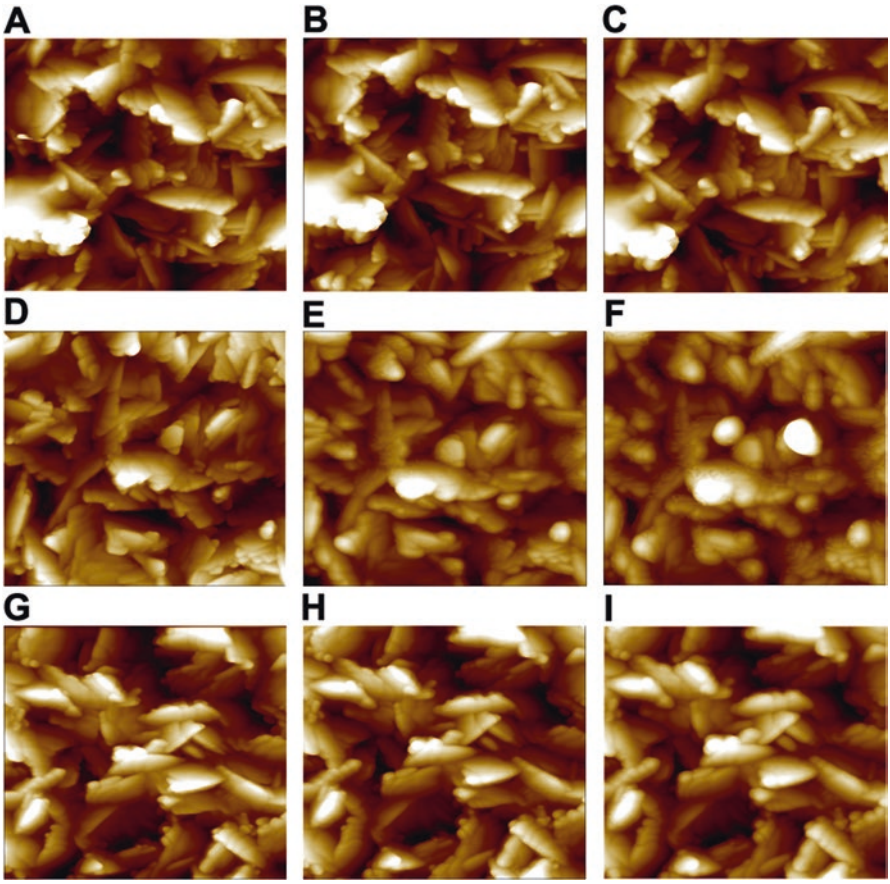

Fig. 10.16 Tip wear under different amplitude setpoint in tapping mode. (**a**)–(**c**) are three topography images obtained in succession at ~4.4 nm amplitude setpoint. So are (**d**)–(**f**) and (**g**)–(**i**) but the amplitude setpoint is ~22 nm and 35.2 nm, respectively

is converted to contact mode, causing tip wear and sample damage. Therefore, low amplitude tapping is good for flat sample surfaces, but not for rough ones.

Due to the nonlinear characteristics of both attractive and repulsive forces, two stable oscillation states coexist in the tip-sample system [72–75], i.e., two solutions to the equation of motion. One state is the tip works in pure attractive regime, the other is the tip mainly works in repulsive regime. The two states have different oscillation amplitudes and phases. In attractive regime, the tip senses long range interaction, produces lower resolution in general. On contrast, repulsive force is short range interaction. In addition, the tip can penetrate through adsorbed water layer on sample surface, which usually happens in ambient environment. Therefore, tapping in repulsive regime often gives more details and sharper images. Besides

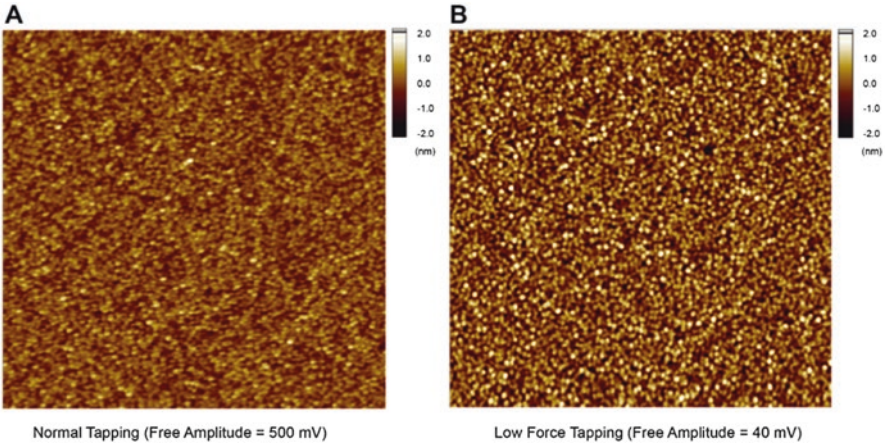

Fig. 10.17 The topography images of polysilicon obtained with (**a**) "normal tapping" and (**b**) "low force tapping" mode. Both images were obtained on Bruker Dimension V system with OTESPA probe, scan size 1 μm × 1 μm, and scan rate 1 Hz

lower resolution in attractive regime, the phase contrast is also low. Figure 10.18 shows the images obtained in attractive regime and repulsive regime. In attractive regime, the features look larger and almost no phase contrast. However, in repulsive regime, the features look sharper and more details can be observed. Phase contrast is clear and the measured roughness is higher. Operation in repulsive regime often produces the higher resolution in both topography and phase images.

For soft biological samples, the situation might be different. When operated in repulsive regime with large force, the tip may deform the soft sample significantly, making high resolution imaging impossible. San Paulo A. et al. studied the performance of both regimes to image single antibody molecules [76]. In attractive regime, the Y-shaped domains of a-HSA molecule can be resolved but in repulsive regime, the large imaging force causes irreversible deformation of the molecule, leading to significant loss in resolution. The imaging forces in two regimes are 0.4 nN and 3.5 nN, respectively. In conclusion, operating in repulsive regime should be preferred for imaging stiff surface, whenever the sample deformation is not an issue [7].

The tricky part in tapping mode imaging is the two states can transit to each other even during one scan. During the transition, one amplitude may correspond to two z values and two-phase values, which generates artifacts in image, as shown in Fig. 10.19. To prevent state transition, proper imaging parameters usually help. It helps keep AFM working in repulsive regime by setting oscillation frequency lower than its resonance and optimizing amplitude setpoint to make it out of bi-stable regime. However, it is not easy to keep AFM always working in attractive regime. By setting oscillation frequency higher than its resonance, adopting small amplitude, and clean imaging environment, the chance that AFM stays in attractive regime increases.

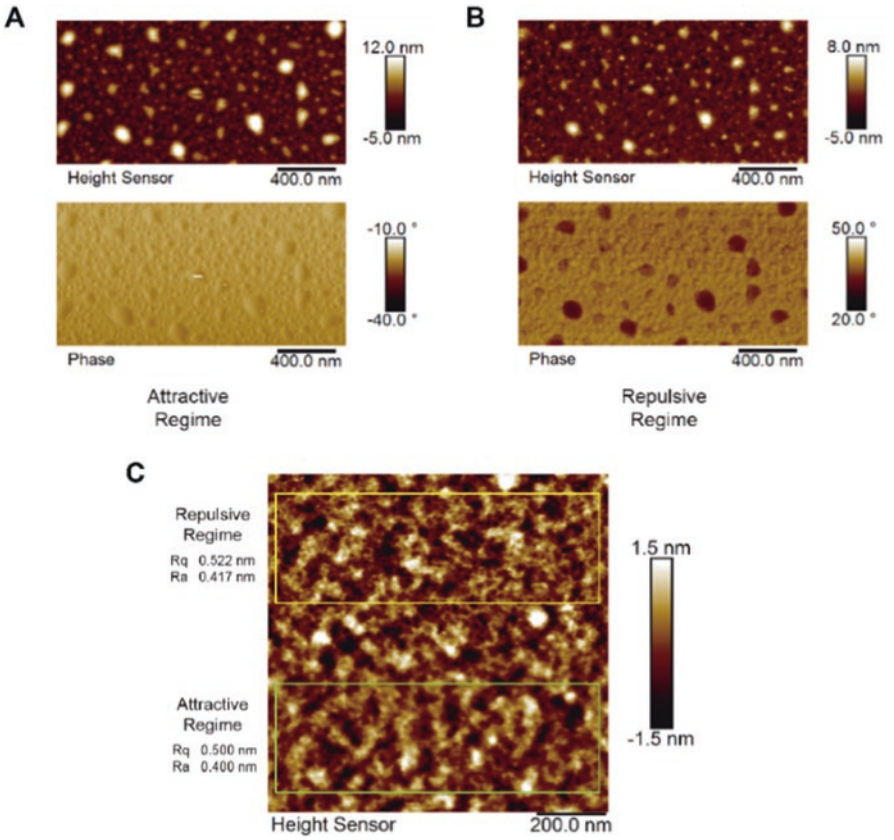

Fig. 10.18 AFM images obtained in attractive and repulsive regime. (**a**) The topography and phase image of a polymer sample obtained in attractive regime. The features are larger and phase contrast is almost indiscernible. (**b**) The topography and phase image of a polymer sample obtained in repulsive regime. The features are sharper and phase image clearly shows the material contrast. (**c**) One image on a polymer sample obtained in both regimes. The topography image obtained in repulsive regime provides more details and has larger measured roughness

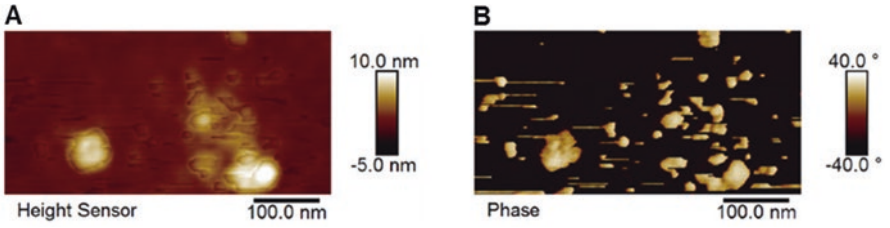

Fig. 10.19 Artifacts induced by the transition between bi-stable states. (**a**) is topography image and (**b**) is Phase image

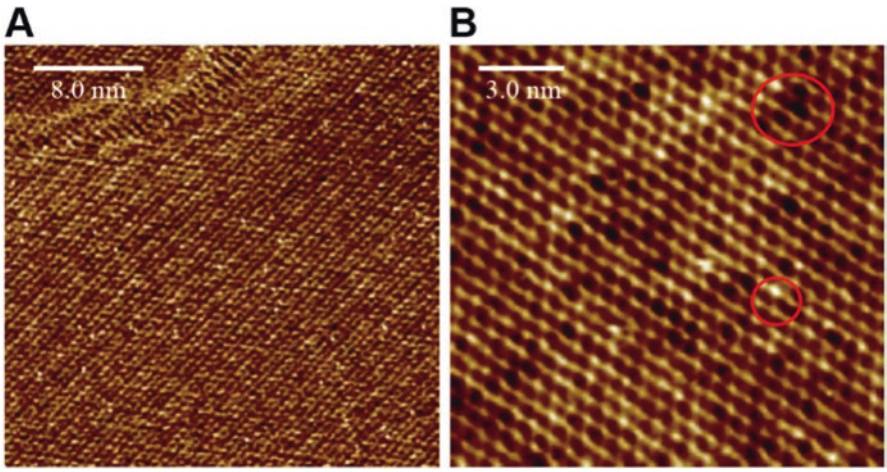

Fig. 10.20 Atomic resolution images obtained with tapping mode in liquid. (**a**) Calcite true atomic resolution obtained on Bruker Dimension Icon system with SNL probe at 16 Hz scan rate. (**b**) Mica true atomic resolution obtained on Bruker MultiMode 8 system with SNL probe at 5 Hz scan rate. The red circles indicate some atomic defects

Despite of the complicating force control in tapping mode, atomic resolution can be achieved in tapping mode. It is usually achieved in liquid environment with small amplitude tapping. Small amplitude helps screen out the long-range force and minimize the imaging force. Imaging in liquid is to eliminate the capillary force to prevent the tip from being stuck to the sample surface. Ohnesorge F. M. et al. used a rather stiff cantilever to make the non-contact attractive regime accessible by preventing jump-to-contact and obtained the calcite lattice in water [77]. In addition to the crystal surface, Voitchovsky K. et al. reported atomic and molecular resolution on both inorganic and organic samples using small amplitude tapping in liquid [78]. Figure 10.20 shows some examples of true atomic resolution achieved by tapping mode.

As discussed in contact mode section, molecular and sub-molecular resolution are of more interest for biological samples and polymer samples than atomic resolution. High resolution imaging on biological and polymer samples has been reported. For example, rhodopsin dimers in native disc membranes were imaged in liquid [79], and true molecular scale imaging of organic crystals of polydiacetylene (PDA) was obtained in air [80]. In the authors' opinion, the true molecular resolution results from 1) low thermal drift (<0.5 nm/min) of the AFM system (Bruker Dimension 5000); 2) small amplitude (7~8 nm); 3) the carbon-spiked probe with sharpness of tip apex (1~3 nm).

In summary, tapping mode can achieve true atomic resolution and molecular resolution with proper force control. To eliminate the capillary force, imaging in liquid is the commonly used method. Cantilever oscillation frequency and amplitude must be optimized to avoid bi-stable state transition and achieve low imaging force, which are critical for high resolution imaging.

2.7.3 PeakForce Tapping Mode

PeakForce Tapping (PFT) mode is a breakthrough new AFM imaging mode introduced by Bruker in 2009 [81, 82]. In this mode, the probe is moved up/down by piezo sinusoidal motion at a frequency much lower than its resonance. In each cycle, the probe contacts the sample surface intermittently and the maximum force or peak force is extracted and used as feedback signal. During a scan, the changes in surface topography cause changes in peak force. The feedback loop maintains a constant peak force by vertically moving the scanner at each location. The constant peak force is called PeakForce setpoint. With the patented background subtraction and synchronization algorithm [82], imaging force at pN can be achieved, making it possible to image very fragile samples. In fact, the system performs a very fast force-distance curve measurement at every pixel, which can be used to calculate mechanical properties. In PFT, the cantilever works at a frequency much lower than its resonance and no cantilever dynamics needs to deal with. PFT works under quasi-static mode and the force on the cantilever is simply determined by Hooke's law, like contact mode. Therefore, the control logic in PFT is as simple as contact mode. As PFT measures the complete force-distance interaction at every pixel, the system always knows the force at every moment. The simplified feedback mechanism makes PFT more stable. On the other hand, the force sensitivity enhancement by cantilever quality factor Q is lost in PFT due to the off-resonance operation, unlike tapping mode where force sensitivity is enhanced by operating cantilever at its resonance. The force sensitivity in PFT is achieved by using soft cantilevers.

Background subtraction and synchronization algorithm are the two core technologies in PFT to reduce the imaging force down to pN level. Vertical deflection drift is corrected at each force curve, and will not affect force control in PFT, unlike contact mode. The fundamental working principle makes PFT feedback loop extremely simple and robust. Users can control the imaging force instantaneously and intuitively at the lowest short-range tip-sample interaction, making it an easiest way to do high resolution imaging in ambient conditions.

To understand the relative importance of proximity and tip radius on spatial resolution, a theoretical simulation was carried out to evaluate the van der Waals interaction between a spherical tip and a flat surface. As shown in Fig. 10.21a, the total tip-sample interaction is obtained by integrating the interaction over the whole surface. The interaction originating from the region limited by Y_0 underneath the tip can also be calculated. With that, we know how many percent of the total interaction is contributed by the region limited by Y_0. The numeric simulation results are shown in Figs. 10.21b, c. For a tip end radius of 10 nm, 80% of the interaction comes from the region $Y_0 = 1.2$ nm if tip-sample separation is 1 nm, while the corresponding region will increase to $Y_0 = 8.5$ nm if tip-sample separation is 10 nm, as shown in Fig. 10.21b. If the tip-sample separation is fixed at 1 nm, surprisingly, the tip radius does not have a huge effect on the resolution. In this case, a tip radius of 1 nm reaches the 80% mark at $Y_0 = 0.85$ nm, while a tip radius of 10 nm gets there at $Y_0 = 1.23$ nm. In other words, if the tip is kept close to the sample surface, but not too close to increase tip-sample contact area significantly, high-resolution imaging

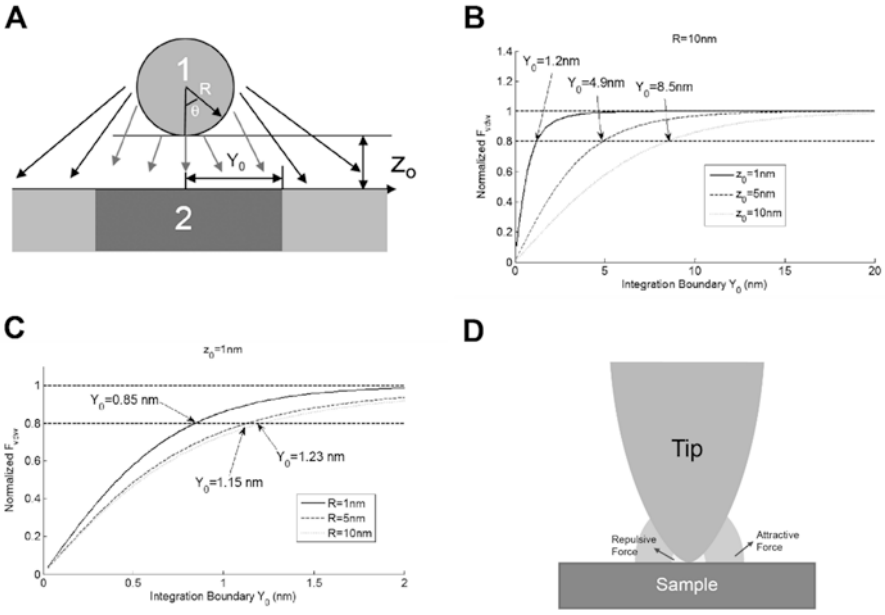

Fig. 10.21 (**a**) Model for theoretical simulation to examine the van der Waals interaction between a spherical tip and a flat surface, where two bodies 1 and 2, tip radius R, tip-sample separation z_0 and lateral resolution Y_0 are defined. The simulation results are shown in (**b**) and (**c**). (**b**) With fixed tip radius, change in tip-sample separation cause the lateral resolution changes significantly. (**c**) With the tip-sample separation fixed at 1 nm, the change in tip radius does not change lateral resolution much. (**d**) When the tip is kept close but not too close to the sample surface, the total peak force is attractive and only the apex of the tip senses the repulsive force. This "lowest short-range interaction" is the source of true atomic resolution

can be achieved even the tip is not very sharp. In tapping mode, this is not easy to achieve as the force control is not instantaneous and intuitive. While in PFT, AFM system knows the interaction force between tip and sample at every moment, and the background subtraction mechanism guarantees that the peak force setpoint does not drift like contact mode, the imaging force suitable for high resolution can be easily achieved. True atomic resolution on appropriate surface can be achieved by PFT when operating with the minimum interaction force, where the repulsive interaction is used for feedback loop control, which arises from the Pauli and ionic repulsions between the atoms on very apex of the probe and the atoms/molecules on the sample, as illustrated in Fig. 10.21d. Under such scenario, the total peak force is still attractive and only the apex of the tip senses the repulsive force. This "lowest short-range interaction" is the source of true atomic resolution.

Atomic resolution images of mica and calcite can be routinely obtained by PFT in liquid. With "PeakForce Capture" function, force-distance curves can be captured along a selected line or the whole image for further analysis. Figure 10.22 shows examples of atomic resolution achieved by PFT in liquid. However, observing atomic defects in air is still a challenge. The major reasons are that sample

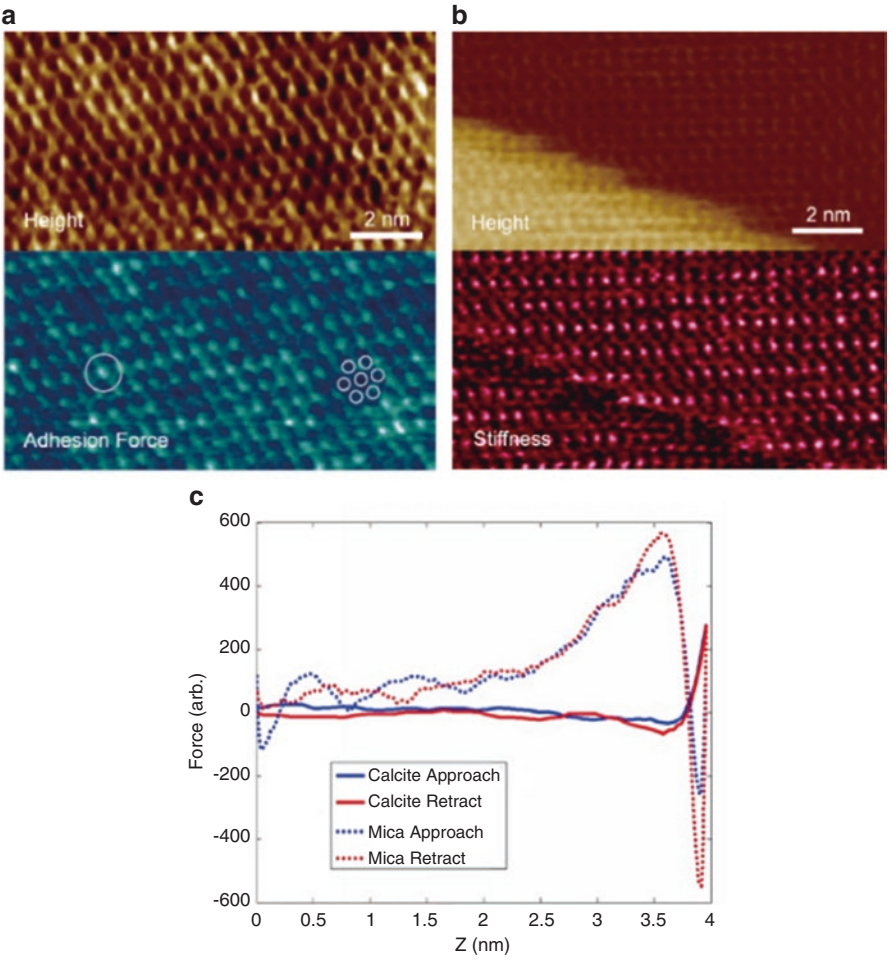

Fig. 10.22 Atomic resolution images obtained under PFT in liquid. (**a**) Mica true atomic resolution obtained on Bruker MultiMode 8 system with SNL+ probe at 1.95 Hz scan rate. Top: Topography image with individual atomic features revealed. Bottom: Adhesion force image with the differences in maximum attractive force between individual atoms and the tip, highlighted with circles. (**b**) Calcite true atomic resolution obtained on Bruker Dimension Icon system with SNL+ probe at 1.95 Hz scan rate. Top: Topography image with individual atomic features and atomic steps revealed. Bottom: Stiffness channel shows that alternate rows of atoms have different contact stiffness and rows are switched for different layers, i.e. stiffer rows in top layer correspond to less stiff rows in the second layer. (**c**) PeakForce Capture enables force spectroscopy captured at the atomic scale. The force distance curves are very different with only very short-range forces on the calcite, and much longer-range forces on the mica

self-cleaning and tip ionization will not happen in air, large adhesion is caused by capillary force. Compared with tapping mode, adhesion causes less problem in PFT. In tapping mode, the tip will be stuck to sample surface if the stored elastic energy in the cantilever is not enough to pull the tip away. It will be challenging for

tapping mode to image sticky samples with soft probe. In PFT, the adhesion force is handled by the large PFT amplitude, usually in hundreds of nm.

In addition to atomic resolution, PFT has also great strengths in molecular and sub-molecular resolution imaging. PFT can image with pN level force and immunes to vertical deflection drift, making it an ideal high-resolution imaging mode for soft or fragile samples. Figure 10.23 shows some sub-nanometer resolution examples, polymer, protein, virus and live cell were imaged with PFT. In contact mode section, a work on sub-nanometer resolution imaging of PFO was introduced, where the

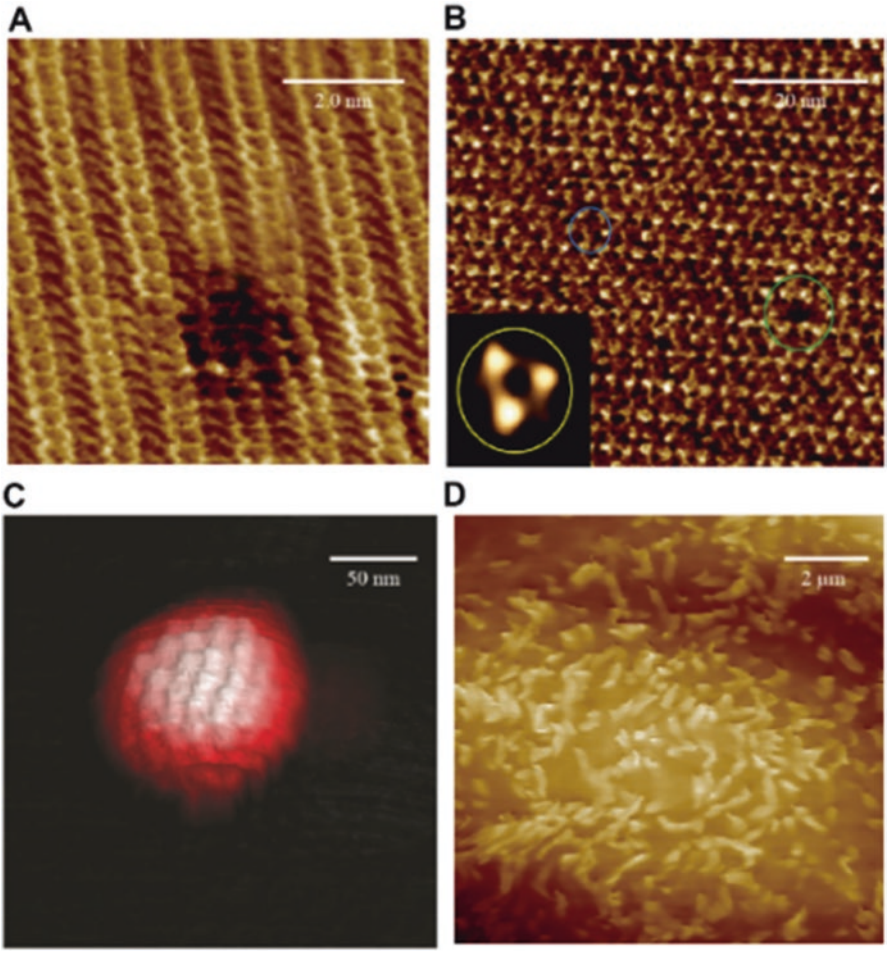

Fig. 10.23 High resolution examples obtained under PFT. (**a**) Molecular resolution on Polydiacetylene (PDA). (**b**) Lattice structure of Bacteriorhodopsin (bR) taken on Bruker Bioscope Resolve AFM with an inverted optical microscope. Inset showing a single particle averaging of the bR trimer, green circle showing a single lattice defect, and blue circle showing the lattice substructures. (**c**) Fine structures of Single Herpes Simplex virus surface. (**d**) MDCK live cell microvilli structure obtained on Bruker Bioscope Resolve AFM with an inverted optical microscope

authors had to scan the sample as fast as possible to keep the imaging force at around 100 pN due to the vertical deflection drift. With PFT, a similar work of imaging Listeriolysin O (LLO) in a buffer solution was done on Bruker MultiMode 8 AFM system [28], where the imaging force is less than 70 pN and imaging is stable for several hours' observation. This is the direct benefits of the good force control and immunity to vertical deflection drift of PFT.

In summary, PFT controls the imaging force instantaneously and intuitively to the level of pN. It is an ideal mode for high resolution imaging in both air and liquid. It has been widely used in high resolution imaging, especially sub-nanometer resolution imaging, since it was invented. Compared with small amplitude tapping mode, PFT is better in handling samples not atomically flat, maintaining low imaging force and preserving the tip sharpness.

2.8 Contamination Control

Contamination control is the key issue for high resolution imaging, especially for atomic resolution imaging. Anything that may touch the sample or tip must be kept clean, including tip, sample itself, tweezers, fluid cell, probe holder, containers, sample pucks etc. It is a general practice for operators to wear gloves and mask while working with clean items. In general, do not pipette pure water from the bottle, as it may contaminate whole bottle. Instead, pour pure water into a clean beaker and pipette from it.

Before doing experiment, fluid cell and all other tools that might be used in the experiment must be cleaned. As high-resolution imaging is mainly done in liquid, a typical cleaning procedure for liquid imaging is described as follow. The same concept can be used for imaging in air. The recommended products listed below have been tested in our lab. Other products may also work.

1) Clean the tools in ultrasonic cleaner with 1~2% ultrasonic soap solution (International Products Corp. Micro-90) for 5 min, then use a clean baby toothbrush to brush them with soap water, which is illustrated in Fig. 10.24.
2) Rinse the cleaned items 4~8 times with ultrapure water (ideally stored in glass), make sure every part, including channels, holes etc., is rinsed. The regular DI water, even filtered with 0.2 μm filter, is still not clean enough and should be avoided. Figure 10.25 shows the calcite surface in DI water and pure water. With DI water, lots of contaminations on the sample surface are observed. The contaminations from DI water are very small, only about 10~30 nm in diameter. Such small particles cannot be filtered out by the 0.2 μm filter. These particles will contaminate both sample surface and sharp tip.
3) Dry the rinsed items with high purity N_2. Canned air usually causes more contaminations and should be avoided.
4) Rinse the dried items with 1:1 IPA/Ethanol mixture (IPA: Sigma Aldrich product #190764-1 L; Ethanol: Sigma Aldrich product #459844-1 L) for 5 min.

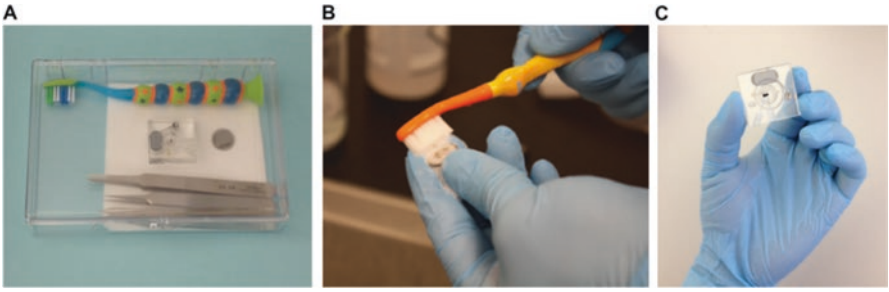

Fig. 10.24 Critical steps to clean tools for high resolution imaging. A fluid cell for Bruker MultiMode 8 system is used for illustration. (**a**) Items need to be cleaned, including baby toothbrush, probe holder or fluid cell, sample puck, tweezers etc. (**b**) Use the cleaned baby toothbrush to brush the sample puck after sonication. Other items follow similar clean steps. (**c**) Always wear gloves when handling parts. Do not breath on the sample and probe holder when handling them

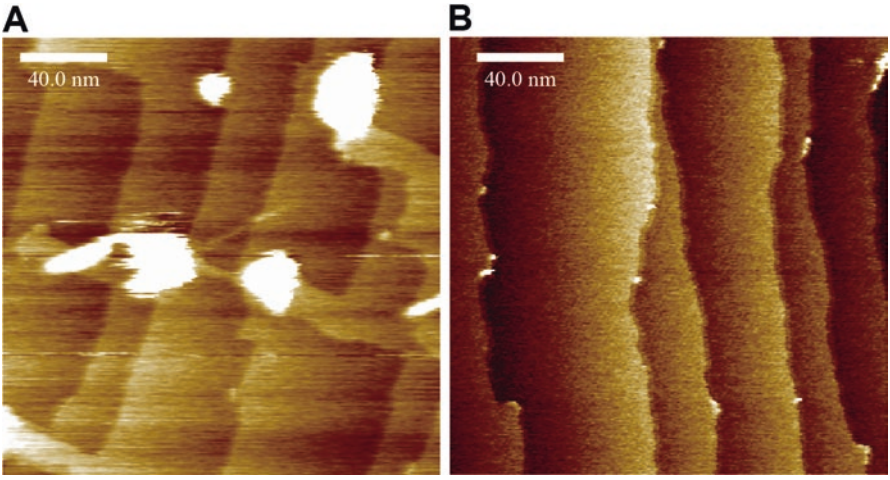

Fig. 10.25 The calcite surface in (**a**) Regular DI water and (**b**) Pure water. The regular DI water, even filtered with 0.2 μm filter, is not clean enough for true atomic resolution imaging. The particles from DI water deposit on calcite surface, and can also easily contaminate the sharp tip

5) Dry the rinsed items again with high purity N_2.
6) Use plasma cleaner (Harrick Plasma PDC series) to clean the dried items. This step is optional.

Once the items are cleaned, put them in a clean container for transportation.

Cleaning probe is another important step for high resolution imaging in fluid. The basic procedure is as follow.

1) Soak the probe with 1:1 IPA/Ethanol mixture (IPA: Sigma Aldrich product #190764-1 L; Ethanol: Sigma Aldrich product #459844-1 L) for 5 min, and use tweezers to swirl probe around.

2) Dry the probe with Kimwipe from the back of substrate using surface tension.
3) Use plasma cleaner (Harrick Plasma PDC series) to further clean the probe with ambient air plasma (~30 W) for about 1 min if possible. The probe must be completely dry before plasma cleaning. Otherwise, the vacuum may flip it.
4) Mount the probe to the probe holder, add hanging drop of water, and put it into the microscope as quick as possible.

3 High Resolution Imaging Step by Step

In this section, the procedures for high resolution imaging will be discussed in detail. Three representative examples, i.e. atomic resolution on Calcite, DNA double helix imaging, and live cell imaging, will be used for case studies. For other samples, the procedure and method should be easily derived from these case studies. For example, imaging soft biomaterials shares most of the procedures as live cell imaging.

3.1 Case Study I: Calcite True Atomic Resolution Imaging

In this case study, true atomic resolution imaging of Calcite will be achieved with tapping mode and PFT in fluid. The objective is to see atomic defects as well as the atomic lattice, more than just lattice imaging as in contact mode. This work can be achieved on Bruker MultiMode 8 system, Dimension Icon system and Dimension Fastscan system. The procedures discussed in this section can be applied to other AFM platforms, as long as their performance can meet the requirements.

3.1.1 AFM System Performance Check

For Bruker MultiMode 8 system, both the A scanner (XY full scan size is 0.4 μm) and E scanner (XY full scan size is 12 μm) are capable for this application. The Bruker Dimension Icon and Fastscan are also capable. To check the system noise, mount a stiff probe (usually spring constant >20 N/m) into the probe holder, scan over HOPG or silicon with tapping mode, adjust feedback loop gains to make the tip track the surface properly, then reduce the scan size to 0 and record the height image. The typical scan rate is 2.44 Hz and pixel density is 256 × 256.

After a first order flattening on the captured image, check the root mean square roughness R_q. This value should be less than 30 pm. It will be ideal if R_q is less than 20 pm. If system noise is higher than 30 pm, the AFM noise isolation system and environment should be checked and necessary rectification should be done to lower the system noise to 30 pm level. First, make sure enclosure and vibration isolation table are used. For compressed air vibration isolation table, make sure the table is floated properly. For active vibration isolation table, make sure the feedback is enabled. Second, minimize acoustic noise in the lab. Third, for closed loop scanner,

turn off the closed loop to reduce the sensor noise. Usually "Height" channel has less noise than "Height Sensor" channel. Height channel should be used for atomic resolution imaging.

3.1.2 Probe Selection

Based on the analysis in Sect. 2.6, probes with smaller and softer cantilever, and sharp tip are preferred for high-resolution imaging. Smaller cantilevers produce higher deflection sensitivity, softer cantilevers help in achieving minimal imaging force, and sharp tips produce good lateral resolution.

For true atomic resolution by PFT, SNL-C probe (Bruker, Santa Barbara, CA) is often used. Each SNL probe has four cantilevers, two wide cantilevers on one side with different lengths, and two narrow cantilevers on the other side with different lengths. The short and narrow one is the SNL-C probe. The cantilever length of SNL-C and SNL-A is ~120 μm while it is ~205 μm for SNL-B and SNL-D. With the same length, the cantilever of SNL-C is narrower and softer than SNL-A. Narrower cantilever also causes less hydrodynamic damping in fluid. It is advisable to break off the other cantilever with sharp tweezers to avoid interference. Besides SNL-C, other probes typically used for this application include ScanAsyst-Fluid+ (Bruker, Santa Barbara, CA) and FastScan-C (Bruker, Santa Barbara, CA). They all have very small and soft cantilevers.

For true atomic resolution by tapping mode, the recommended probe is Arrow-UHFAuD (NanoWorld AG, Switzerland). The cantilever length and width are ~35 μm and ~42 μm respectively and its typical resonance frequency in air is around 2 MHz. In liquid, the resonance frequency decreases to 300~500 kHz. It is a high bandwidth probe allowing fast scan to reduce the deleterious effect of drift. Compared with the probes used in PFT, this probe has higher spring constant. Tapping mode exploits Q factor to achieve low force imaging. The Fastscan-B probe (Bruker, Santa Barbara, CA) can also be used for this application. Compared with Arrow-UHFAuD probe, Fastscan-B probe has a similar small cantilever but lower resonance frequency, so slower scan speed should be used in imaging.

3.1.3 Sample Preparation

As discussed in Sect. 2.8, contamination control is critical for high resolution imaging in liquid. The procedures for cleaning different items have been described in that section and will not be repeated here. The calcite is purchased from Ward's Science (wardsci.com item #491600, 491,602). The preparation procedure for the calcite sample is as follow.

1) Score calcite crystal with a scriber along a face perpendicular to a cleavage plane and 1~2 mm from the edge of crystal. The ideal sample for MultiMode 8 system is a piece of crystal with 10 mm in length, 10 mm in width and 1~2 mm in thickness.

Fig. 10.26 A freshly prepared calcite sample

2) Use a razor blade as a chisel to break the crystal along its cleavage plane.
3) Glue the calcite crystal to a cleaned sample puck and cure for a few hours;
4) For a freshly cleaved sample, just use it without further cleaning. After experiment, dry the sample with Kimwipes without touching the surface;
5) For a used sample, wash the calcite and surrounding area on the puck with soap solution and rinse it thoroughly with DI water for a few minutes, then rinse it with ultrapure water, make drops to roll down from the calcite face, mount the calcite sample into the microscope, and add ~50 μL of ultrapure water to the center of the sample. The ultrapure water will dissolve a few layers of calcite, and further clean the surface. Then remove the water droplets with a pipette, and add another a few drops. Repeat this process several times. Then leave only a small drop of water on the calcite surface to prevent the water from spilling over outside the calcite sample and touching the sample puck. Otherwise the potential contamination on the sample puck may migrate to the calcite sample surface through water. Figure 10.26 shows a freshly prepared sample.

3.1.4 Drift Control

The common method to reduce thermal drift is to stabilize system longer time in enclosure with head installed and scanner on. In addition to stabilization, the following aspects are worth attentions. 1) Keep the instrument and environment temperature as constant. Wearing gloves is helpful to reduce thermal exchange between hands and AFM components. 2) Minimize the time for changing probe and sample. 3) For imaging in fluid, reduce evaporation from open fluid cell by increasing the humidity of surrounding environment. This can be achieved by putting paper towels soaked in warm water in the enclosure. 4) During imaging, increase scan speed till signal to noise ratio starts to degrade.

After the above-mentioned preparation, the experiment can be started. First, setup the tip-sample distance in air and align laser to the probe. This is to minimize

the operations after liquid is added, which helps to control drift as well. It is ideal to carry out these initial setups earlier to give system enough time to warm up and stabilize in the enclosure. Second, mount the sample into the AFM. Third, add a drop of ultrapure water to the probe to wet the tip, mount the tip and adjust the laser and PSPD. Then close the enclosure to stabilize the system. Fourth, wait ~30 min for system warm up and stabilization. Adjust PSPD if needed as the cantilever may bend a little bit after reaching thermal equilibrium with the fluid. Now the system is ready for high-resolution imaging.

3.1.5 Force Control and Feedback Loop Optimization

For PFT, it is easy to control imaging force precisely. For routine high-resolution imaging, the automated parameter optimization is good enough to get perfect images in most cases. But for true atomic resolution imaging, some parameters should be changed a little bit to minimize both the engage force and imaging force. The engage force and imaging force are controlled separately in PFT. The engage force is controlled by "PeakForce Engage Setpoint", set this parameter as small as possible. 0.02~0.04 V is a good start to try. If the system can engage properly, decrease it further till false engage is triggered. If false engage is always triggered, increase it by 0.01 V and try again. With this procedure, the lowest "PeakForce Engage Setpoint" can be found. The imaging force is controlled by "PeakForce Setpoint". For atomic resolution imaging, the automatic setpoint should be turned off, and set it manually to a value around 100 pN. To reduce hydrodynamic damping, a "PeakForce Amplitude" between 6 and 25 nm is usually used for atomic resolution imaging. Set the "PeakForce Engage Amplitude" the same as the "PeakForce Amplitude", which will prevent the system from auto optimizing some parameters twice. Set initial "Feedback Gain" the same as the "Engage Gain", which is usually 3 at 2 kHz "PeakForce Frequency" and 1.5 at 1 kHz "PeakForce Frequency". Set the "LP Deflection BW" to 10~20 kHz range to allow fine "Feedback Gain" adjustment. Set the "Deflection Limit" to 4 V and decrease the "Z Limit" to 0.5~0.7 μm. During imaging, closely monitor the force curve to check whether the feedback is on the peak force in each PFT cycle. If not, the "Sync Distance" should be adjusted by using "Auto config" function or manual adjustment. If the force curves do not look good, adjust "Lift Height" slightly to trigger background subtraction calibration. If 256 × 256 pixel density is used, the maximum scan rate is ~ 4 Hz for 2 kHz "PeakForce Frequency" and ~ 2 Hz for 1 kHz "PeakForce Frequency". Further adjust "PeakForce Amplitude" and "PeakForce Setpoint" to optimize the tracking. Once good tracking is achieved, increase the scan size, e.g. 50 nm range, to find a good location for final scan. During the survey scan, use XY offset to avoid contaminants. Zoom in to a clean area and record images. If cleaning process is done properly and tip is sharp, the atomic lattice should appear. As shown in Fig. 10.27, the single atomic step, as well as the atomic lattice on both the top surface and bottom surface are resolved.

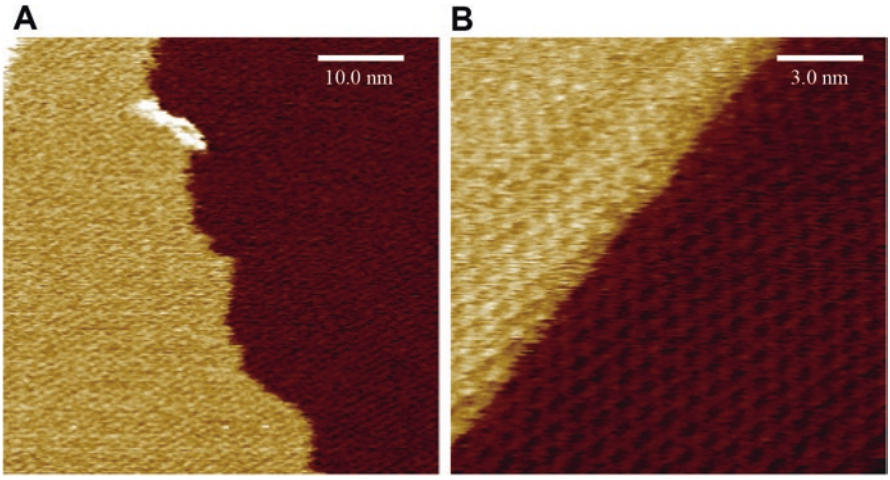

Fig. 10.27 True atomic resolution images of calcite sample in ultrapure water. The images are obtained by PFT on Bruker MultiMode 8 system with Fastscan-C probe at 4 Hz scan rate. (**a**) Survey scan at 50 nm scan size, contaminations are shown on some areas. (**b**) Final scan at 16 nm scan size on a clean area

For tapping mode, even force control is a complicating process, it is not difficult to achieve atomic resolution following the procedure described below. To reduce the engage force, set the "Engage Setpoint" to 1 and "TM Engage Gain" to 0.25. Before engage, find the resonance frequency in liquid by "Fast Thermal Tune" or tapping mode "Auto Tune" and set the "Drive Frequency" slightly lower than the resonance frequency. Once the right frequency is set, adjust the laser spot slightly to maximize the cantilever oscillation amplitude. Change drive amplitude to make the free amplitude around 100 mV, and set the "Lock-in BW" to 25 kHz on Dimension Fastscan system (20 kHz on MultiMode 8 system and 5 kHz on Dimension Icon system). Use the method introduced in Chap. 1 to measure the amplitude sensitivity, adjust the drive amplitude to make cantilever free amplitude to 1~3 nm. Then engage the probe and start scan. After the probe is engaged, decrease the "Z Range" or "Z Limit" to 0.5 μm. Two sets of amplitude setpoint have been tested. 0.7~0.9 nm amplitude setpoint for 1 nm free amplitude, 0.3~0.9 nm amplitude setpoint for 2~3 nm free amplitude. One uses about 80% relative setpoint, the other uses 15–30% relative setpoint. Both settings work well. But the latter produces more stable imaging. Adjust scan rate to 10~20 Hz to reduce the deleterious effect of drift. Similar to PFT, a survey scan is used to find a clean area to do a final scan. Figure 10.28 shows the consecutive images of a calcite sample obtained on Dimension Fastscan system. (a)–(e) indicate the same atomic defects in both images. Figure 10.29 shows the calcite atomic resolution images obtained on Dimension Icon system.

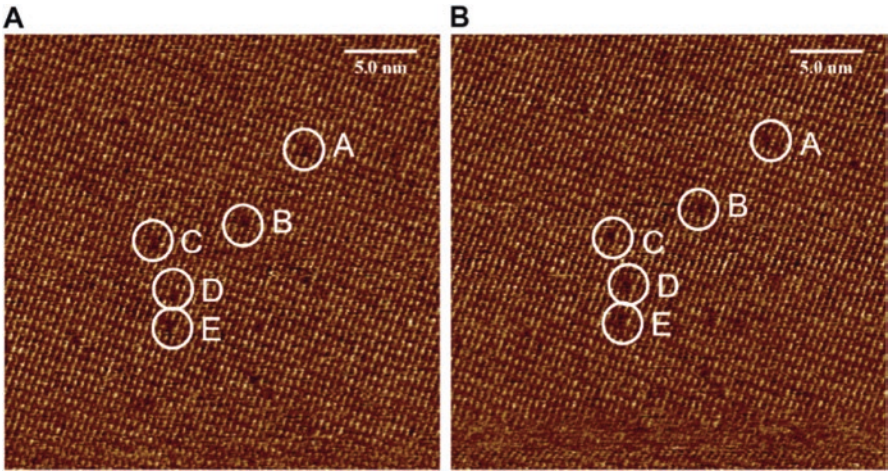

Fig. 10.28 Consecutive images with atomic defects of a calcite sample in ultrapure water. The images are obtained by tapping mode on Bruker Dimension Fastscan system with Arrow-UHFAuD probe at 9.77 Hz scan rate. (**a**)–(**e**) indicate the same atomic defects in both images

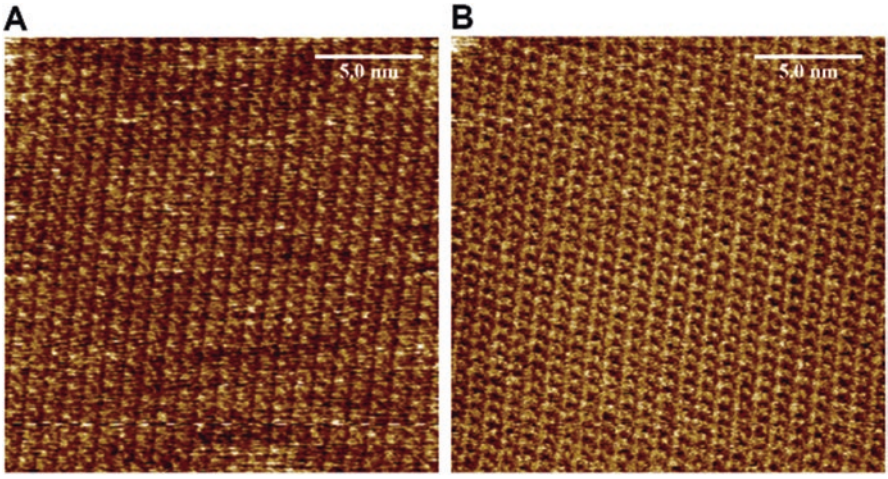

Fig. 10.29 True atomic resolution imaging of a calcite sample in ultrapure water. The images are obtained by tapping mode on Bruker Dimension Icon system with Arrow-UHFAuD probe at 11 Hz scan rate. (**a**) Height image. (**b**) Phase image

3.2 Case Study II: DNA Double Helix Imaging

DNA is a biopolymer molecule. The monomer units are nucleotides and the polymer is known as "polynucleotide". It is normally made up of two polynucleotide strands that form a double helix. B-DNA (most common form) is a right-handed helix that has a helical repeat (pitch) of 3.6 nm with major and minor grooves having widths of 2.2 nm and 1.2 nm, respectively, which is illustrates in Fig. 10.30.

To image DNA double helix, the key elements are almost the same as those for true atomic resolution imaging in fluid. Noise control, contamination control, drift control, force control, suitable probe selection and sample preparation play important roles for this sub-nanometer resolution imaging.

Double helix resolution on DNA can be achieved on Bruker Bioscope Resolve system, MultiMode 8 system, Dimension Icon system, and Dimension Fastscan system. The procedure was developed on Bruker Bioscope Resolve system, but it can be adapted to other AFM platforms easily.

3.2.1 AFM System Performance Check

The low noise requirement for DNA double helix imaging is the same as atomic resolution. The system noise level should be less than 30 pm. If the noise is higher than the required, check the AFM system with the procedures described in atomic resolution section. If the AFM is mounted on an inverted microscope, switch off the microscope helps on noise control.

3.2.2 Contamination Control

The requirements are the same as atomic resolution imaging, just follow the procedures described in Sect. 2.8. After the cantilever holder is cleaned, store it by suspending in 1~2% ultrasonic soap solution in a clean glass beaker, as shown in

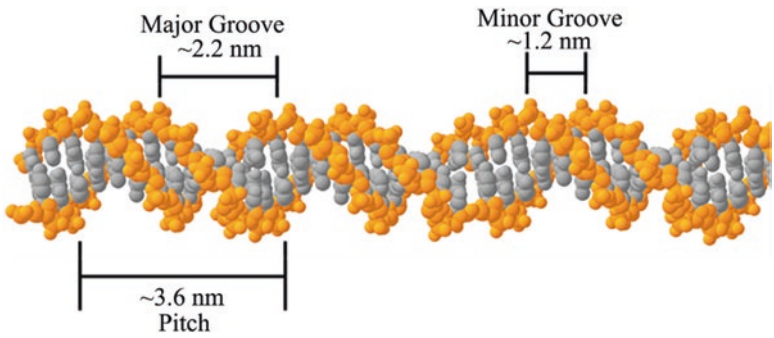

Fig. 10.30 Cartoon of DNA double helix structure. The pitch is ~3.6 nm, major groove is ~2.2 nm, minor groove is ~1.2 nm, and diameter is ~2.0 nm

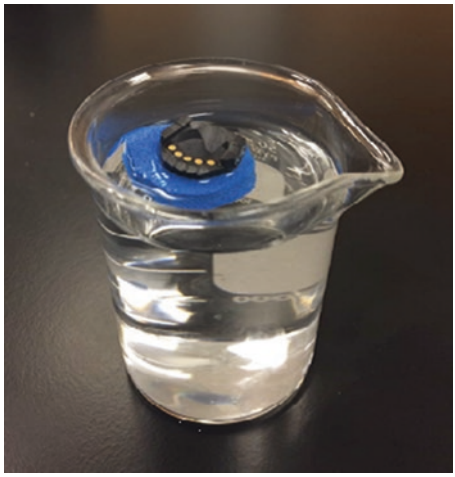

Fig. 10.31 Store the cantilever holder by suspending it in soapy water in a clean glass beaker to remove contaminants from previous experiments

Fig. 10.31. Bioscope Resolve mainly works with biological samples, the probe holder can easily be contaminated during experiments. Soaking in soap solution can help remove contaminants from previous fluid experiments.

3.2.3 Probe Selection

Similar to other high-resolution work, probes with short and soft cantilevers combined with sharp tips are preferred for DNA double helix high-resolution imaging. Shorter cantilevers produce better deflection sensitivity, softer cantilevers are good for better force control, and sharp tips lead to better lateral resolution. Since DNA double helix imaging is carried out in liquid, the additional advantage of short and narrow cantilever is less damping effect.

The PeakForce-HIRS-F-A (Bruker, Santa Barbara, CA), PeakForce-HIRS-F-B (Bruker, Santa Barbara, CA) and Fastscan-D-SS (Bruker, Santa Barbara, CA) are suitable for DNA double helix imaging. All these probes have thin, narrow and soft cantilever plus very sharp tip with ~ 1 nm end radius. Figure 10.32 shows the SEM images of these three probes. They are slightly different from the probes commonly used for other applications.

3.2.4 Sample Preparation

One key element for obtaining high-resolution DNA images is how to immobilize DNA strands on a suitable surface. The DNA used here is pmaxGFP Vector DNA (Lonza, Catalog No. VC-1001 N). 2 vials of 30 μg of DNA (0.5 μg/μL stock solution, ~60 μL in each vial) are included in the transfection kit. Upon receiving, the vials should be stored in freezer and thawed it just before preparing DNA stock solution for AFM imaging.

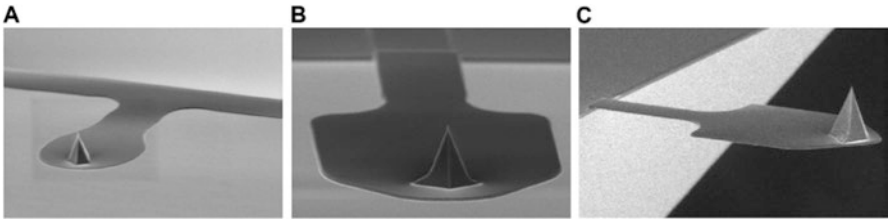

Fig. 10.32 SEM images of probes suitable for DNA double helix imaging. (**a**) Fastscan-D-SS probe. (**b**) PeakForce-HIRS-F-A probe. (**c**) PeakForce-HIRS-F-B probe. All of them have thin, narrow and soft cantilever combined with ultra-sharp tip with end radius ~1 nm

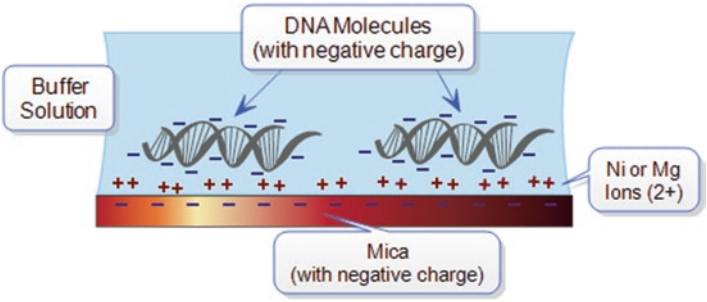

Fig. 10.33 Schematic illustration of DNA binding principle. Negatively charged DNA may be bound to negatively charged mica in the presence of divalent counterions, such as Ni^{2+}

The DNA purchased is too concentrated for AFM imaging, need to dilute 100 times. The dilution procedure is as follow. 1) Dilute 10 μL of original DNA solution in 990 μL of DNA storage buffer (Tris-EDTA Buffer. Sigma Aldrich Catalog No. 93283). Then 1 mL solution of DNA with a concentration of 0.5 μg/mL is obtained. The buffer/solution must be filtered with 0.22 μm syringe filters (Fisher Scientific Catalog No. 09719006) before using. Mix the solution by using pipette or inverting the tube. Vortex should be avoided for DNA. 2) Place 50 μL aliquots of the 0.5 μg/mL DNA solution into microcentrifuge tubes and freeze them at −20°C. 20 tubes of DNA stock solution can be obtained. Each tube is enough for one DNA experiment. Aliquoting the solution is to reduce freeze/thaw cycles. 3) Keep the remaining original DNA solution in the freezer at −20°C until more stock solution needs to prepare.

Mica is commonly used as substrates for DNA imaging. Most of DNA and mica are both negatively charged. To immobilize DNA on the substrate, either the mica surface is modified or DNA counterions are used to facilitate the binding. In the presence of divalent ions, like Ni^{2+} and Mg^{2+}, DNA can be adsorbed on the mica surface. The binding principle is illustrated in Fig. 10.33. In this experiment, $NiCl_2$ solution is used as an example. Other divalent ions are the same. The $NiCl_2$ solution is prepared as follow. 1) Dissolve 0.38888 g of $NiCl_2$ (Sigma Aldrich

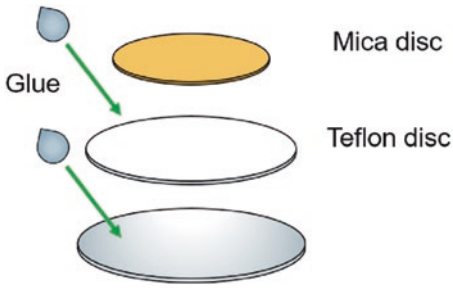

Fig. 10.34 Mica substrate preparation by gluing mica disc and Teflon disc to AFM sample puck

Catalog No. 223387) in 150 mL of purified water (Sigma Aldrich Catalog No. 95280). Then 150 mL 20 mM $NiCl_2$ solution is obtained. 2) Store the solution in fridge at 4°C when not in use. The next solution to be prepared is imaging buffer. 1) Dissolve 0.3575 g of HEPES (Sigma Aldrich Catalog No. H3375) and 0.0195 g of $NiCl_2$ (Sigma Aldrich Catalog No. 223387) in 150 mL of pure water (Sigma Aldrich Catalog No. 95280). 2) Adjust its pH to ~7.0. Then 150 mL 10 mM HEPES buffer with 1 mM $NiCl_2$ is obtained. 3) Store the imaging buffer in fridge at 4 °C when not in use. All buffer solutions, except DNA solution, must be filtered with 0.22 μm syringe filters (Fisher Scientific Catalog No. 09719006) before using.

The mica substrate is prepared by gluing a Teflon disc to an AFM sample puck and then gluing a mica disc to the Teflon disc, as shown in Fig. 10.34. The mica disc should be smaller than the Teflon disc. Mica disc and Teflon disc can be prepared by punching from sheet form. The edge of the discs should be smooth. The Teflon sheet used this experiment was purchased from McMaster-Carr (Catalog No. 8711 K92) and the glue is Loctite Super Glue "Ultra Liquid Control" (water resistant). The glue should be uniformly distributed on the surface, bubbles should be avoided. Bubbles can cause vibration and drift. Wait until the glue is completely hardened (while may take a day), use Scotch tape to cleave the mica disc uniformly. Make sure an entire layer of mica is peeled off. Otherwise the residue from the tape may contaminate the DNA sample during imaging.

Once the solutions and mica substrate are prepared, it is the time to prepare DNA sample for imaging. 1) Take out one tube of DNA stock solution (50 μL of 0.5 μg/mL solution) from the freezer, 20 mM $NiCl_2$ solution and 10 mM HEPES buffer with 1 mM $NiCl_2$ solution from the fridge. Wait until all the items reach room temperature. 2) Filter the $NiCl_2$ and HEPES buffer solutions with 0.22 μm syringe filters. It is better to filter more solution in case that additional solution is needed during experiment. DNA solution should not be filtered. 3) Pipette 25 μL of filtered $NiCl_2$ solution onto a freshly cleaved mica surface and incubate for 2 min. 4) Mix the DNA solution by using a pipette tip and then add 1.5 μL of DNA solution (can vary from 1 to 5 μL) onto the mica substrate. 5) Add 25 μL of filtered HEPES buffer onto the mica substrate and mix the sample using a pipette tip to distribute DNA uniformly on the mica surface. 6) Cover the sample in a petri dish to incubate for at least 30 min before imaging. If the environment is dry, put a small piece of wet

paper tower inside the petri dish to reduce evaporation. Low concentration $NiCl_2$ solution is used for DNA double helix imaging because high concentrations $NiCl_2$ can cause DNA strands to condense and form Ni aggregates which can contaminate the surface.

3.2.5 Drift Control

The drift control in DNA imaging is the same as atomic resolution imaging. Following the same procedure will do. In case more buffer need to add during imaging, it is a good idea to keep the buffer solution inside the acoustic enclosure, making the temperature of buffer closer to that of the sample.

3.2.6 Force Control and Feedback Optimization

PFT provides very precise force control, enabling imaging soft biological samples at extremely low forces. Before engage the probe, add ~20 μL of filtered HEPES buffer onto the probe to avoid bubbles during engage. Probes with calibrated deflection sensitivity and spring constant are preferred because the imaging force can be controlled directly during engage and scan. Similar to atomic resolution imaging, parameters should be modified for low engage force and image force. Set "PeakForce Engage Setpoint" to 0.02~0.05 V and "PeakForce Engage Amplitude" to 50 nm. Turn off "Auto Setup" and "ScanAsyst Auto Control". Set "PeakForce Setpoint" to 30~35 pN, "PeakForce Amplitude" as the same as engage settings, 50 nm, "PeakForce Frequency" to 2 kHz, "Feedback Gain" to 5, "LP Deflection BW" to 10 kHz, both "Sync Distance New" and "Sync Distance QNM" to 85. Turn on both "Auto Sync Distance" and "Auto Sync Distance QNM". After engaged, park the probe ~200 nm above the sample, then change both "PeakForce Engage Amplitude" and "PeakForce Amplitude" to 5 nm from 50 nm, change "Lift Height" to 5 nm, then return to scan. If the baseline of force curves is jumpy or the retract curve crosses over the approach curve, change the lift height slightly to trigger the system to do a background subtraction calibration. "Auto Config" function should be avoided for this application. Now it is ready to image DNA double helix. 1) Set the image size to 1 μm. Several strands of DNA should appear within this area if the DNA concentration is appropriate. If no DNA appears, offset or re-engage in another area until a good region is found. Good region is a region with at least 4~5 DNA strands in 1 μm area, fairly open DNA strands, and clean mica surface without large particulates or aggregates. If DNA strands are too dense and overlap with each other, less DNA stock solution should be used. 2) Once a nice DNA strand is located, zoom in on it. 3) For the zoom in scan, reduce the z range to 1 μm, decrease the imaging force to ~20 pN (to be optimized based on image quality but 20 pN is a good start to try) and increase scan rate to 1.5 Hz. 4) A scan size <200 nm is good to show DNA double helix. The image shown in Fig. 10.35 was obtained on a scan size of 130 nm. 5) Increase feedback gain till noise starts to increase and drop it

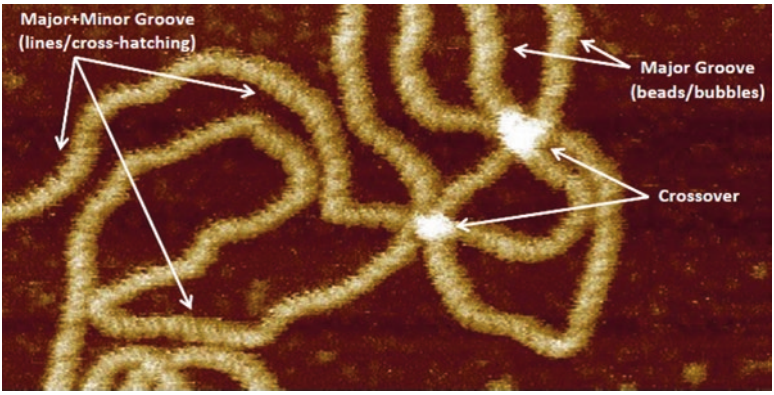

Fig. 10.35 DNA double helix image obtained on Bruker Bioscope Resolve system with a scan size of 130 nm

back a little bit. The double helix is easier to resolve on strands along AFM fast scan axis. Areas where strands cross over each other are often a little more stable and tend to show nice double helix structure.

3.3 Case Study III: Live Cell High-Resolution Imaging

Live cell high-resolution imaging shares the similar principle with other high-resolution imaging applications. Imaging live cell itself is not difficult, but imaging the fine structures on a live cell is a challenge. Essentially, imaging fine structures on the live cell is to image bio-molecules. The procedures and methods discussed in DNA double helix imaging and calcite true atomic resolution imaging, such as noise control, contamination control, drift control, force control, can be adapted to live cell imaging. Only the probe selection and sample preparation are different.

3.3.1 Probe Selection

Live cells are usually large, tall and ultra-soft, sharp tip usually deform cell surface significantly or even damage the cell. Super sharp tip should be avoided in live cell imaging. When scanning over a tall live cell, the interaction between cantilever and the cell will affect AFM imaging. Therefore, the tip height should be larger than the cell height. To minimize the imaging force, soft cantilever is still preferred. To meet these requirements, Bruker release a probe, PFQNM-LC, for live cell imaging. This probe has a tip height of ~17 μm, tip end radius of ~65 nm, and a soft cantilever. This probe is ideal for whole cell imaging. MLCT-Bio probe (Bruker, Santa Barbara, CA) has 6 cantilevers with spring constant in the range of 0.01~0.6 N/m, 2.5~4.5 μm

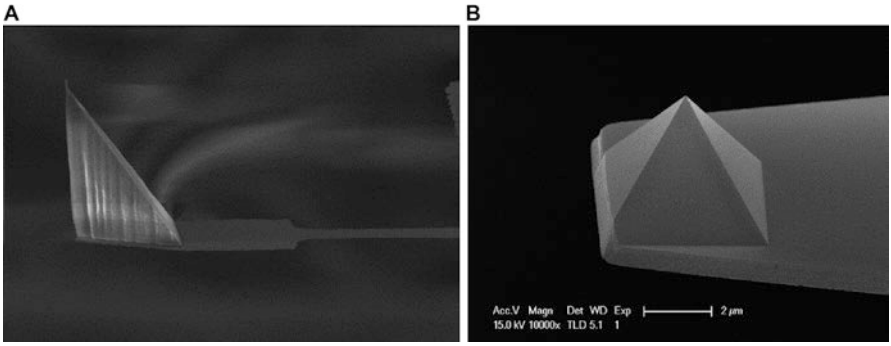

Fig. 10.36 Probes for live cell imaging. (a) PFQNM-LC probe. It has ~17 µm tip height and ~65 nm tip radius. (b) MLCT-Bio probe. It has 6 cantilevers with spring constant ranging from 0.01 to 0.6 N/m, 2.5~4.5 µm tip height and 20 nm tip radius

tip height and 20 nm tip radius. This probe is good for live cell imaging in small area. Incorporating a larger tip radius and apex angle, the probe is good for consistent cell imaging. The SEM images of these two probes are shown in Fig. 10.36.

3.3.2 Sample Preparation

Live cells must attach to the substrate firmly before they can be imaged with AFM. The cell sample preparation methods for contact mode imaging, discussed in Chap 1, can also be used for PFT. The procedures will not be repeated here. Figure 10.37 shows a cell sample good for AFM imaging. The cells, fibroblast, are 50–70% confluent and nicely spread over the surface of petri dish, with very few nonadherent or dead cells (rounded cells). On contrast, bad examples are shown in Fig. 10.38. In Fig. 10.38a, majority of cells are not attached to the surface of dish. Nonadherent cells appear round and will be easily moved around by the AFM probe. In conjunction with the very low number of spread cells, it indicates that these cells are just seeded and need more time to grow. Figure 10.38b shows another situation. While confluency of spread cells is good (~50%), there are lots of unattached cells (rounded), which will be easily moved around with the AFM probe and potentially contaminate the probe. Overgrown is also an issue for cell imaging, as shown in Fig. 10.38c, where cells overlap with each other and many cells are dead, indicating the cells have been growing too long.

Once a nice cell sample is prepared, follow the steps for PFT imaging in liquid to image live cell. 300 pN imaging force and 1 kHz “PeakForce Frequency” are usually used. Figure 10.39 shows an image of microvilli on a Madin-Darby canine kidney (MDCK) cell, which was obtained on Bruker Bioscope Resolve system with PFQNM-LC probe and scan size of 10 µm.

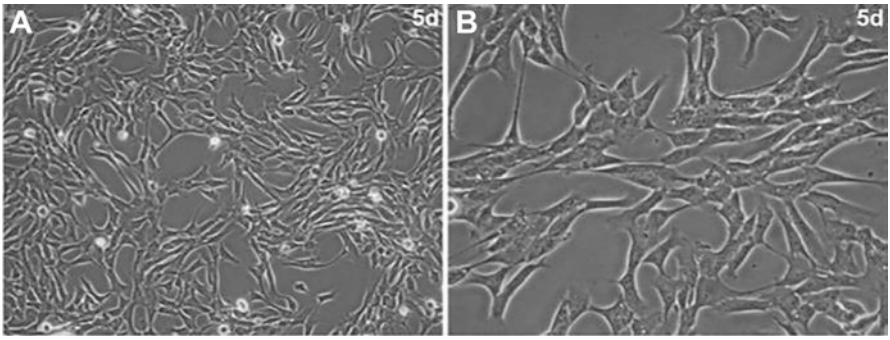

Fig. 10.37 Optical images of good cell sample. (**a**) Low magnification and (**b**) high magnification images of fibroblast cells good for AFM imaging. Cells are 50–70% confluent and nicely spread over the surface of petri dish. Very few nonadherent or dead cells (rounded cells)

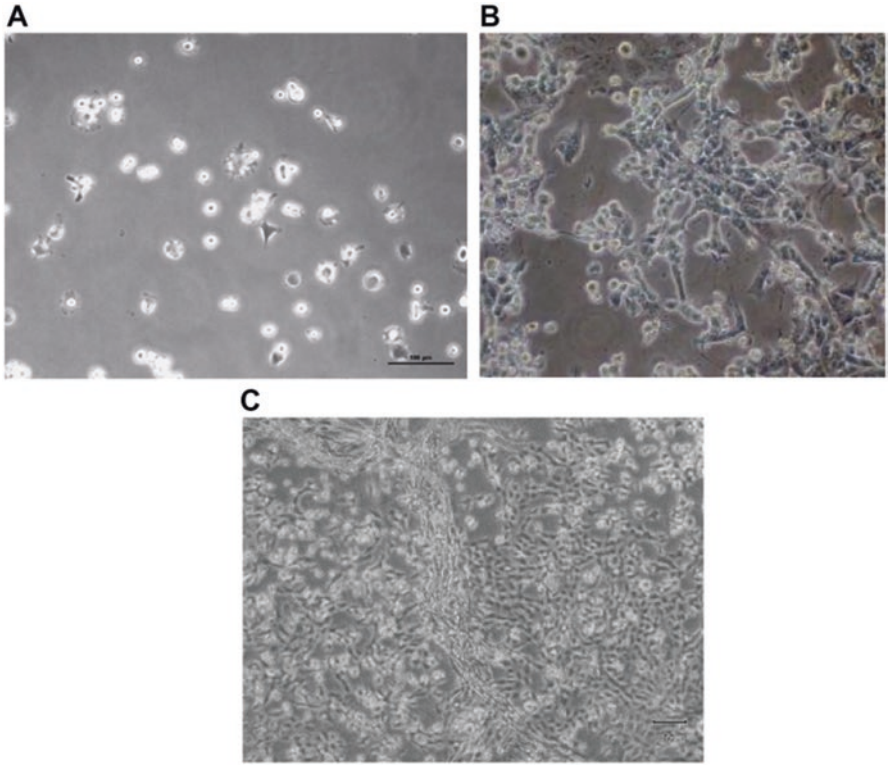

Fig. 10.38 Optical images of bad cell samples. (**a**) Majority of cells are not attached to the surface of dish. (**b**) While confluency of spread cells is good (~50%), there are lots of unattached cells (rounded). (**c**) Overgrown cell sample. Multiple layers of cells and many dead cells

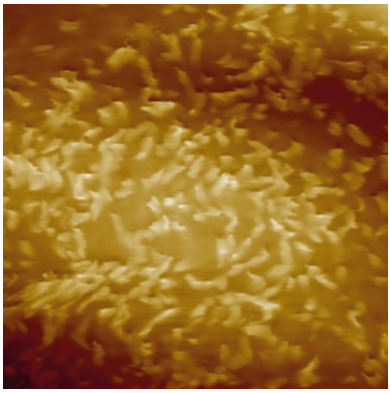

Fig. 10.39 MDCK live cell microvilli structure, obtained by PFT on Bruker Bioscope Resolve system with PFQNM-LC probe and scan size of 10 μm

4 Prospects

4.1 Resolution in Another Dimension – "Temporal Resolution"

With the advances in technology, AFM is able to convey structural information at atomic and sub-nanometer scale. However, it is still an elusive goal to measure time-resolved properties at this length scale to understand the kinetics. With the aim to investigate dynamic phenomena and reduce the effect of thermal drift in high resolution imaging, extensive efforts have been made to develop high speed AFM. The theoretical aspects for the highest possible imaging rate and the future applications in biomolecular system [83], biology, biophysics [84, 85] and material science [86] have been reviewed. For example, the dynamics of phase transition of lipid bilayers was observed with a high speed AFM [87]. Besides this kind of flat samples, the molecular dynamics of live bacterial cell surfaces was imaged and the direct observation of dynamic molecular architectures on a live cell surface was reported for the first time [88].

As an example, Fig. 10.40 shows a set of high-speed AFM data of DNA origami at different scan rates. The scan size is 350 nm and the highest scan rate is 98 Hz, which corresponds to 69 μm/s. At all speed, DNA strands that make up the origami structure and single stranded DNA end piece are resolved.

4.2 High Resolution Quantitative Physical Properties Mapping

Besides the progress in spatial and temporal resolution, another trend in AFM technology developments is to produce high resolution mapping of material properties, including nano mechanical properties and nano electrical properties. In recent years,

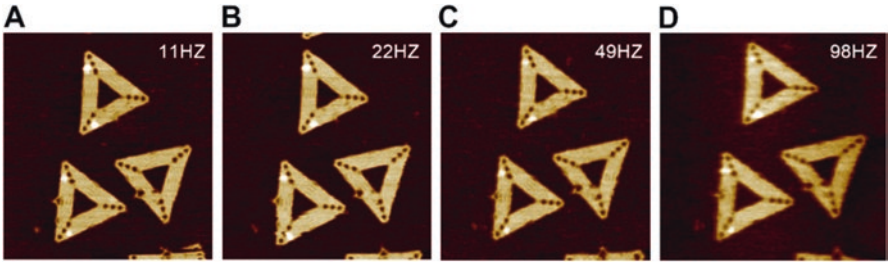

Fig. 10.40 DNA origami images obtained on Bruker Dimension Fastscan system. The scan size is 350 nm. At different scan speed, (**a**) 11 Hz, (**b**) 22 Hz, (**c**) 49 Hz, (**d**) 98 Hz, DNA strands that make up the origami structure and signal stranded DNA end piece are resolved

many secondary imaging modes were developed to do high-resolution quantitative mechanical properties imaging. The properties include Young's modulus [89, 90], stiffness [33], adhesive force [43–45, 90, 91], real-time dynamics [92], and even tip-sample interactions at single atom. The AFM techniques developed to obtain these properties include topography and recognition imaging (TREC) [93], HarmoniX [94], PFQNM [31], Quantitative Imaging (QI) [95] and multifrequency modes [96]. As an example, the mechanical property changes of living HaCat cells under oxidative stress were studied with PFQNM [40], where dynamics of actin stress fibers was observed.

On the side of electrical properties, conductivity [97], potential [98–103], piezo-response [104], even combined with in-situ mechanical information, can now be studied at nanometer spatial resolution by AFM. The PeakForce Tunneling AFM(PFTUNA) [105] allows mapping local conductivity and mechanical information simultaneously at high resolution. Benefitting from PFT, this technique can be used to measure loosely bound nanomaterials and pillar structures, which are difficult for traditional imaging modes. PeakForce Kelvin Probe Force Microscopy (PFKPFM) [106] allows mapping local potential and mechanical properties at the same time. With frequency modulation technique, PFKPFM improves the spatial resolution of potential mapping from traditional micrometer level to nanometer level.

Measuring electrical properties at nanometer scale in liquid is of great interest for many applications. However, the AFM based electrical measurements in liquid are challenging due to the possible current leakage and stray capacitance. Recently, we developed a solution to do electrical measurements in liquid, such as piezo response, conductivity [107] and potential mapping. The solution is based on isolated nano-electrode probes with an exposed Pt tip apex of ~25 nm tip radius, in conjunction with PFT technology and Fast Force Volume (FFV) technology. To study biological piezoelectricity, direct observation of ferroelectric electro-mechanical responses in electrolytes with different salt concentrations is required [108]. The recently developed Piezo-response Force Microscopy (PFM) in liquid enables the study of biological piezoelectricity under physiological environment.

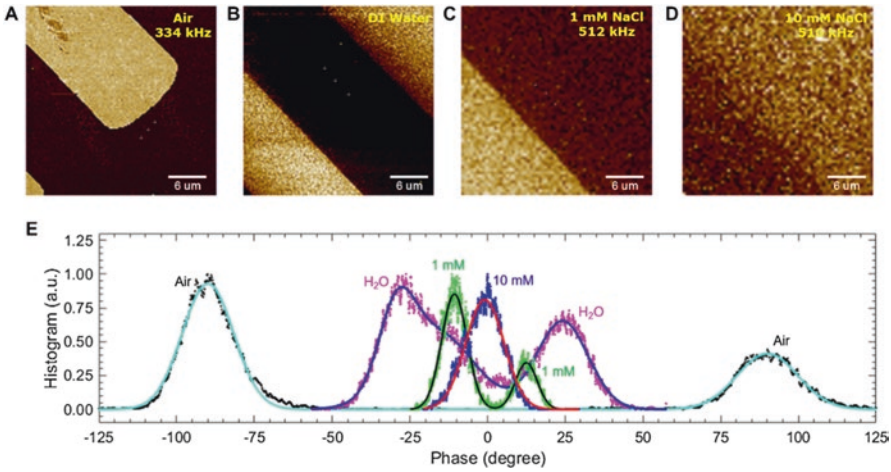

Fig. 10.41 PFM images of PPLN obtained on Bruker Icon system. (**a**) In air, first contact resonance. (**b**) In DI water, second contact resonance. (**c**) In 1 mM NaCl solution, second contact resonance. (**d**) In 10 mM NaCl solution, second contact resonance. (**e**) The phase contrast decreases with the increase in salt concentration due to the EDL

Figure 10.41 shows an example of PFM measurement on a piece of periodically poled lithium niobate (PPLN) in air, DI water and NaCl solutions. The results clearly show the PFM phase contrast decreases with the increase in salt concentration. In addition, local conductivity and potential mapping in liquid have also been achieved with this probe isolation technique, results are not shown in this chapter due to the limited space. These new developments enable many possibilities in future biological system research.

Scanning ion conductance microscopy (SICM) [109] and scanning electrochemical microscopy (SECM) [110] have the ability to detect ionic current and electrochemical current, respectively. AFM based SICM and SECM were recently developed, which enables high-resolution ionic current and high-resolution electrochemical current imaging. For biological systems, these techniques can be used for characterization of proteins and their building blocks, identification of mismatches in double-stranded DNA, evaluation of interaction between antigens and their antibodies, measurement of enzymatic activity, measurement of cellular expression of proteins and study of cellular response to environmental stimuli [111]. Simultaneously high-resolution imaging of single ion channel structure and ionic current on biological membrane by AFM based SICM has been reported [112]. With the breakthrough in the new nanoelectrode probe mentioned above, the electrochemical current resolution of SECM is dramatically improved [113]. As a result, high resolution (< 80 nm) electrochemical activity mapping has been achieved by PeakForce Scanning Electrochemical Microscopy (PFSECM) [114].

4.3 High Resolution AFM Integrated with Other Techniques

High resolution AFM has been extensively used for the characterization of material surfaces at atomic level and nanoscale. With the developments in nano mechanical and nano electrical properties measurements, AFM has further extended its applications. However, it is still lack of some material related properties, such as chemical information. Therefore, integration with other techniques will be the future developments in AFM technology.

By integrating with infrared (IR) spectroscopy and Raman spectroscopy, AFM overcomes the limitation of the traditional IR and Raman technology in spatial resolution. It has demonstrated the new capability of obtaining simultaneously topography, physical and chemical properties of samples at ~10 nm lateral resolution and monolayer sensitivity. The technology developments and applications of AFM-IR and AFM-Raman were reviewed by Fu W. et al. [115]. Readers may refer to this reference for details.

Mass spectroscopy (MS) is another commonly used analytical technique. By integrating with an AFM, the sampling spot can be significantly shrunk and the spatial resolution is improved as a result. A representative work was done by Somnath S. et al. [116]. By tailoring the heating in thermal AFM cantilevers, desorption craters in thermal desorption spot sampling were shrunk. Submicron spatial resolution and a 381× improvement in desorption efficiency over the traditional heating method were achieved.

The combination of AFM and X-ray techniques has also been explored. The uptake of asbestos fibers by mesothelial cells was studied with AFM and soft X-Ray imaging [117]. After exposure to asbestos fibres and fixation, cells were first analyzed with AFM and then imaged with soft X-ray. With this approach, the experimental uncertainty was drastically reduced. Another example is the combination of AFM and small-angle X-ray scattering (SAXS). This combination can be applied to many different macromolecules and sample surfaces depending on characterization need and sample properties [118]. The combination of AFM and X-ray techniques can also be used to study the effect of radiation damage on various biological samples.

5 Summary

High-resolution AFM imaging is a powerful technique to study fine structures, as well as mechanical and electrical properties, at atomic or sub-nanometer scale. In this chapter, after reviewing some applications of high resolution AFM imaging, the fundamentals of “resolution” were discussed, followed by analyzing the challenges and solutions in high resolution AFM imaging. Noise and drift control, probe selection, contamination control, and force control are the key elements to achieve high resolution. In force control, exploiting the lowest short-range tip-sample interaction

is very important for high resolution imaging. The approaches to achieve that were discussed for different imaging modes, i.e. contact mode, tapping mode and PeakForce tapping mode. After the principles being discussed, detailed practical guides for high-resolution AFM imaging were described for three representative applications, i.e. atomic resolution, sub-molecular resolution and live cell imaging. In the last section of this chapter, we provide our prospective view on the future developments in high resolution AFM technology. High speed, high content information at nanoscale, and integration with other analytical techniques are the three development directions.

References

1. Gan Y. Atomic and subnanometer resolution in ambient conditions by atomic force microscopy. Surf Sci Rep. 2009;64(3):99–121.
2. Dufrene YF, Martinez-Martin D, Medalsy I, Alsteens D, Muller DJ. Multiparametric imaging of biological systems by force-distance curve-based AFM. Nat Methods. 2013; 10(9):847–54.
3. Raigoza AF, Dugger JW, Webb LJ. Review: recent advances and current challenges in scanning probe microscopy of biomolecular surfaces and interfaces. ACS Appl Mater Interfaces. 2013;5(19):9249–61.
4. Alsteens D, Muller DJ, Dufrene YF. Multiparametric atomic force microscopy imaging of biomolecular and cellular systems. Acc Chem Res. 2017;50(4):924–31.
5. Dufrene YF, Ando T, Garcia R, Alsteens D, Martinez-Martin D, Engel A, et al. Imaging modes of atomic force microscopy for application in molecular and cell biology. Nat Nanotechnol. 2017;12(4):295–307.
6. Giessibl FJ. Advances in atomic force microscopy. Rev Mod Phys. 2003;75(3):949–83.
7. Garcia R, Perez R. Dynamic atomic force microscopy methods. Surf Sci Rep. 2002;47(6–8):197–301.
8. Morita S, Fujisawa S, Sugawara Y. Spatially quantized friction with a lattice periodicity. Surf Sci Rep. 1996;23(1):1–41.
9. Pfreundschuh M, Martinez-Martin D, Mulvihill E, Wegmann S, Muller DJ. Multiparametric high-resolution imaging of native proteins by force-distance curve-based AFM. Nat Protoc. 2014;9(5):1113–30.
10. Giessibl FJ. AFM's path to atomic resolution. Mater Today. 2005;8(5):32–41.
11. Watson JD, Crick FHC. Molecular structure of nucleic acids: a structure for deoxyribose nucleic acid. Nature. 1953;171(4356):737–8.
12. Han H, Hurley LH. G-quadruplex DNA: a potential target for anti-cancer drug design. Trends Pharmacol Sci. 2000;21(4):136–42.
13. Lyubchenko YL, Shlyakhtenko LS, Ando T. Imaging of nucleic acids with atomic force microscopy. Methods. 2011;54(2):274–83.
14. Hansma HG. Surface biology of DNA by atomic force microscopy. Annu Rev Phys Chem. 2001;52(1):71–92.
15. Mou J, Czajkowsky DM, Zhang YY, Shao ZF. High-resolution atomic-force microscopy of DNA: the pitch of the double helix. FEBS Letter. 1995;371(3):279–82.
16. Ido S, Kimura K, Oyabu N, Kobayashi K, Tsukada M, Matsushige K, et al. Beyond the Helix pitch: direct visualization of native DNA in aqueous solution. ACS Nano. 2013;7(2):1817–22.
17. Maaloum M, Beker AF, Muller P. Secondary structure of double-stranded DNA under stretching: elucidation of the stretched form. Phys Rev E Stat Nonlinear Soft Matter Phys. 2011;83(3 Pt 1):031903.

18. Leung C, Bestembayeva A, Thorogate R, Stinson J, Pyne A, Marcovich C, et al. Atomic force microscopy with nanoscale cantilevers resolves different structural conformations of the DNA double helix. Nano Lett. 2012;12(7):3846–50.
19. Pyne A, Thompson R, Leung C, Roy D, Hoogenboom BW. Single-molecule reconstruction of oligonucleotide secondary structure by atomic force microscopy. Small. 2014;10(16):3257–61.
20. Klejevskaja B, Pyne ALB, Reynolds M, Shivalingam A, Thorogate R, Hoogenboom BW, et al. Studies of G-quadruplexes formed within self-assembled DNA mini-circles. Chem Commun. 2016;52(84):12454–7.
21. Zhang H, Chao J, Pan D, Liu H, Qiang Y, Liu K, et al. DNA origami-based shape IDs for single-molecule nanomechanical genotyping. Nat Commun. 2017;8:14738.
22. Gopinath A, Miyazono E, Faraon A, Rothemund PWK. Engineering and mapping nanocavity emission via precision placement of DNA origami. Nature. 2016;535(7612):401–5.
23. Han DR, Pal S, Nangreave J, Deng ZT, Liu Y, Yan H. DNA origami with complex curvatures in three-dimensional space. Science. 2011;332(6027):342–6.
24. Jiang Q, Song C, Nangreave J, Liu X, Lin L, Qiu D, et al. DNA origami as a carrier for circumvention of drug resistance. J Am Chem Soc. 2012;134(32):13396–403.
25. Lee AJ, Szymonik M, Hobbs JK, Wälti C. Tuning the translational freedom of DNA for high speed AFM. Nano Res. 2015;8(6):1811–21.
26. Herrero-Galan E, Fuentes-Perez ME, Carrasco C, Valpuesta JM, Carrascosa JL, Moreno-Herrero F, et al. Mechanical identities of RNA and DNA double helices unveiled at the single-molecule level. J Am Chem Soc. 2013;135(1):122–31.
27. Ares P, Fuentes-Perez ME, Herrero-Galan E, Valpuesta JM, Gil A, Gomez-Herrero J, et al. High resolution atomic force microscopy of double-stranded RNA. Nanoscale. 2016;8(23):11818–26.
28. Mulvihill E, van Pee K, Mari SA, Muller DJ, Yildiz O. Directly observing the lipid-dependent self-assembly and pore-forming mechanism of the Cytolytic toxin Listeriolysin O. Nano Lett. 2015;15(10):6965–73.
29. Sumino A, Yamamoto D, Iwamoto M, Dewa T, Oiki S. Gating-associated clustering-dispersion dynamics of the KcsA potassium channel in a lipid membrane. J Phys Chem Lett. 2014;5(3):578–84.
30. Milne JLS, Borgnia MJ, Bartesaghi A, Tran EEH, Earl LA, Schauder DM, et al. Cryo-electron microscopy: a primer for the non-microscopist. FEBS J. 2013;280(1):28–45.
31. Pittenger B, Erina N, Su C. Quantitative mechanical property mapping at the nanoscale with PeakForce QNM. *Bruker Application Note* #128. 2012
32. Medalsy I, Hensen U, Muller DJ. Imaging and quantifying chemical and physical properties of native proteins at molecular resolution by force–volume AFM. Angew Chem Int Ed. 2011;50(50):12103–8.
33. Rico F, Su C, Scheuring S. Mechanical mapping of single membrane proteins at submolecular resolution. Nano Lett. 2011;11(9):3983–6.
34. Pfreundschuh M, Alsteens D, Hilbert M, Steinmetz MO, Muller DJ. Localizing chemical groups while imaging single native proteins by high-resolution atomic force microscopy. Nano Lett. 2014;14(5):2957–64.
35. Amo CA, Garcia R. Fundamental high-speed limits in single-molecule, single-cell, and nanoscale force spectroscopies. ACS Nano. 2016;10(7):7117–24.
36. Adamcik J, Lara C, Usov I, Jeong JS, Ruggeri FS, Dietler G, et al. Measurement of intrinsic properties of amyloid fibrils by the peak force QNM method. Nanoscale. 2012;4(15):4426–9.
37. Sweers K, van der Werf K, Bennink M, Subramaniam V. Nanomechanical properties of α-synuclein amyloid fibrils: a comparative study by nanoindentation, harmonic force microscopy, and Peakforce QNM. Nanoscale Res Lett. 2011;6(1):270.
38. Dover RS, Bitler A, Shimoni E, Trieu-Cuot P, Shai Y. Multiparametric AFM reveals turgor-responsive net-like peptidoglycan architecture in live streptococci. Nat Commun. 2015;6:7193.

39. Schillers H, Medalsy I, Hu S, Slade AL, Shaw JE. PeakForce tapping resolves individual microvilli on living cells. J Mol Recognit. 2016;29(2):95–101.
40. Berquand A. Quantitative imaging living biological samples PeakForce QNM. *Bruker Application Note* #135. 2011.
41. Usukura E, Narita A, Yagi A, Ito S, Usukura J. An Unroofing method to observe the cytoskeleton directly at molecular resolution using atomic force microscopy. Sci Rep. 2016;6:27472.
42. Kumar S, Cartron ML, Mullin N, Qian P, Leggett GJ, Hunter CN, et al. Direct imaging of protein organization in an intact bacterial organelle using high-resolution atomic force microscopy. ACS Nano. 2017;11(1):126–33.
43. Alsteens D, Dupres V, Yunus S, Latge JP, Heinisch JJ, Dufrene YF. High-resolution imaging of chemical and biological sites on living cells using peak force tapping atomic force microscopy. Langmuir. 2012;28(49):16738–44.
44. Li A, Lim TS, Shi H, Yin J, Tan SJ, Li Z, et al. Molecular mechanistic insights into the endothelial receptor mediated Cytoadherence of Plasmodium falciparum-infected erythrocytes. PLoS One. 2011;6(3):e16929.
45. Alsteens D, Newton R, Schubert R, Martinez-Martin D, Delguste M, Roska B, et al. Nanomechanical mapping of first binding steps of a virus to animal cells. Nat Nanotechnol. 2017;12(2):177–83.
46. Kenneth RC. Image digitization. In: Microscope Image Processing; 2008. Chap. 3.
47. Fukuma T, Kimura M, Kobayashi K, Matsushige K, Yamada H. Development of low noise cantilever deflection sensor for multienvironment frequency-modulation atomic force microscopy. Rev Sci Instrum. 2005;76(5):053704.
48. Fukuma T, Kobayashi K, Matsushige K, Yamada H. True molecular resolution in liquid by frequency-modulation atomic force microscopy. Appl Phys Lett. 2005;86(19):193108.
49. Fukuma T, Kobayashi K, Matsushige K, Yamada H. True atomic resolution in liquid by frequency-modulation atomic force microscopy. Appl Phys Lett. 2005;87(3)
50. Fukuma T. Wideband low-noise optical beam deflection sensor with photothermal excitation for liquid-environment atomic force microscopy. Rev Sci Instrum. 2009;80(2):023707.
51. Fukuma T, Kobayashi K, Matsushige K, Yamada H. True molecular resolution in liquid by frequency-modulation atomic force microscopy. Appl Phys Lett. 2005;86(19)
52. Ando T, Uchihashi T, Fukuma T. High-speed atomic force microscopy for nano-visualization of dynamic biomolecular processes. Prog Surf Sci. 2008;83(7–9):337–437.
53. Bustamante C, Keller D. Scanning force microscopy in biology. Phys Today. 1995;48(12):32–8.
54. Garcia R. Amplitude modulation atomic force microscope: Chap. 8. 2010
55. Shannon CE. Communication in the presence of noise. Proc Insitute Radio Eng. 1949;31(1):10–21.
56. Ohnesorge F, Binnig G. True atomic-resolution by atomic force microscopy through repulsive and attractive forces. Science. 1993;260(5113):1451–6.
57. Giessibl FJ. Forces and frequency shifts in atomic-resolution dynamic-force microscopy. Phys Rev B. 1997;56(24):16010–5.
58. Butt HJ, Cappella B, Kappl M. Force measurements with the atomic force microscope: technique, interpretation and applications. Surf Sci Rep. 2005;59(1–6):1–152.
59. Weeks BL, Vaughn MW, DeYoreo JJ. Direct imaging of meniscus formation in atomic force microscopy using environmental scanning electron microscopy. Langmuir. 2005;21(18):8096–8.
60. Muller DJ, Schabert FA, Buldt G, Engel A. Imaging purple membranes in aqueous-solutions at subnanometer resolution by atomic-force microscopy. Biophys J. 1995;68(5):1681–6.
61. Scheuring S, Levy D, Rigaud JL. Watching the components of photosynthetic bacterial membranes and their in situ organisation by atomic force microscopy. BBA-Biomembr. 2005;1712(2):109–27.
62. Gross L, Mohn F, Liljeroth P, Repp J, Giessibl FJ, Meyer G. Measuring the charge state of an Adatom with noncontact atomic force microscopy. Science. 2009;324(5933):1428–31.

63. Welker J, Giessibl FJ. Revealing the angular symmetry of chemical bonds by atomic force microscopy. Science. 2012;336(6080):444–9.
64. Jarvis SP, Yamada H, Yamamoto SL, Tokumoto H, Pethica JB. Direct mechanical measurement of interatomic potentials. Nature. 1996;384(6606):247–9.
65. Jarvis MR, Perez R, Payne MC. Can atomic force microscopy achieve atomic resolution in contact mode? Phys Rev Lett. 2001;86(7):1287–90.
66. Albrecht TR, Quate CF. Atomic resolution imaging of a nonconductor by atomic force microscopy. J Appl Phys. 1987;62(7):2599–602.
67. Binnig G, Gerber C, Stoll E, Albrecht TR, Quate CF. Atomic resolution with atomic force microscope. Europhys Lett. 1987;3(12):1281–6.
68. Marti O, Drake B, Gould S, Hansma PK. Atomic resolution atomic force microscopy of graphite and the "native oxide" on silicon. J Vac Sci Technol A. 1988;6(2):287–90.
69. Czajkowsky DM, Hotze EM, Shao ZF, Tweten RK. Vertical collapse of a cytolysin prepore moves its transmembrane beta-hairpins to the membrane. EMBO J. 2004;23(16):3206–15.
70. Hu S, Raman A. Analytical formulas and scaling laws for peak interaction forces in dynamic atomic force microscopy. Appl Phys Lett. 2007;91(12):123106.
71. Su CM, Huang L, Kjoller K, Babcock K. Studies of tip wear processes in tapping mode (TM) atomic force microscopy. Ultramicroscopy. 2003;97(1–4):135–44.
72. San Paulo A, Garcia R. Tip-surface forces, amplitude, and energy dissipation in amplitude-modulation (tapping mode) force microscopy. Phys Rev B. 2001;64(19):193411–4.
73. Anczykowski B, Kruger D, Babcock KL, Fuchs H. Basic properties of dynamic force spectroscopy with the scanning force microscope in experiment and simulation. Ultramicroscopy. 1996;66(3–4):251–9.
74. Anczykowski B, Kruger D, Fuchs H. Cantilever dynamics in quasinoncontact force microscopy: spectroscopic aspects. Phys Rev B. 1996;53(23):15485–8.
75. Garcia R, San Paulo A. Dynamics of a vibrating tip near or in intermittent contact with a surface. Phys Rev B. 2000;61(20):13381–4.
76. San Paulo A, Garcia R. High-resolution imaging of antibodies by tapping-mode atomic force microscopy: attractive and repulsive tip-sample interaction regimes. Biophys J. 2000;78(3):1599–605.
77. Ohnesorge FM. Towards atomic resolution non-contact dynamic force microscopy in a liquid. Surf Interface Anal. 1999;27(5–6):379–85.
78. Voitchovsky K, Kuna JJ, Contera SA, Tosatti E, Stellacci F. Direct mapping of the solid-liquid adhesion energy with subnanometre resolution. Nat Nanotechnol. 2010;5(6):401–5.
79. Fotiadis D, Liang Y, Filipek S, Saperstein DA, Engel A, Palczewski K. Atomic-force microscopy: rhodopsin dimers in native disc membranes. Nature. 2003;421(6919):127–8.
80. Belikov S, Magonov S. True molecular-scale imaging in atomic force microscopy: experiment and modeling. Jpn J Appl Phys 1. 2006;45(3b):2158–65.
81. Su C, Lombrozo PM. Method and apparatus of high speed property mapping. *United States Patent* (Patent No. US 7,658,097 B2). 2010.
82. Hu Y, Hu S, Su C. Method and apparatus of operating a scanning probe microscope. *United States Patent Application Publication* (Pub. No. US 2010/0122385 A1). 2010
83. Ando T, Uchihashi T, Kodera N. High-speed AFM and applications to biomolecular systems. Annu Rev Biophys. 2013;42:393–414.
84. Brown BP, Picco L, Miles MJ, Faul CF. Opportunities in high-speed atomic force microscopy. Small. 2013;9(19):3201–11.
85. Ando T. High-speed AFM imaging. Curr Opin Struct Biol. 2014;28:63–8.
86. Payton OD, Picco L, Scott TB. High-speed atomic force microscopy for materials science. Int Mater Rev. 2016;61(8):473–94.
87. Takahashi H, Miyagi A, Redondo-Morata L, Scheuring S. Temperature-controlled high-speed AFM: real-time observation of ripple phase transitions. Small. 2016;12(44):6106–13.
88. Yamashita H, Taoka A, Uchihashi T, Asano T, Ando T, Fukumori Y. Single-molecule imaging on living bacterial cell surface by high-speed AFM. J Mol Biol. 2012;422(2):300–9.

89. Sweers KKM, Segers-Nolten IMJ, Bennink ML, Subramaniam V. Structural model for α-synuclein fibrils derived from high resolution imaging and nanomechanical studies using atomic force microscopy. Soft Matter. 2012;8(27):7215.
90. Alsteens D, Trabelsi H, Soumillion P, Dufrene YF. Multiparametric atomic force microscopy imaging of single bacteriophages extruding from living bacteria. Nat Commun. 2013;4:2926.
91. Casdorff K, Keplinger T, Bellanger H, Michen B, Schon S, Burgert I. High-resolution adhesion mapping of the odd-even effect on a layer-by-layer coated biomaterial by atomic-force-microscopy. ACS Appl Mater Interfaces. 2017;9(15):13793–800.
92. Cartagena A, Hernando-Perez M, Carrascosa JL, de Pablo PJ, Raman A. Mapping in vitro local material properties of intact and disrupted virions at high resolution using multi-harmonic atomic force microscopy. Nanoscale. 2013;5(11):4729–36.
93. Stroh C, Wang H, Bash R, Ashcroft B, Nelson J, Gruber H, et al. Single-molecule recognition imaging-microscopy. Proc Natl Acad Sci U S A. 2004;101(34):12503–7.
94. Sahin O, Magonov S, Su C, Quate CF, Solgaard O. An atomic force microscope tip designed to measure time-varying nanomechanical forces. Nat Nanotechnol. 2007;2(8):507–14.
95. Chopinet L, Formosa C, Rols MP, Duval RE, Dague E. Imaging living cells surface and quantifying its properties at high resolution using AFM in QI (TM) mode. Micron. 2013;48:26–33.
96. Garcia R, Herruzo ET. The emergence of multifrequency force microscopy. Nat Nanotechnol. 2012;7(4):217–26.
97. Bampoulis P, Sotthewes K, Siekman MH, Zandvliet HJ, Poelsema B. Graphene visualizes the ion distribution on air-cleaved Mica. Sci Rep. 2017;7:43451.
98. Xie H, Zhang H, Hussain D, Meng X, Song J, Sun L. Multiparametric Kelvin probe force microscopy for the simultaneous mapping of surface potential and Nanomechanical properties. Langmuir. 2017;33(11):2725–33.
99. Sugawara Y, Kou L, Ma Z, Kamijo T, Naitoh Y, Jun Li Y. High potential sensitivity in heterodyne amplitude-modulation Kelvin probe force microscopy. Appl Phys Lett. 2012;100(22):223104.
100. Cadena MJ, Misiego R, Smith KC, Avila A, Pipes B, Reifenberger R, et al. Sub-surface imaging of carbon nanotube-polymer composites using dynamic AFM methods. Nanotechnology. 2013;24(13):135706.
101. Kou L, Ma Z, Li YJ, Naitoh Y, Komiyama M, Sugawara Y. Surface potential imaging with atomic resolution by frequency-modulation Kelvin probe force microscopy without bias voltage feedback. Nanotechnology. 2015;26(19):195701.
102. Cadena MJ, Chen Y, Reifenberger RG, Raman A. Sub-surface AFM imaging using tip generated stress and electric fields. Appl Phys Lett. 2017;110(12):123108.
103. Wen HF, Li YJ, Arima E, Naitoh Y, Sugawara Y, Xu R, et al. Investigation of tunneling current and local contact potential difference on the TiO2(110) surface by AFM/KPFM at 78 K. Nanotechnology. 2017;28(10):105704.
104. Enriquez-Flores CI, Gervacio-Arciniega JJ, Cruz-Valeriano E, de Urquijo-Ventura P, Gutierrez-Salazar BJ, Espinoza-Beltran FJ. Fast frequency sweeping in resonance-tracking SPM for high-resolution AFAM and PFM imaging. Nanotechnology. 2012;23(49):495705.
105. Li CZ, Minne S, Pittenger B, Mednick A .Simultaneous electrical mechanical property mapping with PeakForce TUNA. *Bruker Application Note* #132. 2011
106. Li CZ, Minne S, Hu Y, Ma J, He JL, Mittel H, et al. PeakForce KPFM. *Bruker Application Note* #140. 2017.
107. Huang Z, De Wolf P, Poddar R, Li C, Mark A, Nellist MR, et al. PeakForce scanning electrochemical microscopy with Nanoelectrode probes. Microsc Today. 2016;24(06):18–25.
108. Hwang GT, Park H, Lee JH, Oh S, Park KI, Byun M, et al. Self-powered cardiac pacemaker enabled by flexible single crystalline PMN-PT piezoelectric energy harvester. Adv Mater. 2014;26(28):4880–7.
109. Hansma PK, Drake B, Marti O, Gould SAC, Prater CB. The scanning ion-conductance microscope. Science. 1989;243(4891):641–3.

110. Bard AJ. Chemical imaging of surfaces with the scanning electrochemical microscope. Science. 1991;254(5028):68–74.
111. Polcari D, Dauphin-Ducharme P, Mauzeroll J. Scanning electrochemical microscopy: a comprehensive review of experimental parameters from 1989 to 2015. Chem Rev. 2016;116(22):13234–78.
112. Meckes B, Arce FT, Connelly LS, Lal R. Insulated conducting cantilevered nanotips and two-chamber recording system for high resolution ion sensing AFM. Sci Rep. 2014;4:4454.
113. Huang ZQ, DeWolf P, Li CZ, Poddar R, Yermolenko I, Mark A, et al.. PeakForce SECM. *Bruker Application Note* #147. 2017.
114. Nellist MR, Chen Y, Mark A, Godrich S, Stelling C, Jiang J, et al. Atomic force microscopy with nanoelectrode tips for high resolution electrochemical, nanoadhesion and nanoelectrical imaging. Nanotechnology. 2017;28(9):095711.
115. Fu W, Zhang W. Hybrid AFM for nanoscale physicochemical characterization: recent development and emerging applications. Small. 2017;13(11):1603525.
116. Somnath S, Jesse S, Van Berkel GJ, Kalinin SV, Ovchinnikova OS. Improved spatial resolution for spot sampling in thermal desorption atomic force microscopy – mass spectrometry via rapid heating functions. Nanoscale. 2017;9(17):5708–17.
117. Gianoncelli A, Kourousias G, Cammisuli F, Cassese D, Rizzardi C, Radillo O, et al. Combined use of AFM and soft X-ray microscopy to reveal fibres' internalization in mesothelial cells. Analyst. 2017;142(11):1982–92.
118. Costa L, Andriatis A, Brennich M, Teulon JM, Chen SW, Pellequer JL, et al. Combined small angle X-ray solution scattering with atomic force microscopy for characterizing radiation damage on biological macromolecules. BMC Struct Biol. 2016;16(1):18.